Virginia Commonwealth University
VCU Scholars Compass

Theses and Dissertations | Graduate School

2020

The Role of Manganese in *Streptococcus sanguinis*

Tanya M. Puccio
Virginia Commonwealth University

Follow this and additional works at: https://scholarscompass.vcu.edu/etd

 Part of the Bacteria Commons, Bacterial Infections and Mycoses Commons, Bacteriology Commons, Disease Modeling Commons, Genetics Commons, Microbial Physiology Commons, Molecular Biology Commons, Oral Biology and Oral Pathology Commons, Pathogenic Microbiology Commons, and the Systems Biology Commons

© Tanya Marie Puccio

Downloaded from
https://scholarscompass.vcu.edu/etd/6438

This Dissertation is brought to you for free and open access by the Graduate School at VCU Scholars Compass. It has been accepted for inclusion in Theses and Dissertations by an authorized administrator of VCU Scholars Compass. For more information, please contact libcompass@vcu.edu.

© Tanya Marie Puccio 2020
All Rights Reserved

The Role of Manganese in *Streptococcus sanguinis*

A dissertation submitted in partial fulfillment of the requirements for the degree of Doctor of Philosophy at Virginia Commonwealth University

By

TANYA PUCCIO

BS, BA, VIRGINIA WESLEYAN UNIVERSITY, 2015

Director: TODD KITTEN, PhD

PROFESSOR, PHILIPS INSTITUTE, SCHOOL OF DENTISTRY

Virginia Commonwealth University

Richmond, Virginia

October 2020

Table of Contents

Acknowledgements

I could not have succeeded without the loving support of my friends and family. Dad, Mom, Tyler, and Brittany, thank you for always sharing words of encouragement and supporting me throughout this journey. Thank you to my best friends, Laura Thorn and Daylin Stevens, for supportive words and comic relief when I needed it most. Thank you to my partner Brendan Treynor for supporting me, especially during the particularly stressful times in lab and while writing this dissertation.

I would like to thank my Virginia Wesleyan undergraduate science advisors, Dr. Philip Rock and Dr. Joyce Easter. My initial interest in microbiology came from learning about the Human Microbiome Project in my first course with Dr. Rock and this led me to take all of his microbiology and cell biology courses. Both Dr. Rock and Dr. Easter inspired me to pursue a PhD and gave me the opportunity to conduct two different independent research projects related to microbiology. I am so glad that I chose VWC because getting a PhD wasn't even on my radar when I first went to college. Their love of science and effective science teaching was a huge factor in my success as an undergraduate and set the basis for my PhD. I thank them both so much for their continued support.

Thank you so much to my labmates, especially Karina Kunka, Dr. Shannon Green, Dr. Seon-Sook An, Rachel Korba, and Brittany Spivey. Their assistance and advice have been essential and I would not have been able to accomplish nearly as much without them. While our projects rarely overlapped and she was only a year ahead of me, Shannon trained me on many of the lab techniques and gave great feedback and advice on my projects.

I would like to thank my committee members, Dr. Phillip Hylemon, Dr. Janina Lewis, Dr. Heather Lucas, and Dr. Ping Xu. They all have provided invaluable insight and advice that have helped me progress as a scientist. Their support of me and my endeavors has been pivotal in my success as a graduate student.

I'm so grateful to the Oral Health Research Program and current and former members of the Philips Institute for Oral Health Research. Not only has this program provided me with new and unique opportunities, the nature of the Philips Institute and PhD program has always been so welcoming and collaborative. I would especially like to thank my fellow PhD students, particularly those in the first cohort: Erin Mooney and Apurva Tadimari Prabhakar. We've grown so much since 2016 and it's be an absolute pleasure to go through this experience with both of them. I also would like to acknowledge the invaluable assistance, support, and advice of Dr. Oonagh Loughran, Dr. Iain Morgan, Dr. Harvey Schenkein, Dr. Bin Zhu, Dr. Ross Belvin, Dr. Molly Bristol, Dr. Vicki Stone, Dr. Fadi El-Rami, Dr. Kat Sinclair, Ms. Dung Pham, Mrs. Margaret Poland, Ms. Nicai Zollar, Ms. Tara Nulton, and Ms. Tamara Barker. Being able to walk down the hall (pre-COVID) whenever I had questions or needed to borrow reagents was tremendously helpful in allowing me to accomplish as much as I was able to these past 5 years.

I would like to thank my fellow members of the 2015 VCU Biomedical Sciences Doctoral Portal cohort, especially Drs. Erin Garcia, Jackie Grible, Mike Kammerman, Naren

Ganjenthra Kumar, and Chris van Duyn for the biochemistry and immunology study sessions as well as advice, support, and friendship throughout the graduate school.

My collaborations have been fundamental in expanding the techniques and knowledge I have obtained in graduate school. Additionally, there are so many people who have shared their advice and knowledge that assisted with the progression of my project. My sincerest thanks to:

- Dr. Jody Turner (VCU Department of Chemistry)
- Dr. Danny Alexander (Metabolon, Inc.)
- Dr. Darrell Peterson (VCU Department of Biochemistry)
- Dr. Glen Kellogg (VCU Department of Medicinal Chemistry)
- Claudio Catalano (VCU Department of Medicinal Chemistry)
- Dr. Bob Burne (University of Florida)
- Dr. David Culp (University of Florida)
- Dr. Jeannine Brady (University of Florida)
- Dr. Sarah Palmer
- Dr. Brian Kloss (New York Structural Biology Center)
- Dr. Jian Hu (Michigan State University)
- Dr. Rachelle Gaudet (Harvard University)

I would like to thank members of the following facilities and companies for their services:

- VCU Division of Animal Resources
- VCU Microscopy Core Facility
- VCU Genomics Core Facility
- Purdue University Life Sciences Mass Spectrometry Facility
- University of Virginia Genomes Core Facility
- Metabolon, Inc.

I would like to acknowledge the work of specific people contained within this thesis:

- Dr. Shannon Green made the BCC23 marked strain (Chapter 6) for her barcode study.
- Dr. Seon-Sook An generated the BC233 mutant and completed the growth studies and rabbit experiments with this strain (Chapter 6).
- Brittany Spivey completed several of the serum growth studies in Chapter 3.
- Dr. Nick Noinaj and his lab members at Purdue University generated the *E. coli* plasmids and did the initial expression studies prior to my visit to his lab. We met through a mutual collaborator and his support was pivotal in my successful grant application. He and his lab members taught me so much about protein expression and isolation and although I have yet to successfully generate enough protein for my experiments, I am so grateful for the experience, training, and hospitality they gave me.
- Janet Taggart (University of Wisconsin-Madison) completed the *S. cerevisiae* growth experiments and sample collection for me. I am so grateful to her and Dr. David Eide for taking the time and effort to collaborate with us.

- Dr. Biswa Misra reached out through Twitter after I asked for help making sense of our metabolomics data. He contributed so much to the metabolomics analysis, figure generation, and writing of the manuscript. He also gave great feedback on my sections and encouraged me to present at my first metabolomics conference.
- Karina Kunka came to the Kitten Lab first as a summer research student, then as a postbac for 15 months before leaving for the University of Pittsburgh School of Dental Medicine. Karina completed in that short time many of the experiments involving the various mutants of other *S. sanguinis* strains, addition of various components to growth studies, and she generated original versions of several of the figures. She even learned how to do catheterization surgery on our rabbits! This thesis would not have been nearly as thorough of an analysis without her dedication to generating data and checking things off my “wish list” that I likely would have never had time to complete without her help. I am so grateful that she joined our lab for a gap year before dental school and while I know she would have made a great scientist, she will be an even better dentist.

Last but definitely not least, I would like to thank Dr. Todd Kitten. I could not have asked for a better mentor. His guidance and support have been essential to my success and I am so grateful to have had the opportunity to work in his lab. His open-door policy was wonderful, as I could work independently as much as I wanted but I always could pop in to ask questions, troubleshoot problems, discuss ideas, or just chat. He encouraged me to challenge myself and try new techniques. He has taken so much time to give constructive feedback on everything I’ve written and has been so patient through every step of this journey. He has always been so supportive of me, from encouraging my ideas and helping me navigate through challenges in the lab to supporting my career development and through my personal struggles. He genuinely cares about all students and colleagues and it shows in everything that he does. It truly has been a pleasure to work with him. He has set the bar high but I will forever aspire to be as patient and great of a mentor as he is. Thank you Todd.

The works described in this dissertation were funded by the National Institutes of Health. The National Institute of Allergy and Infectious Disease awarded R01 AI114926 to Dr. Todd Kitten. The National Institute of Dental and Craniofacial Research awarded F31 DE028468 to Tanya Puccio.

List of Figures

List of Tables

List of Supplemental Tables

List of Abbreviations

ABC	ATP-binding cassette
ANOVA	Analysis of variance
ATR	Acid tolerance response
BHI	Brain Heart Infusion (media)
CCR	Carbon catabolite repression
Cd	Cadmium
CFU	Colony forming unit
Cm	Chloramphenicol
Co	Cobalt
cre	Carbon responsive element
CSP	Competence-stimulating peptide
C-terminus	Carboxyl terminus
Cu	Copper
Erm	Erythromycin
cdH_2O	Deionized water treated with Chelex-100 resin
cPBS	PBS treated with Chelex-100 resin
DEG	Differentially expressed gene
dH_2O	Deionized water
EDTA	Ethylenediaminetetraacetic acid
FBP	Fructose-1,6-bisphosphate
Fe	Iron
GC	Gas chromatography
GOI	Gene of interest
GSH	Glutathione (reduced)
GSSG	Glutathione (oxidized)
h	Hour(s)
H_2O_2	Hydrogen peroxide
HCl	Hydrochloric acid
HS	Horse serum
ICP-MS	Inductively coupled plasma mass spectrometry
ICP-OES	Inductively coupled plasma optical emission spectroscopy
IE	Infective endocarditis
IFDC	In-frame deletion cassette
IPTG	Isopropyl-β-D-thiogalactoside
Kan	Kanamycin
KO	Knockout
KOH	Potassium hydroxide
LC	Liquid chromatography
lpm	Liters per minute
Mg	Magnesium
min	Minute(s)
Mn	Manganese

MS	Mass spectrometry
N-terminus	Amino terminus
NC	Nitrocellulose
Ni	Nickel
O_2	Molecular oxygen
OD	Optical density
PBS	Phosphate-buffered saline
PCA	Principal component analysis
PCR	Polymerase chain reaction
PMSF	Phenylmethylsulfonyl fluoride
PVDF	Polyvinyldiene fluoride
qRT-PCR	Quantitative real time PCR
RNA-seq	RNA sequencing
RNR	Ribonucleotide reductase
s	Second(s)
SD	Standard deviation
SDM	Site-direct mutagenesis
SEM	Standard error of the mean
SOEing	Splicing by overlap extension
Spc	Spectinomycin
Tet	Tetracycline
TH	Todd-Hewitt broth
TMD	Transmembrane domain
TPEN	N,N,N′,N′-tetrakis(2-pyridinylmethyl)-1,2-ethanediamine
WT	Wild type
Zn	Zinc
ZIP	ZRT-, IRT-like Protein

Abstract

The Role of Manganese in *Streptococcus sanguinis*

By Tanya Marie Puccio

A thesis submitted in partial fulfillment of the requirements for the degree of Doctor of Philosophy at Virginia Commonwealth University.

Virginia Commonwealth University, 2020

Major Director: Todd Kitten, PhD, Professor, Philips Institute for Oral Health Research

Streptococcus sanguinis is primarily associated with oral health as a commensal bacterium. As an opportunistic pathogen, *S. sanguinis* is capable of colonizing heart valve vegetations, leading to the disease infective endocarditis. Previous studies from our lab have identified the high-affinity manganese transporter SsaACB as important for endocarditis virulence. The impact that manganese depletion has on *S. sanguinis* had never been evaluated and a secondary manganese transporter has not been identified. Thus, we employed the use of a fermentor to control large-scale growth over time and depleted manganese in an Δ*ssaACB* mutant using a metal chelator, EDTA. The changes in the transcriptome and metabolome of these cells were measured and it was demonstrated that multiple systems were affected. Many of these systems were linked to carbon catabolite repression through CcpA. We found that levels of the glycolytic metabolite fructose-1,6-bisphosphate, a mediator of CcpA-dependent repression, were increased in manganese-depleted cells despite no change in glucose levels. We also evaluated the impact of low pH on the Δ*ssaACB* mutant and found that growth was

reduced at pH 6.2. The same pH did not affect the growth of the wild-type SK36 strain. Analysis of both strains in fermentor-grown cultures revealed that reducing the pH affected the manganese levels of cells and again influenced the transcription of multiple systems, many of which are members of the CcpA regulon. Finally, we identified and characterized the secondary manganese transporter, here named TmpA. TmpA is a ZIP family protein with orthologs in many prokaryotes and eukaryotes, including fourteen encoded in human cells. Most ZIP proteins primarily transport iron or zinc and can vary in metal affinity and transcriptional regulation. Here we report that this ZIP protein transports manganese and contributes to endocarditis virulence in several strains of *S. sanguinis*. We confirmed that manganese is critical for growth and virulence of *S. sanguinis* and is intricately tied to many systems through its impact on glycolysis. These findings lay the groundwork for future drug development studies targeting either one or both manganese transporters to prevent endocarditis caused by *S. sanguinis* and related species.

Chapter 1 Introduction

Streptococci and the human oral cavity

The human oral cavity is a diverse environment that can host more than 700 bacterial species (1) along with a multitude of viral and fungal species (2). In 2010, the Human Oral Microbiome Database was published (3, 4) as a part of the Human Microbiome Project (5), which provided the baseline for a "healthy" oral microbiota. This project provided a wealth of knowledge and spurred further advances in the understanding of various aspects of the oral microbiota such as community and host interactions (2, 6, 7), health vs. disease states (8-10), and biogeography (11, 12).

The most abundant and ubiquitous genus in the oral cavity is *Streptococcus* (1, 4, 13-15). Streptococci are gram-positive cocci that form chains of varying length. They can be found in many different animals and can be associated with health or disease, depending on the species and location within the body. Beginning in the early 1900s, streptococci were classified by their capacity for hemolysis on blood agar: alpha-hemolysis (green color due to iron oxidation), beta-hemolysis (clearance around colonies), or gamma-hemolysis (no hemolysis) (16-19). In 1933, R. C. Lancefield (20) published her studies on the characterization of streptococci by specific carbohydrate "group" antigens, which led to the Lancefield group classifications that were used for decades (21). In 1937, J. M. Sherman (22) further classified streptococci into four divisions: pyogenic, viridans, lactic, and enterococci. With recent advances in sequencing technology, we now classify streptococcal species based on 16S rRNA (23) and multilocus sequence analysis (24).

In the human oral cavity, several *Streptococcus* species are the primary colonizers of the salivary pellicle and provide a basis for oral biofilm development (25, 26). Oral

streptococci have diverse roles, with many species associated with healthy oral sites (27, 28) whereas others, such as *Streptococcus mutans* and *Streptococcus sobrinus,* are etiological agents of dental caries (29, 30).

Infective endocarditis

Infective endocarditis (IE) is a disease in which the inner lining of the heart (endocardium) is inflamed due to an infection (31, 32). When a heart valve or endocardium is damaged due to prior disease or valve replacement, the body will form a vegetation comprised of platelets and fibrin (33). Certain bacterial species and some fungi can colonize these sterile vegetations, inducing inflammation. IE is estimated to affect more than 40,000 people each year in the United States and kills 12-40% of patients (34-36) due to complications such as congestive heart failure and stroke (37, 38). Although rare, endocarditis can also lead to other conditions such as cellulitis (39), brain abscesses (40), and meningitis (41).

Oral bacteria can get into the blood stream through breaks in the oral mucosa caused by dental procedures (42-44), routine oral hygiene practices (45-47), mastication (48), or poor oral hygiene (49-51). Additionally, bacteria can enter the blood stream through damage to the skin, such as during intravenous drug use (52, 53). In the U.S., prevention depends upon antibiotic prophylaxis prior to dental procedures for at-risk patients (54-56). The economic burden, potential for side effects, and questionable efficacy (57-59) of this practice, as well as the increasing prevalence of antibiotic resistance (60) are all pressing concerns.

Streptococcus sanguinis

In 1946, C. F. Niven and J. C. White at Cornell University discovered a distinct subgroup of viridans streptococci recovered from subacute endocarditis patients (61-64). This group was originally called *Streptococcus s.b.e.* for subacute bacterial endocarditis and was later renamed *Streptococcus sanguis*, the Latin word for "blood." In 1997, *S. sanguis* was renamed *S. sanguinis* (Latin for "of the blood") (65).

S. sanguinis, along with its close relative *Streptococcus gordonii* (21, 66, 67), is among the oral streptococci that can produce (68, 69) and survive in (70) large quantities of hydrogen peroxide (H_2O_2). This capability allows them to compete against caries pathogens such as *S. mutans* (71) and periodontal pathogens such as *Porphyromonas gingivalis* (72). Thus, *S. sanguinis* is found in greater abundance at healthy oral sites than in carious lesions or diseased gingiva (10, 27, 30, 73, 74).

The genome of the *S. sanguinis* strain SK36 was published in 2007 (75). It encodes a variety of adhesins that enable it to act as one of the primary colonizers of the salivary pellicle (25, 76). This trait, which evolved to ensure survival in the highly diverse oral cavity, also allow *S. sanguinis* to act as an opportunistic IE pathogen under the right conditions (77-80). *S. sanguinis* and other viridans group streptococci are among the most common bacteria to be isolated from IE patients (35-45%) (81, 82). There is considerable heterogeneity between *S. sanguinis* strains though, indicating that some may be less virulent than others (83). The duplicity of this species as a mediator of health in the oral cavity vs. as an IE pathogen, as well as the controversial preventative for streptococcal IE, make it an exciting bacterium to study. It is also exceptionally competent

(84), allowing for the rapid generation of mutants through chromosomal integration of antibiotic resistance genes (85).

Metal homeostasis

Metal homeostasis is key for any living organism, as metals are vital for enzymatic function, chaperone stability, and gene regulation (86-88). Metals such as manganese (Mn), zinc (Zn), iron (Fe), magnesium (Mg), cobalt (Co), copper (Cu) and nickel (Ni) are often used by bacterial cells but can be toxic at high levels. Bacteria have evolved elaborate mechanisms for metal homeostasis (89, 90), as concentrations may fluctuate in their environment. For example, the human body exerts “nutritional immunity” by either limiting metals to restrict growth or exposing bacteria to excess metals to kill them (91-97).

Several factors influence which metal binds to a protein such as the metal’s properties, ligand properties, metal coordination number and geometry, and cellular ion concentrations (98). As some metals have similar properties and prefer the same ligands, these metals can sometimes be interchangeable *in vitro,* despite there being a preference for only one *in vivo* (99-101). This discrepancy is due to the relative binding affinity of each metal. In 1953, Irving and Williams (102) published their series which determined that relative binding affinity of metal ions to proteins is $Mg^{2+} < Mn^{2+} < Fe^{2+} < Co^{2+} < Ni^{2+} < Cu^{2+} > Zn^{2+}$. To circumvent mismetallation *in vivo*, organisms have evolved mechanisms to prevent the more competitive metals (Zn, Ni, Cu) from binding to proteins that require low-affinity metals such as Mn or Fe (103, 104). This is often achieved through strict control of bioavailable cellular metal concentrations, with those with low affinity such as Mg maintained at high concentrations whereas Zn and Cu are kept at low levels or

tightly stored (87, 98). In the gram-positive bacterium *Bacillus subtilis*, labile Fe and Mn pools are similar (105), which may lead to competition for binding of the same regulators and enzymes (87). To combat this, bacteria have evolved mechanisms for ensuring proper metallation, such as controlling the location of protein folding (106).

When faced with metal deprivation, bacteria can respond by several mechanisms (87). Bacteria can modulate intracellular metal pools by controlling the expression of metal importers and exporters using metalloregulatory systems (103, 107). Through repression of exporters and derepression of high affinity importers, bacteria attempt to transport any available metal into the cell. If they are unable to return levels to normal, cells may replace a metal-dependent enzyme for one that either is metal-independent or requires a different metal. Additionally, cells will move metals from their reservoirs and modulate their proteomes to enable the limiting metal to be used for enzymes that are most essential for growth, a phenomenon called metal sparing.

Excess metals can also damage bacterial cells (108, 109). This is often due to mismetallation of enzymes (108) or transporters (110) but excess metals can also lead to damage to the cells by other mechanisms. For example, Fe can react with oxygen (O_2) or H_2O_2 to form radicals, a process called the Fenton reaction (111). Cu is also capable of Fenton-like chemistry (112). These radicals then damage DNA, proteins, and other cellular machinery. Some bacteria, such as *Lactobacillus acidophilus* (113) and *Borreliella burgdorferi* (114) have evolved to reduce their requirement for Fe, likely to avoid such issues while growing in an aerobic environment. In bacteria such as streptococci that do utilize Fe in aerobic environments, Fe-mediated oxidative stress is managed by iron-

storage proteins like Dpr (115-119) and by reducing Fe levels (120) in the presence of oxygen.

Manganese

Mn is an essential micronutrient and empowered the evolution of life in the presence of oxygen (121). Mn is estimated to be the cofactor of ~6% of enzymes (122), although this may be an underestimate given its poor binding affinity (99, 102). Mn is capable of protecting cells from oxidative stress through several mechanisms (107, 123-125). When in complex with small molecules such as bicarbonate or phosphate, Mn can detoxify superoxide (126-129). Mn is also a cofactor for some superoxide dismutase enzymes, such as SodA in *S. sanguinis* (130), which catalyzes the disproportionation of superoxide into O_2 and H_2O_2. Mn can also replace Fe in some enzymes, which protects the protein from Fenton reaction-mediated damage (131, 132).

Mn has been linked to virulence in many human pathogens, including streptococci (133-135). In streptococci, the LraI family of ABC transporters has been found to be important for Mn and Fe transport (130, 136, 137). In the early 1990s, the first articles characterizing the lipoprotein component in *S. sanguinis*, SsaB, were published (138, 139). Previous studies from our lab have established that SsaB and the entire *ssaACB* operon are important for virulence, Mn and Fe transport, and oxidative stress tolerance (83, 120, 130). The importance of SsaACB, its conserved nature across most streptococci and many other bacteria, and the lack of a human equivalent make it an excellent drug target. The lipoprotein component of the ortholog in *S. pneumoniae*, PsaA, was the subject of several drug target screens (140, 141) and the ortholog in *Streptococcus parasanguinis*,

FimA, was tested as a vaccine (142). These studies have laid the groundwork for future drug and vaccine screens targeting this transport system.

Expression of *ssaACB* is controlled by the MntR ortholog SsaR (130). In *Bacillus subtilis*, when Mn is present in sufficient levels, it binds to two sites within MntR, stabilizing the protein (143). MntR is then able to bind to DNA and repress transcription of its regulon. In times of Mn depletion, insufficient Mn is available to bind at both metal binding sites in MntR, thus derepressing transcription of *ssaACB* orthologs to facilitate Mn import into the cell. Mismetallation of one MntR metal binding site with Fe in *B. subtilis* leads to distortion of the other site, preventing the conformational change that would normally allow DNA binding (144). Similar derepression was observed with Zn in *S. pneumoniae* (145, 146). Thus, high Fe:Mn or Zn:Mn ratios may prevent repression of *ssaACB* in *S. sanguinis*.

Some *Streptococcus* species also encode a secondary Mn transporter, MntH, from the NRAMP family (147-149). However, the most commonly used strain of *S. sanguinis*, SK36, lacks a MntH ortholog and only four of the sequenced *S. sanguinis* strains encode a MntH protein (83, 150). This indicates that there may be another secondary transporter present in most strains (151), as Δ*ssaACB* mutants grew normally in Mn-replete media, Brain Heart Infusion (BHI) (120). In 12% O_2 rabbit serum, our *in vitro* model of IE (130), the poor growth phenotype of an Δ*ssaACB* mutant could be rescued with only 2 µM Mn (120), providing further evidence for the existence of another Mn transporter. *S. sanguinis* also encodes two putative Mn exporters, MntE (109, 152, 153) and MgtA (154).

Labile Mn pools in lactic acid bacteria (125) and *Deinococcus radiodurans* (155, 156) were found to be primarily bound to phosphoryl-containing ligands and nitrogenous compounds (87). Additionally, most Mn was found to be bound to superoxide dismutase

enzymes in *D. radiodurans* (155) and *Bacillus anthracis* (157), highlighting the key role of Mn in aerobic bacterial growth.

Research Objective

The objective of this dissertation was to evaluate the role of Mn in *Streptococcus sanguinis* growth. While previous studies in *S. sanguinis* and other streptococci have determined that Mn is important for virulence, only a few enzymes and pathways have been found to be Mn dependent. Thus, we hypothesized that there must be other systems that rely on Mn for proper function. We used two approaches, transcriptomics and metabolomics, in order to observe both the regulatory changes as well as their outcomes. Additionally, we set out to determine the role of Mn in growth under low pH conditions to mimic what *S. sanguinis* might encounter in its native environment, the oral cavity. Finally, we identified a secondary Mn transporter and characterized its role in *S. sanguinis* growth and virulence and its transport capabilities.

Chapter 2 General Materials and Methods

Bacterial strains and growth conditions

The *S. sanguinis* strains and mutants are listed in the Materials and Methods section of each chapter. All wild-type (WT) strains, with the exception of VMC66 and BCC23, were donated by Mogens Killian, Aarhus University, Denmark. Unless otherwise specified, WT and all mutants are derived from SK36, which was the first *S. sanguinis* strain to have its whole genome sequenced (75). All strains were grown in overnight cultures from single-use aliquots of cryopreserved cells, diluted 1000-fold in BHI media (Beckinson Dickinson). Mutant strains were incubated with the appropriate antibiotics: kanamycin (Kan; Sigma-Aldrich) 500 ug mL^{-1}; tetracycline (Tet; Sigma-Aldrich) 5 µg mL^{-1}; erythromycin (Erm; Sigma-Aldrich); 10 µg mL^{-1}; chloramphenicol (Cm; Fisher Scientific) 5 µg mL^{-1}; spectinomycin (Spc; Sigma-Aldrich) 200 µg mL^{-1}. The cultures were then incubated 37°C for 16-20 h with the atmospheric condition set to 1% (1% O_2, 9.5% H_2, 9.5% CO_2 and 80% N_2) or 6% (6% O_2, 7% H_2, 7% CO_2 and 80% N_2) oxygen using a programmable Anoxomat™ Mark II jar-filling system (AIG, Inc.).

For growth studies, plating was used to enumerate colony forming units (CFUs). To determine CFUs, samples were sonicated for 90 s using an ultrasonic homogenizer (Biologics, Inc) to disrupt chains prior to dilution in PBS and plated using an Eddy Jet 2 spiral plater (Neutec Group, Inc.). For static growth studies, tubes containing either 100% pooled rabbit serum (Gibco) or BHI were pre-incubated at 37°C at the indicated oxygen concentrations. In addition to 1% or 6% O_2, 12% O_2 (12% O_2, 4.3% CO_2, 4.3% H_2) was used in some experiments, as it is the oxygen concentration of arterial blood (158) and used as our *in vitro* model of IE (130). Each tube was then inoculated with a 10^{-6}-fold

dilution of the overnight pre-culture. The inoculated tubes were returned to incubate at the same oxygen concentration. Cultures were removed after 24 h, sonicated, and diluted in PBS prior to plating on BHI agar. Plates were incubated at 37°C for 24-48 h in 0% O_2 with a palladium catalyst prior to colony enumeration.

Mutagenesis and transformation

Gene knockout mutants were either generated previously (83, 85) or by gene splicing by overlap extension (SOEing) PCR (159) where the gene(s) of interest (GOI) were replaced with an antibiotic resistance gene or cassette. Transformations were performed using the protocol described previously (160). Briefly, an overnight culture of the parent strain was grown in Todd Hewitt (TH; Beckinson Dickinson) broth with horse serum (HS; Invitrogen), then diluted 200-fold and incubated at 37°C. Optical density (OD_{600}) of tube cultures was determined using a ThermoScientific BioMate 3S UV-VIS spectrophotometer. Knockout construct DNA (100 ng) and *S. sanguinis* competence stimulating peptide (70 ng) were added to the culture (OD_{600} ~0.07) and incubated at 37°C for 1.5 h prior to selective plating on BHI agar plates with antibiotics at concentration listed above. All plates were incubated for at least 24 h at 37°C under anaerobic conditions in an Anoxomat jar with a palladium catalyst. All mutants were confirmed to have the expected composition by sequence analysis of the DNA flanking the insertion sites.

Markerless mutants were generated using a mutation system described previously (161, 162). Briefly, the in-frame deletion cassette (IFDC) was amplified from the *S. sanguinis* IFDC2 strain and combined with flanking region from the GOI using gene SOEing. The parent strains were then transformed as described above, plating on BHI agar plates containing Erm. A gene SOEing product merging the two flanking regions of the GOI was

then generated. This SOEing product was then used to transform the Erm^R colonies from the first transformation. Immediately prior to plating on agar plates containing 20 mM 4-chloro-phenylalanine (4-CP; Sigma-Aldrich), the cells were washed twice with PBS to remove excess media. Resulting colonies were then screened for Erm sensitivity and sequenced to confirm removal of the desired gene and IFDC2.

Metal analysis

Cells were collected under various conditions and centrifuged at 3,740 x *g* for 10 min at 4°C. The supernatant was decanted and the cell pellet was washed twice with cold cPBS (PBS treated with Chelex-100 resin (Bio-Rad) for 2 h, then filter sterilized and supplemented with EDTA to 1 mM). The pellet was then divided for subsequent acid digestion or protein concentration determination. Trace metal grade (TMG) nitric acid (15%) (Fisher Chemical) was added to one portion of the pellet. The pellet was digested using an Anton Paar microwave digestion system using a modified Organic B protocol: 120°C for 10 min, 180°C for 20 min, with the maximum temperature set to 180°C. The digested samples were then diluted 3-fold with Chelex-treated dH_2O. Metal concentrations were determined using an Agilent 5110 inductively coupled plasma-optical emission spectrometer (ICP-OES) or an Agilent 8900 ICP-QQQ-MS (ICP-MS). Concentrations were determined by comparison with a standard curve created with a 10 μg ml^{-1} multi-element standard (CMS-5; Inorganic Ventures) diluted in 5% TMG nitric acid. Pb (Inorganic Ventures) was used as an internal standard (10 μg ml^{-1}). The other portion of the pellet was resuspended in PBS and mechanically lysed using a FastPrep-24 instrument with Lysing Matrix B tubes (MP Biomedicals) as described previously (101). Insoluble material was removed by centrifugation. Protein concentrations were

determined using a bicinchoninic acid (BCA) Protein Assay Kit (Pierce) as recommended by the manufacturer, with bovine serum albumin as the standard. Absorbance was measured in a black, flat-bottom 96-well plate (Greiner) using a microplate reader (BioTek).

Fermentor set-up

Fermentor experiments were set up and run as described in T. Puccio and T. Kitten (163). A BIOSTAT® B bioreactor (Sartorius Stedim) with a 1.5-L capacity UniVessel® glass vessel was used for growth of 800-mL cultures at 37°C. Cultures were stirred at 250 rpm and pH was maintained by the automated addition of 2 N KOH (Fisher Chemical). A 40-mL overnight pre-culture of *S. sanguinis* was grown as described above and centrifuged for 10 minutes at 3,740 *x g* in an Allegra X-142 centrifuge at 4°C (Beckman-Coulter). The supernatant was discarded and the cells were resuspended in BHI prior to inoculation. At the peak OD, input flow of fresh BHI was set to 17% (~700 mL h^{-1}), and output flow of waste was set to 34%. Cells were allowed to acclimate to the new conditions for 1 h. The T_{-20} sample was aseptically removed for total RNA isolation, metabolomics, or metal analysis. The fermentor culture was then treated at T_0 with either EDTA or HCl. Samples were taken for each post-treatment time point (T_{10}, T_{25}, T_{50}). In some experiments, a divalent metal (Puratronic™; Alfa Aesar) was added to the carboy (T_{66}) and vessel (T_{70}) at a final concentration of 100 µM and samples were taken for ICP-OES at T_{80}.

RNA isolation

For fermentor samples, 2 mL of culture was added to 4 mL RNAprotect Bacteria Reagent (Qiagen) and immediately vortexed for 10 s. The sample was then incubated at room

temperature for 5-90 min. The samples were then centrifuged for 10 min at 3,740 x *g* at 4°C. The supernatant was discarded and the samples stored at -80°C.

For tube cultures, cells were grown under various conditions and swirled in a dry ice/ethanol bath for 30 s before centrifuging for 10 min at 3,740 x *g* at 4°C. The supernatant was discarded and the samples stored at -80°C.

RNA isolation and on-column DNase treatment were completed using the RNeasy Mini Kit and RNase-Free DNase Kit, respectively (Qiagen). RNA was eluted in 50 µL RNase-Free water (Qiagen). A second DNase treatment was then performed on the samples (Invitrogen). Total RNA was quantified and purity was assessed using a Nanodrop 2000 Spectrophotometer (ThermoScientific).

RNA-seq analysis pipeline

Using Geneious 11.1 (https://www.geneious.com), sequence reads were trimmed using the BBDuk Trimmer prior to mapping to either the SK36 genome or a modified version, in which the *ssaACB* operon was replaced with the *aphA-3* sequence. The locus tags are from the Genbank® annotation (164) available at the time; the annotations were updated shortly before publication and the new locus tags are included in Supplementary Tables 3.1 and 5.1 for reference. PATRIC annotations (https://patricbrc.org/) (165) are also included. Reads for each post-treatment sample were compared to the corresponding pre-treatment (T_{-20}) sample using DESeq2 (166) in Geneious to determine $\log_2$ fold changes and adjusted *P*-values. Principal component analysis was completed using R (version 3.6.1) and RStudio (version 1.2.5033-1) with Bioconductor (Bioconductor.com) package pcaExplorer version 2.13.0 (167). Volcano plots were generated using R and RStudio with Bioconductor package EnhancedVolcano (168). All differentially expressed

genes (DEG) were input into the DAVID database (https://david.ncifcrf.gov/summary.jsp) (169). The KEGG_pathway option was chosen for functional annotation clustering. The *P*-value shows the significance of pathway enrichment. DAVID pathway figures were generated using an R script (https://github.com/DrBinZhu/DAVID_FIG).

Quantitative real-time polymerase chain reaction

RNA was collected as described in the main text. Libraries of cDNA were created using SensiFAST cDNA Synthesis Kit (Bioline). Control reactions without reverse transcriptase were conducted to confirm the absence of contaminating DNA in all samples. qRT-PCR was performed using SYBR Green Supermix (Applied Biosystems) on an Applied Biosystems 7500 Fast Real Time PCR System using the primers listed in each applicable chapter. Relative gene expression was analyzed using the $2^{-\Delta\Delta CT}$ method (170) with *gapA* serving as the internal control (84).

Data analysis and presentation

Statistical tests for small data sets were performed in GraphPad Prism (graphpad.com). Significance was determined by t-test or analysis of variance (ANOVA) as indicated in the figure legends. Tests were paired only if matching was effective. *P*-values ≤ 0.05 were considered significant. For ANOVA, a Tukey-Kramer test for multiple comparisons was used when $P \leq 0.05$. DESeq2 calculations of RNA-Seq datasets were completed in Geneious 11.1 or in the pcaExplorer R package. Confidence intervals (95%) of replicate samples were determined by the pcaExplorer R package. Graphs and figures were constructed using GraphPad Prism (graphpad.com) or Biorender (Biorender.com).

Chapter 3 Impact of Mn Depletion on the Transcriptome of *S. sanguinis*

Rationale

S. sanguinis can grow efficiently in low-Mn conditions due to the presence of a high-affinity Mn transporter, SsaACB. When the genes encoding SsaACB are deleted from the genome, this mutant is severely reduced in virulence. Previous studies have determined that at least two enzymes in *S. sanguinis* require a Mn cofactor but we hypothesized that Mn depletion had a larger impact on the cell.

Copyright Disclaimer

Partial results of this chapter have been accepted for publication by Frontiers in Microbiology as the following manuscript:

Puccio, T., Kunka, K.S., Zhu, B., Xu, P., Kitten, T. 2020. Manganese depletion leads to multisystem changes in the transcriptome of the opportunistic pathogen *Streptococcus sanguinis*. *Front Microbiol* doi:10.3389/fmicb.2020.592615.

Introduction

As discussed in Chapter 1, Mn is important for oxidative stress tolerance and acts as a cofactor for key enzymes in many bacteria. Previous work from our lab established that the ABC transporter SsaACB is important for Mn transport, aerobic serum growth, and virulence in a rabbit model of IE (83, 120, 130). In *S. sanguinis*, Mn acts as a cofactor for superoxide dismutase (SodA) (171, 172) and the aerobic class 1b ribonucleotide reductase (NrdF) (100, 101). Loss of SodA activity alone cannot account for the reduction in virulence (130). NrdF activity is essential for virulence (101), but it is likely that these are not the only two Mn-cofactored enzymes or Mn-dependent pathways in *S. sanguinis*. In a previous microarray analysis of Mn depletion in the related species *S. pneumoniae*

(173), it was found that only a few genes were differentially expressed in response to either deletion of the pneumococcal SsaB ortholog, PsaA, or growth in media without supplemental Mn. However, these data alone are insufficient to explain the decreased growth of these mutants in Mn-deplete media. In this study, we sought to determine the overall effect of Mn depletion on the transcriptome of *S. sanguinis* in an attempt to identify other Mn-dependent pathways. Here we report that while there were some similarities with this previous study, we found a larger number of differentially expressed genes, providing new insights into the role of Mn in streptococci.

Results

Generation of Δ*ssaACB* mutants and previous studies with these strains

While previous studies have examined the function of the SsaB lipoprotein (130) and aspects of the entire SsaACB transporter (83, 120), the generation of the Δ*ssaACB* mutant has not yet been fully described. The mutant was generated by gene SOEing PCR (159) in which flanking region from either side of the operon were spliced with an antibiotic resistance gene between them. Thus, all three genes encoding the transporter were replaced by a single gene, either *aphA-3* (kanamycin; Kan) or *tetM* (tetracycline; Tet) (83), whose expression was dependent upon the promoter and other control elements (130) upstream from *ssaA*.

Of note, it was found that *ssaA* has two putative start sites, as the original annotation called for the protein sequence to begin with MYIKTIEVEM (Figure 3.1). Initial attempts to generate a knockout mutant using this start site yielded few transformants (data not shown). A second potential start site was identified, which appeared much more likely as it was the correct distance from the predicted Shine-Dalgarno sequence. Transformations

starting with *aphA-3* at this second site resulted in many transformants (data not shown). Further analysis by NCBI BLAST (174) comparing the sequences of other *S. sanguinis* strains, as well as *S. gordonii* and *S. mutans* strains, showed that the first methionine is either not present or not in-frame in all strains or species, confirming that the correct start site is likely the second methionine depicted in Figure 3.1.

We previously assessed both Δ*ssaACB* mutants in our rabbit model of IE and both were recovered in similar quantities (175), indicating that the different antibiotic selection markers did not impact virulence. The kanamycin resistant version, JFP169, was utilized in a recent study to determine intracellular metal speciation in *S. sanguinis* (120), where it was also determined that this mutant grew poorly in pooled rabbit serum at 12% O_2. The addition of 5 µM Mn improved the growth to WT-like levels (120). The Δ*ssaACB* mutant was also deficient in Mn and Fe levels as measured by inductively coupled plasma optical emission spectroscopy (ICP-OES) (120). This deficiency was relieved when complemented by insertion of the *ssaACB* genes into an ectopic chromosomal expression site (120, 176). Thus, we used these Δ*ssaACB* mutants for the studies contained within this thesis.

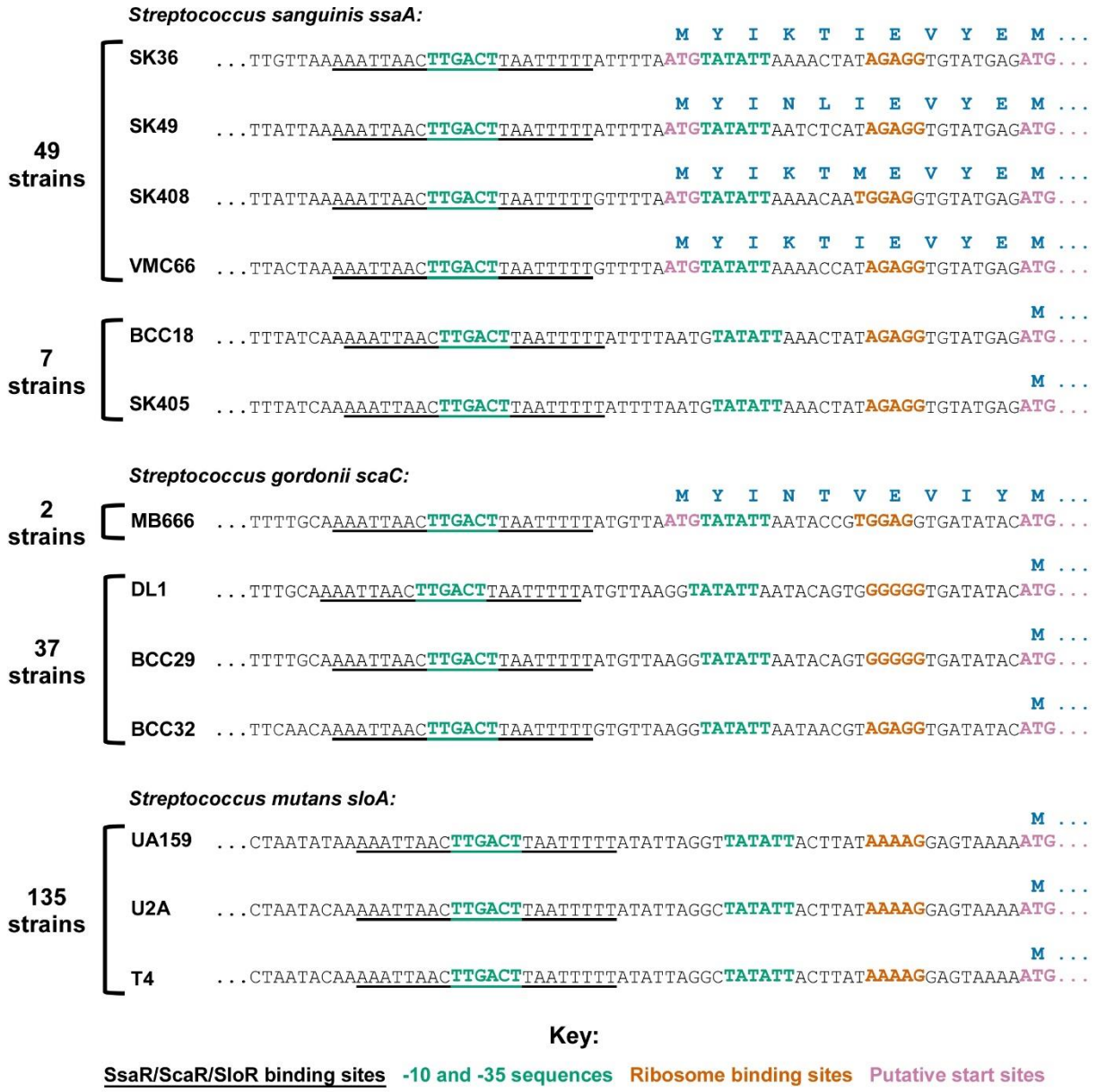

Figure 3.1 *ssaA* start site determination
Sequences are aligned to that of the SK36 *ssaA* gene and upstream region, which are depicted according to the original GenBank annotation. All sequences contained within a given bracket share the same left-most in-frame ATG codon (pink). Other elements are defined above and were originally predicted based on sequence alignments (136), but have been defined experimentally in *S. gordonii* (177) and *S. mutans* (178).

Further assessment of the Δ*ssaACB* mutant

We next examined whether these mutant cells were quiescent or dead after culture in aerobic rabbit serum by adding Mn 24 h after inoculation (Figure 3.2). We observed that when we added Mn after 24 h of incubation and then continued incubation for another 24 h, the cells grew to the same density as those in a tube in which Mn had been added at the time of inoculation (T_0). In contrast, the cell density of the culture to which no Mn had been added declined slightly at 48 h, indicating that the cells are quiescent at 24 h but may start to die between 24-48 h.

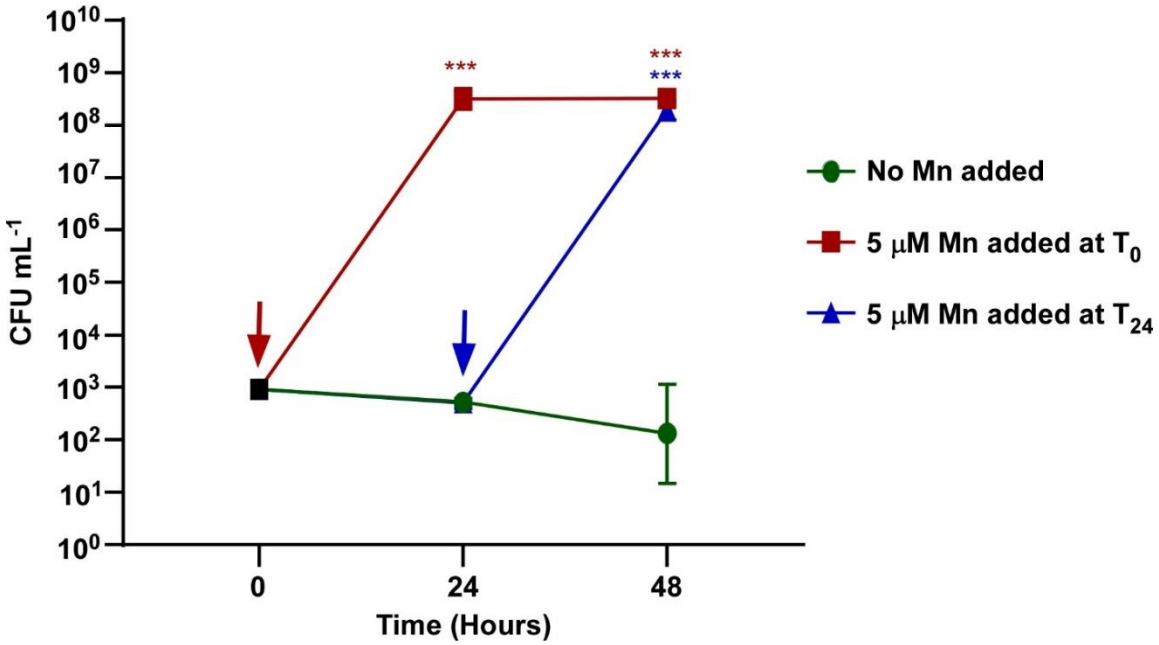

Figure 3.2 Aerobic serum growth of the Δ*ssaACB* mutant after 24 and 48 hours
Cultures were inoculated into rabbit serum that was preincubated at 12% O_2. Mn was added to one culture tube immediately after inoculation (red arrow) and another after 24 h growth (blue arrow). All culture tubes were returned to 12% O_2. Growth was assessed 24 and 48 h after inoculation by plating on BHI agar. The means ± SD of at least three independent experiments are displayed and significance was determined by one-way ANOVA with a Tukey multiple comparisons test. ****P* ≤ 0.001 as compared to the sample with no Mn added at the same time point.

Selection of fermentor growth conditions for Mn depletion

For this study, we were interested in measuring transcriptional changes resulting from Mn depletion in metabolically active cells. We also wanted to examine the cells as they

transitioned from Mn replete conditions to Mn insufficiency, a task that would most easily have been accomplished by addition of a strong and selective Mn chelator to growing cells. However, we were aware of no such chelator. We therefore explored the use of the non-specific chelator EDTA in conjunction with a Δ*ssaACB* mutant. As described above, this mutant was previously found to be deficient in Mn and Fe transport and aerobic growth in low-Mn media (120).

We achieved reproducible, large-scale growth in a fermentor using BHI broth. Typical chemostat conditions (179) could not be identified that supported growth of the SK36 WT strain but not the Δ*ssaACB* mutant, even when aeration was increased (data not shown). However, we found that when the dilution rate was increased to 0.875 vessel volumes per h, addition of 100 μM EDTA to both the fermentor vessel and media carboy dramatically reduced the optical density ($OD_{840\text{-}910}$) of the Δ*ssaACB* mutant cultures (Figure 3.3A), while not affecting the WT strain (Figure 3.3B). The effect of EDTA addition on the OD of the Δ*ssaACB* cultures typically became apparent after 38 min (Figure 3.3A inset). The addition of EDTA slowed the growth of the Δ*ssaACB* mutant but did not kill the cells entirely because when the media pumps were shut off ~80 min post-EDTA addition, the OD began to increase immediately (data not shown). Without EDTA, the Δ*ssaACB* mutant grew similar to WT (data not shown).

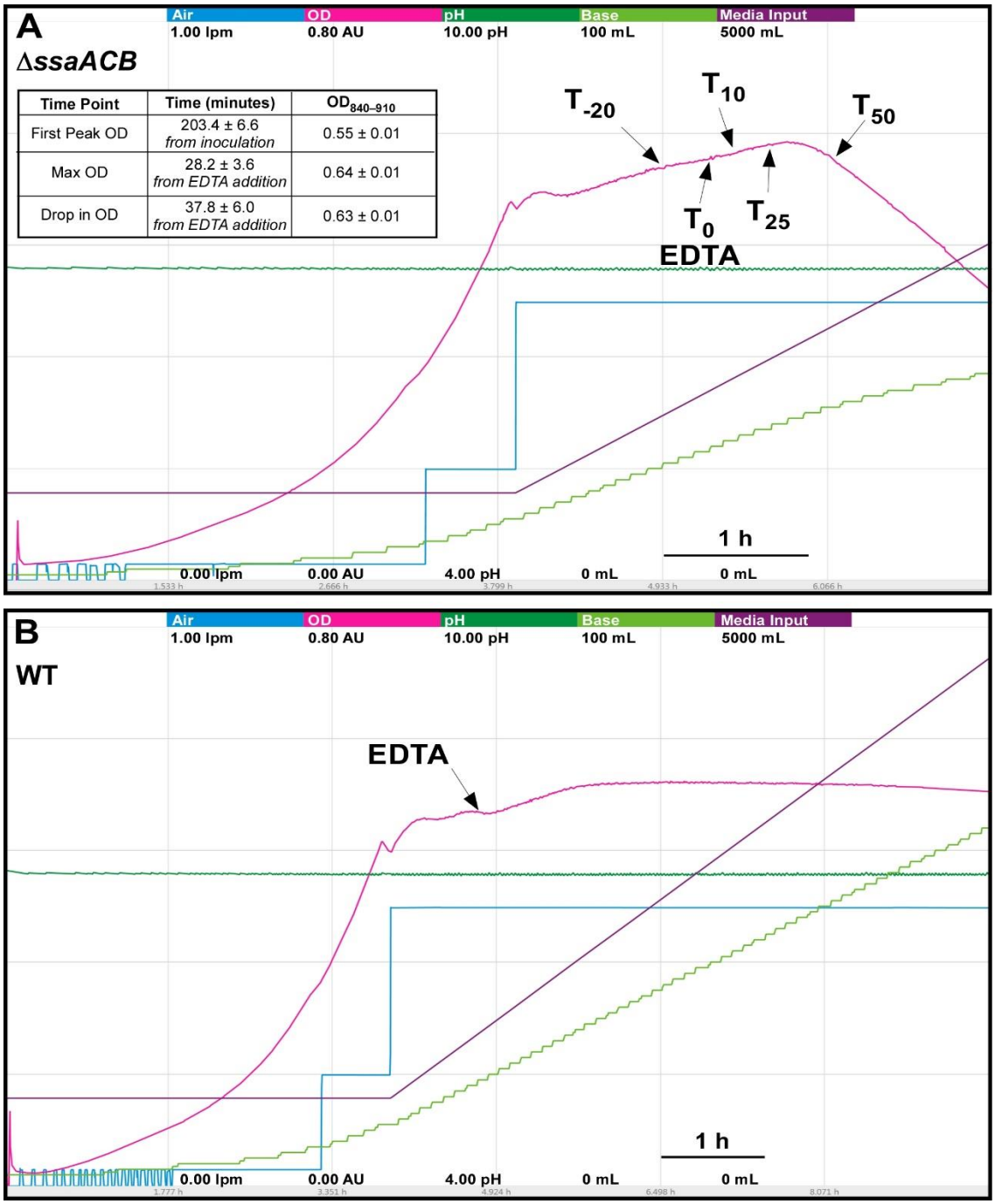

Figure 3.3 Aerobic fermentor growth of Δ*ssaACB* and WT strains

Representative charts for fermentor growth of *S. sanguinis* (A) Δ*ssaACB* and (B) WT cells. Each color represents a different parameter: cyan - air flow (liters per min; lpm), pink - optical density (840-910 nm; absorbance units; AU), dark green - pH, light green - base input (KOH), purple - media input (total volume). Each color represents a different parameter as labeled at the top of the figure. The scale for each parameter is indicated by the values under each respective parameter label (minimum at the bottom, maximum at the top). The time scale is indicated by the bar in the bottom right portion of each chart. Cells were grown under aerobic conditions with EDTA added 80 min (T_0) after the media input and output pumps were turned on and the air flow was set to 0.5 lpm. Each sample time point is labeled.

To determine if a lack of available Mn caused the EDTA-dependent reduction in the Δ*ssaACB* growth rate, samples of both WT and Δ*ssaACB* were collected at T_{-20}, T_{10}, T_{25}, and T_{50}, where 100 µM EDTA was added to the media carboy at T_{-4} and to the vessel at T_0 (Figure 3.3). Washed cells were analyzed using ICP-OES (Figure 3.4). EDTA addition to WT did not significantly alter cellular levels of four of the metals measured—Mn, Fe, zinc (Zn), or magnesium (Mg) (Figure 3.4A). Mn was the only metal significantly reduced in the post-EDTA samples as compared to pre-EDTA for Δ*ssaACB* (Figure 3.4B). While Fe levels were low in the Δ*ssaACB* mutant, they did not drop significantly after the addition of EDTA (Figure 3.4B). This is consistent with the metal content of the Δ*ssaACB* mutant measured previously under aerobic growth conditions (120). Neither Zn nor Mg levels were significantly affected (Figure 3.4). Cobalt and copper levels were at or below the limit of detection in both strains (data not shown).

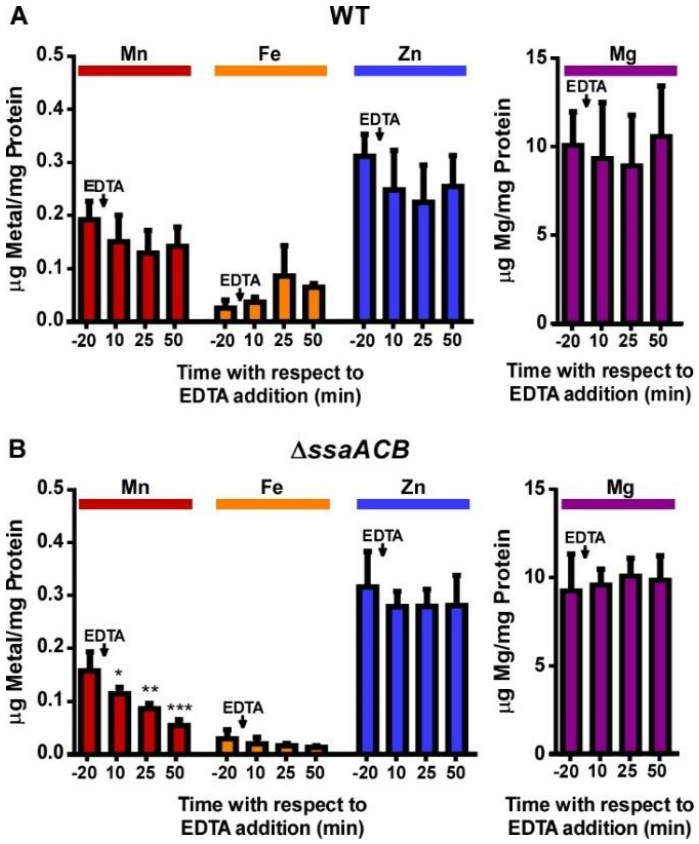

Figure 3.4 Effect of EDTA on metal content of fermentor-grown cells
WT (A) and Δ*ssaACB* (B) cells were collected from the fermentor at each time point and analyzed for cellular metal content using ICP-OES. Means and standard deviations of three replicates are shown. Significance was determined either by repeated measures ANOVA or by one-way ANOVA if matching was not effective, with a Tukey-Kramer multiple comparisons test to T_{-20}. *$P \leq 0.05$, ** $P \leq 0.01$, *** $P \leq 0.001$. Time points not labeled were not significantly different from T_{-20}. For Fe, two T_{-20} replicates in (A) and at least two replicates for each time point in (B) were below the limit of detection.

As another test of metal specificity, 100 µM of either Mn^{2+} or Fe^{2+} sulfate was added to the vessel 70 min post-EDTA addition. The addition of Mn^{2+} eliminated, and then reversed, the post-EDTA decline in OD, while Fe^{2+} had no discernible effect (Figure 3.5). The metal content of samples collected 10 min after addition of Mn^{2+} or Fe^{2+} (T_{80}) revealed that both Mn and Fe were taken up by cells, resulting in significantly higher levels than at T_{-20} (Figure 3.6). Although neither Zn nor Mg levels were significantly affected by addition of EDTA (Figure 3.4), 100 µM of either Zn^{2+} or Mg^{2+} sulfate was added at T_{70} for at least

two fermentor runs each and, like Fe^{2+}, neither produced any apparent effect on the growth (Figure 3.7).

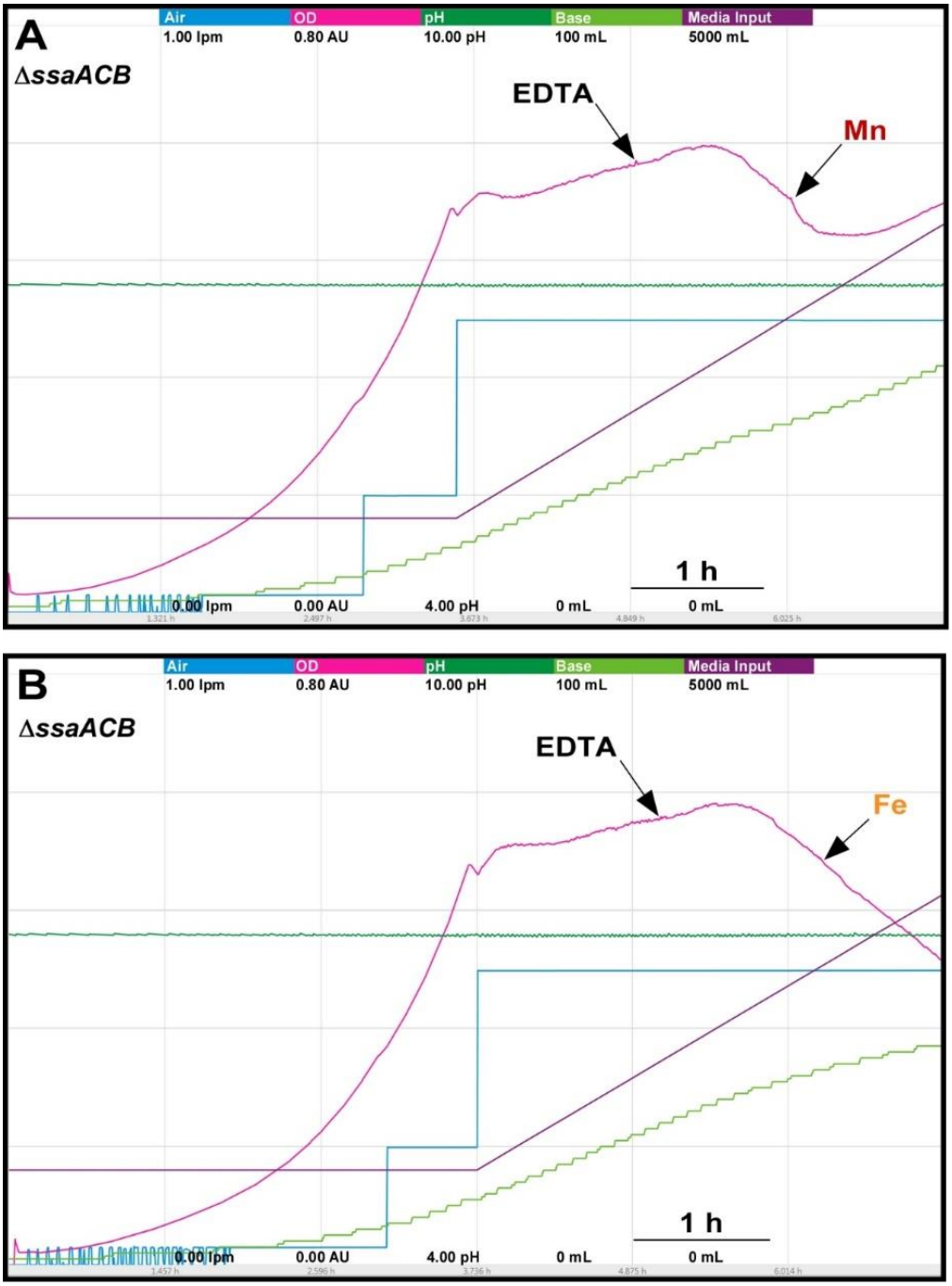

Figure 3.5 Addition of Mn or Fe to fermentor-grown Δ*ssaACB* cells post-EDTA
Fermentor growth of Δ*ssaACB* with the addition of 100 µM EDTA at T_0 as described previously, with 100 µM of either (A) Mn^{2+} or (B) Fe^{2+} added at T_{70}. Colors and labels are as in Figure 3.3. The time scale is indicated by the bar in the bottom right portion of the each chart. Each chart is representative of at least three replicates.

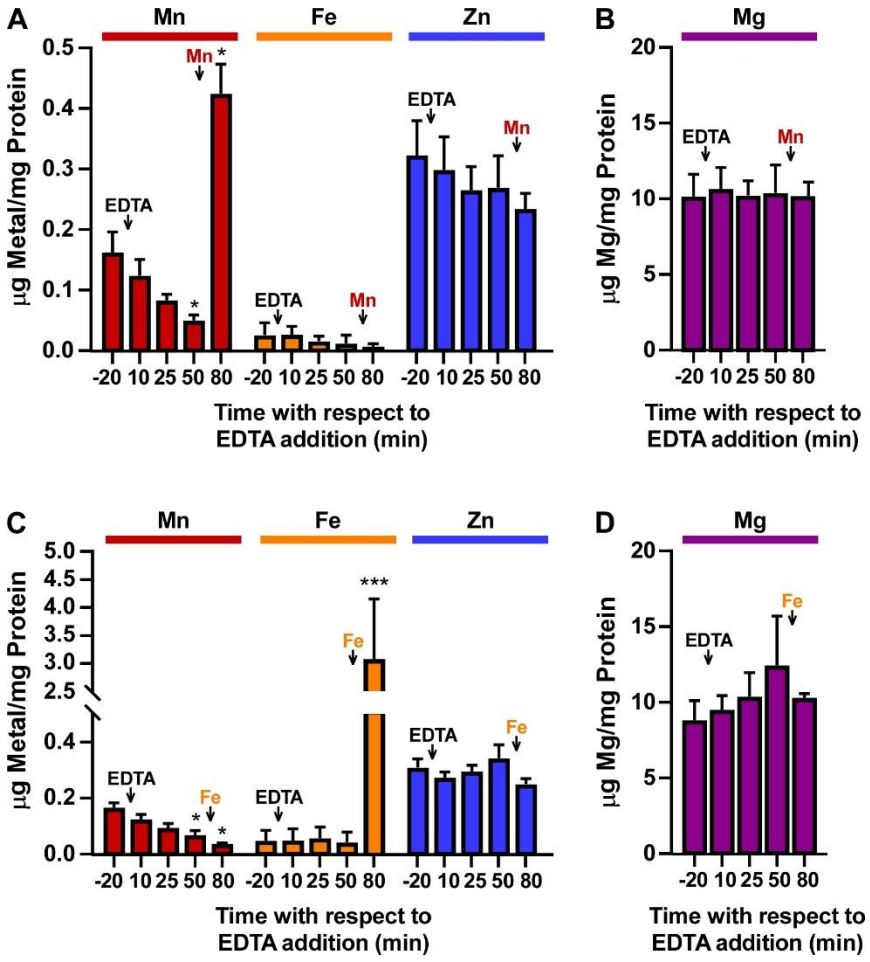

Figure 3.6 Metal content of fermentor-grown Δ*ssaACB* cells with Mn or Fe added
Samples of Δ*ssaACB* cells were collected from the fermentor at each time point and analyzed for cellular metal content using ICP-OES. The T_{80} time point is 10 min after the addition of 100 µM of either (A-B) Mn^{2+} or (C-D) Fe^{2+} added at T_{70} as depicted in Figure 3.5. Means and SD of three replicates are shown. Significance was determined for each metal by repeated measures ANOVA or one-way ANOVA if matching was not effective. A Tukey-Kramer multiple comparisons test was used for comparison to T_{-20} for each metal; $*P \leq 0.05$, $***P \leq 0.0001$.

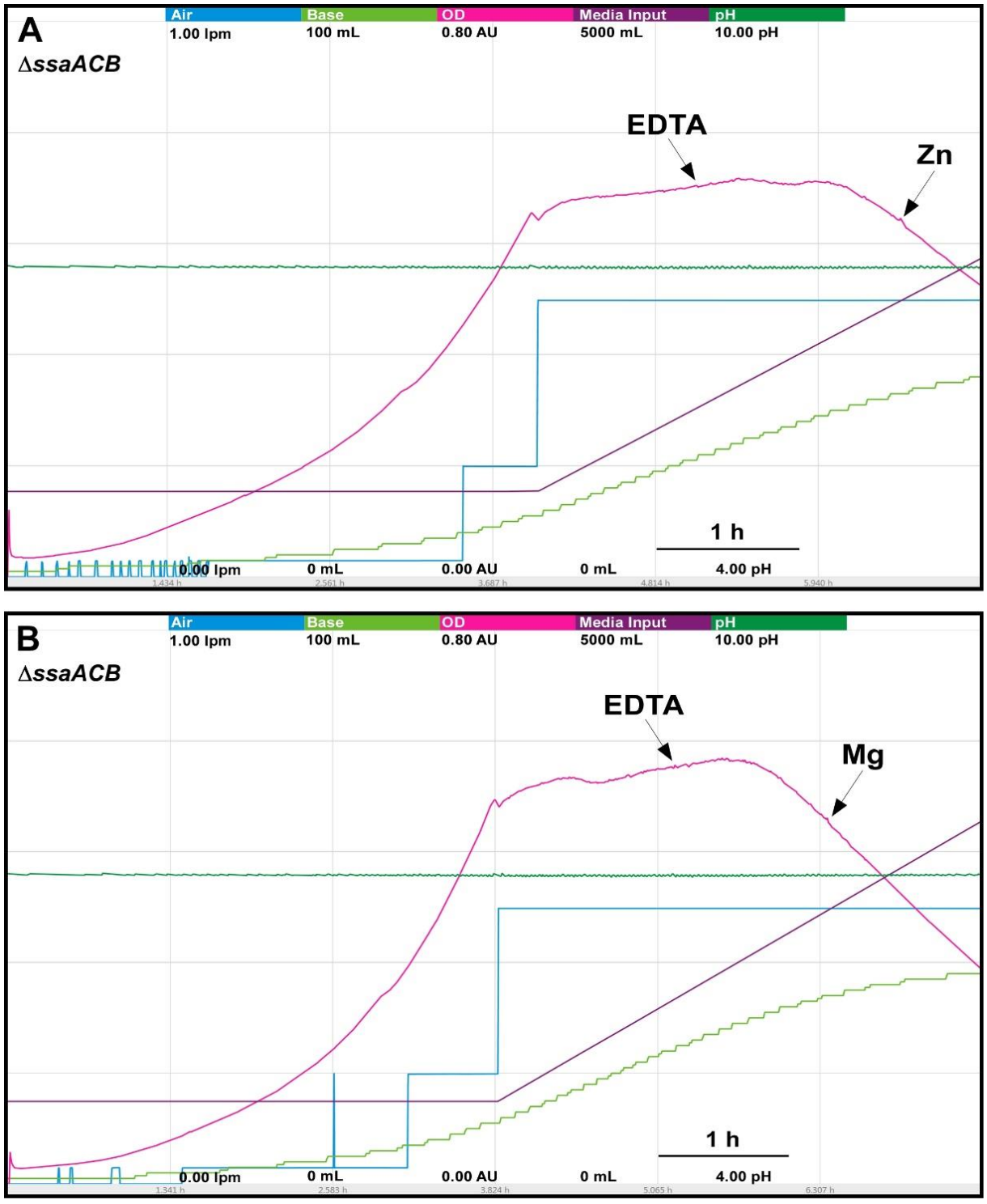

Figure 3.7 Addition of Zn or Mg to fermentor-grown Δ*ssaACB* cells post-EDTA
Fermentor growth of the Δ*ssaACB* mutant with the addition of 100 µM EDTA at T_0 and 100 µM of either (A) Zn^{2+} or (B) Mg^{2+} at T_{70}. Colors and labels are as in Figure 3.3. The time scale is indicated by the bar in the bottom right portion of the each chart. Each chart is representative of at least two replicates

Overview of transcriptional response of *S. sanguinis* to Mn depletion

In order to assess the impact of Mn depletion on the *S. sanguinis* transcriptome, RNA sequencing (RNA-seq) analysis was performed on Δ*ssaACB* fermentor samples collected at the same time points as above (Figure 3.3). Principal component analysis (PCA) revealed that the samples from each time point clustered together, indicating minimal variation between independent replicates (Figure 3.8A). The T_{10} samples overlapped slightly with T_{-20}, indicating few early changes in gene expression. The dissimilarities of the RNA-seq profiles were enlarged at T_{25} and T_{50}, suggesting that EDTA treatment increasingly affected the gene expression of Δ*ssaACB* during the tested period.

Volcano plot analysis of DEGs (defined as $|\log_2| \geq 1$, adjusted *P*-value ≤ 0.05) comparing post-EDTA time points to the pre-EDTA time point revealed that there were only 48 (2.1%) and 139 (6.1%) DEGs at T_{10} and T_{25}, respectively (Figure 3.8B). In contrast, at 50 min post-EDTA, 407 genes (17.9%) were differentially expressed, with a number of genes more severely downregulated (Figure 3.8B). Consistent with these results, the growth rate of Δ*ssaACB* decreased dramatically between T_{25} and T_{50} (Figure 3.3).

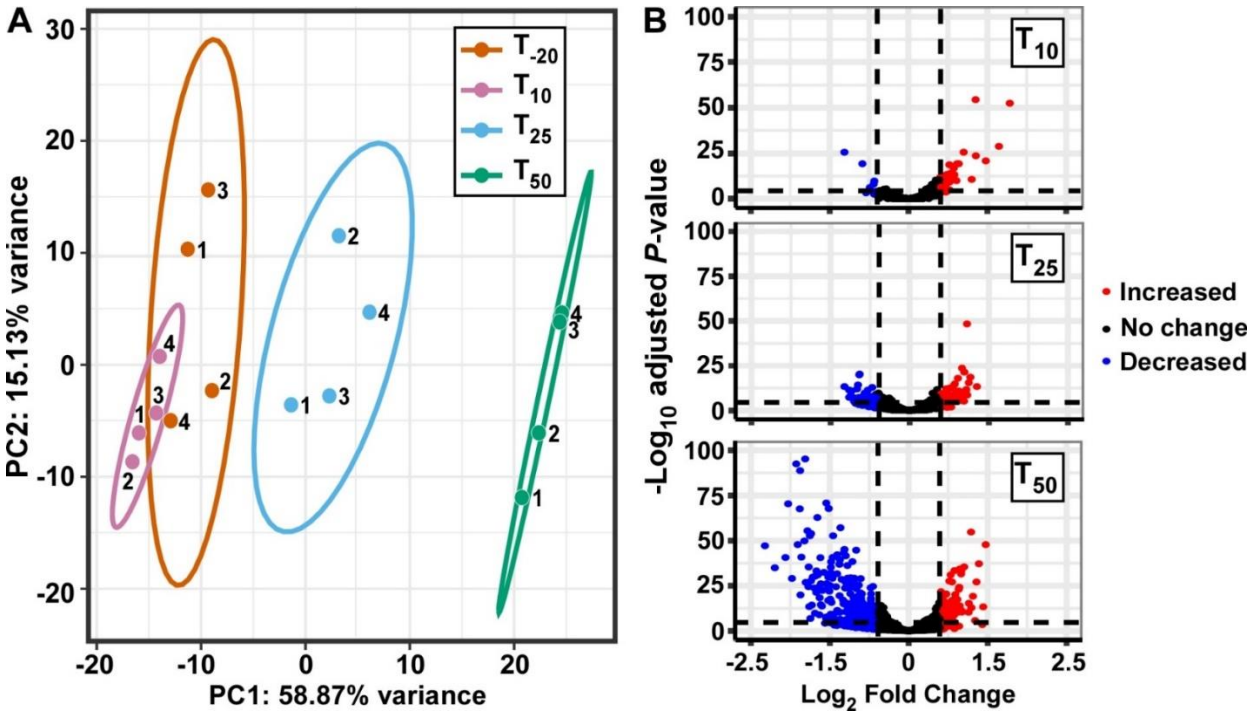

Figure 3.8 Analysis of fermentor-grown Δ*ssaACB* mutant gene expression
(A) Principal component analysis of the RNA-seq samples as determined by the pcaExplorer package for R. Replicates are labeled by fermentor run number. Ellipses are drawn around the 95% confidence interval for each time point. (B) Volcano plots comparing each post-EDTA time point to T_{-20} were generated using DESeq2 analysis in the EnhancedVolcano package for R. Genes that are upregulated in the post-EDTA time point are positive on the x-axis (right) and those that are downregulated are negative (left). Genes exhibiting $|\log_2$ fold change$| > 1$ are depicted by either red (> 1) or blue (< -1) spheres.

RNA-seq trends for several GOIs with moderate to high expression level changes were validated by measuring mRNA levels of fermentor samples via quantitative reverse transcriptase polymerase chain reaction (qRT-PCR) (Figure 3.9). The relative expression levels observed in the qRT-PCR experiments largely replicated the trends observed in the RNA-seq analysis.

In the following sections, we highlight results we believe to be most important.

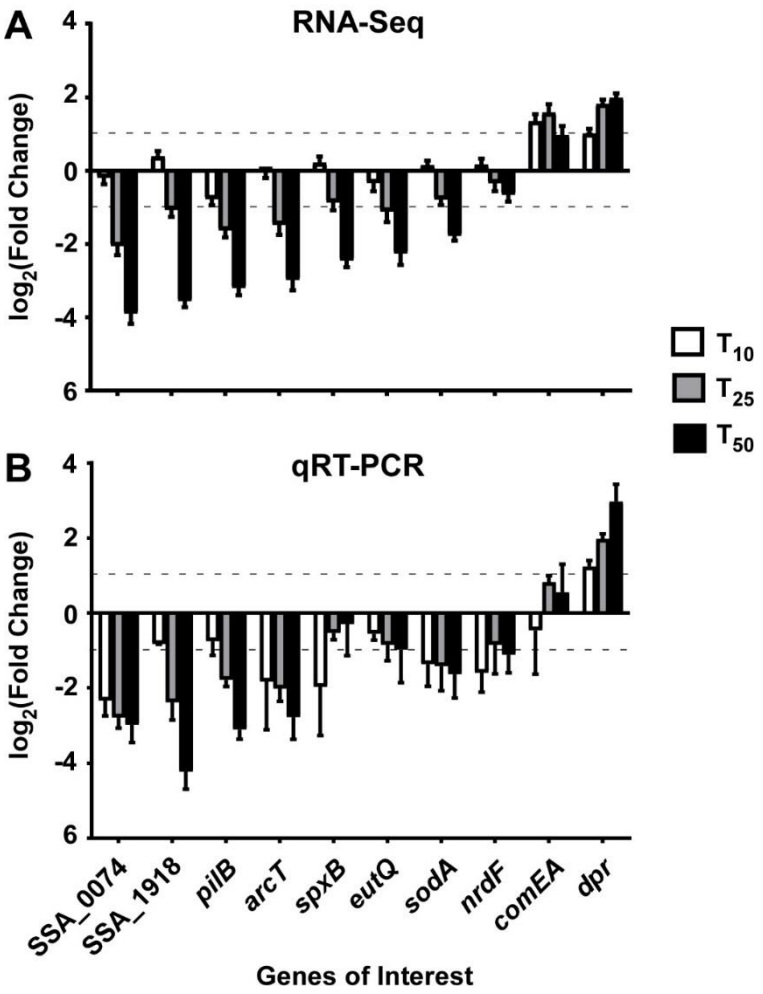

Figure 3.9 Validation of RNA-seq trends using qRT-PCR
(A) The average log_2 fold change values of select GOIs from the DESeq2 RNA-seq analysis, comparing each post-EDTA time point to T_{-20}. The average is from four biological replicates. (B) Log_2 fold change values of the same genes as determined by qRT-PCR of two additional Δ*ssaACB* fermentor run samples. Mean and SEM for each time point are depicted. Horizontal dashed lines indicate log_2 fold expression changes of ± 1.

Regulation of metal transport genes

As seen in Figure 3.4, Mn was the only tested metal whose cellular concentration was decreased upon addition of EDTA to Δ*ssaACB* cells. To further investigate the impact of EDTA on metal transport, we examined the expression of metal transport genes (Figure 3.10). The Kan resistance gene *aphA*-3 that replaced the Mn transporter operon, *ssaACB*, in this mutant strain was upregulated in all three post-EDTA time points (Figure 3.10).

This is consistent with previous results from our lab showing Mn-dependent repression of SsaB expression as measured by western blot (130).

	Locus Tag	Annotation	TPM	Log_2 Ratio		
			T_{-20}	T_{10}/T_{-20}	T_{25}/T_{-20}	T_{50}/T_{-20}
Metal Transport Regulators	SSA_0135	*adcR*, MarR family transcriptional repressor	44	-0.79	**0.97**	-0.16
	SSA_0256	*ssaR*, DtxR family transcriptional repressor	195	-0.19	**-0.50**	0.07
	SSA_0686	*perR*, Fur family transcriptional repressor	367	-0.11	0.03	**0.39**
Mn Transport	SSA_0260	*aphA-3* (kanamycin resistance cassette replacing *ssaACB)*	563	0.28	**0.75**	**0.96**
	SSA_0299	VIT family protein	36	0.38	**0.99**	1.21
	SSA_0851	*mntE*, Mn efflux protein	96	0.31	**0.53**	**1.17**
	SSA_0866	*mgtA*, Mn/Ca exporter	550	0.23	0.28	**0.52**
	SSA_1413	GufA-like, ZIP family protein	119	-0.30	-0.33	**-0.92**
Fe Transport	SSA_0299	VIT family protein	36	0.38	**0.99**	**1.21**
	SSA_0461	*pefC*, heme exporter	144	0.00	-0.08	-0.20
	SSA_1129	Periplasmic iron transport lipoprotein	342	0.03	0.01	-0.01
	SSA_1130	Iron-dependent peroxidase	117	0.00	0.31	**0.52**
	SSA_1131	High-affinity Fe^{2+}/Pb^{2+} permease	150	0.26	**0.43**	**0.73**
	SSA_1413	GufA-like, ZIP family protein	119	-0.30	-0.33	**-0.92**
	SSA_1578	ABC-type Fe^{3+}-siderophore transport system, permease component	75	0.12	-0.34	-0.34
	SSA_1579	ABC-type Fe^{3+}-siderophore transport system, ATPase component	88	-0.10	-0.43	**-0.63**
	SSA_1581	Hemin ABC transporter	121	0.06	-0.41	-0.45
	SSA_1741	ABC-type Fe^{3+}-siderophore transport system, ATPase component	92	0.07	-0.23	-0.01
	SSA_1742	ferrichrome-binding protein	113	0.17	-0.13	0.28
	SSA_1743	ABC-type Fe^{3+}-siderophore transport system, permease component	60	0.04	-0.20	0.15
	SSA_1744	iron ABC transporter permease	53	0.21	0.00	0.55
Zn Transport	SSA_0136	*adcC*, Zn ABC transporter, ATPase	39	-0.11	**1.18**	0.62
	SSA_0137	*adcB*, Zn ABC transporter, permease	45	0.68	**1.78**	**0.75**
	SSA_0138	*adcA*, Zn ABC transporter, lipoprotein	62	**0.69**	**1.87**	**0.79**
	SSA_1339	*phtD*, pneumococcal histidine triad protein D	9	**1.18**	**1.92**	-0.34
	SSA_1340	*adcAIII*, Zn ABC transporter, orphan lipoprotein	8	0.47	0.89	-1.12
	SSA_1413	GufA-like, ZIP family protein	119	-0.30	-0.33	**-0.92**
	SSA_1990	*adcAII*, Zn ABC transporter, orphan lipoprotein	17	**0.98**	**1.49**	-0.17
	SSA_1991	*phtA*, pneumococcal histidine triad protein A	18	**1.03**	**1.55**	-0.20
	SSA_2321	*czcD*, Zn/Cd efflux protein	126	-0.37	**-1.83**	**-1.19**
Mg Transport	SSA_0447	CorA-family protein, magnesium/cobalt transporter	290	-0.28	**-0.51**	**-0.50**
	SSA_0701	CorA-family protein, magnesium/cobalt transporter	559	-0.38	-0.38	**-0.49**
	SSA_0888	*mgtE*, Mg/Co/Ni transporter	152	**-0.51**	0.20	**0.51**
	SSA_1734	Mg/Ni transporter, P-Type ATPase	48	0.33	**0.59**	**0.72**

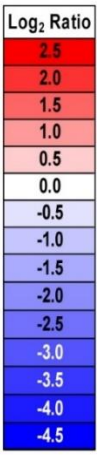

Figure 3.10 Expression of metal transport genes post-Mn depletion
Metal transport genes are depicted with their average transcripts per million reads (TPM) at T_{-20} and log_2 fold change values for each post-EDTA time point. TPM values greater than 1000 are full saturation (green). Positive log_2 fold change values (red) indicate genes upregulated in post-Mn-depletion samples as compared to T_{-20}, while negative values (blue) indicate downregulated genes. Values in bold indicate significant changes in expression by adjusted *P*-value (≤ 0.05).

Given that the cells were Mn-depleted after EDTA addition (Figure 3.4), it was surprising that genes encoding putative orthologs of the *S. pneumoniae* Mn-export proteins MntE (109, 180) and MgtA (154), were significantly upregulated at T_{50} (Figure 3.10). In *S. pneumoniae*, *mntE* was found to be constitutively expressed (181) and *mgtA* expression

was found to be positively regulated by Mn through a metal-dependent riboswitch (154). We therefore sought to test whether a previously generated Δ*mgtA* mutant (85) and a recently made Δ*mntE* mutant exhibited increased Mn sensitivity relative to WT as expected based on previous findings in *S. pneumoniae* and *S. mutans* (109, 153, 154). Preliminary results indicate that the Δ*mgtA* mutant grows as expected, with a lower final density than WT in BHI with 2 mM added Mn (Figure 3.11).

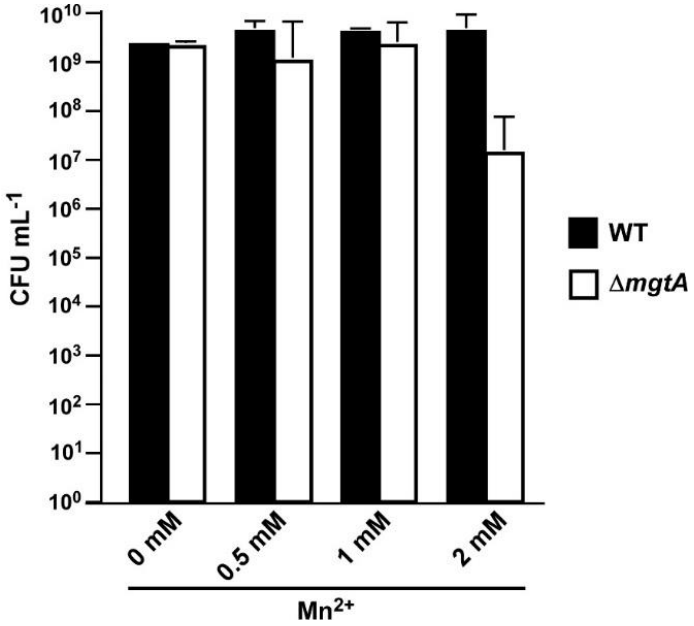

Figure 3.11 Growth of a Δ*mgtA* mutant with excess Mn
Mn was added to BHI that was pre-incubated at 1% O_2 immediately prior to inoculation. Cultures were then inoculated into these tubes, which were returned to 1% O_2. Growth was assessed after 24 h by plating on BHI agar. The mean ± SD of two independent experiments is displayed.

A Δ*mntE* mutant grew to a slightly lower final density than WT in BHI with 5 mM added (Figure 3.12) but Mn precipitated out of the media at this concentration (data not shown). We also tested growth in Chelex-treated BHI (cBHI) with added Mn because we were curious as to whether the lack of other metals would influence the growth. Interestingly, 5 mM Mn did not precipitate out of cBHI like it did in BHI (data not shown). Preliminary results did not yield a distinguishable difference between the WT and Δ*mntE* mutant in cBHI at any Mn concentration (Figure 3.12). We also tested growth of these mutants on

BHI agar plates with added Mn or EDTA (Figure 3.13). Additionally, the loss of *mntE* did not affect growth of the Δ*ssaACB* mutant in either excess Mn or EDTA (Figure 3.13). We also generated an IPTG-inducible complemented mutant and did not observe a difference in growth in BHI with or without Mn upon addition of IPTG (data not shown). Initial metal analysis revealed that the Δ*mntE* mutant accumulated slightly more Mn than WT when excess Mn was added (data not shown). These results indicate that *S. sanguinis* may primarily use MgtA to export excess Mn and MntE may function differently in *S. sanguinis* than in *S. pneumoniae* and *S. mutans*. Future studies be required to elucidate the function of these putative exporters and their transcriptional regulation in *S. sanguinis*.

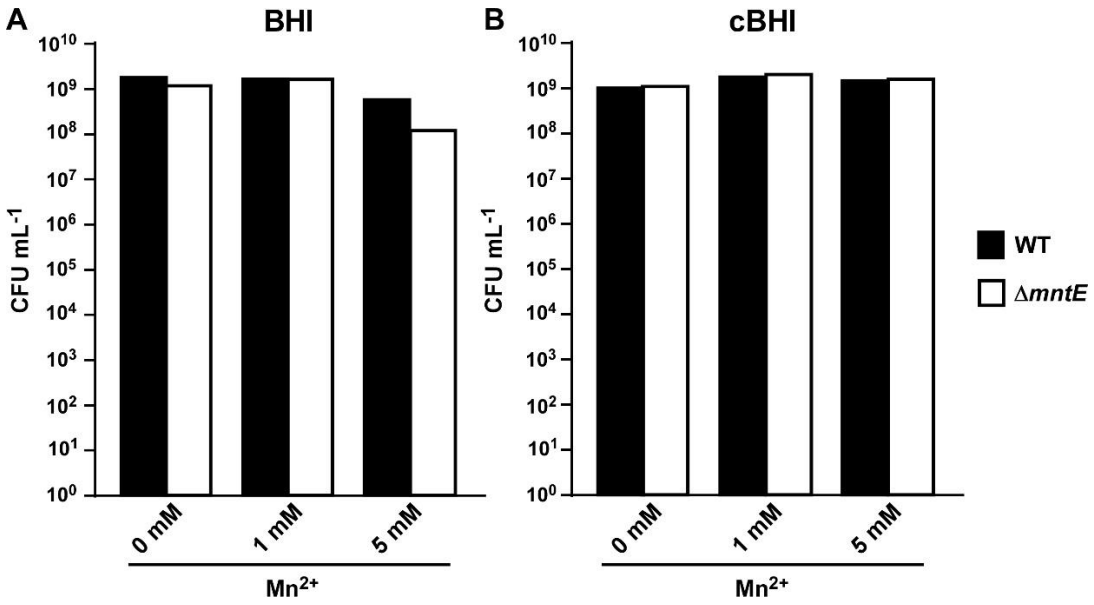

Figure 3.12 Growth of a Δ*mntE* mutant with excess Mn
Cultures were inoculated into BHI (A) or cBHI (B) that was preincubated at 1% O_2. Mn was added to the indicated concentration immediately prior to inoculation. All culture tubes were returned to 1% O_2. Growth was assessed after 24 h by plating on BHI agar. Results from one experiment are displayed.

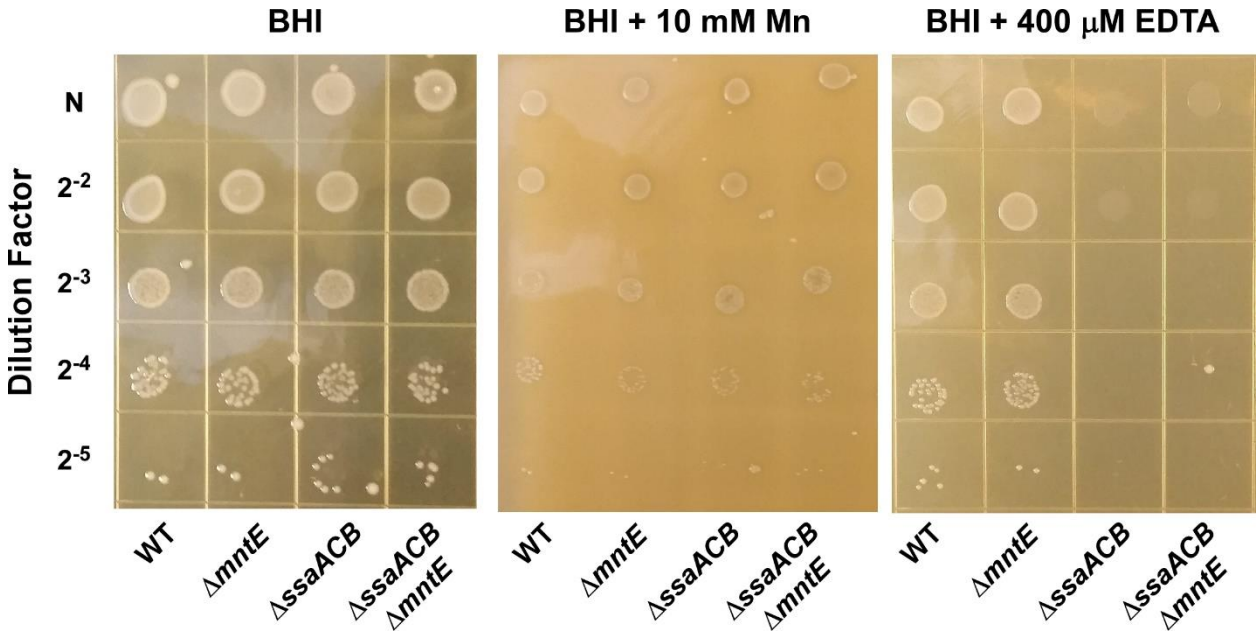

Figure 3.13 Growth of Δ*mntE* mutants on BHI plates with Mn or EDTA
Growth on BHI ± 10 mM Mn or 400 μM EDTA. Overnight broth cultures were normalized (N) to each other by OD_{600} prior to subsequent dilution and spot plating. Plates were incubated for 24 h at 0% O_2. Only one replicate was performed with these conditions.

As seen in Figure 3.4, cellular Zn levels in Δ*ssaACB* were not significantly altered by EDTA addition, despite the high affinity of this chelator for Zn (182). Maintenance of Zn levels may be due to the higher levels of Zn than Mn in BHI (1.7 ± 0.02 vs. 0.02 ± 0.003 μg ml^{-1}, respectively) (120) or through the regulation of Zn transporter genes. *S. sanguinis* possesses orthologs of the Zn ABC transporter AdcCBA of *S. pneumoniae* (183) and all three genes were upregulated post-EDTA (Figure 3.10). Expression of the gene encoding the Zn^{2+} and Cd^{2+} efflux protein, CzcD (184), decreased after EDTA addition (Figure 3.10). Thus, cellular Zn levels appear to have been maintained during EDTA treatment by decreasing export of intracellular Zn and increasing import of any remaining bioavailable Zn through regulation of Zn transporters.

We also examined the regulation of other putative Zn-transport proteins. In *S. pneumoniae*, AdcAII and several histidine triad proteins also contribute to Zn transport

(185). AdcAII is an orphan lipoprotein of the AdcCBA system (186, 187) and PhtD is a histidine triad protein encoded adjacent to AdcAII (188, 189). *S. sanguinis* has two genes, SSA_1340 and SSA_1990, that encode proteins similar to AdcAII, and each is also adjacent to putative histidine triad protein genes, SSA_1339 or SSA_1991. Because AdcAII is more similar to SSA_1990, we have named this protein AdcAII, whereas we have designated SSA_1340 as AdcAIII. Consistent with a potential role in Zn uptake, all four of these genes were upregulated at T_{25} (Figure 3.10). The relative contribution of each of these proteins to Zn import remains to be determined, although we hypothesize that the upregulation of these genes contributes to the tight maintenance of Zn levels in cells post-EDTA.

Less is known about transport of other metals in streptococci. *S. sanguinis* encodes several putative Fe transporters, none of which were differentially expressed, with the exception of a vacuolar iron transporter (VIT) family homolog (Figure 3.10). While this protein family has not been well-characterized in bacteria (190), VIT proteins have been implicated in Fe and Mn transport in other organisms (191-193). Two predicted CorA-family Mg transporters (194, 195) were slightly downregulated post-EDTA (Figure 3.10). This is unsurprising, as levels of Mg in BHI are very high (15.0 ± 1.5 μg ml^{-1}) (120) and EDTA has a lower affinity for Mg than many other metals (8.7 $\log_{\beta 1}$ for Mg vs. 14.1 $\log_{\beta 1}$ for Mn) (182). For reasons that are unclear, expression of genes for two other putative Mg transporters, *mgtE* and *mgtB* (195), was significantly upregulated post-EDTA (Figure 3.10). The role and contribution of each of these gene products to metal homeostasis needs to be validated for *S. sanguinis*.

Examination of known Mn-cofactored enzymes

Superoxide dismutase

S. sanguinis possesses a singular superoxide dismutase, SodA, and it is Mn-cofactored (75, 130). Our previous study indicated that reduced SodA activity could account for only a portion of the reduced virulence and serum growth of the Δ*ssaB* mutant (130). Expression of *sodA* is affected by oxygen levels (130) and given the constant airflow into the fermentor vessel, we expected the levels remain constant. Instead, expression levels decreased significantly at both T_{25} and T_{50} (Figure 3.14), which may be due to Mn-dependent positive regulation of transcription (110, 196). Given that the fermentor growth conditions do not exactly replicate either of our previous *in vitro* or *in vivo* assays, we wondered whether SodA would be important here. To answer this question, we grew our Δ*sodA* knockout mutant in the fermentor under the same growth conditions but without EDTA added. The Δ*sodA* mutant grew normally under these conditions (Figure 3.15), indicating that Mn-dependent SodA activity is not essential for aerobic growth under these conditions. While this does not rule out the possibility that reduced SodA activity after Mn depletion contributed to the reduced growth rate of Δ*ssaACB*, it established that it was not the sole cause, thus encouraging us to investigate other possibilities.

	Locus Tag	Annotation	TPM	Log_2 Ratio		
			T_{-20}	T_{10}/T_{-20}	T_{25}/T_{-20}	T_{50}/T_{-20}
Ribonucleotide Reductases	SSA_0768	*nrdF*, aerobic RNR (Mn-dependent)	695	0.16	-0.35	**-0.66**
	SSA_0769	*nrdK*, aerobic RNR	690	0.20	-0.42	**-0.61**
	SSA_0770	*nrdE*, aerobic RNR	582	0.08	-0.38	**-0.66**
	SSA_0771	*nrdH*, aerobic RNR	3534	-0.09	**-0.55**	**-0.54**
	SSA_1668	*fmnG*, flavodoxin	4	-0.03	-0.07	-0.02
	SSA_1683	*fmnI*, flavodoxin	246	-0.05	-0.16	0.12
	SSA_2226	*nrdG*, anaerobic RNR	14	-0.04	0.58	0.54
	SSA_2227	Acetyltransferase	12	-0.43	0.44	0.83
	SSA_2228	Acetyltransferase	12	-0.41	0.11	0.36
	SSA_2229	Hypothetical protein	38	-0.04	0.22	0.41
	SSA_2230	*nrdD*, anaerobic RNR	67	0.09	0.16	**0.44**
	SSA_2263	*nrdI*, flavodoxin component of aerobic RNR	228	-0.22	0.13	0.31
Competence	SSA_2394	*comC*	5935	0.25	-0.41	**-0.95**
	SSA_2379	*comD*	1397	0.34	-0.16	-0.36
	SSA_2378	*comE*	820	**0.45**	0.16	-0.05
	SSA_0016	*comX*	1517	0.53	**0.74**	0.35
	SSA_0184	*comGA*	315	**0.66**	**1.34**	0.38
	SSA_0185	*comGB*	201	**0.91**	**1.58**	**0.67**
	SSA_0186	*comGC*	114	**0.89**	**1.82**	**1.03**
	SSA_0187	*comGD*	182	0.66	**1.64**	**0.99**
	SSA_0188	*comGE*	177	0.55	**1.63**	**1.13**
	SSA_0189	*comGF*	182	0.61	**1.61**	**1.14**
	SSA_0190	*comGG*	226	0.60	**1.58**	**1.19**
	SSA_0715	*comEA*	196	**1.34**	**1.57**	**0.96**
	SSA_0716	*comEC*	118	**1.12**	**1.79**	**1.22**
	SSA_1497	*comEB*	181	0.05	0.11	0.30
	SSA_1835	*comFC*	124	**1.33**	**1.46**	**1.03**
	SSA_1836	*comFA*	166	**1.43**	**1.42**	**0.87**
Mn-Dependent Enzymes in Streptococci	SSA_1204	*pgm*, phosphatase	567	**0.71**	-0.13	**-1.24**
	SSA_1260	*deoB*, pentophosphomutase	218	0.11	**-0.47**	**-2.08**
	SSA_1271	*papP*, nucleotide phosphatase	205	0.17	**0.32**	**0.55**
	SSA_1748	*ppaC*, phosphatase	651	0.28	0.24	0.25
	SSA_1846	*phpP*, phosphatase	577	0.30	0.21	0.26
	SSA_2224	*cspB*, capsular phosphate	242	**-0.50**	**-0.74**	**-1.97**
Rel Proteins	SSA_0250	*relA*, bifunctional (p)ppGpp synthetase/hydrolase	102	**-0.68**	-0.02	0.09
	SSA_1210	*relQ*, (p)ppGpp synthetase	188	**1.30**	**0.60**	**-1.09**
	SSA_1795	*relP*, (p)ppGpp synthetase	115	0.21	0.39	**0.91**
Stress Responses	SSA_0009	Ribosome-associated heat shock protein (S4)	389	-0.41	-0.35	-0.31
	SSA_0156	ATPase with chaperone activity, ATP-binding subunit	4	-0.32	-0.41	**-1.27**
	SSA_0644	*dpr*, DNA Protection System	473	**1.00**	**1.81**	**1.97**
	SSA_0669	*clpE*, ATP dependent protease	226	0.08	0.18	0.39
	SSA_0721	*sodA*, Mn-cofactored superoxide dismutase	6597	0.14	**-0.79**	**-1.79**
	SSA_1093	*clpX*, ATP-dependent Clp protease ATP-binding subunit	496	0.09	0.18	0.25
	SSA_1136	*clpA*, ATPases with chaperone activity, ATP-binding subunit	17	**0.87**	**0.90**	**-1.03**
	SSA_1731	*clpP*, ATP-dependent Clp protease, proteolytic subunit	1078	0.26	0.07	**-0.29**
	SSA_1745	*csbD*, General stress response protein	6191	-0.77	-0.96	**-2.55**
	SSA_1979	Alkaline-shock protein	1074	0.00	-0.38	**-0.42**
	SSA_2005	*dnaJ*, Chaperone protein	204	-0.11	-0.01	**-0.80**
	SSA_2007	*dnaK*, Chaperone protein	671	0.66	0.14	**-0.56**
	SSA_2008	*grpE*, Molecular chaperone	359	0.39	-0.09	**-1.08**
	SSA_2009	*hrcA*, Heat shock transcription repressor	707	0.04	**-0.71**	**-1.85**
	SSA_0225	*groES*, Heat shock protein	114	-0.34	0.59	0.42
	SSA_0226	*groEL*, Heat shock protein	245	-0.09	0.45	0.17
	SSA_2148	Alkaline shock stress response protein	210	-0.02	0.05	-0.15
	SSA_2190	*hslO*, 33 kDa chaperonin	193	-0.26	-0.27	-0.23
	SSA_2199	*clpC*, ATP-dependent Clp protease, ATP-binding subunit	113	-0.24	0.10	0.11

Log_2 Ratio
2.5
2.0
1.5
1.0
0.5
0.0
-0.5
-1.0
-1.5
-2.0
-2.5
-3.0
-3.5
-4.0
-4.5

Figure 3.14 Expression of select genes after Mn-depletion

Selected GOIs are depicted with their average transcripts per million reads (TPM) at T_{-20} and log_2 fold change values for each post-EDTA time point. TPM values greater than 1000 are full saturation (green). Positive log_2 fold change values (red) indicate genes upregulated in after Mn-depletion samples as compared to T_{-20}, while negative values (blue) indicate downregulated genes. Values in bold indicate significant changes in expression by adjusted *P*-value (≤ 0.05).

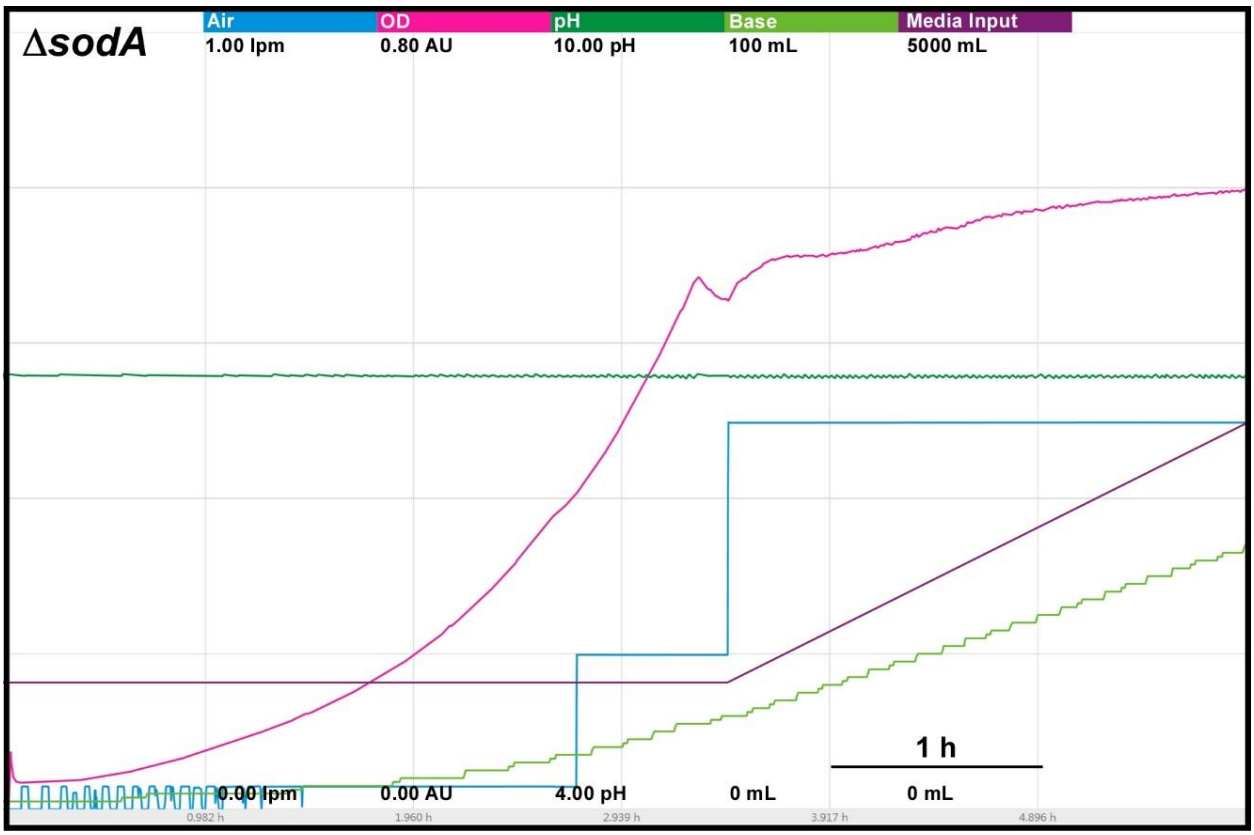

Figure 3.15 Aerobic fermentor growth of a Δ*sodA* mutant
The Δ*sodA* mutant grown under aerobic fermentor conditions as described previously, without EDTA. Each color represents a different parameter, labeled at the top of the figure. The scale for each parameter is indicated by the values under each respective parameter (minimum at the bottom, maximum at the top). The time scale is indicated by the bar in the bottom right portion of the chart. Representative chart from three replicates.

Class Ib ribonucleotide reductase

The other known Mn-cofactored enzyme in *S. sanguinis* is the aerobic class Ib ribonucleotide reductase (RNR), NrdEF (100, 101). RNR enzymes catalyze the production of deoxynucleotides from nucleotides. It was previously found that mutant strains lacking this enzyme were unable to grow in aerobic conditions, whether in serum or BHI. These studies also suggested that Fe could not substitute for Mn as an RNR cofactor *in vivo*, despite its ability to do so *in vitro*. Thus, we considered whether loss of activity of the NrdEF enzyme due to Mn depletion was the cause of the observed growth rate decrease.

In addition to reducing cellular Mn levels, EDTA also led to a decrease in the expression of *nrdHEKF* (Figure 3.14). Although we do not know how the aerobic RNR genes are regulated in *S. sanguinis*, it would be surprising to find that they were downregulated in response to a deoxynucleotide shortage caused by reduced activity of the enzyme. We considered whether the cells were able to obtain nucleotides from some other source.

Although expression of the anaerobic RNR genes *nrdD* and *nrdG* slightly increased after Mn depletion, it seems highly unlikely that this could compensate for loss of NrdEF activity; the anaerobic enzyme is highly sensitive to oxygen in *S. sanguinis* (101). Moreover, the expression level of the *nrdG* gene at the T_{-20} time point was one-fortieth that of any of the genes in the *nrdHEKF* operon. To test that NrdDG was not compensating for loss of NrdEF activity, we generated Δ*nrdD* KO mutants in WT and Δ*ssaACB* backgrounds and tested these mutants in a serum growth study (Figure 3.16). Neither of the Δ*nrdD* mutants grew significantly differently from its respective parent strain (Figure 3.16). We also assessed the growth of the quadruple mutant in aerobic fermentor conditions (Figure 3.17). While the results of the fermentor growth are preliminary (n = 1), the Δ*ssaACB* Δ*nrdD* mutant exhibited a growth pattern similar to that of the Δ*ssaACB* parent (Figure 3.17).

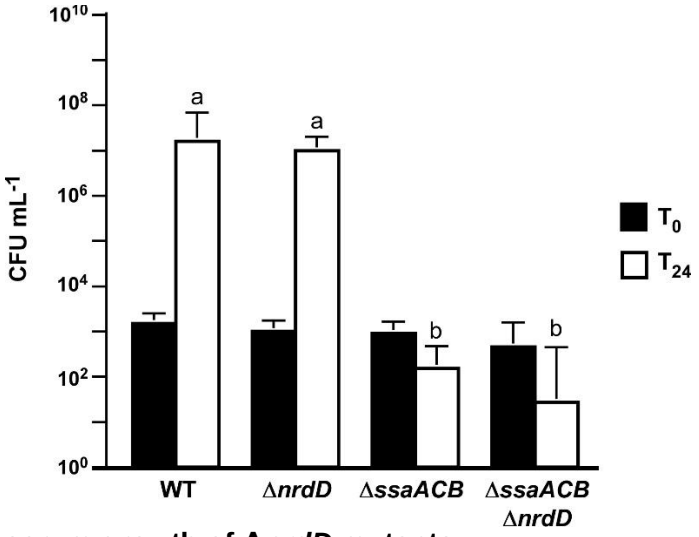

Figure 3.16 Aerobic serum growth of Δ*nrdD* mutants
Overnight pre-cultures were inoculated into rabbit serum that was preincubated at 12% O_2 and returned to the same conditions. Growth was assessed after 24 h by plating on BHI agar. The mean ± SD of at least three independent experiments is displayed. Significance of T_0 and T_{24} values were determined separately by one-way ANOVA with a Tukey multiple comparisons test. Bars with the same letter are not significantly different from each other. No T_0 values were significantly different from each other.

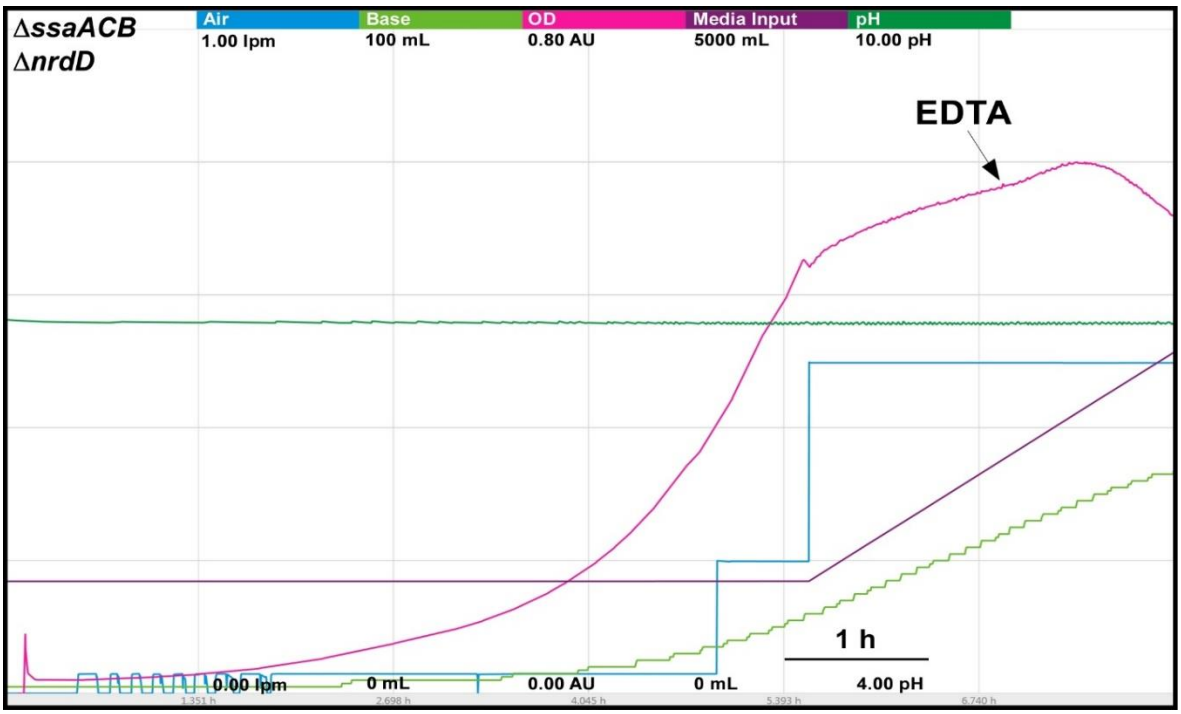

Figure 3.17 Aerobic fermentor growth of an Δ*ssaACB ΔnrdD* mutant
The Δ*ssaACB* Δ*nrdD* mutant grown under aerobic fermentor conditions as described previously, with 100 µM EDTA added. Each color represents a different parameter, labeled at the top of the figure. The scale for each parameter is indicated by the values under each respective parameter (minimum at the bottom, maximum at the top). The time scale is indicated by the bar in the bottom right portion of the chart. Only one replicate was completed.

As *S. sanguinis* is naturally competent (197), we also considered the possibility that it was compensating for reduced NrdEF activity through the uptake of DNA from its environment. While several early competence genes (84) were either unchanged or downregulated, *comX* and most of the late competence genes were upregulated significantly at T_{25} (Figure 3.14). Interestingly, this upregulation was sustained at T_{50} for most genes, despite the fact that competence has been characterized as a transient state in *S. sanguinis* (84). Elimination of genetic competence genes *comCDE* (198) did not influence aerobic serum growth in Mn-deplete media in the WT or Δ*ssaACB* background (Figure 3.18). This suggests that the cells are probably not obtaining nucleotides from other cells.

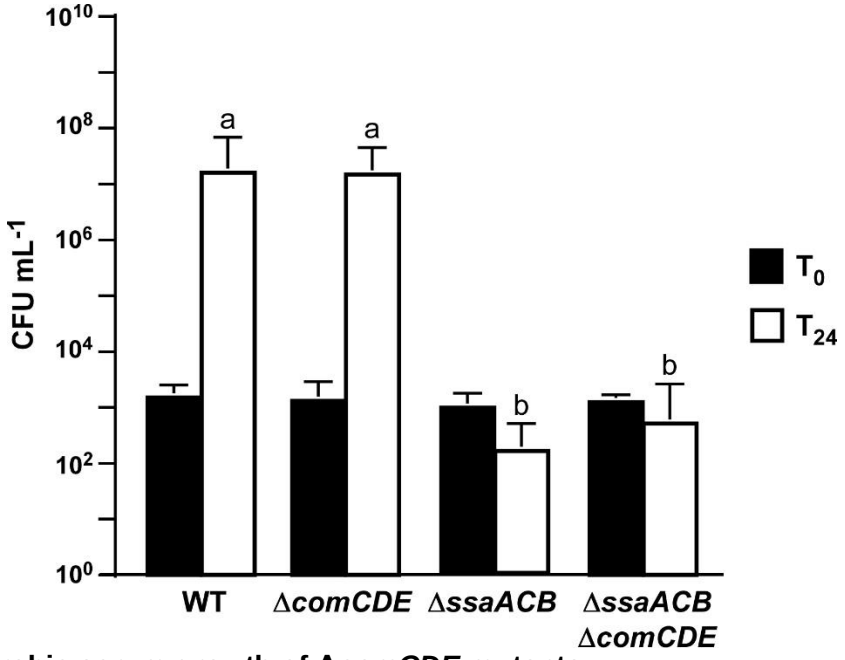

Figure 3.18 Aerobic serum growth of Δ*comCDE* mutants
Overnight pre-cultures were inoculated into rabbit serum that was preincubated at 12% O_2 and returned to the same conditions. Growth was assessed after 24 h by plating on BHI agar. The mean ± SD of at least three independent experiments is displayed. Significance of T_0 and T_{24} values were determined separately by one-way ANOVA with a Tukey multiple comparisons test. Bars with the same letter are not significantly different from each other. No T_0 values were significantly different from each other.

We recently analyzed the metabolome of *S. sanguinis* cells under the same conditions as this study (199). The results suggested that deoxynucleotides in cells increased or were

unchanged after Mn depletion, which is inconsistent with a deoxynucleotide shortage. Thus, while NrdEF requires Mn for activity, our data suggest that nucleotides were not a limiting factor for growth in our study. The simplest explanation for the above results is that *S. sanguinis* possesses at least one other Mn-dependent, essential enzyme in addition to NrdEF, such that when Mn levels fall, the reduced activity of one or more of these other enzymes becomes growth limiting.

Mn-dependent phosphatases in *S. pneumoniae*

In the related species *S. pneumoniae*, there are six additional enzymes (Figure 3.14) that have been found to be co-factored by Mn (200, 201). Orthologs of all six enzymes are encoded in the *S. sanguinis* genome, although their functions have not been confirmed. Pgm and CpsB are phosphatases that have been implicated in capsule biosynthesis in *S. pneumoniae,* although *S. sanguinis* lacks a true capsule. DeoB is a phosphopentomutase that functions to connect the pentose phosphate pathway to purine biosynthesis and was also significantly downregulated at T_{50}. Expression of *papP*, encoding a nucleotide phosphatase, was significantly increased at the later time points and has been shown to affect membrane lipid homeostasis (201). A significant morphological difference was observed in Δ*papP* mutants in *S. pneumoniae,* but Δ*ssaACB* cells from the T_{50} sample did not appear morphologically different from cells at T_{-20} (Figure 3.19). Of note, we observed changes in fatty acid synthesis under these same fermentor growth conditions (202) suggesting that PapP activity may be reduced but not to the extent required to affect morphology.

Genes encoding the other two phosphatases, PhpP and PpaC, were not differentially expressed at any time point (Figure 3.14). While this indicates lack of Mn-dependent

regulation, it does not rule out the possibility that their activity decreased. PhpP is a serine/threonine protein phosphatase that is a key regulator of cell division and has been shown to be regulated by the bioavailable Zn:Mn ratio in *S. pneumoniae* (200). While the Zn:Mn ratio did increase over time in our study (Table 3.3), Δ*ssaACB* cells from the T_{50} sample did not appear morphologically different from cells at T_{-20} (Figure 3.19), indicating that PhpP may not be affected by Mn limitation under these conditions. In our recent study, loss of PhpP did not significantly affect the growth of *S. sanguinis* in human serum (203), which indicates that it is likely not responsible for the growth rate decrease observed here. The last phosphatase, PpaC, is essential for *S. sanguinis* (85), so if PpaC activity was decreased due to Mn depletion, this could have contributed to the decreased growth rate phenotype observed post-EDTA. Another possibility is that similar to NrdEF, the reduced expression of non-essential Mn-dependent enzymes such as SodA may allow for increased availability of Mn for PpaC. Further studies utilizing the knockout mutants of each nonessential phosphatase (85) or an approach such as CRISPR interference (204) for PpaC will enhance our understanding of relative contributions of each phosphatase to the growth and morphology of *S. sanguinis*.

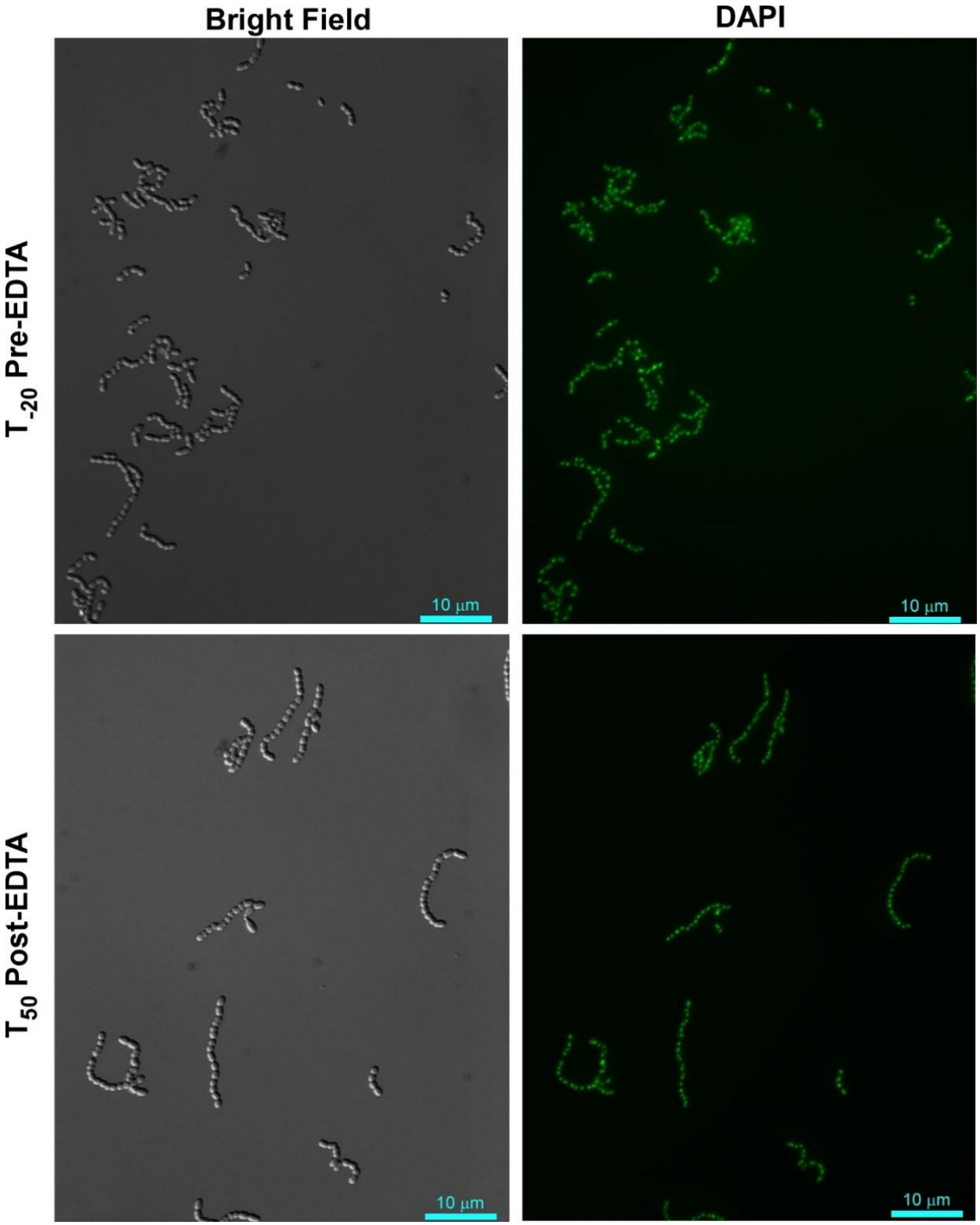

Figure 3.19 Morphology of aerobic fermentor grown cells
Fixed Δ*ssaACB* cells from T_{-20} and T_{50} time points were stained with DAPI. Images were taken with a Zeiss Cell Observer Spinning Disc confocal microscope with a 100x oil immersion lens. Scale is indicated by the cyan bar in the bottom left corner of each image.

Table 3.1 Zn:Mn ratios in fermentor-grown cells

Strain	T_{-20}	T_{10}	T_{25}	T_{50}
WT	1.64	1.66	1.75	1.81
Δ*ssaACB*	2.02	2.47*	3.30*	5.36*

ICP-OES ratios as determined in Figure 3.4 were assessed by one-way ANOVA. * indicates $P \leq 0.01$ as compared to T_{-20}.

RelA (p)ppGpp hydrolase domain

In streptococci and enterococci, Mn acts as a cofactor for the hydrolase domain of the bifunctional (p)ppGpp synthetase/hydrolase, RelA (also called RSH for RelA/SpoT Homologs) (205). As an alarmone, (p)ppGpp serves as an effector of the stringent response in bacteria (206). Expression of *relA* was unchanged after EDTA addition and expression of the other two small alarmone synthetase genes, *relP* and *relQ* (207), were significantly increased and decreased, respectively (Figure 3.14). Both RelP and RelQ were found to produce less (p)ppGpp than RelA in *S. mutans* (207) and appear to be important during different environmental conditions or growth stages in gram-positive bacteria (208).

In an attempt to determine whether loss of hydrolase activity in RelA could account for the phenotypes we observed in Mn-depleted cells, we attempted to construct a hydrolase-deficient mutant by altering specific residues (R44, H62, T151) shown by Hogg et al. (209) to be important for (p)ppGpp hydrolase, but not synthetase activity. Similar to Kaspar et al. (210), we were unable to generate any of the three point mutants without unintended mutations arising in other regions of the gene (data not shown). This indicates that hydrolase activity may be essential for growth of *S. sanguinis*. We then obtained strains from the comprehensive *S. sanguinis* mutant knockout library (85) that were deleted for each of the *rel* genes. We then generated a rel^0 strain by knocking out all three *rel* genes

utilizing a markerless mutagenesis system originally described by Xie et al. (162), but modified to contain the IFDC specific to *S. sanguinis* (161). We also made these *rel* knockout mutants in the Δ*ssaACB* background. We then assessed the growth of these mutants in aerobic serum. As shown in (Figure 3.20), neither Δ*relP* nor Δ*relQ* grew to a density that differed significantly from its parent strain, whether in the WT or Δ*ssaACB* background. Likewise, in both backgrounds, Δ*relA* was more attenuated than *rel*^{0}, suggesting that is it more detrimental to lose activity of RelA than to lack all (p)ppGpp.

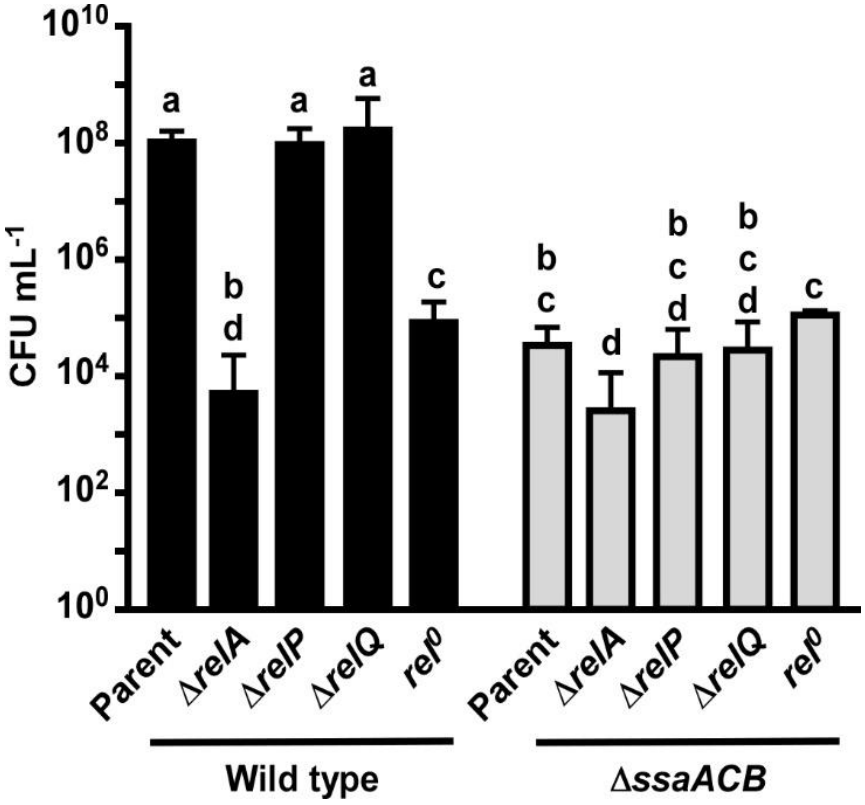

Figure 3.20 Aerobic serum growth of *rel* mutants
Various *rel* mutants were grown for 24 h in 6% O_2 in pooled rabbit serum. Means and SD at least three replicates are displayed. Significance was determined by one-way ANOVA with a Tukey-Kramer multiple comparisons test. T_{24} bars that share a letter are not significantly different from each other.

Assessment of stress and stress responses in Mn-depleted cells through gene expression

We next sought to determine whether the RNA-seq data suggested anything concerning stresses experienced by the cells*. S. sanguinis* is known to generate copious amounts of hydrogen peroxide (H_2O_2), presumably to more effectively compete against other oral species, such as the caries-forming pathogen *S. mutans* (71, 211). Simple Mn compounds have been reported to prevent oxidative stress by catalyzing the decomposition of H_2O_2 (212) and superoxide (127, 128). We observed a significant decrease in expression of the gene encoding the H_2O_2-generating enzyme pyruvate oxidase, *spxB*, at T_{25} and T_{50} (Figure 3.21A) (211, 213). To determine whether the decreased growth rate of the Δ*ssaACB* strain during aerobic fermentor growth after Mn depletion was due to excess H_2O_2 generation or the inability of cells to cope with H_2O_2 without Mn, H_2O_2 levels were measured in spent supernatant. Concentrations ranged between 1 and 5 µM, far lower than has been observed in previous studies employing SK36 (68) despite the constant influx of air into the vessel (Figure 3.21B). H_2O_2 levels also decreased significantly at T_{25} and T_{50} as compared to T_{-20} (Figure 3.21B), which correlates with the decreased expression of *spxB* (Figure 3.21A). These results indicate that oxidative stress related to excess H_2O_2 levels is unlikely to be the cause of the growth rate decrease observed after Mn depletion.

A

		TPM	Log$_2$ Ratio		
		T_{-20}	T_{10}/T_{-20}	T_{25}/T_{-20}	T_{50}/T_{-20}
SSA_0391	*spxB*, pyruvate oxidase	1824	0.21	-0.87	-2.46

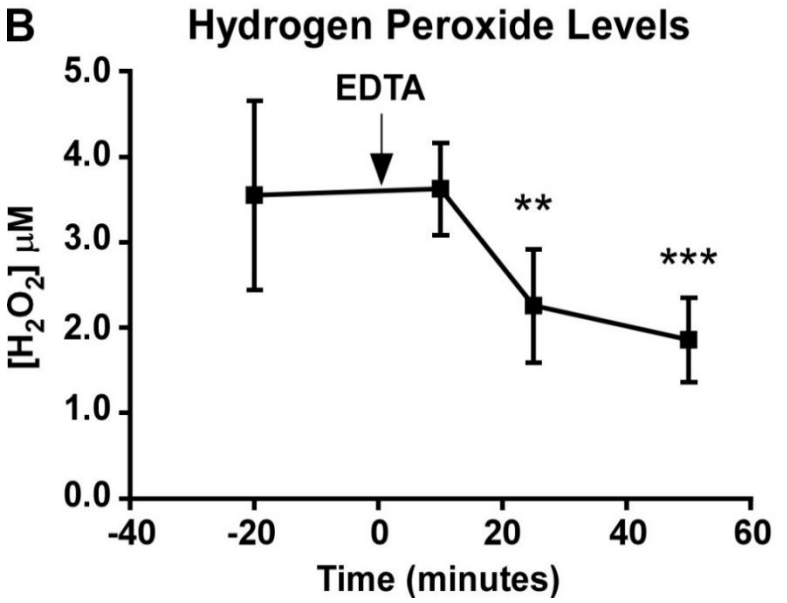

Figure 3.21 Expression of *spxB* and quantitation of H_2O_2 in fermentor culture
(A) Expression of the *spxB* gene in fermentor-grown Δ*ssaACB* cells as determined by RNA-seq analysis. Average transcripts per million reads (TPM) at T_{-20} and $\log_2$ fold change values for each after Mn-depletion time point are displayed. TPM values greater than 1000 are full saturation (green). Positive $\log_2$ fold change values (red) are genes upregulated in after Mn-depletion samples as compared to T_{-20}, while negative values (blue) indicate downregulated genes. Values in bold indicate significant changes in expression by adjusted *P*-value (≤ 0.05). (B) H_2O_2 levels of the BHI culture supernatant were measured at each time point. Means and standard deviations of at least 4 replicates are shown. Significance was determined by one-way ANOVA with a Tukey-Kramer multiple comparisons test, comparing each after Mn-depletion time point to T_{-20}. ** $P < 0.01$, *** $P < 0.001$.

Expression levels of various stress response genes were assessed, and most were either downregulated or unchanged at T_{50} (Figure 3.14), indicating that the reduced growth rate is likely not due to an overwhelming stress response. The only stress response-related gene to show a significant increase in expression at T_{50} was that encoding the Dps-like peroxide resistance protein, Dpr, (214). Dpr is a ferritin-like protein that has been shown to be imperative for oxidative stress tolerance in several streptococci (115, 116, 214, 215), including *S. sanguinis* SK36 (70) and was one of the most highly upregulated genes at

all three time points. We generated a Δ*dpr* mutant as well as a strain with this mutation in the Δ*ssaACB* background and assessed their growth in aerobic serum. Each strain grew similarly to its corresponding parent strain in aerobic serum (Figure 3.22). This indicates that Dpr does not significantly contribute to aerobic growth in these conditions.

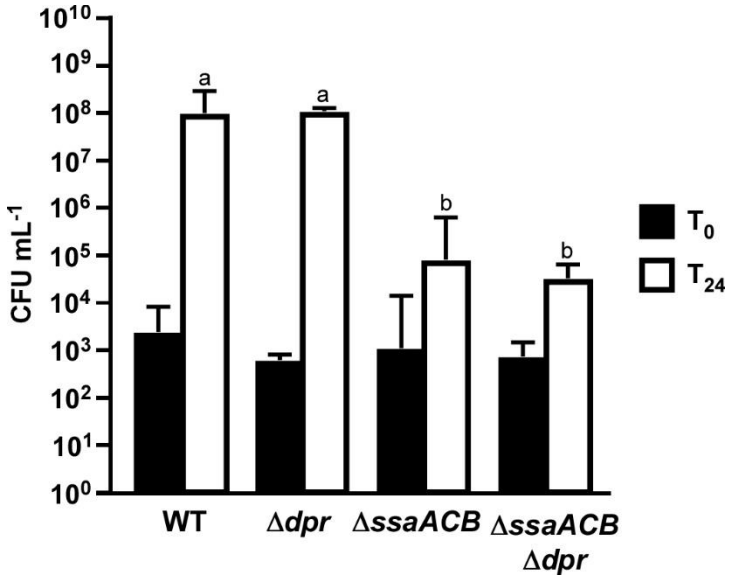

Figure 3.22 Aerobic serum growth of Δ*dpr* mutants
Overnight pre-cultures were inoculated into rabbit serum that was preincubated at 12% O_2 and returned to the same conditions. Growth was assessed after 24 h by plating on BHI agar. The mean ± SD of at least three independent experiments is displayed. Significance of T_0 and T_{24} values were determined separately by one-way ANOVA with a Tukey multiple comparisons test. Bars with the same letter are not significantly different from each other. No T_0 values were significantly different from each other.

We then assessed the growth of the Δ*dpr* mutants under the same fermentor conditions as described above, including the addition of 100 µM EDTA. Both strains took exceptionally long times to reach their peak OD in the vessel without media flow (Figure 3.23). Once they peaked, airflow was set to the max and both strains grew similarly to their parent strains. After EDTA was added, though, both strains dropped in OD like the Δ*ssaACB* mutant. This indicates that loss of Dpr may increase the sensitivity to Mn depletion, although more replicates and further studies are required to confirm these results.

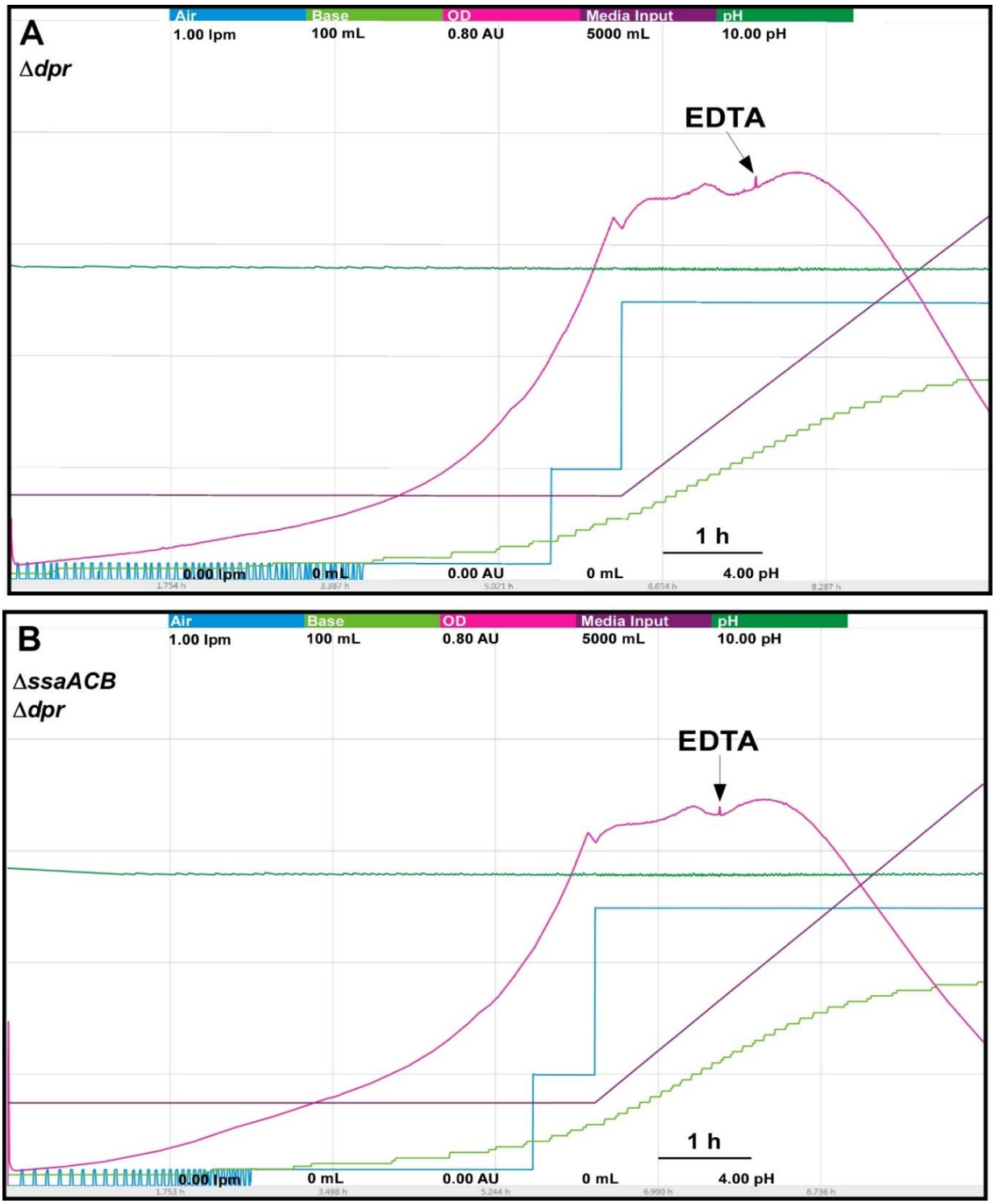

Figure 3.23 Aerobic fermentor growth of Δ*dpr* mutants

Growth of Δ*dpr* (A) and Δ*ssaACB* Δ*dpr* (B) mutants in aerobic fermentor conditions as described previously, with 100 µM EDTA added. Each color represents a different parameter, labeled at the top of the figure. The scale for each parameter is indicated by the values under each respective parameter (minimum at the bottom, maximum at the top). The time scale is indicated by the bar in the bottom right portion of the chart. Only one replicate was completed of (B), while (A) is representative of two replicates.

Analysis of carbon catabolite repression and sugar transport

Examination of transport gene clusters revealed that the majority of those thought to transport sugars were downregulated (Table S3.2), and of these, the majority belonged to the phosphotransferase system (PTS) family, which is regulated by carbon catabolite repression (CCR). CCR is a regulatory mechanism that gives bacteria the ability to utilize carbon sources in order of preference (216). In gram-positive bacteria, a carbon catabolite protein such as CcpA binds to catabolite responsive elements (*cre*) and represses transcription of genes encoding non-preferred carbon source transport and utilization systems (217). To determine the extent to which CcpA binding could be responsible for the observed downregulation, *cre* sites identified previously by RegPrecise (218) and by our custom searches were collected and compared. Using these methods, 393 putative binding sites were identified (Table S3.2). Several PTS and sugar ABC transport genes were predicted to have 5' *cre* sites, the majority of which were downregulated at T_{50}. Other genes known to be CcpA-regulated, such as *spxB* (219, 220), were downregulated as well. This is surprising given that the glucose-containing media was replenished at a constant rate throughout the experiment, indicating that there could be a Mn-related mechanism for CcpA repression. Cells also did not appear to be starved for glucose; when excess glucose (2% final concentration) was added to the media, the post-EDTA growth rate was similar to that of normal BHI, which contains 0.2% glucose (Figure 3.24). This is not entirely unexpected, as it has been established by Redanz et al. (220) that CcpA repression of *spxB* in *S. sanguinis* is glucose-independent.

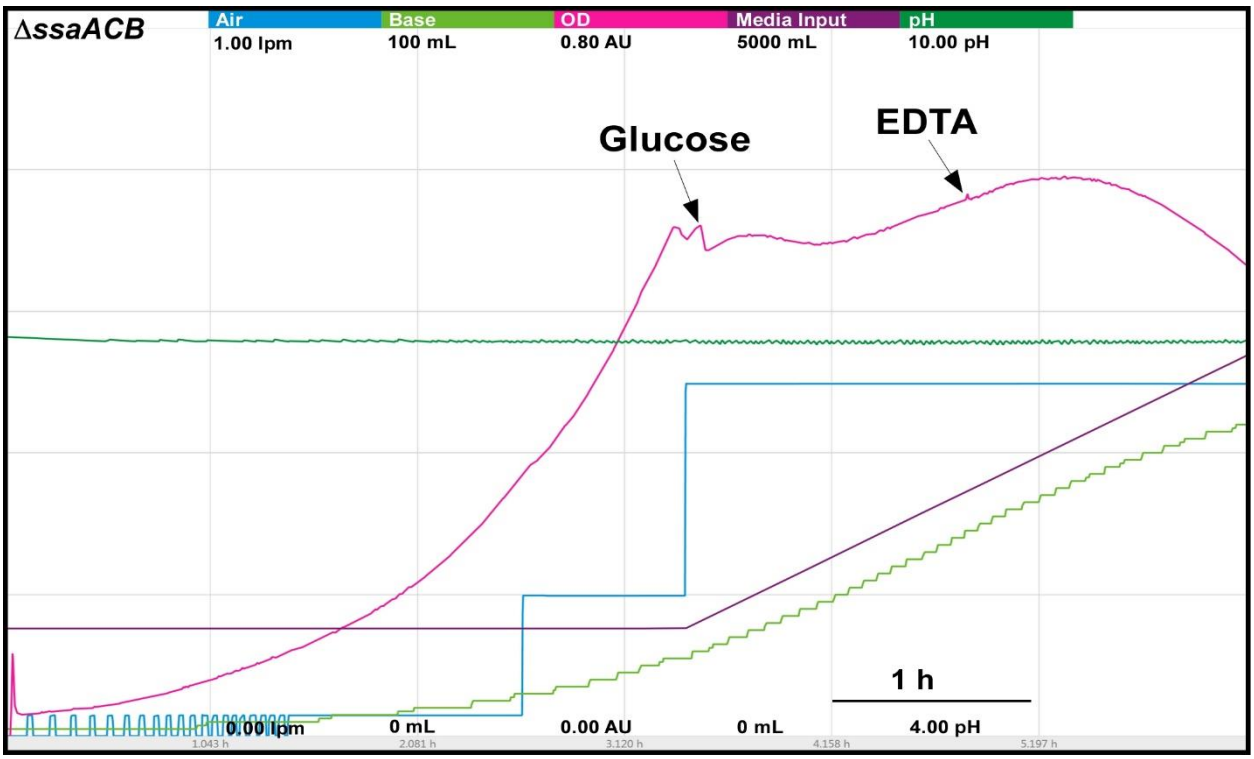

Figure 3.24 Aerobic fermentor growth of an Δ*ssaACB* mutant with glucose
Growth of an Δ*ssaACB* mutant in aerobic fermentor conditions as described previously. Glucose (final concentration 2%) was added to the carboy and vessel when the media pumps were turned on. Eighty min later, 100 µM EDTA added as described. Each color represents a different parameter, labeled at the top of the figure. The scale for each parameter is indicated by the values under each respective parameter (minimum at the bottom, maximum at the top). The time scale is indicated by the bar in the bottom right portion of the chart. This chart is representative of two replicates.

Other findings

We observed that several amino acid transporters and synthetases were differentially regulated after Mn depletion (Figure 3.25A). We were interested in learning whether a defect in amino acid synthesis could be responsible for the observed growth rate reduction.

Locus Tag	Annotation	TPM	Log_2 Ratio		
		T_{-20}	T_{10}/T_{-20}	T_{25}/T_{-20}	T_{50}/T_{-20}
SSA_0363	*dagA*, sodium:alanine symporter family protein	120	0.23	**1.26**	**1.22**
SSA_0364	*dctA*, serine/threonine transporter	102	0.30	**1.16**	**1.14**
SSA_0369	NADP oxidoreductase	767	0.52	**1.02**	**1.68**
SSA_0370	GNAT family N-acetyltransferase	1070	0.48	**1.00**	**1.61**
SSA_0371	*gdhA*, NADP-specific glutamate dehydrogenase	1079	0.29	**0.84**	**1.41**
SSA_0385	*opuAb*, ABC transporter permease/substrate binding protein	275	-0.03	**-1.09**	**-1.74**
SSA_0386	*opuAa*, glycine betaine/L-proline ABC transporter ATP-binding protein	287	-0.26	**-1.32**	**-2.00**
SSA_0572	2,3-butanediol dehydrogenase	147	0.10	-0.19	**-1.75**
SSA_0635	*trpC*, indole-3-glycerol phosphate synthase	18	0.26	-0.02	**-1.03**
SSA_0637	*trpB*, tryptophan synthase subunit beta	55	**1.22**	**1.25**	**1.38**
SSA_0638	*trpA*, tryptophan synthase subunit alpha	83	**1.30**	**1.28**	1.07
SSA_0703	citrate synthase	4	-0.10	0.56	**1.54**
SSA_0704	NADP-dependent isocitrate dehydrogenase	7	-0.51	0.44	1.03
SSA_0737	*sagP*, arginine deiminase	292	**1.17**	0.09	**-1.92**
SSA_0738	*arc*, ornithine carbamoyltransferase	666	**0.47**	**-0.93**	**-2.40**
SSA_0739	*arcC*, carbamate kinase	58	0.24	**-1.45**	**-3.15**
SSA_0741	*arcT*, acetylornithine deacetylase/succinyl-diaminopimelate desuccinylase	76	-0.01	**-1.49**	**-2.99**
SSA_0917	5-methyltetrahydropteroyltriglutamate-homocysteine methyltransferase	5	0.17	0.33	**1.34**
SSA_0921	*adhB*, alcohol dehydrogenase catalytic domain-containing protein	128	-0.04	**0.75**	**1.23**
SSA_1341	*carB*, carbamoyl-phosphate synthase large subunit	23	-0.03	**0.65**	**1.31**
SSA_1342	*carA*, glutamine-hydrolyzing carbamoyl-phosphate synthase small subunit	20	0.27	**0.77**	**1.26**
SSA_1360	amino acid ABC transporter ATP-binding protein	724	**0.50**	**0.81**	**1.16**
SSA_1401	PLP-dependent aminotransferase family protein	17	-0.09	0.24	**1.05**
SSA_1439	*hisK*, hypothetical protein	73	**0.62**	**0.78**	**1.41**
SSA_1440	*hisE*, phosphoribosyl-ATP diphosphatase	75	0.16	0.47	**1.11**
SSA_1569	amino acid ABC transporter permease	112	**0.77**	**0.91**	**1.01**
SSA_1615	alanine dehydrogenase	368	**0.88**	-0.35	**-3.45**
SSA_1621	amino acid permease	80	0.28	**-1.19**	**-3.17**
SSA_1713	*serA*, D-3-phosphoglycerate dehydrogenase	51	0.36	**1.37**	**2.22**
SSA_1715	*serC*, 3-phosphoserine/phosphohydroxythreonine transaminase	40	0.05	**1.07**	**2.03**
SSA_1949	peptide ABC transporter substrate-binding protein	182	**0.40**	**-0.95**	**-2.27**
SSA_1950	peptide ABC transporter ATP-binding protein	95	-0.16	**-0.68**	**-1.38**
SSA_1967	*ilvA*, threonine ammonia-lyase	58	0.21	**0.81**	**1.32**
SSA_1968	*ilvC*, ketol-acid reductoisomerase	210	0.31	**0.88**	**1.39**
SSA_1969	*ilvH*, acetolactate synthase small subunit	108	-0.09	0.57	**1.09**
SSA_1970	*ilvB*, acetolactate synthase large subunit	114	-0.34	**0.49**	**1.01**
SSA_2039	amino acid permease	23	0.01	**-0.97**	**-1.18**
SSA_2141	*argH*, argininosuccinate lyase	14	0.06	0.39	**1.24**

Log_2 Ratio
2.5
2.0
1.5
1.0
0.5
0.0
-0.5
-1.0
-1.5
-2.0
-2.5
-3.0
-3.5
-4.0
-4.5

Figure 3.25 Impact of Mn depletion on amino acid transport and synthesis
Expression of amino acid transport and synthesis genes in the Δ*ssaACB* mutant are depicted with their average TPM at T_{-20} and log_2 fold change values for each post-EDTA time point. Only genes with log_2 fold change values ≥ |1| are depicted in this chart. For all genes, see Table S 3.1. TPM values greater than 1000 are full saturation (green). Positive log_2 fold change values (red) are upregulated in post-EDTA samples as compared to T_{-20}, while negative values (blue) are downregulated. Values in bold are significant by adjusted *P*-value (≤ 0.05).

Addition of casamino acids resulted in slightly improved growth of Δ*ssaACB* cells in 12% O_2 and pooled rabbit serum (data not shown). Further studies were conducted wherein individual amino acids were added alone or in addition to casamino acids and it was

determined that the addition of 4 mM cysteine alone improved the growth to WT-like levels (Figure 3.26A). Cysteine also improved growth of Δ*ssaACB* cells in BHI + 100 µM EDTA in static cultures set to 12% O_2, although not quite to WT-like levels (Figure 3.26B). Addition of the reduced form of the tripeptide glutathione (γ-L-glutamyl-L-cysteinyl-glycine; GSH) led to similar results (Figure 3.26). Both cysteine and GSH can act as antioxidants (221), which may explain the improvement in aerobic tube growth. Interestingly, though, neither improved the growth of Δ*ssaACB* cells cultured in the fermentor with EDTA (Figure 3.27). We hypothesize that this difference may be due to the increased aeration in the fermentor vessel from the constant influx of air compared to the static tube cultures.

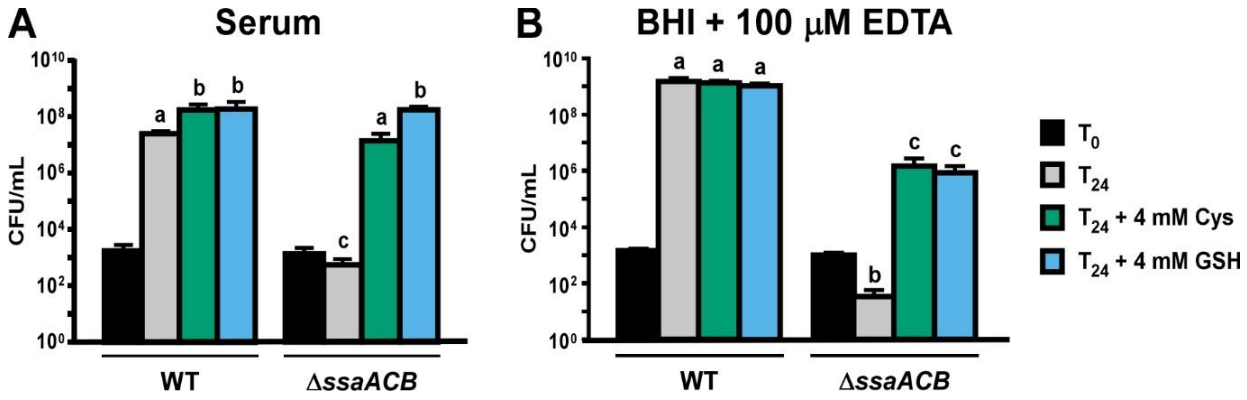

Figure 3.26 Addition of Cys or GSH to aerobic Mn deplete cultures
WT and Δ*ssaACB* cells were grown for 24 hours at 12% O_2 in either (A) pooled rabbit serum or (B) BHI + 100 µM EDTA with 4 mM of either Cys or GSH added. The means and standard deviations of at least three replicates are displayed. Significance was determined by repeated measures ANOVA with a Tukey-Kramer multiple comparisons test. T_{24} bars with the same letter are not significantly different from each other. T_0 values from each experiment were compared to each other by Student's two tailed t-test and found to be not significantly different.

Finally, we also observed decreased expression of large, contiguous loci encoding ethanolamine utilization, a type IV pilus system, and CRISPR-associated proteins (Figure 3.28), in addition to many smaller loci and individual genes (Table S3.1).

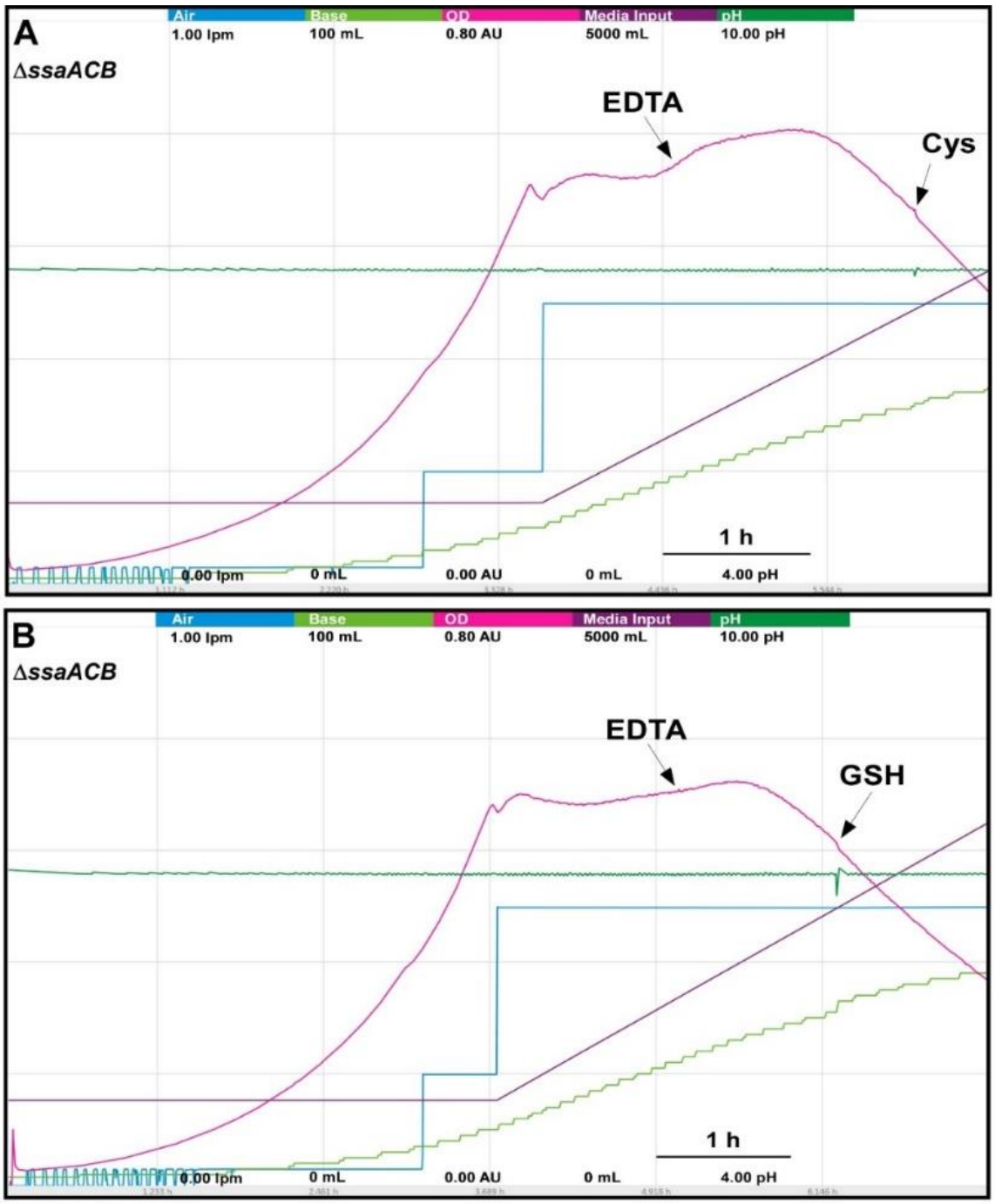

Figure 3.27 Aerobic fermentor growth of Δ*ssaACB* with Cys or GSH
Fermentor growth of Δ*ssaACB* with the addition of 100 µM EDTA at T_0 as described previously, with 100 µM of either (A) Cys or (B) GSH added at T_{70}. Each color represents a different parameter, labeled at the top of the figure. The scale for each parameter is indicated by the values under each respective parameter (minimum at the bottom, maximum at the top). The time scale is indicated by the bar in the bottom right portion of the chart. Only one replicate of each experiment was completed.

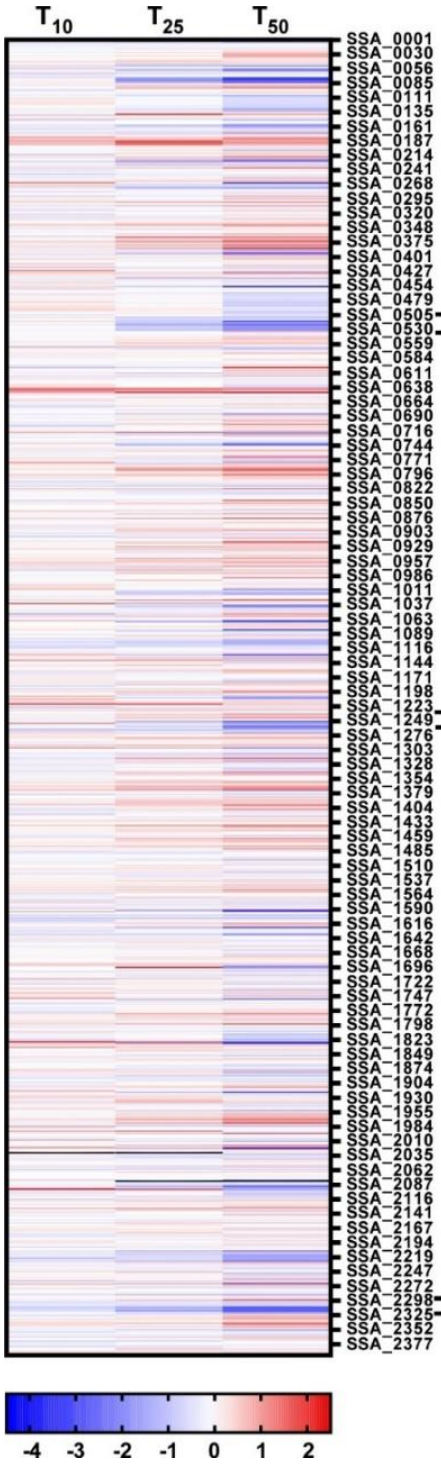

Locus Tag	Annotation	TPM	Log2 Ratio		
		T-20	T10/T-20	T25/T-20	T50/T-20
Ethanolamine Utilization Proteins					
SSA_0507	hypothetical protein	539	-0.36	**-0.90**	**-1.06**
SSA_0508	Phosphoserine phosphatase	63	**0.67**	**-0.87**	**-2.07**
SSA_0509	Propanediol utilization protein, PduV/EutP	84	0.17	**-1.15**	**-2.28**
SSA_0510	L-threonine-O-3-phosphate decarboxylase, CobD	157	0.12	**-0.61**	**-0.65**
SSA_0511	L-threonine kinase, PduX	145	-0.04	**-0.66**	**-0.61**
SSA_0512	Phosphoribosyltransferase, CobT	169	0.01	**-0.69**	**-0.62**
SSA_0513	Ethanolamine utilization, CobO	165	-0.03	**-0.80**	**-0.52**
SSA_0514	Ethanol dehydrogenase, EutG	160	**0.47**	**-0.97**	**-3.52**
SSA_0515	Ethanolamine utilization protein, EutS	1683	0.07	**-0.83**	**-2.06**
SSA_0516	Ethanolamine two-component response regulator, EutV	1069	0.07	**-0.79**	**-1.84**
SSA_0517	Ethanolamine transduction histidine kinase, EutW	957	0.27	**-0.80**	**-1.84**
SSA_0518	Ethanolamine utilization protein EutA	48	**0.71**	**-0.97**	**-1.82**
SSA_0519	Ethanolamine ammonia-lyase large subunit, EutB	62	0.13	**-1.26**	**-1.97**
SSA_0520	Ethanolamine ammonia-lyase small subunit, EutC	50	0.10	**-1.02**	**-1.72**
SSA_0521	Ethanolamine utilization, EutL	85	-0.24	**-1.42**	**-2.55**
SSA_0522	Ethanolamine utilization, EutK	52	0.24	**-0.77**	**-1.57**
SSA_0523	Acetaldehyde dehydrogenase,EutE	70	0.02	**-0.88**	**-1.66**
SSA_0524	Ethanolamine utilization protein, PduA/PduJ	79	-0.15	**-0.91**	**-1.58**
SSA_0525	Ethanolamine utilization protein, PduA/PduJ	115	-0.10	**-0.77**	**-1.88**
SSA_0526	Ethanolamine utilization, EutT	95	-0.13	**-0.92**	**-1.87**
SSA_0527	Ethanolamine utilization, EutD	99	-0.06	**-0.84**	**-1.86**
SSA_0528	hypothetical protein	79	-0.03	**-0.83**	**-1.79**
SSA_0529	Ethanolamine utilization, EutN	96	-0.14	-0.72	**-1.76**
SSA_0530	Ethanolamine permease, EutH	122	-0.21	**-1.10**	**-1.94**
SSA_0531	Ethanolamine utilization protein, EutQ	161	-0.35	**-1.12**	**-2.26**
CRISPR-Associated Proteins					
SSA_1246	CRISPR-associated protein Csm6	130	0.02	**-1.31**	**-2.88**
SSA_1247	CRISPR-associated protein, Csm5 family	74	-0.33	**-1.33**	**-2.38**
SSA_1248	CRISPR-associated RAMP protein, Csm4 family	67	-0.27	**-1.21**	**-2.47**
SSA_1249	CRISPR-associated RAMP Csm3	61	-0.08	**-1.20**	**-2.53**
SSA_1250	CRISPR-associated protein, Csm2 family	54	-0.06	**-1.01**	**-2.03**
SSA_1251	CRISPR-associated protein, Csm1 family	42	0.22	-0.61	**-2.01**
SSA_1252	CRISPR-associated endoribonuclease Cas6	101	**1.45**	0.35	**-1.88**
SSA_1253	CRISPR-associated protein Cas2	8	*-0.46*	-0.38	-1.15
SSA_1254	hypothetical protein	3	*-0.28*	*-0.29*	-1.06
SSA_1255	CRISPR-associated protein Cas1	5	*-0.49*	-0.94	**-1.68**
Type IV Pilus Proteins					
SSA_2302	Prepilin peptidase	396	**-0.36**	**-0.45**	**-0.70**
SSA_2303	hypothetical protein	499	**-0.33**	**-0.47**	**-0.88**
SSA_2304	hypothetical protein	645	**-0.37**	**-0.55**	**-0.68**
SSA_2305	AAA ATPase	440	**-0.40**	**-0.70**	**-1.20**
SSA_2307	Type IV pilus biogenesis protein PilO	48	**-0.69**	**-1.15**	**-2.83**
SSA_2308	Type IV pilus biogenesis protein PilN	28	-0.62	**-0.89**	**-1.92**
SSA_2309	Type IV pilus biogenesis protein PilM	44	**-0.62**	**-1.45**	**-2.74**
SSA_2310	hypothetical protein	62	**-0.87**	**-1.46**	**-3.10**
SSA_2311	hypothetical protein	56	**-0.62**	**-1.38**	**-2.75**
SSA_2312	hypothetical protein	35	-0.72	**-1.05**	**-2.62**
SSA_2313	Type IV pilin PilA	183	-0.48	**-1.61**	**-2.82**
SSA_2314	Type IV pilin PilA	311	**-0.61**	**-1.66**	**-2.96**
SSA_2315	Type IV pilus biogenesis protein PilE	991	-0.35	**-1.23**	**-2.42**
SSA_2316	Type IV fimbrial assembly protein PilC	107	-0.49	**-1.42**	**-2.55**
SSA_2317	Twitching motility protein PilT	107	**-0.91**	**-1.36**	**-2.60**
SSA_2318	Type IV fimbrial assembly, ATPase PilB	406	**-0.78**	**-1.63**	**-3.21**

Figure 3.28 Transcriptomic heatmap of Δ*ssaACB* aerobic fermentor grown cells
Heatmap displaying the log_2 fold change values of each gene at the time indicated as compared to T_{-20}. Positive log_2 fold change values (red) are upregulated in later samples as compared to T_{-20}, while negative values (blue) are downregulated. Select genes are depicted with their average TPM at T_{-20} and log_2 fold change values for each post-EDTA time point. TPM values greater than 1000 are full saturation (green). Log_2 fold change values follow the same color scale as depicted in the heatmap. Values in bold are significant by adjusted *P*-value (≤ 0.05).

Discussion

Only two enzymes have been confirmed to be Mn-dependent in *S. sanguinis,* and few others have been identified in other streptococci. Despite this, we observed changes in a wide variety of systems after Mn depletion of the Δ*ssaACB* mutant using EDTA. One possible explanation for this discrepancy is that Mn binds with low affinity to most proteins, resulting in Mn loss or replacement during purification. In fact, initial studies of the aerobic class Ib RNR identified Fe as the exclusive cofactor based on RNR activity *in vitro* and the fact that Fe was present in many different bacterial RNRs heterologously expressed in *E. coli*. Only later was it discovered that these enzymes were Mn-cofactored when natively expressed (99) and despite the *in vitro* activity of both forms of the *S. sanguinis* RNR, only the Mn-cofactored version was active *in vivo* (100, 101). Additional Mn-dependent enzymes may have similarly escaped detection. Another possible explanation is that Mn depletion impacts several key regulatory systems, such as CCR and (p)ppGpp, which leads to changes in the expression of many different genes. Mn levels have been found to be related to each of these systems in other gram-positive bacteria (134, 222). Here we highlight Mn-related systems we identified in this study of *S. sanguinis* for future investigation.

Mn-deplete transcriptome comparison in streptococci

Much like Mn depletion of *S. pneumoniae* (173), the depletion of Mn in *S. sanguinis* led to increased expression of a bacteriocin transport accessory protein (*bta*; SSA_1205), alcohol dehydrogenase (*adhB*; SSA_0921), and a hypothetical protein (SSA_1161). Similarly, several genes were decreased in expression in both species, including acetylornithine deacetylase (*arcT*; SSA_0741), pyruvate formate lyase (*pfl*; SSA_0342),

sodA (SSA_0721), thiamine biosynthesis protein (*apbE*; SSA_1126), *blpT* (SSA_0080), glycerol kinase (*glpK*; SSA_1826), and alpha-glycerophosphate oxidase (*glp*; SSA_1827). This indicates that there are many shared Mn-dependent pathways between these two species. Interestingly, we found that several significant DEGs in both studies had opposite trends, such as *czcD* (described above), galactose-1-phosphate uridylyltransferase (*galT*; SSA_1009), zinc metalloprotease (*zmpC*; SSA_1018), general stress response protein (*csbD*; SSA_1745), and a transcriptional antiterminator (SSA_1695) which were significantly downregulated in our study, but upregulated in *S. pneumoniae*.

Another Mn depletion study was recently published using *S. mutans* (148). This study also had fewer DEGs than our study and very few overlapped between all three studies. Of note, *dpr* and several conserved hypothetical proteins (SSA_0299, SSA_1397, SSA_0768) were upregulated in both *S. mutans* and *S. sanguinis*. Several amino acid transporters (SSA_2097-2102), an acyl-CoA dehydrogenase (SSA_1928), and an ABC bicarbonate/nitrate/sulfonate transporter (SSA_2353) were downregulated in both species. Additionally, the *S. mutans* type II CRISPR system was downregulated, as was the *S. sanguinis* type III version. While the genes encoding the DnaK chaperone protein (SSA_2007) and XRE family transcriptional regulator (SSA_0622) were significantly upregulated in *S. mutans*, they were slightly downregulated in our study of *S. sanguinis*. There were also several genes that were downregulated in *S. mutans* but upregulated in *S. sanguinis*, including *purC* (SSA_0028), *gtfD* (SSA_0613), an uncharacterized transporter (SSA_0798), and an acyltransferase (SSA_1199).

These results indicate that either (*i*) these three species have different Mn-dependent pathways or (*ii*) the different growth conditions led to differing Mn depletion responses. Further transcriptomic studies of other streptococci will be required to determine the core transcriptional response to Mn depletion in this Mn-centric genus.

Metal homeostasis is tightly regulated in *S. sanguinis*

Despite the fact that EDTA is a non-specific metal chelator (182), Mn was the only metal affected by EDTA addition. It appears that *S. sanguinis* was able to access the remaining available Fe, Zn, and Mg by upregulating metal importers and downregulating exporters. It was unable to compensate for lack of Mn by upregulating the only known secondary Mn transporter in SK36, SSA_1413 (Chapter 6), indicating that SsaACB is the only high affinity Mn transporter. SsaB was previously found to contribute to Fe transport (130) which we observed in this study as Fe levels were lower in the Δ*ssaACB* mutant as compared to WT. We noted that there was a slight, non-significant increase in Fe levels in the WT but not in the Δ*ssaACB* mutant. Fe levels are much higher than Mn in BHI (120) and we hypothesize that EDTA reduces the intracellular Mn concentration sufficiently to lessen SsaR repression of the *ssaACB* operon (130). This would result in the increase in Fe uptake in WT but not the Δ*ssaACB* mutant.

We were also able to determine that when *S. sanguinis* Mn levels drop below a certain threshold (~0.05-0.08 µg Mn per mg protein), cells enter a state where they are still viable but are unable to replicate as quickly until supplemental Mn is added. This was confirmed with both aerobic serum growth studies and fermentor growth in BHI with EDTA. We also hypothesize that there is a protective effect due to high cell density, as we were unable to generate reproducible fermentor results with slower media flow rates (data not shown).

The increase in expression of the putative Mn exporters, *mntE* and *mgtA,* is interesting, especially given the regulation and function of these proteins in other streptococci (109, 153, 180). It is possible that their regulation is affected by concentrations of other metals in *S. sanguinis* so that the change in metal ratios, such as Zn:Mn (Table 3.1), may have led to the observed upregulation. Recently, O'Brien et al. (153) found that transcription of *mntE* in *S. mutans* was repressed by the SsaR ortholog, SloR, which could potentially explain why Mn depletion lead to increased expression in our study. Although we were unable to confirm that MntE is indeed a Mn exporter in *S. sanguinis*, it shares 73% and 62% identity with orthologs in *S. pneumoniae* and *S. mutans*, respectively. Thus, we plan to evaluate the function and regulation further in future studies.

Modulation of expression of stress response genes

In other streptococci, it has been shown that while *sodA* can be highly upregulated under aerobic stress conditions, it is downregulated in the absence of Mn (173, 196). While this observed decrease in *sodA* expression under aerobic conditions possibly contributes to the slow growth observed post-EDTA, there must be other contributing factors as complete loss of the gene did not impact aerobic fermentor growth (Figure 3.15). This study confirms previous results from our lab that implicated SsaB as having a greater impact on aerobic stress tolerance in Mn-deficient media than SodA (130).

Mn depletion does not appear to induce a traditional stress response, although expression of an oxidative stress tolerance protein, Dpr, significantly increased, which is consistent with a recent study on Mn depletion in *S. mutans* (148). The observation that the loss of *dpr* alone led to sensitivity to Mn depletion in aerobic fermentor conditions indicates that it is a key component of the oxidative stress response and either Mn levels

or ratios of Mn to Fe contribute to its regulation and function. While it has primarily been characterized in other species for its role in H_2O_2-mediated oxidative stress resistance (116, 117, 223), we hypothesize that it plays a broader role in oxidative stress tolerance as we determined that H_2O_2 levels decreased after EDTA addition in the Δ*ssaACB* mutant. Indeed, Dpr protects *S. pyogenes* from multiple stresses (118) and was found to be regulated by both oxidative stress and metal ions (224). In *S. mutans*, loss of a Fe transport system reversed the oxygen sensitivity of the Δ*dpr* mutant (119). Although the levels of Fe in WT did not increase significantly, the ratio of Fe to Mn increased (Table 3.2). This may have contributed to the sensitivity of the *S. sanguinis* Δ*dpr* mutant in aerobic fermentor conditions after EDTA addition. We did not measure H_2O_2 levels in the early growth phase prior to turning on the media pumps. Thus, we cannot rule out whether H_2O_2 led to the delayed growth of these Δ*dpr* mutants in the vessel in this initial stage.

Table 3.2 Fe:Mn ratios in fermentor-grown cells

Strain	**T_{-20}**	**T_{10}**	**T_{25}**	**T_{50}**
WT	0.12	0.25	0.63*	0.48
Δ*ssaACB*	0.19	0.17	0.16	0.22

ICP-OES ratios as determined in Figure 3.4 were assessed by one-way ANOVA. * indicates $P \leq 0.05$ as compared to T_{-20}.

Ribonucleotide reductase activity and expression

The other known Mn-cofactored protein in *S. sanguinis*, the aerobic ribonucleotide reductase *nrdEF*, decreased in expression at T_{50}. Expression of *nrdEF* is also regulated by Fur-family regulators (225, 226). The SK36 genome (75) encodes a single Fur-family regulator, PerR, which is both metal- and H_2O_2-dependent in most bacteria (227). In our study though, PerR does not appear to be repressing expression of *nrdEF*, despite decreased H_2O_2 levels post-EDTA (Figure 3.21), and other members of the PerR regulon

in *S. pyogenes*, such as *hylIII* and *purE* (226), are not repressed as would be expected. Thus, we consider the possibility that cells are not stressed for nucleotides under these conditions.

One possible explanation could be that NrdEF activity is not limited because it has a higher affinity for Mn than other Mn-requiring enzymes. Another possibility is that the cells are obtaining nucleotides from another source. BHI contains abundant nucleosides that are taken up by cells (199), although we are unsure of the mechanism for conversion into nucleotides without NrdEF activity. It is possible that nucleotides are taken up from other cells, although we do not think that competence-induced fratricide is the mechanism responsible because cells incapable of competence are not deficient in serum growth. In summary, we believe that decrease in NrdEF activity is likely not limiting for growth under these conditions. A more likely possibility is a metal-sparing response, where essential enzymes are given priority for metal cofactors. SodA makes up ~1.5-2% of all protein in *S. gordonii* under aerobic conditions (196). Because s*odA* is not essential under these conditions (Figure 3.15), its decreased expression (Figure 3.14) could be a mechanism to increase the concentration of Mn available for NrdEF. Thus, the cells may not be starving for deoxynucleotides after EDTA addition because any remaining Mn is likely bound to NrdEF.

Mn depletion leads to glucose-independent changes in the regulon of CcpA

Given that BHI contains glucose, it was expected that *S. sanguinis* would preferentially transport and utilize it as a preferred carbon source under standard fermentor conditions. This is supported by the fact that glucose levels decreased in the media after cell growth in our corresponding metabolomics study (Chapter 4 and (202)) as well as by the high

expression of putative glucose transporters SSA_1752, SSA_1918-1920, and SSA_1298-1300 (228) at T_{-20} (Table S3.2). Surprisingly, expression of nearly all sugar transport systems decreased after Mn depletion (Table S3.2), despite nearly constant levels of glucose in the cells (199). CcpA is known to repress its own expression in a glucose-dependent manner (229), and yet much like the glucose transporters, *ccpA* expression was high at T_{-20} and significantly decreased by T_{50} (Table S3.2). Potential explanations could include: (*i*) 2 g/L glucose in BHI is not sufficient to induce CcpA repression; (*ii*) other regulatory mechanisms are preventing proper CCR under these conditions; or (*iii*) much like *spxB*, many other systems in *S. sanguinis* are subject to glucose-independent CcpA repression. Redanz et al. (220) used 0.3% as the low glucose condition in their study of CcpA-repression of *spxB*, whereas Bai et al. (229) used BHI alone (0.2% glucose) to observe differences in the transcriptome between the WT and Δ*ccpA* strains. Thus, the glucose concentration of BHI may indeed be low, yet sufficient to induce some repression of its regulon.

It is interesting that Mn depletion leads to an apparent increase in CcpA repression because we are not aware of this having ever been reported. The strongest evidence for CcpA-dependent regulation is *spxB.* In *S. sanguinis*, *spxB* expression has been shown to be positively regulated by SpxA1 (230) and VicK (231) and negatively regulated by CcpA (219). The *spxA1* gene was in the top 10% of all genes based on expression at T_{-20} and remained unchanged after EDTA addition (Table S3.1), indicating that repression by CcpA is likely responsible for the decrease in *spxB* expression as opposed to changes in induction by SpxA1. The mechanism by which CcpA represses *spxB* expression in *S. sanguinis* is unique from other streptococci in that it is independent of glucose (232). It

was previously determined that Mn may play a role in *spxB* expression in *S. pneumoniae*, as a Δ*mntE* mutant in *S. pneumoniae* accumulated Mn and produced more H_2O_2 than WT under excess Mn conditions (109).

In Firmicutes, phosphorylation of histidine phosphocarrier protein (HPr) to HPr(Ser-P) occurs when FBP and ATP levels are high (216). HPr(Ser-P) then binds to CcpA which in turn, induces the binding of the repressor to *cre* sites on the DNA. Additionally, FBP enhances the binding interaction of HPr(Ser-P) and CcpA, increasing repression. In our concurrent metabolomics study, we found that Δ*ssaACB* cells accumulated high levels of FBP at T_{50} after Mn depletion (199), which may explain the strong evidence for CcpA repression. As expected if CcpA were responsible for the changes in expression, we found that of the 169 DEGs found by Bai et al. (229) when comparing a *ccpA* mutant to SK36, 48 were changed in the opposite direction as our T_{50} sample. However, 15 significant DEGs were in the same direction and the remainder were unchanged in our study. Additionally, most of the DEGs we observed in our study did not overlap with those of Bai et al. (229). This comparison indicates that CcpA-dependent repression could be responsible for some of the changes in expression post-Mn depletion, but it does not explain all of the observed results.

The connection between Mn and sugar catabolism is not unprecedented, as previous studies have implicated Mn as important for sugar catabolism enzymes in other bacteria (134). Additionally, recent studies in *S. mutans* and *S. pneumoniae* have shown that fluctuations in metal homeostasis influence the regulation of carbohydrate metabolism (148, 233). The accumulation of FBP observed in our metabolomics data (Chapter 4 and (199)) might explain the glucose-independent CcpA repression we observed in most

genes with putative *cre* sites (Table S3.2). To determine potential causes for the accumulation, we examined the enzymes required for synthesizing and catabolizing FBP. We noted that in UniProt (uniprot.org), fructose-1,6-bisphosphatase (Fbp; SSA_1056) was annotated as Mn-cofactored. Fbp is the only enzyme in *S. sanguinis* known to catalyze the reaction from FBP to fructose-6-phosphate (F6P) through gluconeogenesis, as depicted in KEGG (https://www.genome.jp/kegg/) (234). While this may contribute to an accumulation of FBP, it is unlikely to be the principal factor, as expression levels of *fbp* are low at T_{-20} (Figure 3.29). Another contributing factor may be fructose-bisphosphate aldolase (Fba; SSA_1992), which catalyzes the production of glyceraldehyde 3-phosphate and glycerone phosphate from FBP. While the UniProt annotation states that SSA_1992 is co-factored by Zn, BRENDA (brenda-enzymes.org) (235) shows that several Fba orthologs are cofactored by Mn, including one from *Deinoccocus radiodurans* (236). Thus, it is possible that reduced activity of both Fba and Fbp due to Mn depletion led to the accumulation of FBP, which in turn induced CcpA repression after Mn depletion (Figure 3.29). Enzymatic activity assays will be required to determine the true cofactor for these enzymes in *S. sanguinis*, but accumulation of FBP is strong evidence that the activity of at least one enzyme in this pathway is affected by Mn depletion.

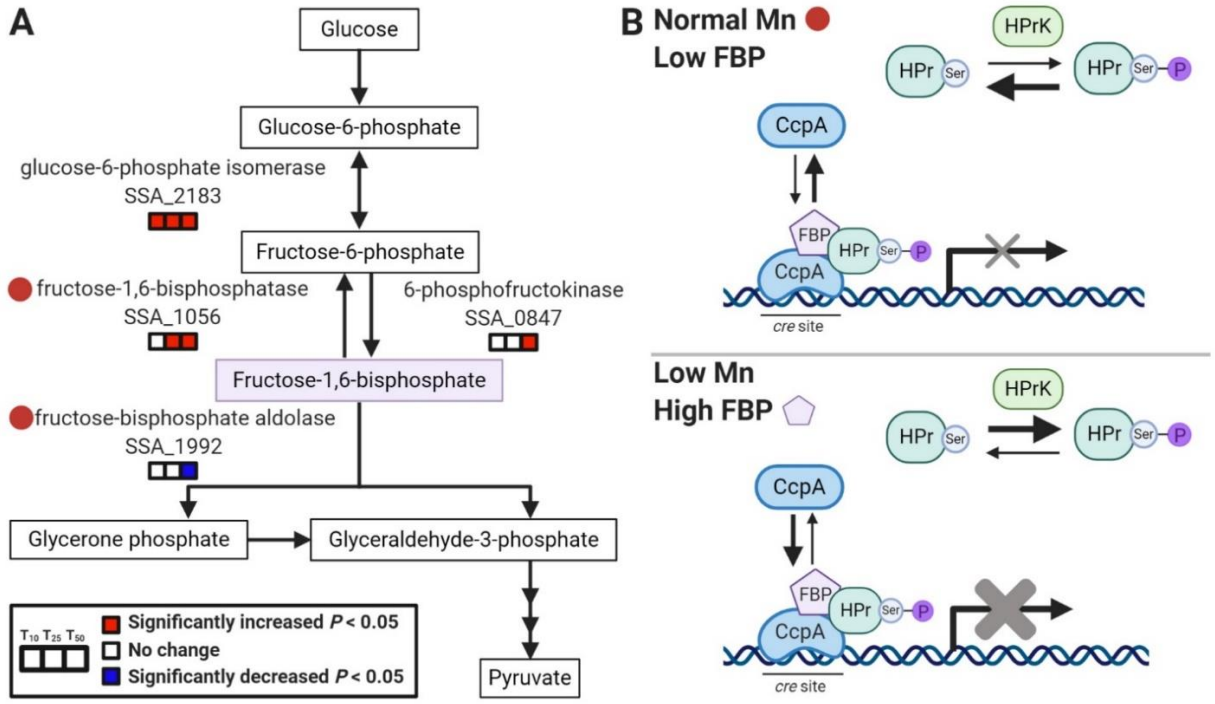

Figure 3.29 Model of Mn-dependent CcpA repression
(A) Depiction of a segment of the glycolysis and gluconeogenesis pathway in *S. sanguinis* from KEGG (Kanehisa and Goto, 2000). Red circles indicate potentially Mn-cofactored enzymes. Gene expression for each post-EDTA time point compared to T_{-20} is indicated by the colored boxes. Significant changes ($P < 0.05$) are indicated by red (increased) or blue (decreased). (B) Model of Mn-dependent CcpA repression based on CCR in Firmicutes as described by Gorke and Stulke (2008). In the top panel, normal Mn levels in BHI result in low FBP, which leads to less phosphorylation of HPr to HPr(Ser-P) by HPrK. With low FBP and HPr(Ser-P), CcpA exists mainly in its free state, unbound to *cre* sites in the DNA. This results in little to no repression of the CcpA regulon. The bottom panel depicts Mn depletion, where reduced activity of fructose-1,6-bisphosphatase and fructose-bisphosphate aldolase leads to an accumulation of FBP. This induces the phosphorylation of HPr so that it is primarily in the HPr(Ser-P) state. Increased FBP levels also enhance binding of CcpA to HPr(Ser-P) and to DNA. This results in significant repression of the CcpA regulon.

Expression of putative Mn-dependent enzymes may be related to CcpA-repression

Three putative Mn-dependent phosphatases, *pgm, cpsB,* and *deoB*, were downregulated at T_{50}, indicating potential for Mn-dependent regulation. Interestingly, our bioinformatic analysis predicted that *pgm* has putative 5' *S. suis cre* and *cre*2 sites and the *cpsA* gene, immediately upstream of *cpsB,* has a putative *cre*2 site (Table S3.2). This provides further support for the theory that Mn levels are related to CCR. DeoB links glucose metabolism

with purine biosynthesis (237, 238). As mentioned above, nucleotide levels seem to be unaffected as evidenced by the metabolomics data (Chapter 4). Thus the impact of decreased *deoB* expression, and likely decreased activity, does not appear to affect nucleotide levels, although it may have other unappreciated effects on the cell.

Another putative phosphatase, PhpP, may be able to utilize Mg^{2+} instead of Mn^{2+} as it was crystallized as Mg-bound in *Streptococcus agalactiae* (239) and as Mn-bound in *Staphylococcus aureus* (240). While the *S. sanguinis* protein is more similar to the *S. agalactiae* protein (60% identity compared to 37% for *S. aureus*), all three proteins contain the same putative metal-binding residues, although only two of the actual binding sites were conserved between the crystal structures. Further studies are required to determine the actual cofactor required for *S. sanguinis* PhpP *in vivo* and whether Mg can replace Mn following Mn depletion.

PpaC and PapP are essential pyrophosphatases in *S. sanguinis* (85). PpaC is an inorganic pyrophosphatase and PapP is a highly conserved nucleotide phosphatase (201). While we noted changes in the fatty acid profile of EDTA treated cells (Chapter 4), we did not observe morphological changes like those in the Δ*papP* mutant of *S. pneumoniae*. Additionally, AMP levels were observed to increase in EDTA-treated cells (199), which is the opposite of what would be expected if PapP activity was decreased. Thus, while we cannot rule out the possibility that these phosphatases have reduced activity and contribute to the slowed growth after Mn depletion, it is more likely that there are a multitude of Mn-dependent factors that culminate in the decrease in growth rate.

Reduced (p)ppGpp hydrolase activity may contribute to the post-Mn depletion phenotype

The relationship between (p)ppGpp and carbon source utilization has been previously established (241). When we examined the genome for *cre* sites, *relQ* was predicted to have a 5' *S. suis cre* site and was downregulated at T_{50} (Table S3.2), indicating that it could be under CcpA control. Very little is known about the transcriptional regulation of *relA* in streptococci (206, 242), although regulation of activity has been established in other species (243). Expression of *relP* and *relQ* appears to be growth phase-dependent, as well as regulated by environmental factors (244). In *S. mutans*, expression of *relP* is activated by a two-component system, RelRS, which is thought to sense oxidative stressors (245). It was hypothesized by Kim et al. (246) that (p)ppGpp production by RelP in *S. mutans* may be an attempt by the cell to slow growth to minimize damage from oxygen radicals produced during metabolism. While it was observed in this study that H_2O_2 levels decreased in response to EDTA addition, it is possible that other ROS were present due to a decrease in SodA activity. Thus, increased expression and activity of RelP, in addition to lack of hydrolase activity by RelA, could be at least partly responsible for the reduced growth rate.

In analyzing previous transcriptome studies in related species using Δ*relA* or *rel*^{0} mutants producing little to no (p)ppGpp, we noted many expression patterns similar to our study (242, 247, 248). While these studies utilized different species and growth conditions and thus are not a direct comparison to ours, it is remarkable that reduction in (p)ppGpp levels would lead to similar changes in gene expression as Mn depletion. Of special interest to us, several PTS genes were downregulated in all three previous studies. Similar to the results we observed in this study, the *S. pneumoniae* Δ*relA* mutant showed decreased

expression of *spxB* and *sodA* (247). These comparisons indicate either that dysregulation of (p)ppGpp levels leads to changes in expression of these genes in response to stress, or that decreased activity of the Rel hydrolase domain is not responsible for the observed changes in expression of these genes.

Based on these results, we hypothesize that reduced activity of the RelA hydrolase domain may contribute to the observed reduction in growth rate in the fermentor studies but is not entirely responsible. Specifically, our inability to eliminate the cell's only known (p)ppGpp hydrolase, combined with our finding that the Δ*relA* strains, which also have no hydrolase, exhibited poorer growth than *rel*^{0} mutants having no synthetase and therefore no (p)ppGpp, suggests that (p)ppGpp accumulation is highly detrimental to growth. A definitive test of this hypothesis will require measurement of (p)ppGpp levels in fermentor-grown cells. We are currently assessing various approaches for feasibility. In addition, the significant decrease in growth of the Δ*ssaACB* Δ*relA* strain as compared to the Δ*ssaACB* parent shows that there is an additive effect, indicating that the impact of the loss of RelA is not entirely Mn-dependent.

Connection between CCR and amino acid metabolism

Similar to our study, metals and CCR have been found to impact amino acid transport in other gram-positive bacteria. In *B. subtilis,* expression of biosynthetic genes for amino acids such as arginine, cysteine, and histidine was affected by addition of excess metals (249). In addition, expression of amino acid transporters and synthetases has been shown to be regulated by various CCR mechanisms (229, 250), as well as by VicRK orthologs (251). In *S. aureus*, decreasing expression of PTS and increasing the use of amino acids for glycolysis reduced the need for cellular Mn (251, 252). VicRK may also

be responsive to Mn through SsaR, as the *S. mutans* ortholog, SloR, was shown to positively regulate VicRK expression (253). Consistent with this, the expression of VicR (SSA_1565) was slightly, yet significantly decreased at T_{50} (Table S3.1). Thus, our results implicate Mn depletion as another potential influence on the regulation of amino acid transport and synthesis, either directly by decrease in function of an unidentified Mn-dependent enzyme or indirectly by influencing other regulatory systems, such as CCR or VicRK.

Other systems impacted by Mn depletion may also be related to CCR

In this study, all of the ethanolamine utilization (*eut*) genes were downregulated at T_{25} and T_{50} (Figure 3.25). Ethanolamine (EA) is a potential carbon and nitrogen source for bacteria derived from phosphotidylethanolamine found in membranes (254). Much like the gut microbe *Enterococcus faecalis* (255), the *S. sanguinis* genome (75) encodes a large cluster of *eut* and 1,2-propanediol utilization (*pdu*) genes (256). In *E. faecalis*, *eut* expression is positively regulated in the presence of EA by a two-component system (TCS) composed of the proteins EutW and EutV (257). Recently, it was discovered that the EutV/EutW TCS itself is negatively regulated by CcpA, and there are multiple putative *cre* sites within the *eut* gene cluster (256). These *cre* sites were not found in the RegPrecise search of *S. sanguinis* (Table S3.2), which was also noted by Bai et al. (229). The exact role of EA catabolism in *S. sanguinis* growth is still to be determined. Of note, despite a putative *cre* site upstream of *pduB* (256), expression of the *pdu* gene cluster was unchanged in our study (Table S3.1). However, this may be due to minimal expression pre-EDTA (T_{-20}).

Expression of most clustered regularly interspaced short palindromic repeats (CRISPR)-associated proteins was significantly decreased in the latter two post-EDTA time points (Figure 3.25). CRISPR-associated proteins that make up the CRISPR-Cas system are found in 40% of bacterial species (258). In addition to providing cells with adaptive immunity against foreign mobile elements, including phages and plasmids, these systems have been implicated in modulating oral biofilm development, DNA repair, and DNA uptake (259). Of particular interest, the type I and type II CRISPR systems of *S. mutans* have also been implicated in modulating stress response phenotypes, such as to pH, temperature, and oxidative stress (260). The type I mutant was able to grow faster in an acidic environment but was more sensitive to H_2O_2, paraquat, and SDS (260). Oral bacteria tend to have either type I or type II systems (259) but *S. sanguinis* SK36 has a type III system as determined by CRISPRCasFinder (261). The decrease in expression was unexpected, as the Δ*ssaACB* fermentor-grown cells are likely experiencing more oxidative stress due to decreased expression and function of SodA. Thus, it is possible that there is another function or mechanism for regulation of the CRISPR-associated protein genes. As mentioned, the *S. mutans* type II CRISPR system was one of the few gene clusters that were also significantly downregulated in a recent Mn-depletion study (148). Additionally, Csm1 (SSA_1251) was found to be a part of the CcpA regulon (229), although no *cre* site was identified (Table S3.2). The role and regulation of the CRISPR-Cas system of *S. sanguinis*, as well as its relationship to Mn levels, should be examined further.

The expression of a type IV pilus was significantly downregulated after Mn depletion (Figure 3.25). *S. sanguinis* is unusual in that it is the only streptococcal species to encode

a gene cluster for the biosynthesis of a type IV pilus system (T4P) (262) that is distinct from the T4P competence pilus (263), and yet few strains exhibit the twitching motility normally mediated by T4P (264). In SK36, T4P appears to be important for adherence to host cells and may be regulated by CcpA, despite the lack of a *cre* site in the promoter region (229, 264). In *S. pneumoniae*, the SsaR ortholog, PsaR, negatively regulates the expression of type I pilus genes in the presence of Mn (265) whereas a Δ*mntE* mutant containing excess intracellular Mn showed increased expression of the same genes (109). While the pilus type differs between these two streptococcal species, the shared Mn-dependent regulation may indicate that interplay between the Mn homeostasis and pilus expression is a conserved characteristic. Further studies are required to investigate this relationship and its role in the virulence of *S. sanguinis*.

Conclusions

The effect of Mn depletion on a multitude of diverse systems indicates that the impact of Mn is not relegated to only a few enzymes. Depletion of Mn does not induce a traditional stress response, instead inducing what appears to be dysregulation of many different genes that leads to rapid reduction in the growth rate, despite plentiful nutrients and other metals. While decreased function of the known Mn-cofactored enzymes, such as NrdF and the hydrolase domain of RelA, likely contributed to the decreased growth rate we observed upon Mn depletion, it is probably a combination of multiple systems leading to the observed phenotype. Additionally, a majority of the affected systems appear to be regulated by CCR through CcpA-dependent repression in a glucose-independent manner. Future research will focus on determining the respective contribution of each

putative Mn-dependent enzyme as well as whether there is a direct relationship between Mn and CCR.

Materials and Methods

Bacterial strains and transformation

Strains used in this study are listed in Table 3.3 and were generated using methods described in Chapter 2 with the primers listed in Table S3.3.

Table 3.3 Strains used in this study

Strain	Description	Source or Reference
SK36	Human oral plaque isolate	M. Killian; Xu et al. (75)
JFP49	Δ*comCDE::aad9*	Callahan et al. (198)
JFP132	Δ*sodA*::*aphA-3*	Crump et al. (130)
SSX_0866	Δ*mgtA*::*aphA-3*	Xu et al. (85)
SSX_0850¥	Δ*mntE*::*aphA-3*	Xu et al. (85)
JFP190	Δ*mntE*::*aphA-3*	This study
JFP192	Δ*ssaACB*::*tetM* Δ*mntE*::*aphA-3*	This study
JFP169†	Δ*ssaACB*::*aphA-3*	Baker et al. (83)
JFP173‡	Δ*ssaACB*::*tetM*	Baker et al. (83)
SSX_0256¥	Δ*ssaR*::*aphA-3*	Xu et al. (85)
JFP235	Δ*ssaR*::*aphA-3*	This study
JFP236	Δ*ssaACB*::*tetM* Δ*ssaR*::*aphA-3*	This study
JFP239	Δ*ssaACB*::*tetM* Δ*comCDE::aad9*	This study
SSX_2230¥	Δ*nrdD*::*aphA-3*	Xu et al. (85)
JFP246	Δ*nrdD*::*aphA-3*	This study
JFP247	Δ*ssaACB*::*tetM* Δ*nrdD*::*aphA-3*	This study
SSX_0250¥	Δ*relA*::*aphA-3*	Xu et al. (85)
JFP259	Δ*relA*::*aphA-3*	This study
JFP260	Δ*ssaACB*::*tetM* Δ*relA::aphA-3*	This study
SSX_1210¥	Δ*relQ*::*aphA-3*	Xu et al. (85)
JFP279	Δ*relQ*::*aphA-3*	This study
JFP281	Δ*ssaACB*::*tetM* Δ*relQ::aphA-3*	This study
SSX_1795¥	Δ*relP*::*aphA-3*	Xu et al. (85)
JFP275	Δ*relP*::*aphA-3*	This study
JFP277	Δ*ssaACB*::*tetM* Δ*relP::aphA-3*	This study
JFP276	Δ*relA*::*aphA-3* Δ*relP*	This study
JFP278	Δ*ssaACB*::*tetM* Δ*relA*::*aphA-3* Δ*relP*	This study
JFP280	Δ*relA*::*aphA-3* Δ*relP* Δ*relQ* (*rel*^{0})	This study
JFP282	Δ*ssaACB*::*tetM* Δ*relA*::*aphA-3* Δ*relP* Δ*relQ* (*rel*^{0})	This study
SK36 IFDC	*pheS* ermAM*	Cheng et al. (161)

†Strain used for RNA-seq studies
‡Strain used to generated multi-gene mutants
¥SSX strains used as template to generate identical JFP versions; JFP versions were used for experiments.

Growth studies

Cultures were grown as described in Chapter 2 with some modifications. For experiments with Mn^{2+} added, all $MnSO_4$ was Puratronic™ (Alfa Aesar, >99.999% pure). For the experiment with a 48 h time point, 1 mL of cells were removed from 24 h cultures for

plating. Mn to 5 uM final concentration was added to the remaining culture in one of the tubes and all tubes were returned to incubate at 37°C for another 24 h. For experiments with additives in agar plates, either 1 M $MnSO_4$ or 0.5 M sterile EDTA (Invitrogen) was added immediately prior to pouring the plates. Overnight cultures were grown in BHI and OD_{600} was measured. Cells were normalized to OD of the least dense culture using PBS and sequentially diluted in PBS prior to spot plating. Plates were then incubated anaerobically for 24 h.

Fermentor growth conditions

Cells were grown in aerobic fermentor conditions as described in Chapter 2 (163, 202). Airflow was increased stepwise as described and set at 0.5 lpm for all samples. EDTA was added to a final concentration of 100 µM at T_{-4} to the carboy and T_0 to the vessel. In some experiments, 100 µM Puratronic™ metals ($MnSO_4$, $FeSO_4$, $ZnSO_4$, $MgSO_4$), 2% dextrose (Fisher Chemical), or 4 µM cysteine (Alfa Aesar) or reduced glutathione (ACROS Organics) were added to the carboy at T_{66} and to the vessel at T_{70}.

RNA-seq library preparation and sequencing

Total RNA quantity and integrity were determined using an Agilent Bioanalyzer RNA Pico assay. All samples passed quality control assessment with RNA Integrity Numbers (RIN) above 8. Two sequential rounds of ribosomal reduction were then performed on all samples using Illumina's Ribo-Zero rRNA Removal Kit. The resulting depleted RNA was assessed using an Agilent Bioanalyzer RNA Pico assay to confirm efficient rRNA removal. Stranded RNA-seq library construction was then performed on the rRNA-depleted RNA using the Ultra II Directional RNA Library Prep Kit for Illumina (New England Biolabs), following the manufacturer's specifications for library construction and

multiplexing. Final Illumina libraries were assessed for quality using an Agilent Bioanalyzer DNA High Sensitivity Assay and qPCR quantification was performed using NEBNext Library Quant kit for Illumina (New England Biolabs). Individual libraries were pooled equimolarly, and the final pool was sequenced on an Illumina MiSeq, with 2 x 150-bp paired-end reads. Demultiplexing was performed on the Illumina MiSeq's on-board computer and resulting demultiplexed files uploaded to Illumina BaseSpace for data delivery. The University of Virginia Department of Biology Genomics Core Facility (Charlottesville, Virginia) completed all RNA-seq library preparation and sequencing.

Raw RNA-seq data from this chapter have been deposited in NCBI's Gene Expression Omnibus (266) and are accessible through GEO Series accession number GSE150593 (https://www.ncbi.nlm.nih.gov/geo/query/acc.cgi?acc=GSE150593).

Inductively coupled-optical emission spectroscopy

Additional 40-mL cell culture samples were collected from WT and Δ*ssaACB* cells at the same fermentor growth time points. They were then subjected to metal analysis as described in Chapter 2.

Microscopy

Cells were collected from the fermentor at T_{-20} and T_{50} time points. They were then fixed using glutaraldehyde (Fisher Chemical) and paraformaldehyde (Alfa Aesar) (267). Mounting medium containing DAPI (Vector Laboratories) was added prior to attaching a coverslip. Images were taken on a Zeiss Cell Observer Spinning Disc confocal microscope at VCU Microscopy Core.

Hydrogen peroxide quantification

Culture supernatants without RNAprotect were collected at each time point and stored at -20°C. Hydrogen peroxide concentration was measured using a Fluorometric Hydrogen Peroxide Assay Kit (Sigma). Standards were prepared from 3% hydrogen peroxide provided with the kit as recommended by the manufacturer. Fluorescence was measured in a black-walled, flat-bottom 96-well plate (Greiner) using a microplate reader (BioTek).

Putative *cre* site identification

Putative *cre* sites identified in the SK36 genome by RegPrecise (http://regprecise.sbpdiscovery.org:8080) (218) and listed within the "propagated regulon" collection were collected. Further analyses were performed by obtaining non-overlapping sequences ≤ 250 bp in length upstream of all SK36 genes using RSAT (http://rsat.sb-roscoff.fr/) (268, 269), then searching for putative *Streptococcus suis* pseudopalindromic *cre* and *cre*2 motifs (270) in these sequences using FIMO from MEME Suite (http://meme-suite.org/doc/fimo.html) (271). Motifs used for each search, as well as scores given for the RegPrecise and FIMO outputs, are listed in Table S3.2. Due to the variable length of the cre_{var} sites (272), seqinR v 3.6-1 (273) was used for this search. The FIMO cutoff was set to *P*-value ≤ 10^{-4}. Putative sites located within 10 bp of the start site of the corresponding gene were removed from the list.

Chapter 4 Impact of Mn Depletion on the Metabolome of *S. sanguinis*

Rationale

While transcriptomics can tell us about how genes are being regulated, this does not always reflect exactly what is going on in the cell. Thus, we employed the use of metabolomics so that we could determine the changes that occurred on a molecular level. We examined cells grown under the same conditions as Chapter 3 in order to observe changes in the metabolome post-Mn depletion. Additionally, we are unaware of studies that have evaluated the metabolome of *S. sanguinis* or BHI media. Thus, we wanted to evaluate what metabolites may be in BHI as well as what *S. sanguinis* generates during aerobic fermentor growth.

Copyright Disclaimer

Partial results of this chapter have been submitted to a scientific journal and are currently under review. The preprint citation is:

Puccio, T., Misra, B.B., and Kitten, T. (2020). Time-course analysis of *Streptococcus sanguinis* after manganese depletion reveals changes in glycolytic, nucleotide, and redox metabolites. *bioRxiv.* doi: 10.1101/2020.08.30.274233.

Introduction

Metabolomics is the comprehensive study of small molecules in the molecular weight range of 50-2000 Da in biological systems. Diverse mass spectrometry platforms such as LC-MS/MS, GC-MS, and CE-MS with and without chromatography, and spectroscopy technologies such as NMR have enabled high-throughput discovery metabolomics in various biological systems, including bacteria, plants, and humans (274). Recent studies have described the metabolomes of certain streptococci using various mass spectrometry

methods: *Streptococcus intermedius* under various oxygen conditions (275); *S. pneumoniae* in chemically defined medium (276); and *Streptococcus thermophilus* in batch fermentation (277-279). To our knowledge, the metabolome of *S. sanguinis* has yet to be investigated. Here we report the first untargeted metabolomic analysis of *S. sanguinis* or, indeed, of any *Streptococcus*, under Mn replete vs. deplete conditions.

Results

EDTA treatment of Δ*ssaACB* cells leads to Mn depletion and slowed growth

As described in Puccio et al. (202) and Chapter 3, EDTA treatment of Δ*ssaACB* aerobic fermentor-grown cells results in the depletion of Mn but no other biologically relevant metals, such as Fe or Zn, as determined by ICP-OES (Figure 4.1). Beginning ~38 min post-EDTA addition, cell growth slowed, resulting in a steady drop in OD (Figure 4.1).

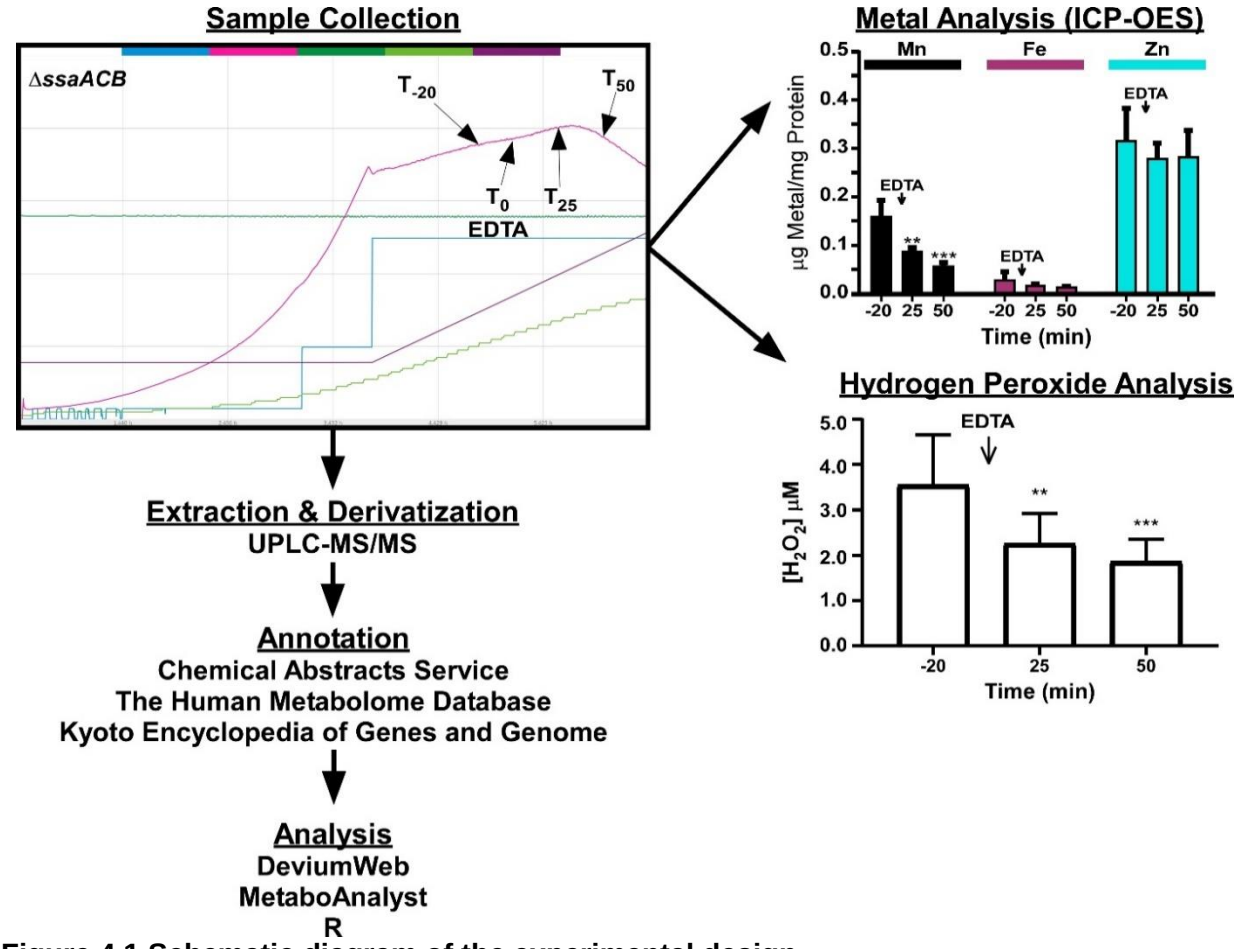

Figure 4.1 Schematic diagram of the experimental design
Fermentor sample collection, metal, and hydrogen peroxide analysis charts were adapted from Chapter 3 and Puccio et al. (202). Extraction, derivatization, and annotation were completed by Metabolon, Inc. ICP-OES, inductively coupled plasma optical emission spectroscopy; UPLC-MS/MS, ultra performance liquid chromatography with tandem mass spectrometry.

Global metabolomics of *S. sanguinis* cells and BHI media

Our goal was to understand the metabolic consequences of Mn depletion during growth of a *S. sanguinis* Mn-transporter mutant in a rich medium (BHI), as well as to survey changes in the conditioned media during the growth and treatment periods. Extensive global untargeted metabolomics analysis revealed 534 metabolites in cells and 422 metabolites in conditioned media. The raw metabolite abundance values alongside the identified metabolite IDs, super pathways and sub-pathway names, average mass, and identifiers such as Chemical Abstracts Service (CAS), PubChem, Kyoto Encyclopedia of

Genes and Genomes (KEGG), and Human Metabolome Database (HMDB) IDs are provided for both cellular and media metabolites (Tables S4.1-4.2). These datasets were refined through normalization, transformation, and scaling, followed by imputation (Tables S4.3-S4.4). The 534 metabolites belong to 57 different KEGG metabolic pathways (Table S4.5). The 422 metabolites identified in the conditioned BHI media belonged to 50 different metabolic pathways (Table S4.6), all of which overlap with the metabolic pathways found in the cells.

BHI has as its chief constituents bovine and porcine brain and heart extracts. Based on comparison with the pre-inoculation media samples, we identified several metabolites that appear to originate from BHI, and were excluded from further statistical processing as they were unique to the growth media alone (Table S4.7). Any metabolite that occurred in fewer than 75% of the samples was also excluded from the analysis, which resulted in the exclusion of 9 of the 534 metabolites detected in cells (Table S4.7).

Differential accumulation patterns of metabolites over time course and post-Mn depletion

We used a false discovery rate (FDR)-corrected ANOVA to determine metabolites that were significantly different in abundance between the different time-points. ANOVA revealed 173 and 13 metabolites that were significantly different in cells and media, respectively (Tables S4.8-4.9). To investigate whether these differential metabolites would map to metabolic pathways, we mapped the set of metabolites using the *S. pyogenes* M1 476 KEGG database within MetaboAnalyst by implementing overrepresentation analysis with Fisher's exact test and pathway topology analysis using relative-betweenness centrality (280). Pathway enrichment analysis of the 173 cellular

metabolites that were differential along the time course of EDTA treatment identified only purine and pyrimidine metabolism (nominal *P*-value < 0.05) (Figure 4.2; Table S4.10). Surprisingly pathway enrichment analysis of the 13 media metabolites that were differential along the time course identified purine and pyrimidine metabolism as above, but also glyoxylate and dicarboxylate metabolism, and alanine, aspartate, and glutamate metabolism (nominal *P*-value < 0.05) (Figure 4.2; Table S4.11). When metabolite abundances were compared for the two post-EDTA time points vs. T_{-20}, it was revealed that 1, 5, 13, and 30 metabolites were increased in T_{25} and T_{50} in media and T_{25} and T_{50} in cells, respectively (Figure 4.2). Of these, only 2'-deoxyadenosine increased in both cells and media at T_{50} (Tables S4.12-4.13). The 30 metabolites increased in T_{50} in cells were mostly lipids, energy metabolites, nucleotide phosphates, and dinucleotides (Table S4.12). When significantly decreased metabolites were compared, it was revealed that 1, 1, 13, and 30 metabolites were decreased in T_{25} and T_{50} in media and T_{25} and T_{50} in cells, respectively (Figure 4.2). Only glutamine levels decreased in both media samples (Table S4.13). The five metabolites that decreased in cells at T_{25} included cCMP and cUMP, while the 18 metabolites that decreased at T_{50} in the cells included IMP and XMP (Table S4.12).

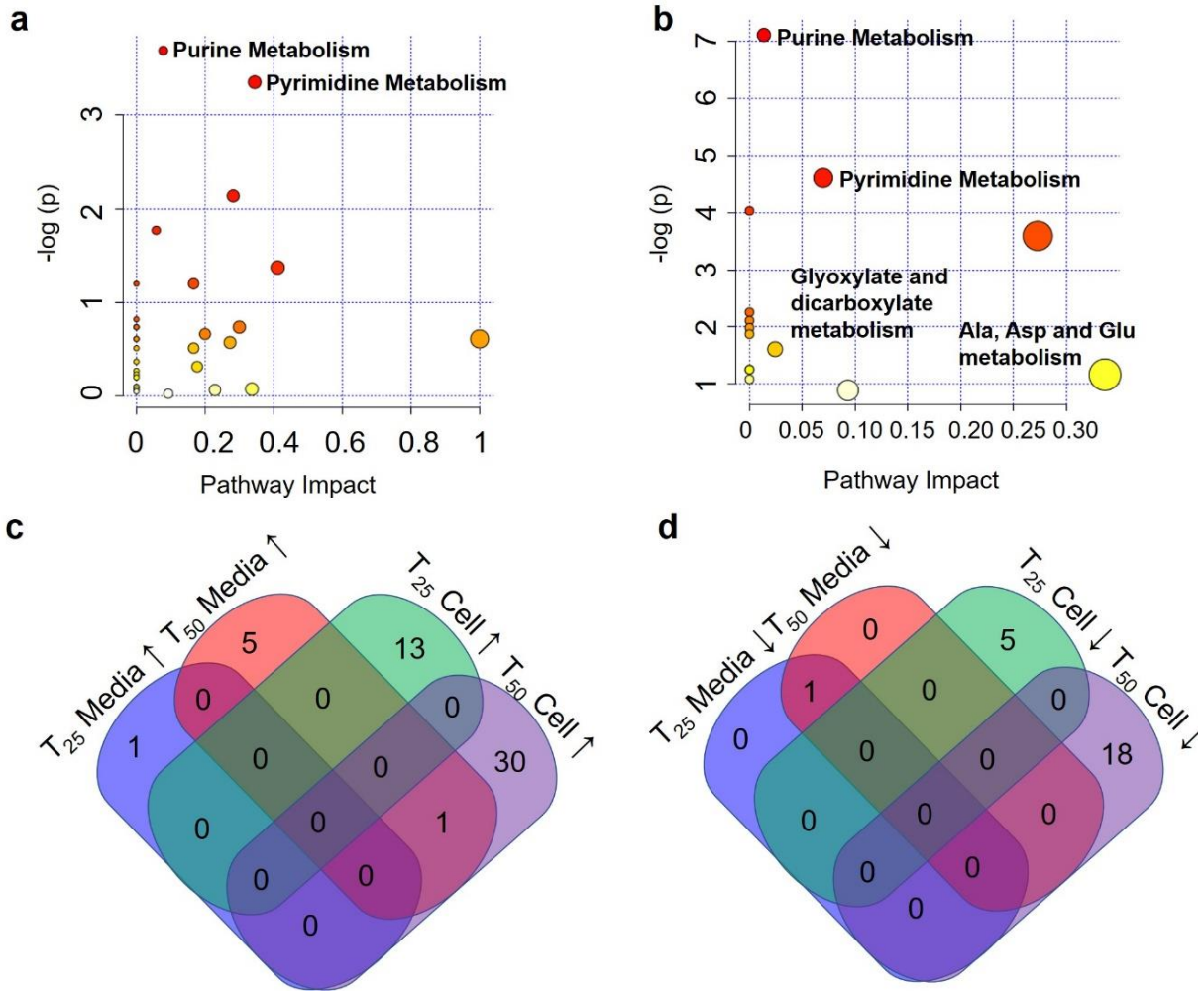

Figure 4.2 Pathway enrichment analysis for differential metabolites
Pathway enrichment analysis for significantly differential metabolites (ANOVA) in cells (A) and spent media (B). A 4-way Venn diagram displaying significantly increased (C) and decreased (D) metabolites at T_{25} and T_{50} compared to T_{-20}.

Multivariate and hierarchical clustering analysis

To define the metabolomic changes caused by Mn depletion, we used multivariate analysis and HCA. Using an unsupervised multivariate analysis, PCA, we observed that metabolite abundances alone were able to discriminate between the samples and explain 58.8% of the variation in the dataset by virtue of the first 2 PCs (PC1, PC2) in cells (Figure 4.3A) and 67.5% in media (Figure 4.3B).

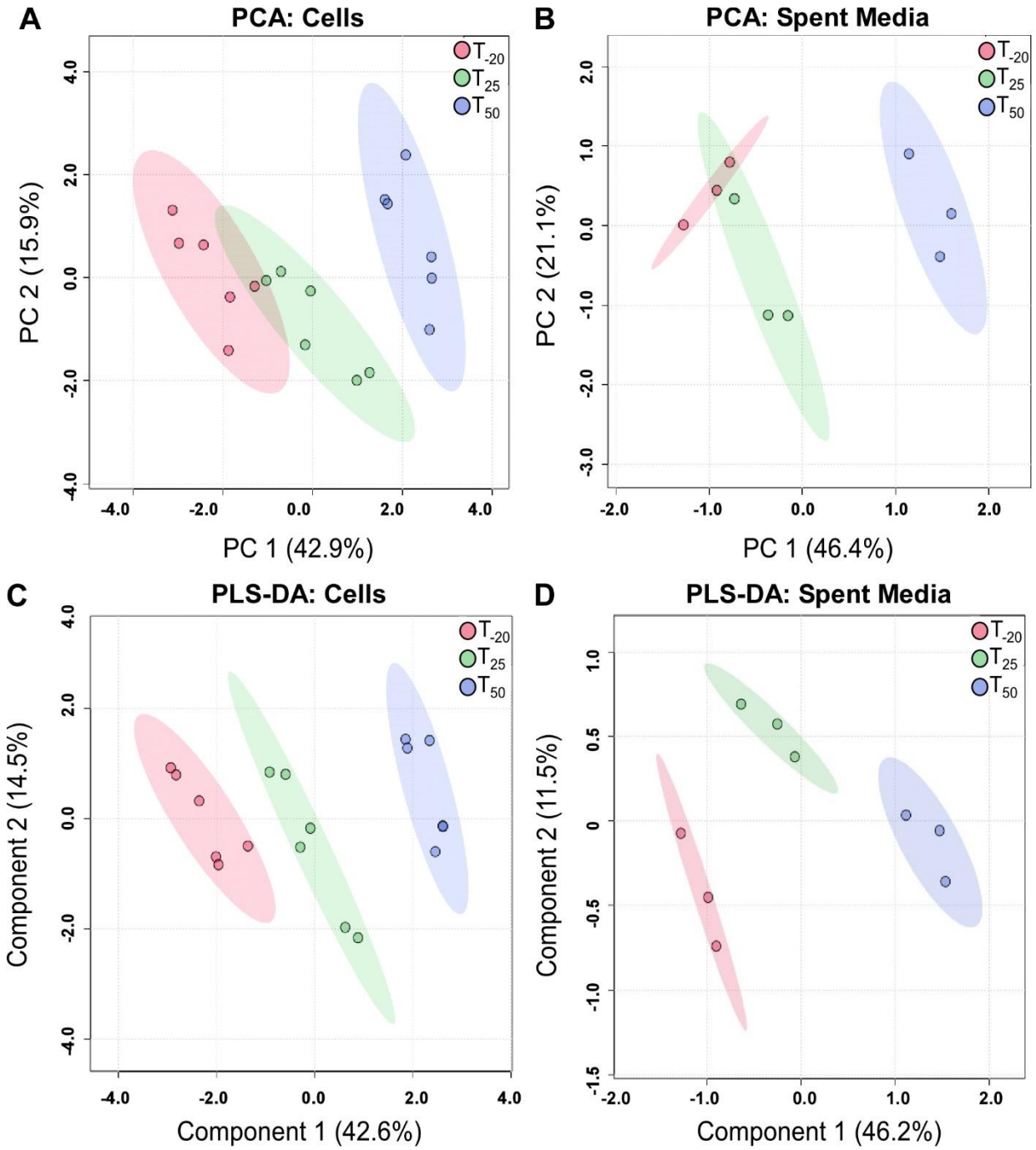

Figure 4.3 Multivariate analysis of cells and spent media samples
Score plots of PCA displaying the separation of time-points in cells (A) and spent media (B). Supervised multivariate analysis (PLS-DA) of cells (C) and spent media (D). Cell samples n = 6; media samples n = 3.

Using supervised multivariate analysis, PLS-DA, we observed that metabolite abundances alone were able to discriminate between the samples and explain 57.1 % of the variation in the dataset by virtue of the first 2 PCs (Component 1 and 2) in cells (Figure

4.3C) and 57.7% in media (Figure 4.3D). Additionally, PLS-DA and PCA performed on spent media samples explained 93.4% and 93.5% of the variation, respectively, by virtue of the first 2 PCs (Figure 4.4).

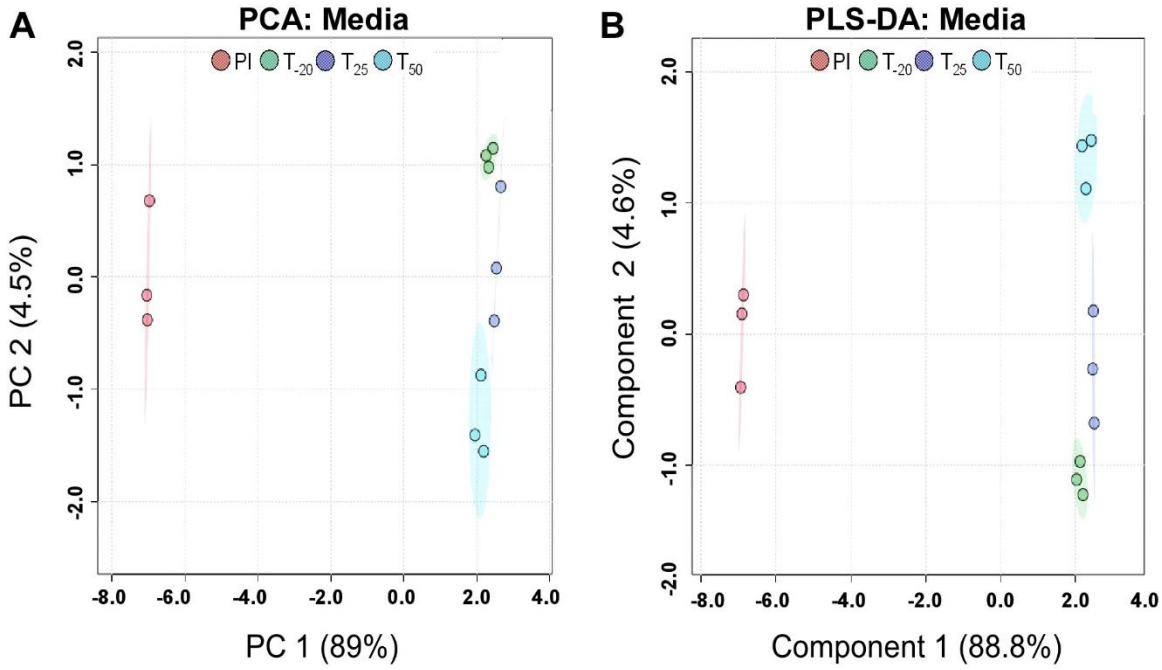

Figure 4.4 Multivariate analysis of all media samples
PCA (A) and PLS-DA (B) displaying the separation of time points in all media samples.

To identify the metabolites responsible for the discrimination among the metabolomic profiles, the variable importance in projection (VIP) score was used to select features with the most significant contribution in a PLS-DA model. VIP scores are a weighted sum of PLS weights for each variable and measure the contribution of each predictor variable to the model. Further, the VIP statistic summarizes the importance of the metabolites in differentiating the sample time points in multivariate space. Metabolites exhibiting high VIP scores (≥ 1.5) are the more influential variables. Our VIP analysis revealed that the top 15 metabolites for cells included lipids, cCMP, cUMP, and redox metabolites (Figure 4.5A). The VIP analysis revealed that the top 15 metabolites for spent media included amino acids and organic acids (Figure 4.5B). Of these VIP metabolites (cut off ≥ 1.5),

seven (glutamine, adenosine, adenine, glycerate, forminoglutamate, citrulline, and orotate) were shared between cells and media across all the time points, indicating their importance.

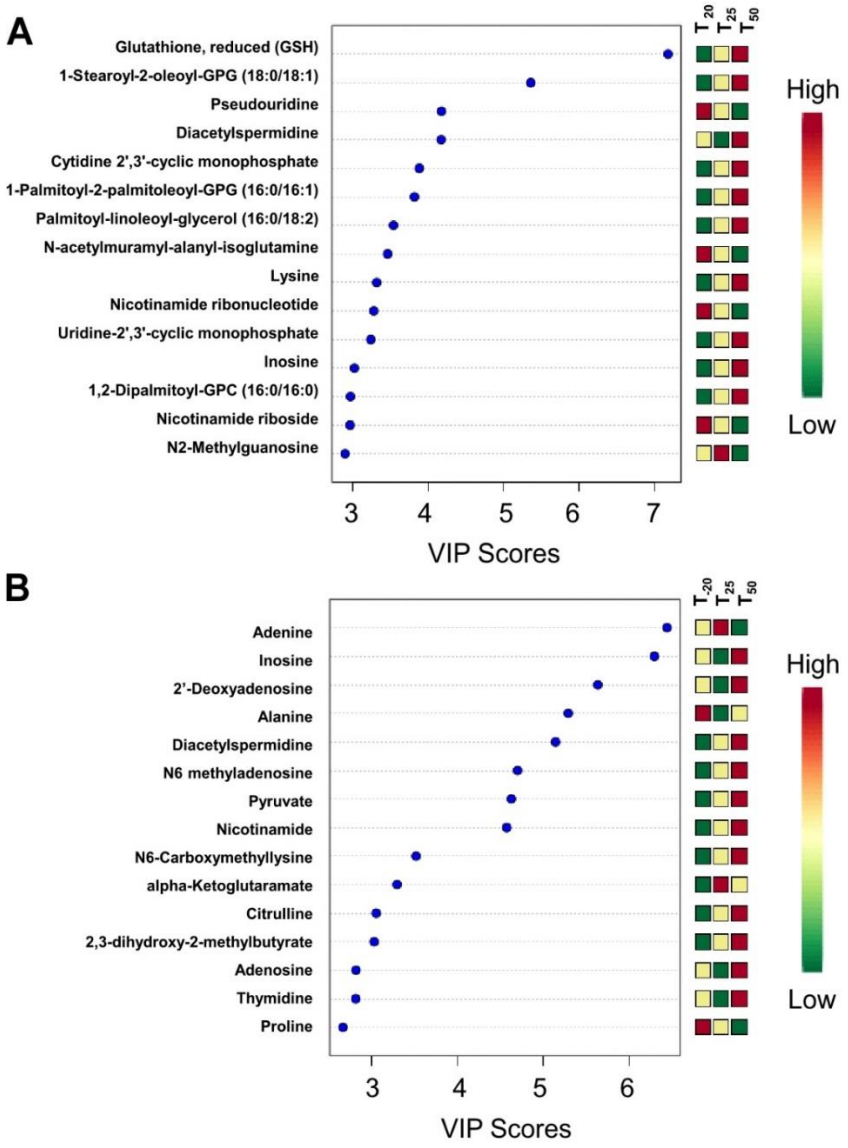

Figure 4.5 VIP analysis of cellular and media metabolism
Top 15 metabolites (variables) based on VIP scores from PLS-DA analysis of cells (A) and spent media (B).

We performed an HCA using the z-score-normalized metabolite abundances of the cellular and media metabolites, separately (Figure 4.6). Results indicated a clear clustering for the three time points as shown for the top 25 metabolites obtained from the

ANOVA for individual sample groups. In cells, two distinct clusters were formed based on the metabolite abundances, where the upper cluster (decreased in T_{50}) was represented by acetylated metabolites, purines and pyrimidines, and glutamyl dipeptides, and the bottom cluster (increased in T_{50}) contained several amino acids and lipids, and cCMP, cUMP, and UTP (Figure 4.6). In media, two distinct clusters were formed based on the metabolite abundances, with the upper cluster (increased in T_{50}) represented by several important metabolites such as uracil, ribose, pyruvate, nicotinamide, inosine, adenosine, guanosine, and the bottom cluster (decreased in T_{50}) containing glutamine, adenine, and 3’AMP (Figure 4.6b).

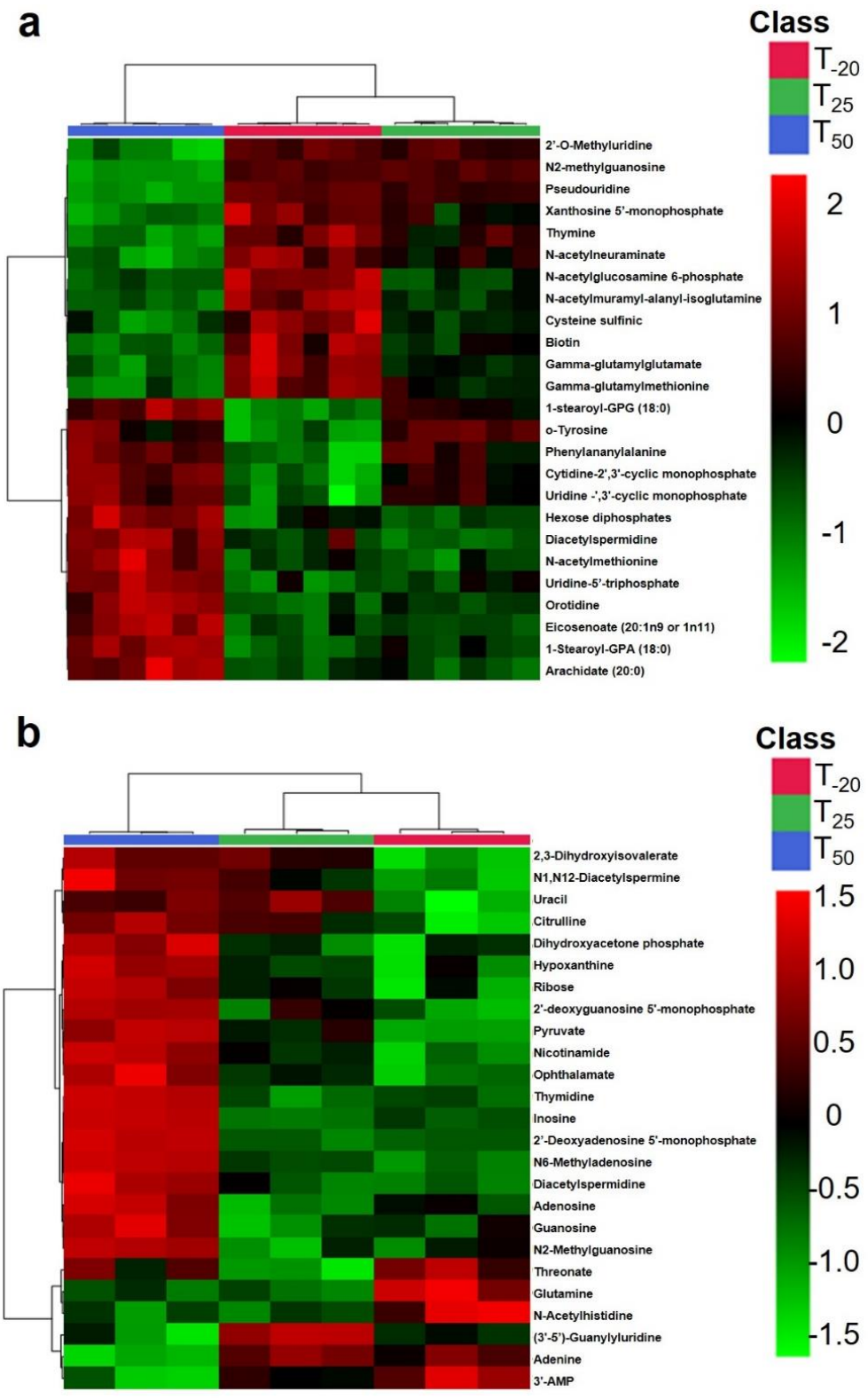

Figure 4.6 Hierarchical clustering analysis of cellular and media metabolism
Top 25 ANOVA-derived differential metabolites for HCA in cells (A) and spent media (B).

Time-course analysis of cellular and media metabolites

To understand the time course-dependent changes in metabolite accumulation patterns across the three time points in this complex study design, we started with a clustering analysis. Using STEM analysis, we interrogated the time course changes of the metabolites in the cells and media. The metabolite abundances were put into 20 model clusters, which revealed differential accumulation of metabolites as a function of time. For the cells, the top two significant models were #19 (pattern 0, 1, 1, -1, *P*-value 5e-115) and #18 (pattern 0, 1, -1, 0, *P*-value 4e-12) representing 193 and 80 metabolites, respectively (Figure 4.7A; Table S4.14). Metabolites following the pattern in model #19 were enriched for amino acid metabolic pathways: valine, leucine and isoleucine biosynthesis and degradation, alanine, aspartate and glutamate metabolism, and glycine, serine and threonine metabolism (*P*-value, < 0.1). Model #18 metabolites were enriched for arginine biosynthesis, arginine and proline metabolism, histidine metabolism, glyoxylate and dicarboxylate metabolism, and pyrimidine metabolism (*P*-value < 0.1). For the media, the top three models were #18 (0, 1, -1, 0, *P*-value 3e-59), #19 (pattern 0, 1, 1, -1, *P*-value 3e-23) and #14 (pattern 1, 1, 1, 1, *P*-value 6e-24) representing 132, 81, and 4 metabolites, respectively (Figure 4.7B and Table S4.15). Metabolites following the pattern in model #18 were enriched for alanine, aspartate and glutamate metabolism, amino acid metabolism, and arginine and proline metabolism. Those in model #19 were enriched for arginine biosynthesis, valine, leucine and isoleucine biosynthesis and degradation, glyoxylate and dicarboxylate metabolism, pyrimidine metabolism, alanine, aspartate and glutamate metabolism, and glycine, serine and threonine metabolism. The metabolites in model #14 included 2-deoxyadenosine, N6-methyladenosine, inosine, and nicotinamide.

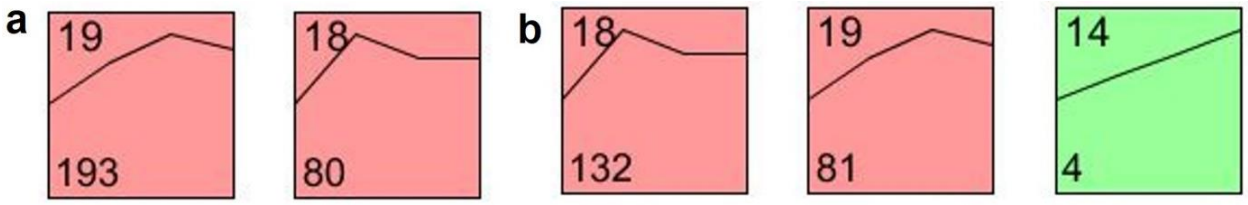

Figure 4.7 Time course analysis of cellular and media metabolism
Models displaying the statistically significant time-dependent changes in metabolite abundance in cells (A) and spent media (B).

Metabolomic analysis of BHI spent media reveals metabolic interactions of *S. sanguinis* with the extracellular environment

Our purpose in conducting this study was to examine the role of Mn in *S. sanguinis* metabolism, particularly in relation to IE. While the perfect medium for such a study would have been serum or plasma, this would not have been feasible, and so we instead used another complex yet commercially accessible medium—BHI. As with plasma, BHI has glucose as its most abundant sugar (0.2% w/v in BHI and ~0.1% w/v in plasma). Although serum and plasma have been the subject of many metabolomic studies, we are not aware of any previous metabolomic analysis of BHI. Thus, the analysis of the pre-inoculated BHI (Table S4.2) may be of interest to the many investigators who use this medium. Likewise, the comparison of the pre-inoculated and T_{-20} media samples tells us much concerning the metabolic and transport capabilities of *S. sanguinis* under Mn-replete conditions (Table S4.13).

As expected, we observed a significant decrease of glucose in spent media (Figure 4.8A), indicating its utilization as carbon source. Levels of fructose and mannose significantly decreased as well (Figure 4.8A), indicating that they are catabolized by cells. *S. sanguinis* encodes a number of putative sugar transport systems (75, 228). Lactate and pyruvate levels increased significantly in the media after cell growth (Figure 4.8B), indicating that these products of glycolysis were secreted from cells. Pyruvate has been shown to be

secreted by *S. sanguinis*, presumably to protect the cells from H_2O_2 stress by acting as an antioxidant (281).

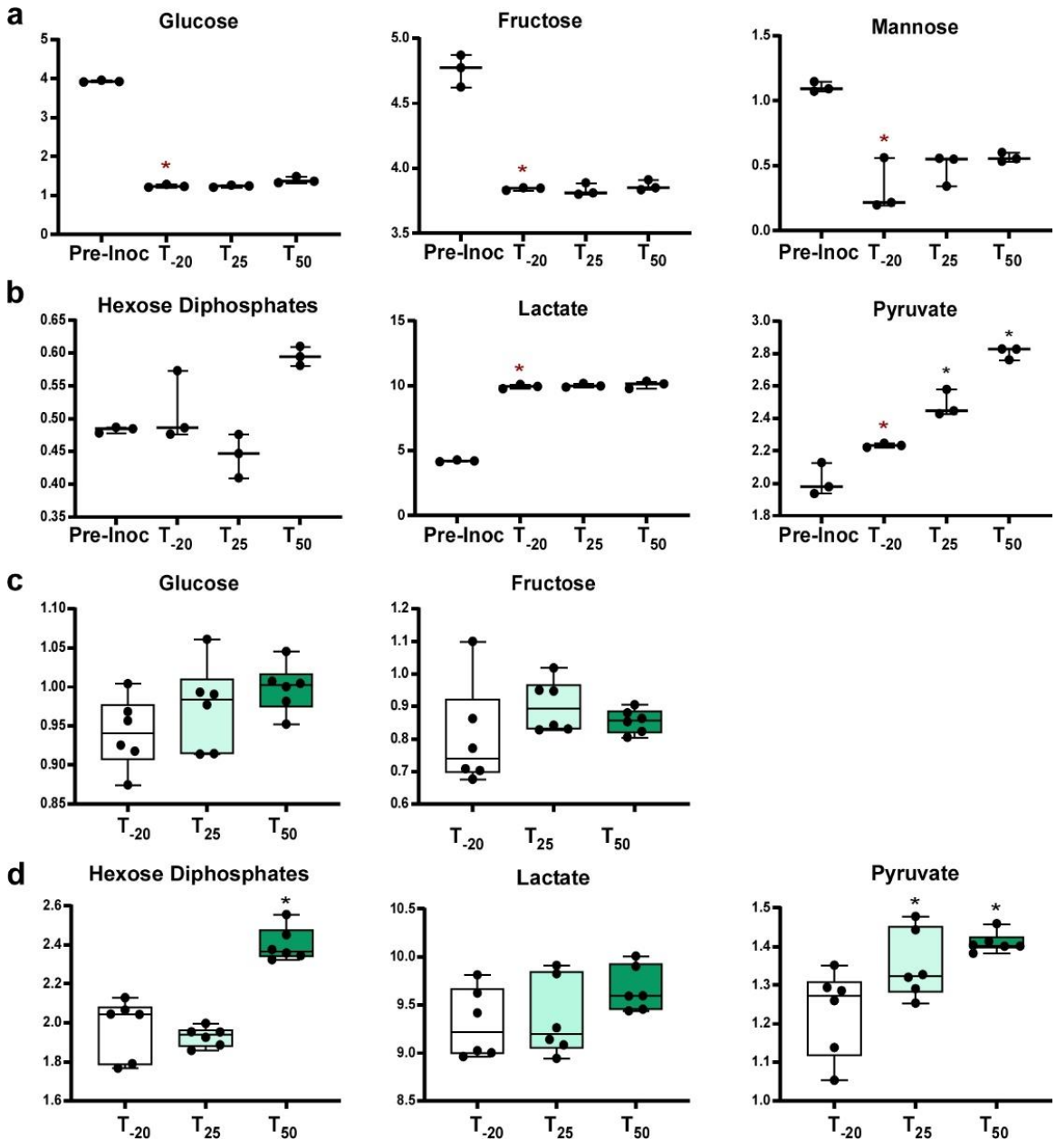

Figure 4.8 Relative abundance of carbohydrates and glycolytic intermediates
Levels of sugars in media (A) and cells (C) are depicted. Products of glycolysis in media (B) and cells (D). Y-axes indicate normalized relative abundances. Whiskers indicate the range; horizontal bars represent the mean. A two-tailed t-test was used to compare the pre-inoculum (Pre-Inoc) media samples to post-inoculum (T_{-20}). Red asterisks indicate *P*-value ≤ 0.05. Spent media and cell metabolite levels were compared using one-way ANOVA with a Fisher's least significant difference test to compare the post-EDTA samples to pre-EDTA. Black asterisks indicate *P*-value ≤ 0.05.

Also of interest, all nucleosides were significantly decreased after *S. sanguinis* growth (Figure 4.9 and Figure 4.10A-B). The opposite trend was observed with nucleobases, where most were significantly increased after cell growth (Figure 4.9 and Figure 4.10A-B). Nucleoside transport for salvage has been characterized in many bacteria, including the related species *Lactococcus lactis* (282) and *S. mutans* (283).

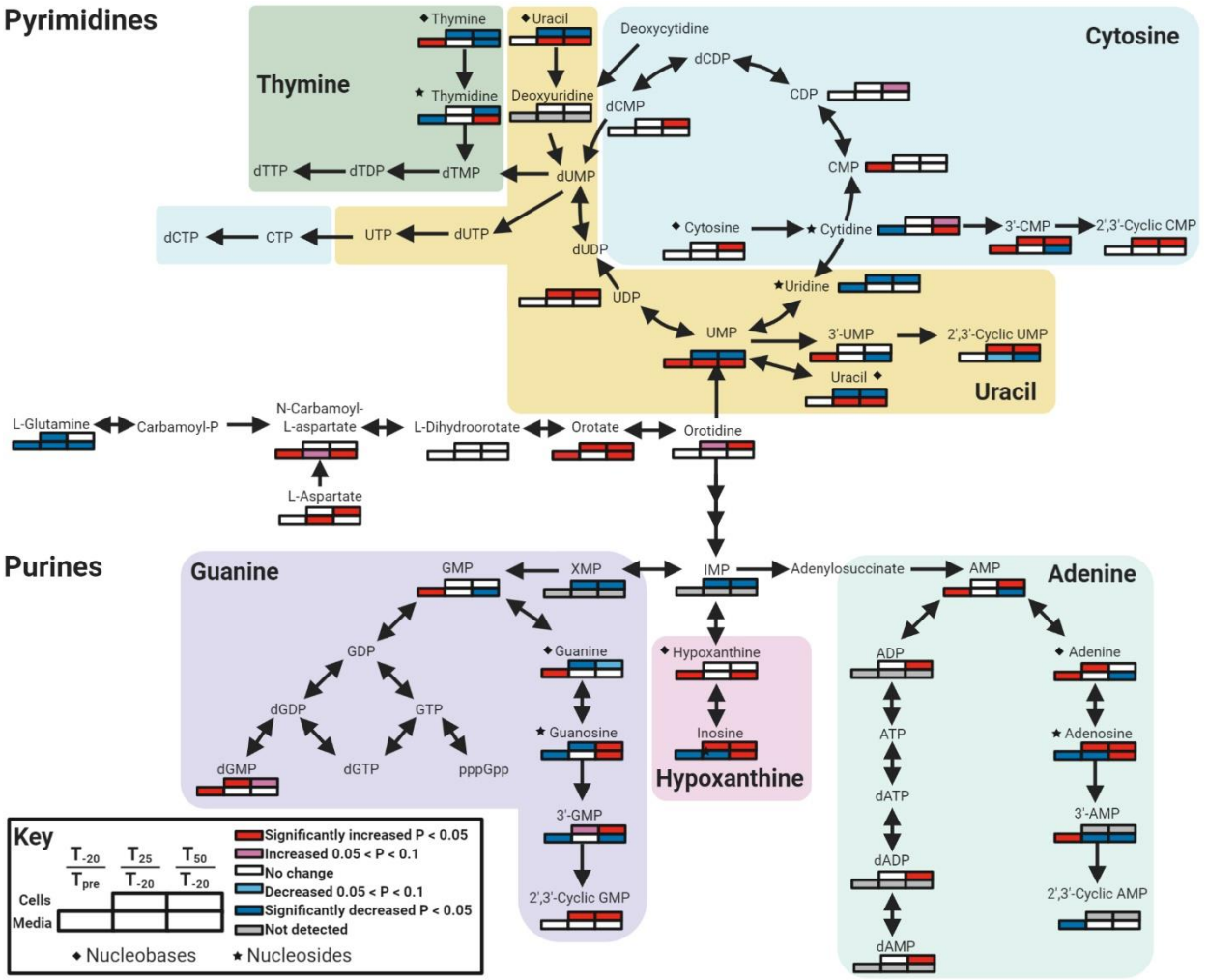

Figure 4.9 Quantitative changes in nucleotide metabolism after Mn depletion
The direction of change in metabolite concentration is depicted in shades of red or blue, for increasing or decreasing concentration, respectively. Significance was determined by a t-test using the comparisons shown in the key. Metabolites that do not have a set of boxes were not detected in any sample. Diamonds indicate nucleobases and stars indicate nucleosides. Figure was made using Biorender.com.

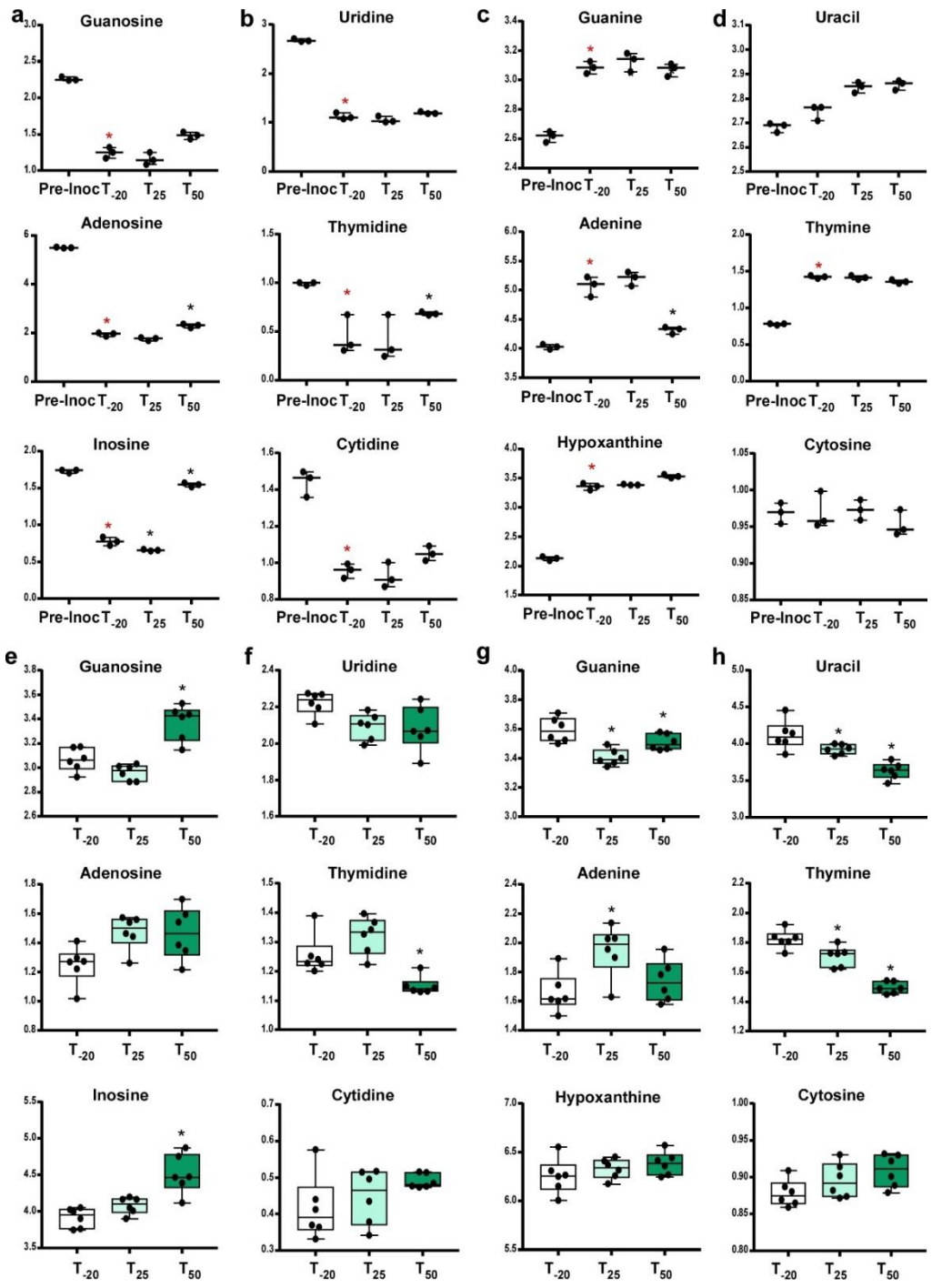

Figure 4.10 Quantitative changes in nucleotide metabolism

Purine nucleosides in media (A) and cells (E). Pyrimidine nucleosides in media (B) and cells (F). Purine nucleobases in media (C) and cells (G). Pyrimidine nucleobases in media (D) and cells (H). Y-axes indicate normalized relative abundances. Whiskers indicate the range; horizontal bars represent the mean. A two-tailed t-test was used to compare the pre-inoculum (Pre-Inoc) media samples to post-inoculum (T_{-20}). Red asterisks indicate when *P*-value ≤ 0.05. Spent media and cell metabolite levels were compared using an ANOVA with a Fisher's least significant difference test to compare the post-EDTA samples to pre-EDTA. Black asterisks indicate *P*-value ≤ 0.05.

Carbohydrate metabolism and glycolytic regulation in *S. sanguinis* cells show Mn dependence

The levels of glycolytic byproducts in *S. sanguinis* cells and spent media were impacted by Mn depletion. Glucose, fructose, and lactate levels remained constant in cells at all three time points while pyruvate levels increased after Mn depletion (Figure 4.8D). Mannose was not detected in cells at any time point, indicating rapid catabolism by cells (Table S4.1). Lactate is known to be produced in high levels by streptococci and other lactic acid bacteria (15), which explains the observed increase of lactate in the media after cellular growth. Pyruvate is produced through metabolism of sugars or amino acids. The observed increase in pyruvate levels in cells after Mn depletion (Figure 4.8) is not due to increased sugar levels, as the flow of media remained constant throughout the experiment. Most amino acid levels remained unchanged or decreased in cells after Mn depletion (Table S4.11). One potential explanation for the increase in pyruvate levels is that fewer pyruvate molecules were oxidized by pyruvate oxidase (SpxB) into H_2O_2 and acetyl phosphate, consistent with our finding of a significant decrease in H_2O_2 levels after Mn depletion (Figure 4.1) (202).

There was a significant accumulation of hexose diphosphates in cells at T_{50} and a slight increase in spent media as well (Figure 4.8B & D). Since levels of other glycolytic intermediates such as glucose-6-phosphate, glycerone, and glyceraldehyde-3-phosphate could not be measured using our platform (Tables S4.1-4.2), we are unable to assess the impact on this pathway using metabolomics alone. We hypothesize that the hexose diphosphate is primarily fructose-1,6-bisphosphate and its accumulation results from the reduced activity of two potentially Mn-cofactored fructose-1,6-bisphosphate-consuming enzymes in the glycolytic pathway: fructose-1,6-bisphosphatase (Fbp; SSA_1056) and

fructose-bisphosphate aldolase (Fba; SSA_1992) (202). We further hypothesize that fructose-1,6-bisphosphate accumulation is at least partly responsible for the glucose-independent CcpA repression observed in the transcriptome of *S. sanguinis* after Mn depletion (202).

Previous studies with other bacteria support a role for Mn in carbon metabolism. Mn deprivation was previously found to induce flux to the pentose phosphate pathway in *S. pneumoniae* (173). *S. aureus* was found to be more susceptible to calprotectin-mediated Mn starvation when glucose was the sole carbon source than when amino acids were also present (251). Excess Mn modulated glycolysis in *Escherichia coli* biofilms by decreasing levels of glucose-6-phosphate and glyceraldehyde-3-phosphate (284). Here we provide further evidence that Mn levels impact central carbon metabolism.

Purine and pyrimidine metabolism in Mn-deplete *S. sanguinis* reveal nucleoside utilization from media and nucleobase accumulation in cells

Mn is known to impact nucleotide metabolism through its role as cofactor for the aerobic ribonucleotide reductase NrdF (100, 101). Here, we observed further impacts of Mn on nucleotide metabolism. Mean levels of guanosine, inosine, and adenosine increased in both cells and media at T_{50} (Figure 4.9 and Figure 4.10). In cells, guanine levels decreased while hypoxanthine and adenine levels were unchanged at T_{50} (Figure 4.9 and Figure 4.10G). This indicates that there may be blockages in the conversion of purine nucleosides into nucleobases and nucleosides are likely being supplied from the BHI media. There are three enzymes encoded by *S. sanguinis* that can catalyze this reaction: PunA (SSA_1259), DeoD (SSA_1258), and SSA_2046. None of these enzymes have been found to use Mn (BRENDA; https://www.brenda-enzymes.org/) (235). In our

transcriptomics study (Chapter 3), expression of *punA* and *deoD* were significantly decreased after Mn depletion (202). The operon encoding *deoD* and *punA* has a carbon responsive element (*cre*) upstream of the first gene, *rpiA* (229), which is the recognition sequence for the carbon catabolite repression (CCR) regulator CcpA (217). As observed in Chapter 3, Mn depletion results in many changes in the CcpA regulon, which may explain the repression of this operon at T_{50}. Thus, this may be but one example of a non-carbon catabolite pathway impacted by Mn depletion through its effect on CCR.

Similar to the purines, the pyrimidine nucleosides appear to be taken up from the media and the nucleobases were likely generated by cells (Figure 4.9 and Figure 4.10). Mean uridine levels in cells decreased slightly in cells after Mn depletion, whereas UMP (Figure 4.9) and uracil (Figure 4.9 and Figure 4.10) levels dropped significantly. Uracil levels in cells likely decreased due to lower UMP production. Interestingly, orotidine levels increased in cells (Figure 4.9), indicating a potential blockage in the conversion to UMP, although the explanation for this remains elusive as no PyrF enzyme is known to utilize a Mn cofactor (https://www.brenda-enzymes.org/).

Levels of thymine decreased in cells after Mn depletion (Figure 4.9 and Figure 4.10D & H). which corresponds to a decrease in expression of *pdp* (pyrimidine nucleoside phosphorylase; SSA_1035; thymidine to thymine conversion) (202). Oddly, thymidine levels decreased as well, although this may be explained by the increase in dTDP-rhamnose levels at T_{50} (Table S4.10), indicating that thymidine may have been shuttled to sugar metabolism. Mean cytosine and cytidine levels increased slightly in cells after Mn depletion (Figure 4.9 and Figure 4.10F & H), which is the opposite trend from the other pyrimidines. Levels of downstream products 3’-CMP and 2’, 3’-cyclic CMP

increased as well (Figure 4.9). The discrepancy may be explained by decreased conversion to uridine as its levels dropped after Mn depletion (Figure 4.9 and Figure 4.10F). This is supported by a decrease in expression of *cdd* (cytidine deaminase; SSA_1037) after Mn depletion (202) and Cdd may be Mn-cofactored (285).

Oxidized and reduced glutathione levels in Mn-depleted *S. sanguinis* cells

Glutathione (γ-glutamyl-cysteinylglycine) is a nonprotein thiol produced by cells to prevent damage caused by reactive oxygen species (ROS) (286, 287). The SK36 genome (75) encodes a bifunctional γ-glutamate-cysteine ligase/glutathione synthetase (GshF; SSA_2168) (288). Mean levels of the glutathione precursors cysteine, glutamine, and γ-glutamylcysteine all decreased slightly in cells after Mn depletion, consistent with active synthesis, although glycine levels did not change (Figure 4.11). Interestingly, levels of reduced glutathione (GSH) increased in cells after Mn depletion, whereas levels of the oxidized form (GSSG) remained constant (Figure 4.11B). Since the air flow was kept constant throughout the experiment, we expected that GSH would have been utilized by redox enzymes for ROS remediation. While ROS levels were not measured directly by the metabolomics analysis, levels of *ortho*-tyrosine increased (Figure 4.11C), which is an indicator of high ROS states (289, 290). Thus, the accumulation of GSH is probably due to Mn depletion, either because of a blockage of GSH utilization by redox enzymes or due to a reduction of ROS.

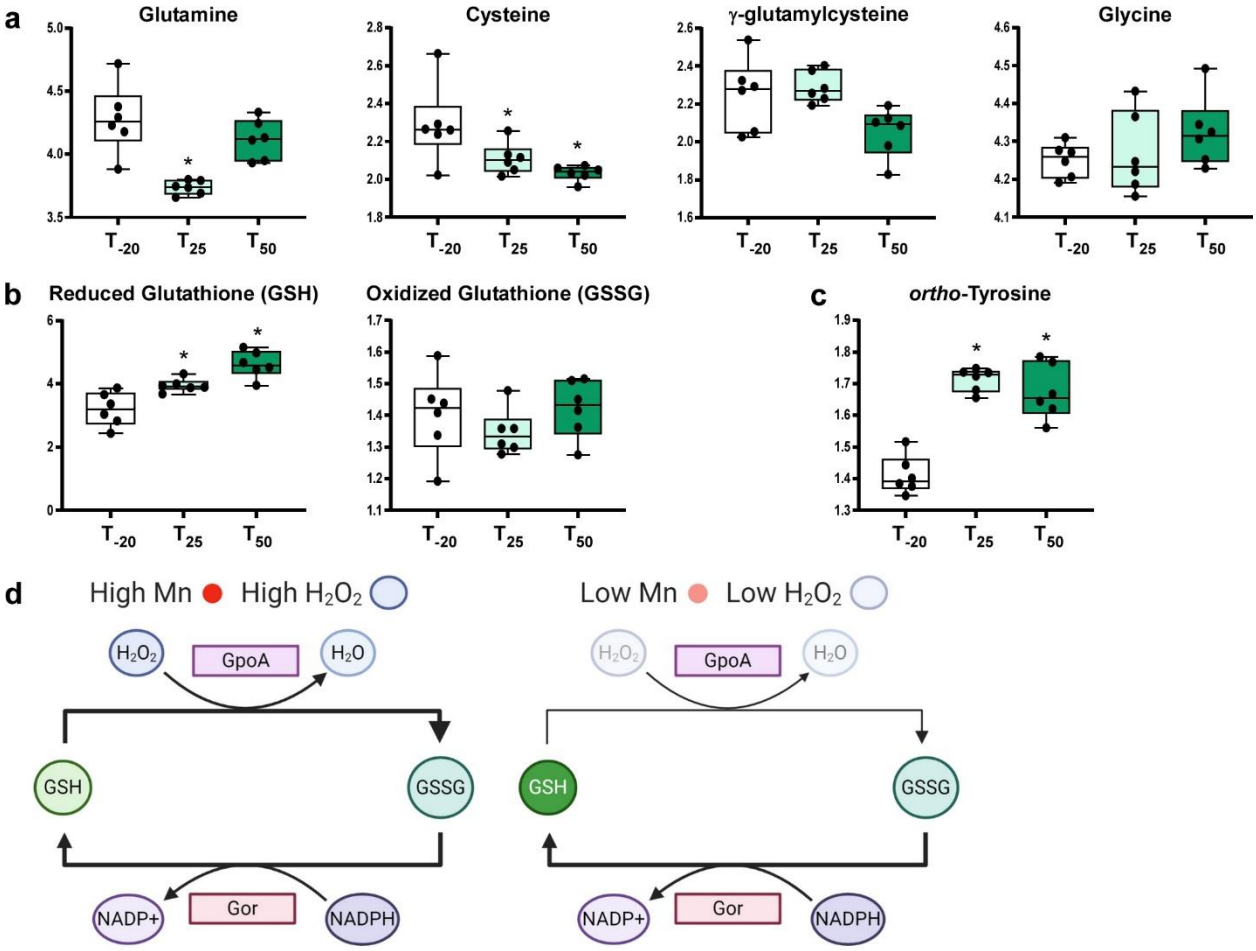

Figure 4.11 Glutathione abundance and model of Mn depletion
Levels of glutathione precursors (A), glutathione (B), and the oxidative stress indicator *ortho*-tyrosine (C) are shown. Y-axes indicate normalized relative abundances. Whiskers indicate the range; horizontal bars represent the mean. Metabolite levels were compared using one-way ANOVA with a Fisher's least significant difference test to compare the post-EDTA samples to pre-EDTA. Black asterisks indicate *P*-value ≤ 0.05. (D) Model of glutathione utilization by glutathione peroxidase (GpoA) and reduction by glutathione reductase (Gor) under normal and low-Mn conditions. Figure (D) was made using Biorender.com.

Due to the presumed decrease in activity of the Mn-cofactored superoxide dismutase, SodA (130), it is unlikely that all ROS levels would have decreased after Mn depletion. The notable exception is H_2O_2, which was found to decrease after Mn depletion due to reduced expression of *spxB* (202). This likely led to a decrease in the direct detoxification of H_2O_2 by GSH, although the extent to which this occurs in cells is controversial (291). Additionally, *S. sanguinis* does not encode any known glutaredoxins and the only enzyme

thought to utilize GSH in *S. sanguinis* is glutathione peroxidase (GpoA*;* SSA_1523), which uses GSH to detoxify H_2O_2 (Figure 4.11) (286). This enzyme has been found to contribute to oxidative stress tolerance in *S. pneumoniae* (221) and virulence in *S. pyogenes* (292). Additionally, the enzyme that converts GSSG to GSH, glutathione reductase (Gor; SSA_1533), is likely metal-cofactored, which could explain why GSSG levels remained constant instead of decreasing as GSH levels increased. Thus, Mn depletion could explain the accumulation of both reduced and oxidized glutathione.

Metabolic pathway and enrichment analysis

Pathway enrichment analysis was performed using MetaboAnalyst 4.0 and reported pathways are KEGG-based (234). The Chemical Translation Service (CTS: http://cts.fiehnlab.ucdavis.edu/conversion/batch) was used to convert the common chemical names into their KEGG, HMDB, Metlin, PubChem CID, and ChEBI identifiers.

Membrane and cell wall composition is affected by Mn depletion

Streptococci often modify the composition of their cellular membrane in response to the environmental conditions (293) and growth phase (294). The lipidomes of *Streptococcus mitis*, *Streptococcus oralis* (295), and *S. pneumoniae* (296) were recently characterized and found to contain phosphatidylcholine (PC), which is rare in bacterial membranes. Here we confirm that *S. sanguinis* cells also contain PC and consistent with the findings of Joyce et al. (296), PC may be synthesized from glycerophosphocholine (GPC) obtained from the media. Interestingly though, both PC and phosphatidylglycerols (PG) levels increased slightly after Mn depletion (Figure 4.12). The reason for these increases are unclear, although it is known that streptococci can modulate their membrane composition as part of a stress response (293).

Sub Pathway	Biochemical Name	Log_2 Fold Change	
		T_{25}/T_{-20}	T_{50}/T_{-20}
Phoshatidylcholine (PC)	**1-myristoyl-2-palmitoyl-GPC (14:0/16:0)**	1.025	1.023
	1,2-dipalmitoyl-GPC (16:0/16:0)	1.024	1.049
	1-palmitoyl-2-palmitoleoyl-GPG (16:0/16:1)*	**1.108**	**1.081**
	1,2-dipalmitoleoyl-GPC (16:1/16:1)*	1.086	1.100
	1-linoleoyl-2-arachidonoyl-GPC (18:2/20:4n6)*	1.004	**1.112**
Phosphatidylglycerol (PG)	**1-myristoyl-2-palmitoyl-GPC (14:0/16:0)**	1.025	1.023
	1-myristoyl-2-palmitoleoyl-GPG (14:0/16:1)*	1.070	1.017
	1,2-dipalmitoyl-GPC (16:0/16:0)	1.024	1.049
	1-palmitoyl-2-palmitoleoyl-GPG (16:0/16:1)*	**1.108**	**1.081**
	1-palmitoyl-2-oleoyl-GPG (16:0/18:1)	**1.137**	**1.176**
	1-palmitoyl-2-linoleoyl-GPG (16:0/18:2)	**1.118**	**1.177**
	1,2-dipalmitoleoyl-GPG (16:1/16:1)*	1.062	0.984
	1-palmitoleoyl-2-oleoyl-GPG (16:1/18:1)*	**1.087**	1.044
	1-stearoyl-2-oleoyl-GPG (18:0/18:1)	**1.227**	**1.383**

Fold Change
1.50
1.25
1.00
0.75
0.50

Figure 4.12 Lipid levels in cells post-Mn depletion
Levels of various PC and PG species in cells post-Mn depletion. Increases in log_2 fold change are depicted in red and decreases are depicted in blue. Statistical significance was determined by t-tests comparing each post-EDTA sample to the pre-EDTA sample. Bold values indicate $P \leq 0.05$.

Amino sugars are major components of bacterial cell walls. N-acetylglucosamine and N-acetylgalactosamine were likely present in the media and taken up by cells, as the levels decreased after the growth of *S. sanguinis* cells (Figure 4.13). Alternatively, most N-

acetylneuraminate was probably generated by cells, as levels significantly increased in media after cell growth. Mn depletion led to a significant decrease in these acetylated amino sugars in cells (Figure 4.13). Cellular levels of N-acetylglucosamine-1-phosphate are not depicted due to the fact that it was not detected in any of the T_{50} samples (Table S4.7). It is unlikely that the components are being entirely lost to the media, as levels remained constant after Mn depletion. Instead, we believe that reduction in Mn levels led to catabolism of these components, possibly through deacetylation, although expression of N-acetylglucosamine-6-phosphate deacetylase (*nagA*; SSA_1893) was only slightly increased in our transcriptomics study (Chapter 3 and (202)).

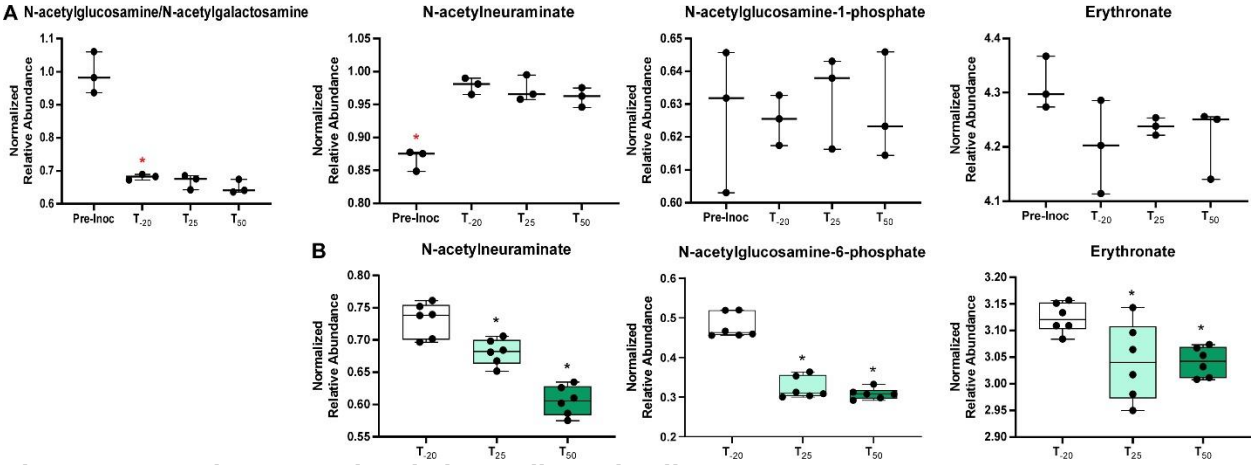

Figure 4.13 Amino sugar levels in media and cells
Amino sugar levels in media (A) and cells (B). Whiskers indicate the range; horizontal bars represent the mean. A two-tailed t-test was used to compare the pre-inoculum (Pre-Inoc) media samples to post-inoculum (T_{-20}). Red asterisks indicates *P*-value ≤ 0.05. Spent media and cell metabolite levels were compared using an ANOVA with a Fisher's least significant difference test to compare the post-EDTA samples to pre-EDTA. Black asterisks indicate *P*-value ≤ 0.05.

Unique metabolites in cells and media

Interestingly, both taurine and hypotaurine were detected in cells and were slightly increased in media at T_{25}, although only hypotaurine was significant (Figure 4.14). *S. sanguinis* lacks the enzymes to synthesize or degrade these molecules, so the changes in the media were unexpected. Additionally, urea was undetected in two pre-inoculation

media samples but was detected in all samples after cell growth (Tables S4.1 and S4.2). This was interesting, given that there is no known urea biosynthesis pathway in *S. sanguinis.* Both of these pathways should be investigated further.

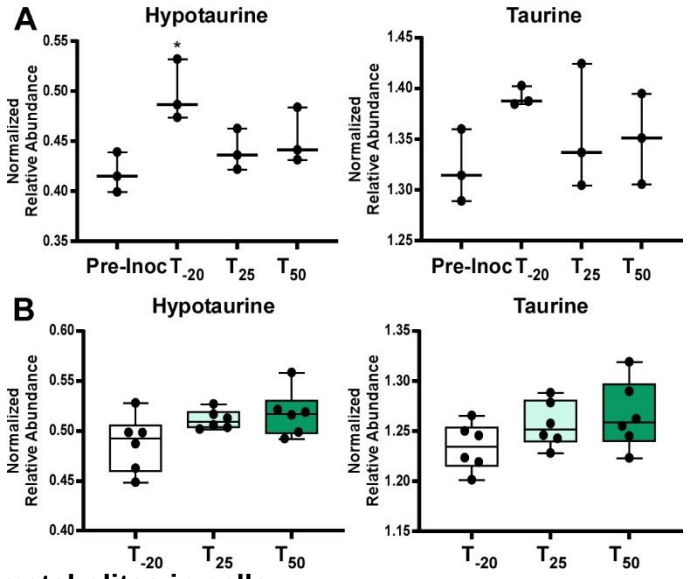

Figure 4.14 Taurine metabolites in cells
Hypotaurine and taurine levels in media (A) and cells (B). Whiskers indicate the range; horizontal bars represent the mean. A two-tailed t-test was used to compare the pre-inoculum (Pre-Inoc) media samples to post-inoculum (T_{-20}). Asterisk indicates *P*-value ≤ 0.05. Spent media and cell metabolite levels were compared using an ANOVA and none were significantly different.

Discussion

In this study, we showed system-wide metabolomic changes induced in *S. sanguinis* Mn-transporter mutant cells and spent media in response to EDTA treatment over time. This study captured the Mn-responsive metabolic processes, such as dysregulations in carbohydrate, nucleotide, and redox metabolism, many of which may contribute to the reduction in bacterial growth rate and virulence. The decrease in available Mn led to the accumulation of fructose-1,6-bisphosphate, which likely resulted in induction of carbon catabolite repression. This has widespread consequences, such as the blockage of nucleobase conversion into nucleosides and accumulation of reduced glutathione. In addition, we provide insights into the metabolic composition of BHI and the components

streptococci may utilize from this undefined medium (Tables S4.4 and S4.7). The connection between the transcriptomic and metabolomic analyses will be discussed further in Chapter 7.

Materials and Methods

Bacterial strains and fermentor growth

The Kan resistant Δ*ssaACB* mutant (JFP169) was used in this study and described in Chapter 3 (83, 120). Fermentor growth conditions were described in Chapters 2 & 3 (163). Cell samples (n = 6) and spent media (n = 3) were taken from the same runs as in Chapter 3 (202). Fresh media (n = 3) was removed from the vessel prior to inoculation. Cells were harvested from 40-mL culture samples and media samples were 500 µL. All samples were stored at -80°C then shipped on dry ice to Metabolon, Inc. (Durham, North Carolina).

Sample preparation

Metabolomics sample processing was completed by Metabolon, Inc. as described in the in previous publications (297, 298).

Samples stored at -80˚C, upon shipment were accessioned into the Metabolon LIMS system were prepared using the automated MicroLab STAR® system from Hamilton Company. Several recovery standards were added prior to the first step in the extraction process for QC purposes. Samples were extracted with methanol under vigorous shaking for 2 min (Glen Mills GenoGrinder 2000) to precipitate protein and dissociate small molecules bound to protein or trapped in the precipitated protein matrix, followed by centrifugation to recover chemically diverse metabolites. The resulting extract was divided into five fractions: two for analysis by two separate reverse phase (RP)/UPLC-MS/MS

methods using positive ion mode electrospray ionization (ESI), one for analysis by RP/UPLC-MS/MS using negative ion mode ESI, one for analysis by HILIC/UPLC-MS/MS using negative ion mode ESI, and one reserved for backup. Samples were placed briefly on a TurboVap® (Zymark) to remove the organic solvent. The sample extracts were stored overnight under nitrogen before preparation for analysis.

Metabolomics data generation using ultrahigh performance liquid chromatography-tandem mass spectroscopy (UPLC-MS/MS)

All methods utilized a Waters ACQUITY ultra-performance liquid chromatography (UPLC) and a Thermo Scientific Q-Exactive high resolution/accurate mass spectrometer interfaced with a heated electrospray ionization (HESI-II) source and Orbitrap mass analyzer operated at 35,000 mass resolution. The sample extract was dried then reconstituted in solvents compatible to each of the four methods. Each reconstitution solvent contained a series of standards at fixed concentrations to ensure injection and chromatographic consistency. One aliquot was analyzed using acidic positive ion conditions, chromatographically optimized for more hydrophilic compounds. In this method, the extract is gradient-eluted from a C18 column (Waters UPLC BEH C18-2.1x100 mm, 1.7 µm) using water and methanol, containing 0.05% perfluoropentanoic acid (PFPA) and 0.1% formic acid (FA). A second aliquot was also analyzed using acidic positive ion conditions, but chromatographically optimized for more hydrophobic compounds. In this method, the extract is gradient eluted from the aforementioned C18 column using methanol, acetonitrile, water, 0.05% PFPA and 0.01% FA, and is operated at an overall higher organic content. A third aliquot was analyzed using basic negative ion optimized conditions using a separate dedicated C18 column. The basic extracts were gradient-eluted from the column using methanol and water, however with 6.5mM

Ammonium Bicarbonate at pH 8. The fourth aliquot was analyzed via negative ionization following elution from a HILIC column (Waters UPLC BEH Amide 2.1x1$_{50}$ mm, 1.7 µm) using a gradient consisting of water and acetonitrile with 10 mM Ammonium Formate, pH 10.8. The MS analysis alternated between MS and data-dependent MS^n scans using dynamic exclusion. The scan range varies slightly between methods, but covers approximately 70-1000 m/z. Raw data files were archived and extracted as described below.

Data extraction and compound identification

Raw data were extracted, peak-identified, and QC processed using Metabolon's hardware and software. These systems are built on a web-service platform utilizing Microsoft's .NET technologies, which run on high-performance application servers and fiber-channel storage arrays in clusters to provide active failover and load-balancing. Compounds were identified by comparison to library entries of purified standards or recurrent unknown entities. Metabolon maintains a library based on authenticated standards that contains the retention time/index (RI), mass to charge ratio (*m/z)*, and chromatographic data (including MS/MS spectral data) on all molecules present in the library. Furthermore, biochemical identifications are based on three criteria: retention index within a narrow RI window of the proposed identification, accurate mass match to the library +/- 10 ppm, and the MS/MS forward and reverse scores. MS/MS scores are based on a comparison of the ions present in the experimental spectrum to ions present in the library entry spectrum. While there may be similarities between these molecules based on one of these factors, the use of all three data points can be utilized to distinguish and differentiate biochemicals. More than 4500 commercially available purified standard

compounds have been acquired and registered into LIMS for analysis on all platforms for determination of their analytical characteristics. Additional mass spectral entries have been created for structurally unnamed biochemicals, which have been identified by virtue of their recurrent nature (both chromatographic and mass spectral). Putative identification of each metabolite was made based on mass accuracy (m/z) Chemical Abstracts Service (CAS), Kyoto Encyclopedia of Genes and Genomes (KEGG), Human Metabolome Database (HMDB), and LIPID MAPS identifiers.

Curation

A variety of curation procedures were performed to ensure that a high quality data set was made available for statistical analysis and data interpretation. The QC and curation processes were designed to ensure accurate and consistent identification of true chemical entities, and to remove those representing system artifacts, mis-assignments, redundancy, and background noise. Metabolon data analysts used internally-developed visualization and interpretation software to confirm the consistency of peak identification among the various samples. Library matches for each compound were checked for each sample and corrected if necessary.

Statistical analysis of metabolomics and transcriptomics datasets

Statistical analysis of the metabolomics data sets was performed using statistical software R (Version 3.5.2) (299). Normalized, transformed, imputed, outlier-removed, and scaled-peak areas representative of relative metabolite amounts obtained using DeviumWeb (300) are presented. Hierarchical clustering analysis (HCA) was performed on Pearson distances using MetaboAnalyst 4.0 (www.metaboanalyst.ca) (301), with the data normalized using z-scores of the relative abundance of the metabolites for heat map

display. Correlations reported are Spearman rank correlations. Principal component analysis (PCA) and partial least squared discriminant analyses (PLS-DA) were performed using MetaboAnalyst, with the output displayed as score plots for visualization of sample groups. One-way analysis of variance (ANOVA) followed by post-hoc analysis using Fisher's least significant difference (LSD) test was used for analysis of statistical significance using MetaboAnalyst.

Time-course analysis of cellular and media metabolomes

For our 70 min time course, we used the Short Time series Expression Miner (STEM) tool. The following parameters were used for our analysis: no normalization of data; 0 added as the starting point; number of model profiles = 20; maximum unit change in model profiles between time points = 3. To explain the model profiles, we used an expression of -1 if levels of a metabolite decreased, 0 if levels were unchanged, and 1 if levels increased. For instance, a model profile with an expression of -1, -1, 0, represents decreased, decreased, and unchanged, levels of a given set of metabolites for the 3 time points.

Chapter 5 Effect of Acid on the Transcriptome and Mn levels of *S. sanguinis*

Rationale

The native environment of *S. sanguinis* is the oral cavity and one of its natural competitors, *S. mutans*, produces high levels of lactic acid in order to outcompete its neighbors within the oral biofilm. Preliminary data suggested that a Mn transporter mutant had a growth defect at reduced pH. We wanted to understand why this mutant was more drastically affected by low pH than the WT strain.

Introduction

As the oral cavity is a complex environment with dynamic microbial communities, fluctuating metabolite availability, and diverse conditions (1, 3, 6, 7, 25, 302, 303), microorganisms have had to adapt by utilizing the available nutrients and competing against each other. One way that oral streptococci have adapted to this ever-changing habitat is through the production of lactic acid in the absence of oxygen (304, 305). Lactic acid production allows them to survive in both anaerobic and aerobic environments, making them the most abundant genera in the oral cavity (1, 11). Some species such as *S. mutans* and *S. sobrinus* even utilize acid production to carve out their own niche by lowering the pH of their local environment. This results in demineralization of the tooth enamel and eventually to the formation of dental caries (30, 306, 307). While *S. sanguinis* is acidogenic (acid-producing), it is not as aciduric (acid tolerant) as *S. mutans* (308-311).

Bacteria have evolved multiple mechanisms for acid stress tolerance (305, 312-315). In *S. sanguinis* (75), the cells have adapted to acid stress by encoding F-ATPases (316), an arginine deiminase system (317-319), various chaperones and proteases (320-322), and superoxide dismutase (130, 323, 324). Acid tolerance response (ATR) is another mechanism in which some bacteria can survive exposure to lethal pH levels after being briefly exposed to sub-lethal acid levels (315). *S. sanguinis* appear to exhibit some ATR, although not to the same extent as the related species *S. gordonii* (161). Each of these systems have evolved to combat the acidic environment it creates through its own acid production, as well as the acid produced by neighboring bacteria.

Mn has recently been implicated in acid stress tolerance in *S. agalactiae* (147) and *S. mutans* (148). In both of these species, loss of the NRAMP Mn transporter MntH led to a

reduction in growth in low-pH conditions. In *S. mutans*, the loss of the lipoprotein component of the ABC Mn transporter, SloC, did not impact the growth in low pH media (148). Similarly, it was previously determined that the *fimCBA* operon was not important for acid tolerance of *Streptococcus parasanguinis* (325) although they tested acid killing instead of growth and the tested strain contains an NRAMP protein. Here we report the first characterization of the poor growth of a streptococcal ABC Mn transporter mutant in low-pH media.

Results

Effect of acid on the growth of *S. sanguinis*

We first assessed the growth of the Δ*ssaACB* mutant by comparing growth in low pH BHI to the WT strain (Figure 5.1). To rule out oxidative stress as a confounding factor, cells were grown in low O_2 conditions (1% O_2). Under normal pH (~7.3), the strains were not significantly different from each other. When the pH was lowered to 6.4 and 6.3, growth of the WT strain was not significantly different from pH 7.3 whereas growth of the Δ*ssaACB* mutant was progressively worse. The growth of both strains at pH 6.2 was significantly lower than at pH 7.3, although the difference between WT growth in these two conditions was not as drastically different as that of the Δ*ssaACB* mutant. We note also that the Δ*ssaACB* mutant also grew significantly less well than WT in the overnight pre-cultures that were used to inoculate these tubes, so that part of the decrease in final density of the Δ*ssaACB* mutant cultures may have been due to a lesser inoculum. Nevertheless, this was not a major contributor, as there was no significant difference between the WT and Δ*ssaACB* strains after 24 h at pH 7.3.

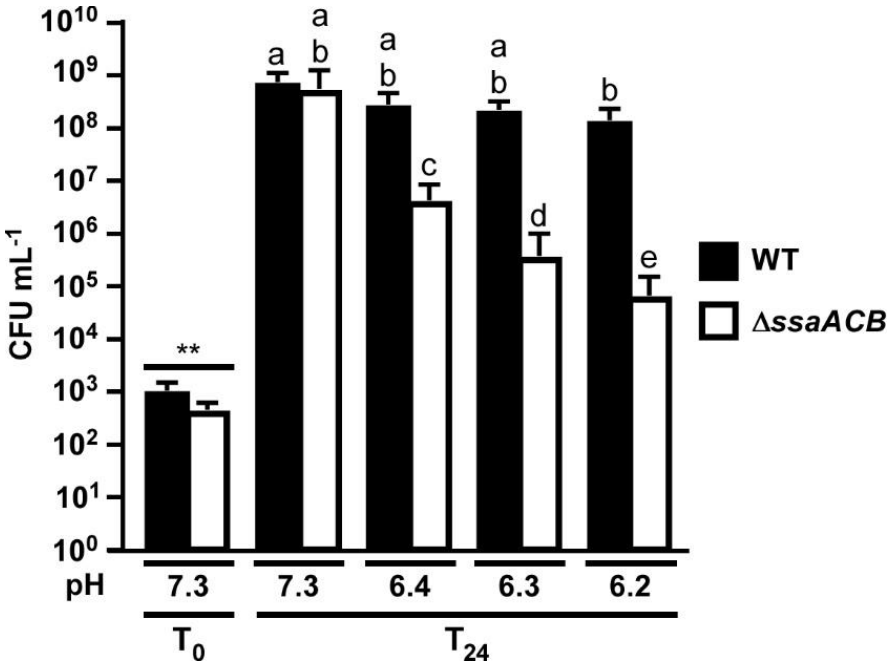

Figure 5.1 Growth of the *S. sanguinis* SK36 WT and an Δ*ssaACB* mutant in low pH
BHI at different pH levels was preincubated at 1% O_2 and inoculated from an overnight culture. Cultures were incubated for 24 h before plating. Means ± SD of at least three replicates are displayed. Significance was determined by one-way ANOVA of T_{24} cultures; bars with the same letter are not significantly different from each other ($P \leq 0.05$). T_0 values were compared by two-tailed t-test; $^{**}P \leq 0.01$.

We then assessed whether the reduced capacity of the Δ*ssaACB* mutant to transport Mn (120) may be the cause for the poor growth phenotype (Figure 5.2). BHI contains ~0.36 µM Mn (120). We added exogenous Mn to pH 6.2 cultures and the addition of 1 µM Mn^{2+} was sufficient to rescue the growth of the Δ*ssaACB* mutant, suggesting that the reduced Mn levels in this mutant (120) may be contributing to the reduction in acid stress tolerance. Interestingly, only addition of 10 µM Mn^{2+} led to an increase in WT growth that was not significantly different from pH 7.3, indicating that there are other factors besides Mn that may be impacting the growth in low pH.

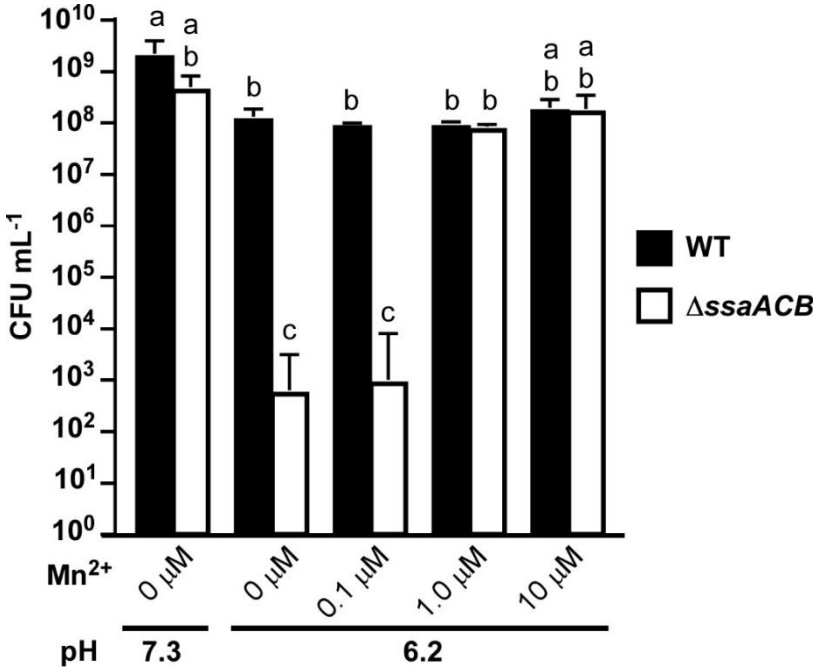

Figure 5.2 Growth of *S. sanguinis* in low pH BHI with added Mn
BHI pH 7.3 or 6.2 was pre-incubated at 1% O_2 and inoculated from an overnight culture. Exogenous Mn^{2+} was added at listed concentrations. Cultures were incubated for 24 h before plating. Means ± SD of at least three replicates are displayed. Significance was determined by one-way ANOVA of T_{24} cultures; bars with the same letter are not significantly different from each other ($P \leq 0.05$).

Effect of acid on growth in a fermentor

We then assessed the effect of low pH on both WT and Δ*ssaACB* mutant cells by examining the transcriptome before and after acid addition. To ensure large-scale, reproducible growth along a time course, we employed the use of a fermentor (Figure 5.3). To minimize the impact of oxidative stress, we used the minimum possible airflow (0.03 lpm) throughout the experiment. We were unable to turn off the air entirely because cultures without airflow grew poorly (data not shown). We took the pre-acid sample (pH 7.4) for RNA-seq 1 h after the pumps were set (T_{-20} min) and then added HCl into the vessel 20 min later at T_0.The pH was maintained at 6.2 by an indwelling pH probe and addition of 2 N HCl and 2 N KOH. A pH of 6.2 was chosen because it was the pH that lead to the decrease in growth rate of the Δ*ssaACB* mutant (Figure 5.3A) but not the WT

strain (Figure 5.3B). Post-acid samples were removed at T_{10}, T_{25}, and T_{50} min and processed as described in Chapter 2.

We next wanted to determine if Mn levels were affected by low pH. We assess the metal content of cells at each sample time point using ICP-OES (Figure 5.4). Mn levels significantly decreased in both strains, suggesting that low pH conditions are not conducive for Mn transport. Interestingly, Fe levels increased in both strains after acid addition, although not significantly (Figure 5.4). Mg increased significantly at T_{10} and T_{50} only in the Δ*ssaACB* mutant strain (Figure 5.4A). Zn levels were not significantly affected in either strain (Figure 5.4).

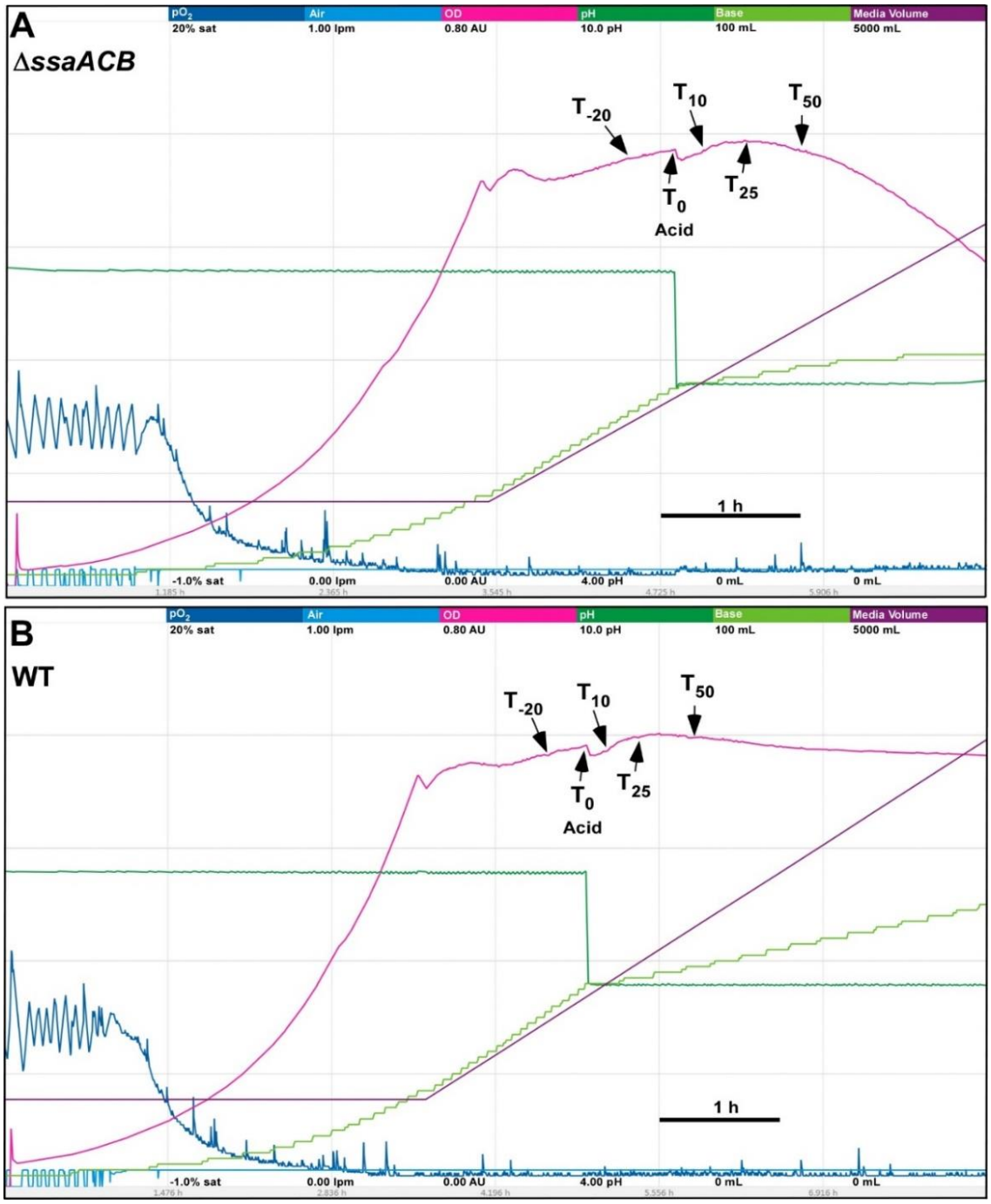

Figure 5.3 Fermentor growth of Δ*ssaACB* and WT cells after pH reduction
Representative charts for fermentor growth of *S. sanguinis* (**A**) Δ*ssaACB* and (**B**) WT cells. Each color represents a different parameter: cyan - air flow (liters per min; lpm), pink - optical density (840-910 nm; absorbance units; AU), dark green - pH, light green - base input (KOH), purple - media input (total volume). The scale for each parameter is indicated by the values under each respective parameter label (minimum at the bottom, maximum at the top). The time scale is indicated by the bar in the bottom right portion of each chart. Cells were grown under low oxygen conditions with acid added 80 min (T_0) after the media input and output pumps were turned on. Each sample time point is labeled.

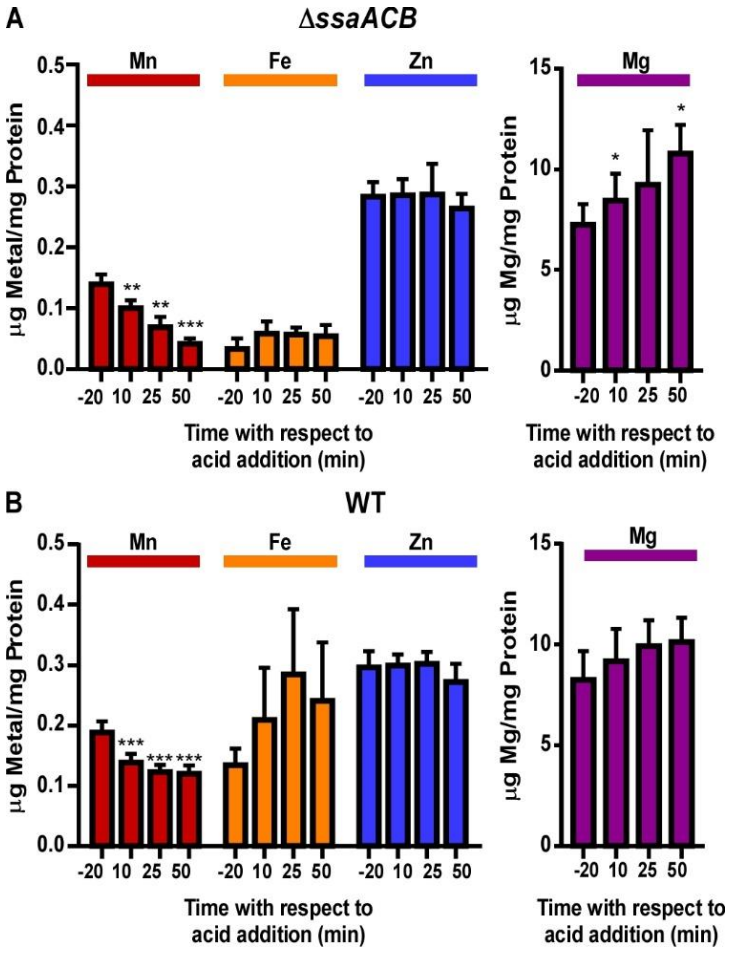

Figure 5.4 Metal analysis of fermentor-grown cells after pH reduction
Fermentor-grown Δ*ssaACB* (A) and WT (B) cells were collected at each time point and analyzed for cellular metal content using ICP-OES. Metal concentrations were normalized to protein concentrations. Means and standard deviations of at least three replicates are shown. Significance was determined either by repeated measures ANOVA or by one-way ANOVA if matching was not effective, with a Tukey-Kramer multiple comparisons test to T_{-20}. **P* ≤ 0.05, ** *P* ≤ 0.01, *** *P* ≤ 0.001.

RNA-seq analysis of fermentor-grown cells after pH reduction

We then examined the results of the RNA-seq using two types of comparisons: time course within a strain pre- and post-acid and comparison between each strain (Table S5.1). The number of DEGs (defined as $P \leq 0.05$, $|\log_2$ fold change$| \geq 1$) are listed in Table 5.1.

Table 5.1 Differentially expressed genes in fermentor-grown cells after pH reduction

	T_{-20}	T_{10}	T_{25}	T_{50}
WT		**83 | 56**	**122 | 69**	**140 | 65**
Δ*ssaACB*		**140 | 68**	**178 | 191**	**285 | 143**
Strain Comparison	**9 | 0**	**0 | 0**	**0 | 0**	**48 | 12**

Tallies of DEGs, which are defined as $P \leq 0.05$ and $|\log_2$ fold change$| \geq 1$. Values in blue indicate genes downregulated at that time point relative to T_{-20}, red indicates upregulated. Green values indicate genes that were more highly expressed in WT and purple indicates genes that were more highly expressed in the Δ*ssaACB* mutant.

Using principal component analysis (PCA), we were able to explain 44.37% and 76.19% of the variance by the first two PCs for WT and Δ*ssaACB*, respectively (Figure 5.5A-B). The pH 6.2 samples for the WT strain overlap with each other, whereas those for Δ*ssaACB* do not. The pH 7.4 samples separate from the pH 6.2 samples in both strains (Figure 5.5A-B). When comparing all samples, each time point overlapped between strains, although WT T_{50} overlapped more with the Δ*ssaACB* T_{25} samples than those of T_{50} (Figure 5.5C). These results correspond with what is seen in the volcano plots in Figure 5.6A-B and heatmaps in Figure 5.7A-B. Many of the changes occurred at the T_{50} time point as compared to T_{-20} for both strains, although there were fewer changes in WT than Δ*ssaACB*. When comparing the strains to each other, the T_{10} and T_{25} time points were almost identical, whereas T_{-20} and T_{50} time points had more variation (Figure 5.6C & Figure 5.7C).

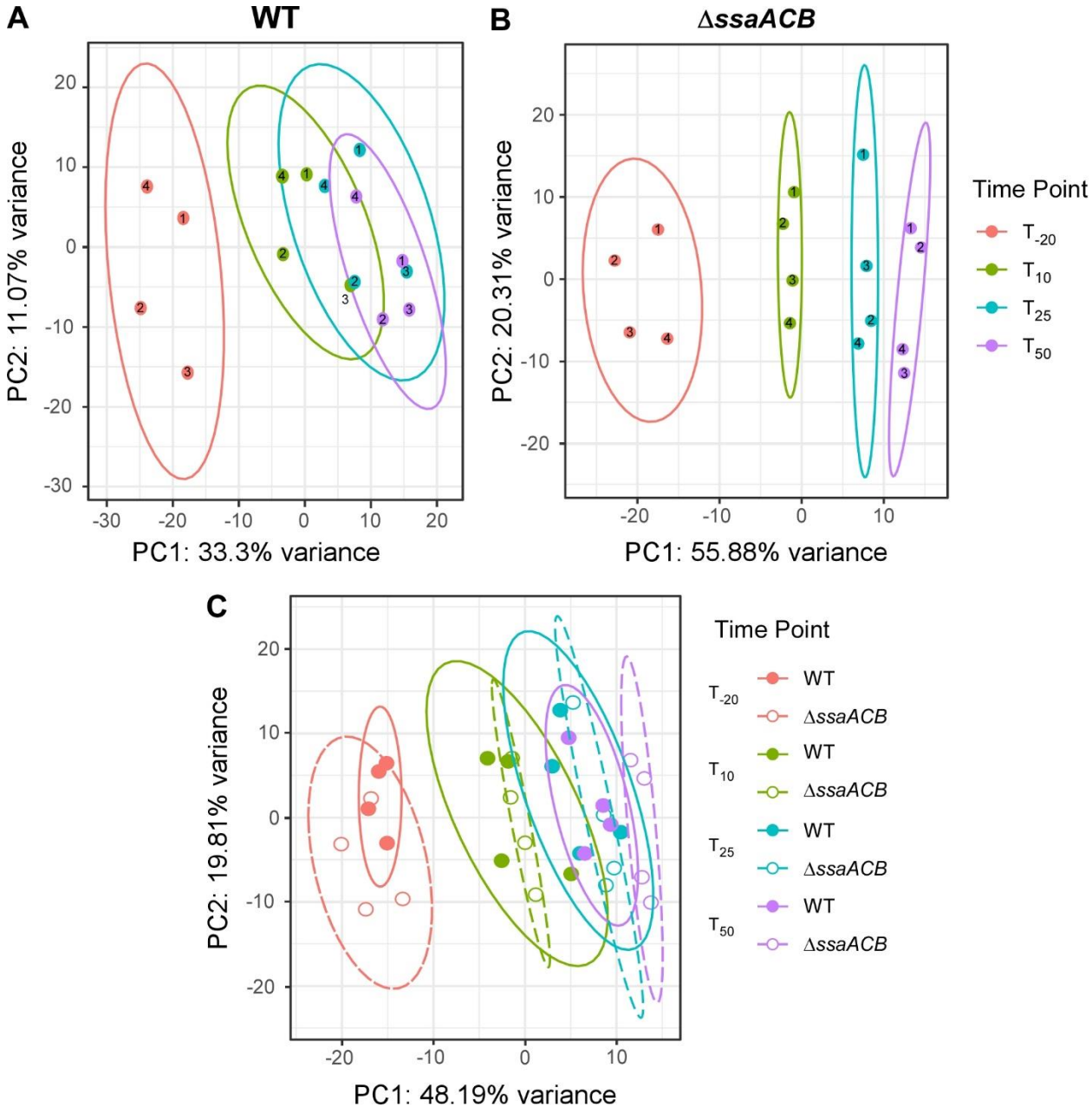

Figure 5.5 Multivariate analysis of RNA-seq results
PCA of WT (A) and Δ*ssaACB* (B) RNA-seq results generated using pcaExplorer in R. PCA of both strains together (C), where filled circles and lines depict WT and empty circles and dashed lines are Δ*ssaACB*. Ellipses represent 95% confidence intervals.

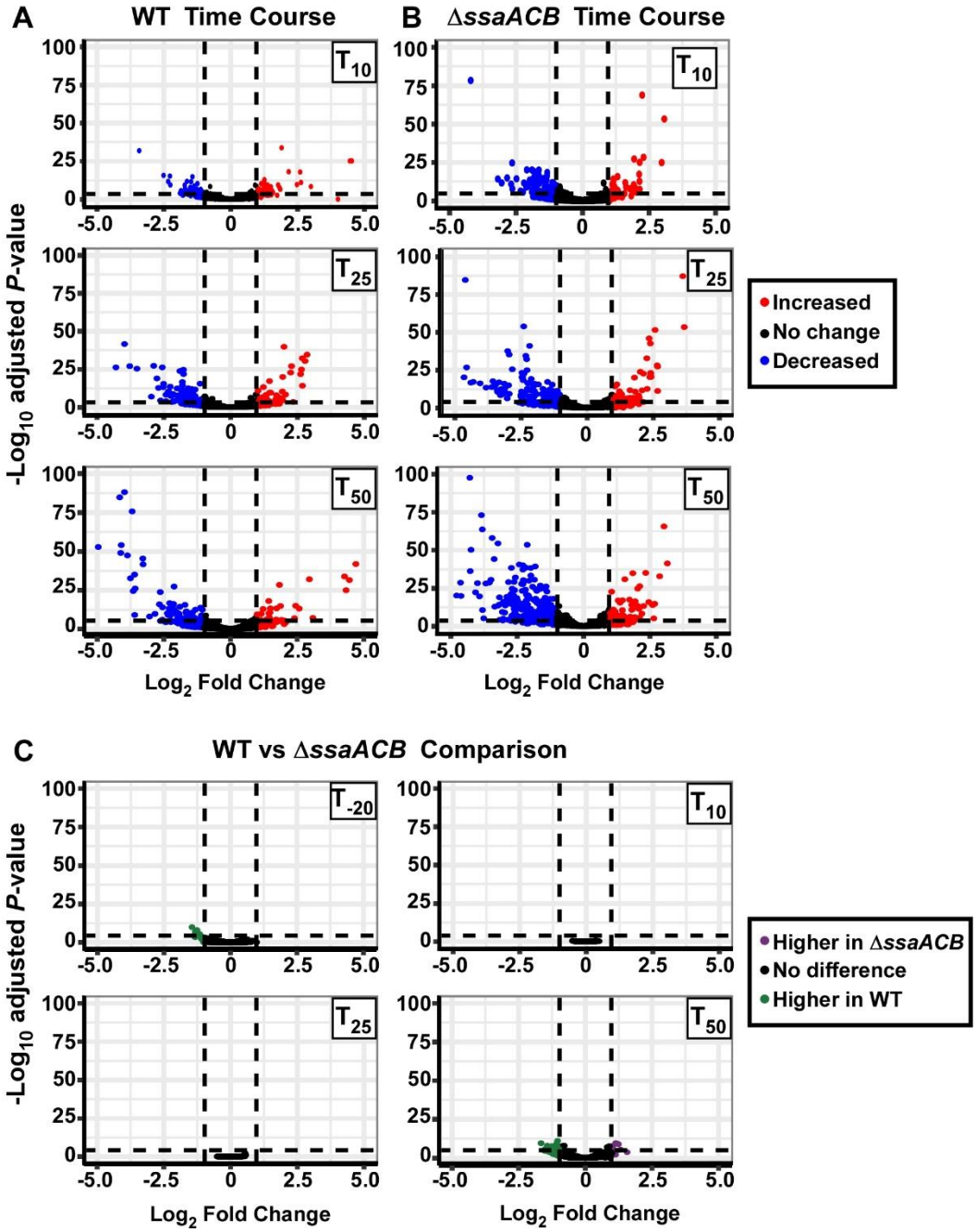

Figure 5.6 Volcano plots of RNA-seq analysis

Volcano plots comparing each post-acid time point to T_{-20} in WT (A) and Δ*ssaACB* (B) were generated using log_2 fold changes generated in Geneious in the EnhancedVolcano package for R. Genes that are upregulated in the post-acid time point are positive on the x-axis (red) and those that are downregulated are negative (blue). (C) Volcano plots were generated using log_2 fold changes comparing the Δ*ssaACB* mutant to WT. Genes that were more highly expressed in Δ*ssaACB* are positive on the x-axis (purple) and those that were more highly expressed in WT are negative (green).

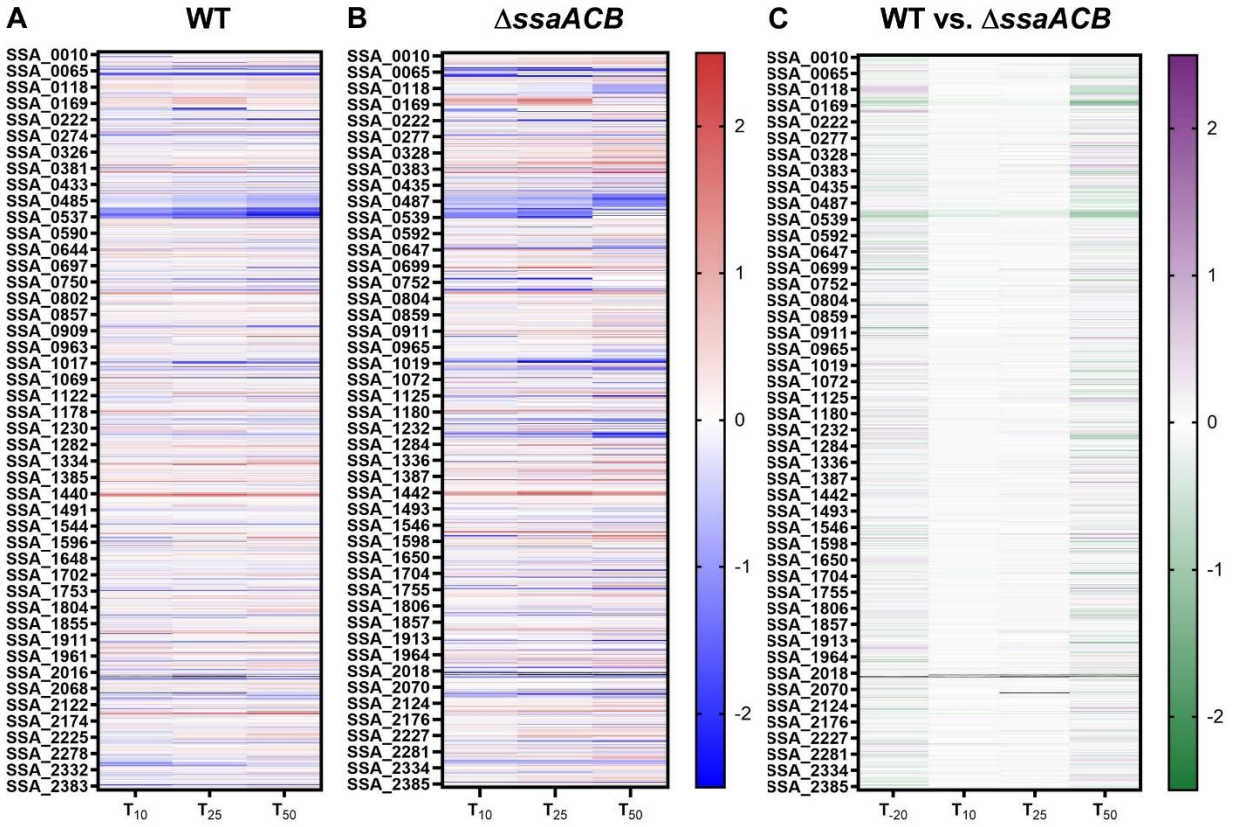

Figure 5.7 Heatmaps of RNA-seq analysis
Heatmap displaying the log_2 fold change values of each gene at the time indicated as compared to T_{-20} for WT (A) and Δ*ssaACB* (B) strains. Positive log_2 fold change values (red) are upregulated in later samples as compared to T_{-20}, while negative values (blue) are downregulated. (C) Heatmap comparing log_2 fold change values between the two strains at each time point where purple means the gene was expressed more in Δ*ssaACB* and green indicates it was expressed more in WT.

In examining the KEGG pathways assigned to the DEGs at T_{50}, the only pathway that overlapped in all three comparisons was phosphotransferase systems (PTS). In fact, it was the top pathway for Δ*ssaACB* and the comparison between the two strains, indicating that this pathway is especially tied to Mn levels. This is supported by our previous analysis using RNA-seq to analyze EDTA-treated cells (Chapter 3 and Puccio et al. (202)). Also similar to our previous study, all three comparisons were significantly enriched for various carbon metabolism, amino acid metabolism, and secondary metabolite pathways.

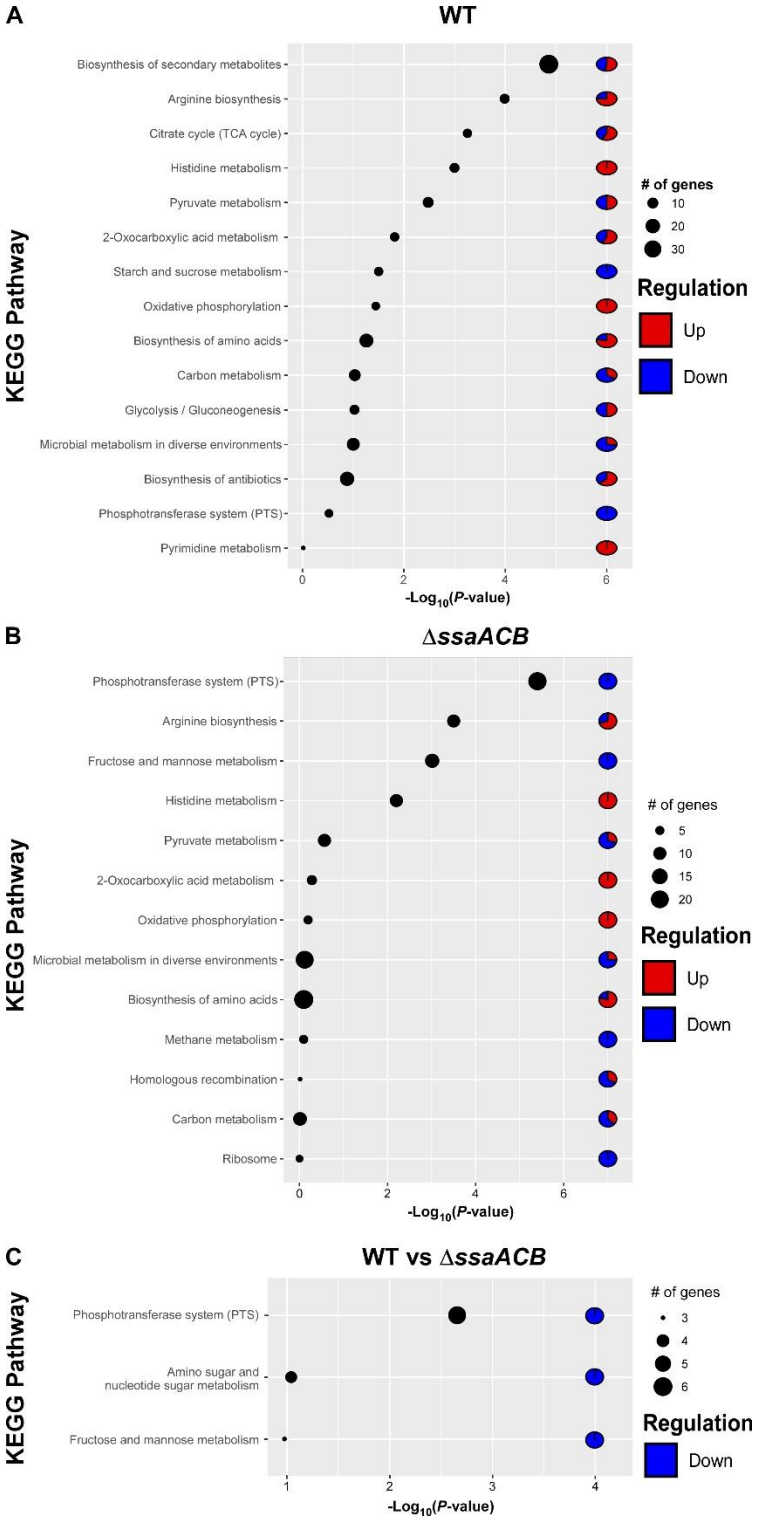

Figure 5.8 KEGG pathway analysis of DEGs

Pathway enrichment analysis of differentially expressed genes at T_{50} using DAVID classification of genes and KEGG annotations of WT (A) and Δ*ssaACB* (B) as compared to T_{-20}. Analysis of WT vs Δ*ssaACB* T_{50} samples is depicted in (C).

Effect of low pH on expression of stress response genes

In order to assess the cellular state, we evaluated the expression of stress response genes. In the Δ*ssaACB* mutant, genes encoding heat shock proteins (*groES, groEL, hrcA*), chaperone proteins (*dnaJ, dnaK*), recombinase (*recA*), and an alkaline shock protein (SSA_1979) all decreased significantly (Figure 5.9). The genes encoding the other alkaline stress protein (SSA_2148), exinulcease subunit A (*uvrA*), and all subunits of the F-Type ATP synthase (316) significantly increased; all others were unchanged (Figure 5.9). Interestingly, expression of *dpr* significantly increased at T_{10} and T_{25} but slightly decreased at T_{50} (Figure 5.9). Dpr is a Dps-like protein (described in Chapter 3) and has been shown to be important for acid stress tolerance at pH 3 in *S. pyogenes* (118). Additionally, expression of *sodA* and *clp* were unchanged (Figure 5.9). Although not unprecedented (326), there is a strong connection between SodA and acid stress response in other bacteria (322-324, 327-329). Additionally, *nox*, the gene encoding NADP peroxidase, was significantly downregulated. In *S. sanguinis*, the *nox* gene was previously demonstrated to be important for acid stress tolerance (330) so this decrease in expression is surprising.

These stress response genes had similar expression patterns in WT (Figure 5.10), although changes were often at a lower magnitude.

Locus Tag	Annotation	TPM	Log_2 Ratio		
		T_{-20}	T_{10}/T_{-20}	T_{25}/T_{-20}	T_{50}/T_{-20}
SSA_0009	Ribosome-associated heat shock protein (S4)	418	0.22	0.20	-0.08
SSA_0156	ATPase with chaperone activity, ATP-binding subunit	26	**1.07**	**1.81**	0.09
SSA_0225	*groES* , Heat shock protein	1086	-0.45	**-0.80**	**-0.44**
SSA_0226	*groEL* , Heat shock protein	1206	**-0.45**	**-0.83**	**-0.42**
SSA_0448	*uvrA,* Excinuclease ABC subunit A	204	0.48	0.43	**0.59**
SSA_0644	*dpr* , DNA Protection System	1008	**2.02**	**1.70**	-0.25
SSA_0669	*clpE* , ATP dependent protease	232	0.17	0.09	0.15
SSA_0721	*sodA* , Mn-cofactored superoxide dismutase	1031	-0.19	-0.27	-0.50
SSA_0782	*uncE,* ATP synthase F0 sector subunit c	866	**1.07**	**1.11**	**0.96**
SSA_0783	*uncB* , ATP synthase F0 sector subunit a	833	**1.13**	**1.04**	**0.97**
SSA_0784	*uncF,* ATP synthase F0 sector subunit b	1176	**1.17**	**1.12**	**1.06**
SSA_0785	*uncH,* ATP synthase delta chain	1009	**1.09**	**1.01**	**0.92**
SSA_0786	*uncA,* ATP synthase alpha chain	1067	**1.10**	**1.09**	**1.07**
SSA_0787	*uncG,* ATP synthase gamma chain	1225	**1.08**	**1.07**	**1.03**
SSA_0788	*uncD* ,ATP synthase beta chain	1195	**1.16**	**1.10**	**1.12**
SSA_0789	*atpC* , ATP synthase epsilon chain	1552	**1.20**	**1.22**	**1.19**
SSA_1093	*clpX* , ATP-dependent Clp protease ATP-binding subunit	635	0.18	-0.04	0.01
SSA_1136	*clpA* , ATPases with chaperone activity, ATP-binding subunit	32	0.44	0.74	0.49
SSA_1731	*clpP* , ATP-dependent Clp protease, proteolytic subunit	1064	0.09	-0.32	-0.51
SSA_1745	*csbD* , General stress response protein	1797	0.05	0.31	-0.25
SSA_1979	Alkaline-shock protein	1860	**-0.79**	**-1.30**	**-1.06**
SSA_2005	*dnaJ* , Chaperone protein	756	**-0.94**	**-1.40**	**-0.89**
SSA_2007	*dnaK* , Chaperone protein	2523	**-1.25**	**-1.61**	**-1.10**
SSA_2008	*grpE* , Molecular chaperone	1636	**-1.56**	**-1.67**	**-1.43**
SSA_2009	*hrcA* , Heat shock transcription repressor	1306	**-1.33**	**-1.50**	**-1.35**
SSA_2148	Alkaline shock stress response protein	43	**0.84**	**1.07**	**1.46**
SSA_2190	*hslO* , 33 kDa chaperonin	207	-0.11	-0.16	0.13
SSA_2199	*clpC* , ATP-dependent Clp protease, ATP-binding subunit	274	0.15	0.09	0.17
SSA_2245	*recA,* Recombinase	1780	-0.72	**-1.14**	**-1.21**

Figure 5.9 Expression of stress response genes in the Δ*ssaACB* mutant
Stress response genes are depicted with their average transcripts per million reads (TPM) at T_{-20} and log_2 fold change values for each post-acid time point. TPM values greater than 1000 are full saturation (green). Positive log_2 fold change values (red) indicate genes upregulated in after acid addition samples as compared to T_{-20}, while negative values (blue) indicate downregulated genes. Values in bold indicate significant changes in expression by adjusted *P*-value (≤ 0.05).

Locus Tag	Annotation	TPM	Log_2 Ratio		
		T_{-20}	T_{10}/T_{-20}	T_{25}/T_{-20}	T_{50}/T_{-20}
SSA_0009	Ribosome-associated heat shock protein (S4)	564	-0.12	-0.02	-0.09
SSA_0156	ATPase with chaperone activity, ATP-binding subunit	64	0.56	0.79	0.15
SSA_0225	*groES* , Heat shock protein	897	-0.38	-0.38	0.06
SSA_0226	*groEL* , Heat shock protein	946	-0.09	-0.41	0.05
SSA_0448	*uvrA,* Excinuclease ABC subunit A	229	0.35	0.33	0.44
SSA_0644	*dpr* , DNA Protection System	3945	**1.08**	0.66	-0.48
SSA_0669	*clpE* , ATP dependent protease	224	0.45	0.09	0.11
SSA_0721	*sodA* , Mn-cofactored superoxide dismutase	1163	-0.09	0.10	0.05
SSA_0782	*uncE,* ATP synthase F0 sector subunit c	797	**1.07**	**0.91**	**1.02**
SSA_0783	*uncB* , ATP synthase F0 sector subunit a	811	**1.07**	**0.90**	**0.95**
SSA_0784	*uncF,* ATP synthase F0 sector subunit b	1146	**1.14**	**1.03**	**1.00**
SSA_0785	*uncH,* ATP synthase delta chain	1024	**0.96**	**0.85**	**0.82**
SSA_0786	*uncA,* ATP synthase alpha chain	917	**1.21**	**1.06**	**1.12**
SSA_0787	*uncG,* ATP synthase gamma chain	1043	**1.21**	**1.14**	**1.12**
SSA_0788	*uncD* ,ATP synthase beta chain	1049	**1.23**	**1.14**	**1.15**
SSA_0789	*atpC* , ATP synthase epsilon chain	1339	**1.29**	**1.22**	**1.22**
SSA_1093	*clpX* , ATP-dependent Clp protease ATP-binding subunit	597	0.32	0.20	0.06
SSA_1136	*clpA* , ATPases with chaperone activity, ATP-binding subunit	52	-0.23	-0.17	-0.48
SSA_1731	*clpP* , ATP-dependent Clp protease, proteolytic subunit	946	0.32	0.03	0.04
SSA_1745	*csbD* , General stress response protein	3218	-0.49	0.06	-0.49
SSA_1979	Alkaline-shock protein	1643	**-0.75**	**-1.05**	**-0.77**
SSA_2005	*dnaJ* , Chaperone protein	531	-0.55	**-0.86**	-0.31
SSA_2007	*dnaK* , Chaperone protein	1801	-0.72	**-1.04**	-0.43
SSA_2008	*grpE* , Molecular chaperone	1132	**-0.82**	**-0.98**	-0.45
SSA_2009	*hrcA* , Heat shock transcription repressor	1258	**-1.05**	**-1.13**	**-0.68**
SSA_2148	Alkaline shock stress response protein	48	**1.34**	**1.43**	**1.84**
SSA_2190	*hslO* , 33 kDa chaperonin	206	-0.17	-0.23	0.16
SSA_2199	*clpC* , ATP-dependent Clp protease, ATP-binding subunit	259	0.39	0.11	0.25
SSA_2245	*recA,* Recombinase	1104	-0.17	**-0.69**	**-0.65**

Figure 5.10 Expression of stress response genes in the WT strain
Stress response genes are depicted with their average transcripts per million reads (TPM) at T_{-20} and log_2 fold change values for each post-acid time point. TPM values greater than 1000 are full saturation (green). Positive log_2 fold change values (red) indicate genes upregulated in after acid addition samples as compared to T_{-20}, while negative values (blue) indicate downregulated genes. Values in bold indicate significant changes in expression by adjusted *P*-value (≤ 0.05).

Expression of metal transport genes in response to low pH

Due to the change in levels of some metals but not others (Figure 5.4), expression of genes encoding known and putative metal transporters was assessed. Expression of the *aphA-3* gene replacing *ssaACB* in the mutant strain was significantly increased post-acid (Figure 5.11). Similarly, in WT the *ssaACB* genes were highly expressed at T_{-20} and significantly increased across all three low-pH time points (Figure 5.12). Thus, the

observed decrease in Mn levels are likely due to either reduction in the bioavailability of Mn or to reduced function of a secondary Mn transporter. Interestingly, *mntE* expression was increased in the Δ*ssaACB* mutant but not the WT. This is similar to what we observed in the EDTA study (202) although we were unable to explain this odd result (Chapter 3).

Corresponding with the increase in Fe levels in both strains after the pH reduction, expression of many putative Fe and heme transporters increased at T_{50}. There were no differentially expressed Zn transport genes in the WT. In the Δ*ssaACB* mutant, expression of *adcC* and *adcB* went up at T_{50}, as well as the Zn exporter *czcD* (Figure 5.11). Expression of one of the genes encoding a histidine triad protein, *phtD*, was significantly decreased. The only putative Zn transporter to be affected in WT was *phtA* (Figure 5.12). Thus, metal regulation appears to be affected by both low pH conditions and Mn levels, since WT experiences low pH but not low Mn. However, this does not significantly impact Zn levels (Figure 5.4).

Mg significantly increased in the Δ*ssaACB* mutant but not WT (Figure 5.4). This corresponds with a significant increase in expression of a CorA-family protein (SSA_0447) in Δ*ssaACB* but no change in expression of any putative Mg transporter in WT (Figure 5.11-12).

Δ*ssaACB* Acid	Locus Tag	Annotation	TPM	Log_2 Ratio		
			T_{-20}	T_{10}/T_{-20}	T_{25}/T_{-20}	T_{50}/T_{-20}
Metal Transport Regulators	SSA_0135	*adcR*, MarR family transcriptional repressor	91	**-1.08**	-0.53	0.53
	SSA_0256	*ssaR* , DxtR family transcriptional repressor	88	0.18	0.04	0.28
	SSA_0686	*perR* , Fur family transcriptional repressor	102	0.65	0.64	0.69
Mn Transport	SSA_0260	*aphA-3* (kanamycin resistance gene replacing *ssaACB)*	592	**1.10**	**1.37**	**1.76**
	SSA_0299	VIT family protein	75	**1.98**	**1.77**	-0.34
	SSA_0851	*mntE* , Mn efflux protein	76	0.32	0.57	**0.86**
	SSA_0866	*mgtA* , Mn/Ca exporter	406	-0.08	-0.07	-0.18
	SSA_1413	GufA-like, ZIP family protein	154	0.12	0.38	**0.36**
Fe Transport	SSA_0299	VIT family protein	75	**1.98**	**1.77**	-0.34
	SSA_0461	*pefC* , heme exporter	174	**1.31**	**1.05**	**0.65**
	SSA_1129	Periplasmic iron transport lipoprotein	357	**-0.95**	-0.35	**0.81**
	SSA_1130	Iron-dependent peroxidase	150	-0.63	-0.19	**0.96**
	SSA_1131	High-affinity Fe^{2+}/Pb^{2+} permease	155	-0.84	-0.22	**0.90**
	SSA_1413	GufA-like, ZIP family protein	154	0.12	0.38	**0.36**
	SSA_1578	ABC-type Fe^{3+}-siderophore transport system, permease component	15	**-1.67**	-0.62	**2.05**
	SSA_1579	ABC-type Fe^{3+}-siderophore transport system, ATPase component	25	**-1.65**	-0.94	**1.69**
	SSA_1581	Hemin ABC transporter	32	**-2.24**	-0.79	**1.63**
	SSA_1741	ABC-type Fe^{3+}-siderophore transport system, ATPase component	38	**-0.94**	-0.69	**0.84**
	SSA_1742	ferrichrome-binding protein	37	**-1.48**	-0.21	**1.25**
	SSA_1743	ABC-type Fe^{3+}-siderophore transport system, permease component	28	-0.72	0.03	**1.27**
	SSA_1744	iron ABC transporter permease	24	-0.72	0.04	**1.40**
Zn Transport	SSA_0136	*adcC,* Zn ABC transporter, ATPase	114	**-0.99**	-0.24	**0.65**
	SSA_0137	*adcB,* Zn ABC transporter, permease	92	**-0.93**	-0.15	**0.60**
	SSA_0138	*adcA,* Zn ABC transporter, lipoprotein	165	**-1.12**	**-0.59**	0.18
	SSA_1339	*phtD,* pneumococcal histidine triad protein D	12	**-1.80**	**-1.26**	**-0.73**
	SSA_1340	*adcAIII,* Zn ABC transporter, orphan lipoprotein	3	-0.51	0.08	-0.17
	SSA_1413	GufA-like, ZIP family protein	154	0.12	0.38	**0.36**
	SSA_1990	*adcAII,* Zn ABC transporter, orphan lipoprotein	20	-0.77	0.01	0.55
	SSA_1991	*phtA,* pneumococcal histidine triad protein A	18	-0.73	-0.17	0.34
	SSA_2321	*czcD,* Zn/Cd efflux protein	78	**1.97**	**1.98**	**1.47**
Mg Transport	SSA_0447	CorA-family protein, magnesium/cobalt transporter	164	0.28	0.08	0.08
	SSA_0701	CorA-family protein, magnesium/cobalt transporter	202	0.59	1.13	**1.13**
	SSA_0888	*mgtE* , Mg/Co/Ni transporter	128	0.35	0.54	0.58
	SSA_1734	Mg/Ni transporter, P-Type ATPase	115	0.24	-0.09	-0.06

Figure 5.11 Expression of metal transport genes in the Δ*ssaACB* mutant
Putative and confirmed metal transport genes are depicted with their average transcripts per million reads (TPM) at T_{-20} and log_2 fold change values for each post-acid time point. TPM values greater than 1000 are full saturation (green). Positive log_2 fold change values (red) indicate genes upregulated in after acid addition samples as compared to T_{-20}, while negative values (blue) indicate downregulated genes. Values in bold indicate significant changes in expression by adjusted *P*-value (≤ 0.05).

WT Acid	Locus Tag	Annotation	TPM	Log_2 Ratio		
			T_{-20}	T_{10}/T_{-20}	T_{25}/T_{-20}	T_{50}/T_{-20}
Metal Transport Regulators	SSA_0135	*adcR*, MarR family transcriptional repressor	110	**-0.97**	-0.73	-0.14
	SSA_0256	*ssaR* , DxtR family transcriptional repressor	110	-0.17	0.02	-0.04
	SSA_0686	*perR* , Fur family transcriptional repressor	128	0.58	0.46	0.47
Mn Transport	SSA_0260	*ssaB*, Mn ABC transporter, lipoprotein	1751	**1.26**	**1.45**	**1.44**
	SSA_0261	*ssaC*, Mn ABC transporter, permease	1458	**1.15**	**1.45**	**1.44**
	SSA_0262	*ssaA*, Mn ABC transporter, ATP binding protein	1648	**1.20**	**1.50**	**1.48**
	SSA_0299	VIT family protein	295	**0.94**	0.50	-0.91
	SSA_0851	*mntE* , Mn efflux protein	101	-0.01	-0.01	0.04
	SSA_0866	*mgtA* , Mn/Ca exporter	449	-0.24	-0.20	-0.04
	SSA_1413	GufA-like, ZIP family protein	147	0.11	0.16	0.17
Fe Transport	SSA_0299	VIT family protein	295	**0.94**	0.50	-0.91
	SSA_0461	*pefC* , heme exporter	209	**0.91**	**0.75**	**0.52**
	SSA_1129	Periplasmic iron transport lipoprotein	270	**-0.73**	0.00	**0.71**
	SSA_1130	Iron-dependent peroxidase	102	-0.33	0.25	**0.84**
	SSA_1131	High-affinity Fe^{2+}/Pb^{2+} permease	95	-0.29	0.15	**0.96**
	SSA_1413	GufA-like, ZIP family protein	147	0.11	0.16	0.17
	SSA_1578	ABC-type Fe^{3+}-siderophore transport system, permease component	9	-0.94	-0.13	1.07
	SSA_1579	ABC-type Fe^{3+}-siderophore transport system, ATPase component	6	-0.77	-0.11	**1.59**
	SSA_1581	Hemin ABC transporter	13	-1.04	-0.25	1.25
	SSA_1741	ABC-type Fe^{3+}-siderophore transport system, ATPase component	26	-0.41	-0.09	0.55
	SSA_1742	ferrichrome-binding protein	25	-0.90	0.21	0.56
	SSA_1743	ABC-type Fe^{3+}-siderophore transport system, permease component	25	-0.86	-0.31	0.41
	SSA_1744	iron ABC transporter permease	18	-0.14	0.04	0.68
Zn Transport	SSA_0136	*adcC*, Zn ABC transporter, ATPase	125	**-0.73**	-0.31	0.17
	SSA_0137	*adcB*, Zn ABC transporter, permease	81	-0.44	-0.13	0.32
	SSA_0138	*adcA*, Zn ABC transporter, lipoprotein	131	**-0.72**	-0.28	0.39
	SSA_1339	*phtD*, pneumococcal histidine triad protein D	10	**-1.28**	**-1.10**	-0.47
	SSA_1340	*adcAII*, Zn ABC transporter, orphan lipoprotein	8	-0.82	-0.99	-0.87
	SSA_1413	GufA-like, ZIP family protein	147	0.11	0.16	0.17
	SSA_1990	*adcAII*, Zn ABC transporter, orphan lipoprotein	16	-0.39	0.31	0.87
	SSA_1991	*phtA*, pneumococcal histidine triad protein A	10	-0.15	0.22	**1.06**
	SSA_2321	*czcD*, Zn/Cd efflux protein	134	**1.38**	**1.44**	0.83
Mg Transport	SSA_0447	CorA-family protein, magnesium/cobalt transporter	255	-0.39	-0.15	-0.40
	SSA_0701	CorA-family protein, magnesium/cobalt transporter	396	-0.19	0.26	0.18
	SSA_0888	*mgtE* , Mg/Co/Ni transporter	178	-0.05	-0.10	0.00
	SSA_1734	Mg/Ni transporter, P-Type ATPase	130	0.25	-0.18	-0.26

Figure 5.12 Expression of metal transport genes in the WT strain
Putative and confirmed metal transport genes are depicted with their average transcripts per million reads (TPM) at T_{-20} and log_2 fold change values for each post-acid time point. TPM values greater than 1000 are full saturation (green). Positive log_2 fold change values (red) indicate genes upregulated in after acid addition samples as compared to T_{-20}, while negative values (blue) indicate downregulated genes. Values in bold indicate significant changes in expression by adjusted *P*-value (≤ 0.05).

Expression of sugar transporters and CcpA-regulated genes

Much like in the EDTA transcriptomic study in Chapter 3, we observed significant decreases in the expression of sugar transport genes. This led us to evaluate whether acidic conditions could also lead to glucose-independent CcpA-mediated carbon catabolite repression. We evaluated expression of all genes found to be within the CcpA-

regulon (229) as well as those that we identified that have putative upstream *cre* sites (202). We found that 73 of the 392 genes with putative *cre* sites (18.6%) were downregulated by at least 1 $\log_2$ fold change in the Δ*ssaACB* mutant at T_{50}, whereas 36 were upregulated (9%) (Table S5.2). Only 47 were downregulated in WT and 18 were upregulated. In our EDTA transcriptomic study (Chapter 3), we found that 78 of these 392 genes were downregulated at T_{50}, although the genes downregulated in the Δ*ssaACB* mutant under both conditions don't match precisely. For example, *spxB* was significantly upregulated in low pH but significantly downregulated in low Mn (Table S5.2). This indicates that while there may be some overlap between the studies due to the decrease in Mn levels, there are also changes that are specific to each condition.

Expression of amino acid transporters and synthases

As acid stress tolerance has been previously linked to amino acid biosynthesis and transport (312, 314, 331, 332), we evaluated the expression of genes annotated with these functions (Figure 5.13-14). Many of these genes were significantly affected by acid addition, although more were affected in the Δ*ssaACB* mutant. Interestingly, aconitate hydratase, citrate synthase, and isocitrate dehydrogenase were significantly upregulated in the Δ*ssaACB* mutant (Figure 5.13) but significantly downregulated in the WT strain at T_{50}, despite the WT strain having higher expression at T_{-20} (Figure 5.14). Additionally, we saw a decrease in expression of the operon encoding the arginine deiminase system in both strains.

Locus Tag	Annotation	TPM	Log_2 Ratio		
		T_{-20}	T_{10}/T_{-20}	T_{25}/T_{-20}	T_{50}/T_{-20}
SSA_1615	alanine dehydrogenase	772	**-1.50**	**-2.34**	**-4.24**
SSA_0293	hypothetical protein	95	-0.41	0.44	**0.83**
SSA_0294	hypothetical protein	80	-0.12	0.48	**0.93**
SSA_0306	glnR	756	**0.97**	**0.83**	**0.79**
SSA_0307	glnA	589	**1.01**	**1.01**	**1.03**
SSA_0363	dagA	88	0.10	**0.98**	**1.45**
SSA_0364	dctA	106	0.43	**1.10**	**1.47**
SSA_0369	NADP-specific glutamate dehydrogenase	1217	**1.26**	**0.81**	**0.62**
SSA_0386	opuAa	150	**0.71**	0.38	**-0.61**
SSA_0390	hypothetical protein	21	**0.92**	0.86	**1.16**
SSA_0430	cationic amino acid transporter	23	0.51	-0.02	**0.89**
SSA_0494	peptide ABC transporter ATPase	176	**-0.71**	**-0.88**	**-1.26**
SSA_0495	peptide ABC transporter ATPase	161	-0.71	**-0.93**	**-1.39**
SSA_0497	nickel ABC transporter	152	-0.57	-0.63	**-1.05**
SSA_0500	peptide ABC transporter, permease protein	119	-0.63	**-0.75**	**-1.17**
SSA_0510	L-threonine-O-3-phosphate decarboxylase	330	**-1.05**	**-1.42**	**-2.05**
SSA_0572	dehydrogenase	562	**-1.09**	**-1.70**	**-2.61**
SSA_0632	trpE	40	-0.39	-0.35	**-0.91**
SSA_0633	trpG	36	-0.54	-0.45	**-1.05**
SSA_0634	trpD	45	-0.50	-0.19	**-0.99**
SSA_0635	trpC	51	-0.19	0.14	-0.67
SSA_0636	trpF	59	-0.59	0.12	-0.86
SSA_0637	trpB	99	-0.65	-0.68	**-1.06**
SSA_0638	trpA	117	-0.59	-0.82	**-1.18**
SSA_0702	citB, aconitate hydratase	58	**1.27**	**1.79**	**0.77**
SSA_0703	citrate synthase	53	**1.32**	**2.01**	**1.03**
SSA_0704	icd, isocitrate dehydrogenase	57	**1.20**	**2.13**	**1.21**
SSA_0737	arcA, arginine deiminase	1064	**-1.17**	**-1.51**	**-2.57**
SSA_0738	arcB, ornithine carbamoyltransferase	1409	**-1.36**	**-1.72**	**-2.72**
SSA_0739	arcC, carbamate kinase	161	**-1.99**	**-2.46**	**-4.07**
SSA_0740	arcD, arginine/ornithine antiporter	209	**-1.84**	**-2.46**	**-3.22**
SSA_0741	arcT, Sapep family Mn^{2+}-dependent dipeptidase	114	**-1.76**	**-1.99**	**-3.17**
SSA_0760	acetylornithine aminotransferase	8	**5.25**	**6.81**	**5.47**
SSA_0917	cobalamin-independent methionine synthase II	3	0.62	1.12	1.01
SSA_0921	adhB	121	0.71	0.56	0.66
SSA_0977	leuB	205	0.09	0.13	-0.63
SSA_0981	leuD	254	-0.02	-0.17	-0.53
SSA_1111	brnQ	16	0.35	**1.01**	**1.07**
SSA_1225	ilvE	177	0.69	0.60	0.63
SSA_1341	carB	127	0.51	**2.66**	**1.81**
SSA_1342	carA	104	0.64	**2.64**	**1.73**
SSA_1439	hisK	117	**0.81**	**1.12**	**0.90**
SSA_1440	hisE	129	0.53	**1.04**	0.70
SSA_1447	hisG	40	**1.14**	**1.45**	**1.21**
SSA_1448	hisZ	30	**1.21**	**1.75**	**1.38**
SSA_1568	arginine/histidine ABC transporter permease	114	**2.14**	**2.40**	**2.04**
SSA_1569	arginine/histidine ABC transporter permease	107	**1.94**	**2.39**	**2.11**
SSA_1621	amino acid transporter	127	**-1.04**	**-1.60**	**-2.19**
SSA_1713	serA	397	**-0.91**	**-0.80**	**-0.55**
SSA_1715	serC	367	**-1.15**	**-0.92**	**-0.82**
SSA_1736	L-cysteine desulfhydrase	103	0.31	0.39	**0.62**
SSA_1737	metB	78	**0.65**	**0.67**	**0.81**
SSA_1839	cysK	3950	-0.44	-0.43	-0.57
SSA_1944	oligopeptide transport ATP-binding protein	1219	-0.18	**-0.40**	**-0.67**
SSA_1949	AliA protein	638	**-1.14**	**-1.38**	**-2.42**
SSA_1950	peptide ABC transporter periplasmic protein	307	**2.24**	**2.34**	**1.85**
SSA_1961	amino acid ABC transporter substrate-binding protein	122	0.21	0.47	**0.71**
SSA_1962	amino acid ABC transporter ATP-binding protein	194	0.07	0.40	**0.73**
SSA_2099	arginine/histidine ABC transporter permease	622	**-0.82**	**-0.50**	**-0.60**
SSA_2101	amino acid ABC transporter substrate-binding protein	589	**-0.88**	-0.38	**-0.77**
SSA_2141	argH	48	**3.07**	**3.61**	**3.03**
SSA_2142	argG	47	**2.97**	**3.67**	**3.16**

Figure 5.13 Expression of amino acid-related genes in the Δ*ssaACB* mutant
Differentially expressed amino acid-related genes are depicted with their average transcripts per million reads (TPM) at T_{-20} and log_2 fold change values for each post-acid time point. TPM values greater than 1000 are full saturation (green). Positive log_2 fold change values (red) indicate genes upregulated in after acid addition samples as compared to T_{-20}, while negative values (blue) indicate downregulated genes. Values in bold indicate significant changes in expression by adjusted *P*-value (≤ 0.05).

Locus Tag	Annotation	TPM	Log_2 Ratio		
		T_{-20}	T_{10}/T_{-20}	T_{25}/T_{-20}	T_{50}/T_{-20}
SSA_0497	nickel ABC transporter	141	-0.11	-0.48	**-0.61**
SSA_0510	L-threonine-O-3-phosphate decarboxylase	430	**-1.02**	**-1.34**	**-1.60**
SSA_0572	dehydrogenase	362	-0.11	-0.43	-0.96
SSA_0588	L-cystine ABC transporter substrate-binding component	13219	**-0.83**	**-0.63**	**-0.81**
SSA_0702	citB, aconitate hydratase	182	-0.22	-0.37	**-1.62**
SSA_0703	citrate synthase	134	-0.04	0.05	**-1.33**
SSA_0704	isocitrate dehydrogenase	154	-0.11	0.02	**-1.23**
SSA_0737	arcA, arginine deiminase	668	-0.39	-0.61	**-0.87**
SSA_0738	arcB, ornithine carbamoyltransferase	977	-0.57	**-0.90**	**-1.05**
SSA_0741	arcT, Sapep family Mn^{2+}-dependent dipeptidase	87	-0.74	**-1.30**	**-1.92**
SSA_0739	arcC, carbamate kinase	90	-0.77	**-1.23**	**-1.69**
SSA_0740	arcD, arginine/ornithine antiporter	147	-0.85	**-1.17**	**-1.60**
SSA_0760	acetylornithine aminotransferase	11	4.01	**5.84**	**4.28**
SSA_1341	carB	101	**0.92**	**2.68**	**1.50**
SSA_1342	carA	79	**1.13**	**2.62**	**1.46**
SSA_1439	hisK	89	**1.04**	**1.29**	**1.15**
SSA_1447	hisG	24	**1.52**	**1.69**	**1.45**
SSA_1448	hisZ	36	**1.02**	**1.00**	**0.85**
SSA_1615	alanine dehydrogenase	550	-0.57	-0.93	**-1.58**
SSA_1621	amino acid transporter	133	-0.74	**-1.29**	**-1.35**
SSA_1713	serA	357	**-0.69**	**-0.78**	**-0.80**
SSA_1715	serC	272	**-0.53**	**-0.82**	**-0.54**
SSA_1949	AliA protein	570	-0.72	**-0.96**	**-1.09**
SSA_1950	peptide ABC transporter periplasmic protein	398	**1.90**	**2.00**	**1.84**
SSA_2097	amino acid ABC transporter ATP-binding protein	642	**-0.75**	**-0.61**	**-0.62**
SSA_2098	arginine/histidine ABC transporter permease	604	**-0.75**	**-0.72**	**-0.68**
SSA_2099	arginine/histidine ABC transporter permease	637	**-0.63**	**-0.53**	**-0.54**
SSA_2101	amino acid ABC transporter substrate-binding protein	692	**-0.89**	**-0.75**	**-0.85**
SSA_2141	argH	66	**2.47**	**2.78**	**1.73**
SSA_2142	argG	60	**2.63**	**2.86**	**1.87**

Figure 5.14 Expression of amino acid-related genes in the WT strain
Differentially expressed amino acid-related genes are depicted with their average transcripts per million reads (TPM) at T_{-20} and log_2 fold change values for each post-acid time point. TPM values greater than 1000 are full saturation (green). Positive log_2 fold change values (red) indicate genes upregulated in after acid addition samples as compared to T_{-20}, while negative values (blue) indicate downregulated genes. Values in bold indicate significant changes in expression by adjusted *P*-value (≤ 0.05).

We previously discovered that the addition of Cys or GSH improved the growth of the Δ*ssaACB* mutant in aerobic serum and BHI + 100 µM EDTA but not in the fermentor with EDTA (Chapter 3). We were then curious as to whether this improvement was related to oxidative stress and the reductive capabilities of each of these molecules. We assessed

whether addition of Cys or GSH improved the growth of the Δ*ssaACB* mutant in pH 6.2 BHI at 1% O_2 (Figure 5.15). We found that in these conditions, addition of these molecules improved the growth, indicating that this phenotype is likely not related to oxidative stress and Cys and GSH are relieving the poor growth of the Δ*ssaACB* mutant through another mechanism.

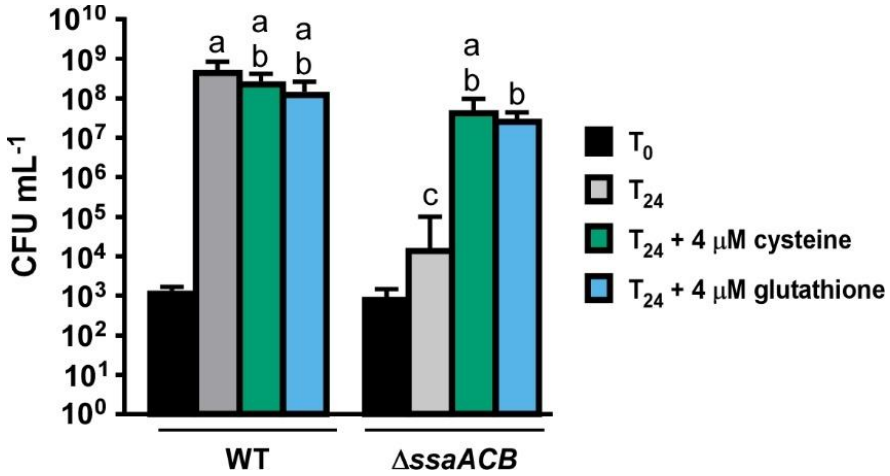

Figure 5.15 Growth in low pH with Cys and GSH at 1% O_2
BHI pH 6.2 was preincubated at 1% O_2 and inoculated from an overnight culture. Cys and GSH were added prior to inoculation. Cultures were incubated for 24 h before plating. Means ± SD of at least three replicates are displayed. Significance was determined by one-way ANOVA of T_{24} cultures; bars with the same letter are not significantly different from each other ($P \leq 0.05$). T_0 values were compared by two-tailed t-test and found to not be significantly different.

Expression of other relevant GOIs

In addition to the GOIs described in other sections, we also examined whether other genes were differentially expressed in low pH growth. We observed a significant increase in the expression of the anaerobic RNR genes in the Δ*ssaACB* mutant (Figure 5.16) and in both aerobic and anaerobic RNR genes in the WT strain (Figure 5.17). In both strains, we observed large decreases in competence genes at T_{25} and T_{50} time points, with the exception of *comEB*, which was unchanged (Figure 5.16-17). Expression of other putative Mn-dependent enzymes were unchanged in WT (Figure 5.17), while *pgm* and *deoB* were significantly downregulated in Δ*ssaACB* (Figure 5.16). Rel protein expression was

unchanged in WT (Figure 5.17) but *relQ* was significantly decreased in the Δ*ssaACB* mutant at T_{50} and *relA* increased slightly but significantly (Figure 5.16).

Δ*ssaACB* Acid	Locus Tag	Annotation	TPM	Log_2 Ratio		
			T_{-20}	T_{10}/T_{-20}	T_{25}/T_{-20}	T_{50}/T_{-20}
Ribonucleotide Reductases	SSA_0768	*nrdF*, Aerobic RNR (Mn-dependent)	947	0.22	0.35	0.22
	SSA_0769	*nrdK*, Aerobic RNR	1014	0.13	0.49	0.09
	SSA_0770	*nrdE*, Aerobic RNR	761	0.35	0.41	0.13
	SSA_0771	*nrdH*, Aerobic RNR	921	**0.53**	**0.80**	0.45
	SSA_2226	*nrdG*, Anaerobic RNR	61	0.54	**0.89**	**1.23**
	SSA_2227	Acetyltransferase	61	0.44	**1.13**	**1.31**
	SSA_2228	Acetyltransferase	72	0.45	**0.85**	**0.89**
	SSA_2229	Hypothetical protein	166	0.31	**0.77**	**1.34**
	SSA_2230	*nrdD*, Anaerobic RNR	175	0.43	**0.80**	**1.11**
Competence	SSA_2394	*comC*	439	**-1.62**	-1.26	**-1.90**
	SSA_2379	*comD*	508	**-1.96**	**-1.68**	**-2.00**
	SSA_2378	*comE*	573	**-2.10**	**-1.91**	**-2.17**
	SSA_0016	*comX*	1165	**-3.04**	**-4.40**	**-5.79**
	SSA_0184	*comGA*	1176	**-1.15**	**-3.40**	**-5.04**
	SSA_0185	*comGB*	1017	**-1.27**	**-3.61**	**-5.45**
	SSA_0186	*comGC*	798	**-1.28**	**-3.82**	**-5.09**
	SSA_0187	*comGD*	1187	**-1.19**	**-3.39**	**-5.20**
	SSA_0188	*comGE*	1135	**-1.16**	**-3.28**	**-5.09**
	SSA_0189	*comGF*	1119	**-1.09**	**-3.17**	**-4.62**
	SSA_0190	*comGG*	1169	-1.00	**-2.95**	**-4.78**
	SSA_0715	*comEA*	587	**-1.06**	**-3.53**	**-5.79**
	SSA_0716	*comEC*	633	**-1.00**	**-3.47**	**-5.48**
	SSA_1497	*comEB*	164	0.32	0.46	0.18
	SSA_1835	*comFC*	397	-0.76	**-2.42**	**-3.92**
	SSA_1836	*comFA*	339	**-1.07**	**-3.25**	**-4.63**
Mn-Dependent Enzymes in Streptococci	SSA_1204	*pgm*, phosphatase	751	-0.45	**-0.70**	**-1.54**
	SSA_1260	*deoB*, pentophosphomutase	1061	**-0.92**	**-0.97**	**-1.78**
	SSA_1271	*papP*, nucleotide phosphatase	183	0.24	-0.14	0.00
	SSA_1748	*ppaC*, phosphatase	545	-0.03	-0.23	-0.22
	SSA_1846	*phpP*, phosphatase	892	-0.05	0.03	0.03
	SSA_2224	*cspB*, capsular phosphate	459	-0.09	0.15	0.05
Rel Proteins	SSA_0250	*relA*, bifunctional (p)ppGpp synthetase/hydrolase	275	0.32	0.31	**0.37**
	SSA_1210	*relQ*, (p)ppGpp synthetase	334	-0.13	-0.48	**-1.22**
	SSA_1795	*relP*, (p)ppGpp synthetase	124	-0.02	0.03	0.31

Figure 5.16 Other GOIs in the Δ*ssaACB* mutant

GOIs are depicted with their average transcripts per million reads (TPM) at T_{-20} and log_2 fold change values for each post-acid time point. TPM values greater than 1000 are full saturation (green). Positive log_2 fold change values (red) indicate genes upregulated in after acid addition samples as compared to T_{-20}, while negative values (blue) indicate downregulated genes. Values in bold indicate significant changes in expression by adjusted *P*-value (≤ 0.05).

WT Acid	Locus Tag	Annotation	TPM	Log_2 Ratio		
			T_{-20}	T_{10}/T_{-20}	T_{25}/T_{-20}	T_{50}/T_{-20}
Ribonucleotide Reductases	SSA_0768	*nrdF*, Aerobic RNR (Mn-dependent)	810	0.48	0.60	0.53
	SSA_0769	*nrdK*, Aerobic RNR	760	0.60	0.68	0.68
	SSA_0770	*nrdE*, Aerobic RNR	622	0.54	**0.65**	**0.59**
	SSA_0771	*nrdH*, Aerobic RNR	947	0.52	0.71	**0.62**
	SSA_2226	*nrdG*, Anaerobic RNR	56	0.49	0.71	**0.85**
	SSA_2227	Acetyltransferase	73	0.28	0.62	0.55
	SSA_2228	Acetyltransferase	81	0.30	0.44	0.51
	SSA_2229	Hypothetical protein	202	0.29	0.47	0.58
	SSA_2230	*nrdD*, Anaerobic RNR	192	0.36	**0.63**	**0.63**
Competence	SSA_2394	*comC*	804	**-2.51**	**-1.62**	**-2.15**
	SSA_2379	*comD*	838	**-2.34**	**-2.12**	**-2.37**
	SSA_2378	*comE*	788	**-2.27**	**-2.01**	**-2.17**
	SSA_0016	*comX*	1575	**-1.80**	**-4.29**	**-3.59**
	SSA_0184	*comGA*	679	**-0.62**	**-2.34**	**-4.16**
	SSA_0185	*comGB*	491	**-0.69**	**-2.26**	**-3.98**
	SSA_0186	*comGC*	313	-0.17	**-2.34**	**-3.65**
	SSA_0187	*comGD*	552	-0.56	**-2.24**	**-4.12**
	SSA_0188	*comGE*	503	-0.47	**-1.90**	**-3.58**
	SSA_0189	*comGF*	600	**-0.73**	**-2.51**	**-3.60**
	SSA_0190	*comGG*	621	-0.42	**-1.98**	**-3.29**
	SSA_0715	*comEA*	322	-0.65	**-2.88**	**-3.87**
	SSA_0716	*comEC*	317	-0.44	**-2.56**	**-4.10**
	SSA_1497	*comEB*	201	-0.06	0.04	0.13
	SSA_1835	*comFC*	264	-0.61	**-1.75**	**-2.64**
	SSA_1836	*comFA*	198	-0.60	**-2.76**	**-3.28**
Mn-Dependent Enzymes in Streptococci	SSA_1204	*pgm*, phosphatase	594	-0.19	-0.24	-0.34
	SSA_1260	*deoB*, pentophosphomutase	741	-0.39	-0.43	-0.52
	SSA_1271	*papP*, nucleotide phosphatase	162	0.42	0.09	0.04
	SSA_1748	*ppaC*, phosphatase	426	0.37	0.21	0.25
	SSA_1846	*phpP*, phosphatase	830	0.05	0.12	0.20
	SSA_2224	*cspB*, capsular phosphate	501	-0.25	0.10	0.24
Rel Proteins	SSA_0250	*relA*, bifunctional (p)ppGpp synthetase/hydrolase	322	-0.01	0.07	0.10
	SSA_1210	*relQ*, (p)ppGpp synthetase	309	-0.09	-0.03	-0.42
	SSA_1795	*relP*, (p)ppGpp synthetase	106	0.30	0.07	0.07

Figure 5.17 Other GOIs in the WT strain
GOIs are depicted with their average transcripts per million reads (TPM) at T_{-20} and log_2 fold change values for each post-acid time point. TPM values greater than 1000 are full saturation (green). Positive log_2 fold change values (red) indicate genes upregulated in after acid addition samples as compared to T_{-20}, while negative values (blue) indicate downregulated genes. Values in bold indicate significant changes in expression by adjusted *P*-value (≤ 0.05).

Discussion

Connection between Mn and acid tolerance

While the connection between Mn and acid tolerance is not unprecedented (320), it has yet to be fully characterized. In 1982, D. Beighton (333) noted that Mn induced *S. mutans* to form caries and influenced carbohydrate metabolism. In *S. pneumoniae* (334) and *S.*

agalactiae (326), the orthologs of SsaACB were upregulated in response to acid stress. In *S. mutans*, expression of the Mn-dependent regulator SloR was previously linked to ATR (335). Recently, it was appreciated that loss of the Nramp transporter MntH in *S. mutans* (148) and *S. agalactiae* (147) led to a reduction in acid tolerance. Here we report that loss of the high affinity Mn ABC transporter in *S. sanguinis,* SsaACB*,* reduces acid tolerance and characterize the transcriptional changes that accompany the poor growth phenotype in low pH conditions.

Initially, we were unsure whether the poor growth phenotype we observed was directly related to Mn but the reduction in intracellular Mn levels in both WT and Δ*ssaACB* strains (Figure 5.4) indicates that low pH impacts the ability of Mn to enter the cell. We hypothesize that either the function of the secondary Mn transporter is affected by low pH or that bioavailability of Mn is affected. Preliminary studies of three *S. sanguinis* strains that encode NRAMP proteins, VMC66, SK408, and BCC23, indicated that loss of *ssaACB* alone was not sufficient to affect growth at pH 6.2 (data not shown). This suggests that the Mn is still bioavailable but the secondary transporter in SK36 is unable to transport Mn efficiently in low pH conditions. *S. sanguinis* encodes a ZIP protein that acts as a secondary Mn transporter (to be discussed in Chapter 6). One of the human ZIP proteins, hZIP4, functions normally at pH 6.2 (336) whereas the ortholog in *E. coli*, ZupT, functions best near neutral pH (337). This protein family appears to be diverse in terms of metal selectivity and transport function so it is possible that the function of the *S. sanguinis* version is negatively impacted by low pH.

When comparing the low pH RNA-seq results in each strain directly to each other, few genes were differentially expressed and those that were only occurred at the T_{-20} and T_{50}

time points (Table 5.1). Despite this, we observed a drastic difference in the fermentor growth rate between WT and Δ*ssaACB* after acid addition (Figure 5.3). Thus, we hypothesize that either: (*i*) subtle changes between strains have a large combined effect; (*ii*) WT has achieved ATR, whereas Δ*ssaACB* has not; or (*iii*) post-transcriptional changes not captured by transcriptomics may be influencing the growth. It is also possible that all three options are occurring simultaneously.

Acid stress response

As expected, both strains began activating their acid stress response by upregulating expression of genes encoding F-ATPases and a putative stress response protein, SSA_2148. This protein shares identity with the Gls24 protein family, which has been linked to Cu stress in *Enterococcus hirae* (338). A Gls24 KO mutant in *E. faecalis* was deficient for virulence (339) and displayed differing morphology but there was no difference in acid growth between the mutant and its parent (340). Its role in *S. sanguinis* acid stress tolerance remains to be determined. Streptococcal membranes are permeable to weak acids (315), which can cross the cell membrane since it maintains a neutral charge. Since the cytoplasmic pH is generally higher than the medium, the proton disassociates from the acid, leading to acidification of the cytoplasm and damage to cellular machinery and proteins. Additionally, cell membranes may be at least somewhat permeable to protons (314, 341, 342). Thus membrane-bound F-ATPases are useful because they utilize ATP to actively pump protons out of the cell (314). Thus, the increase in expression after lowering the pH is a potent mechanism by which the cells control their intracellular pH in an acidic environment (343, 344).

The decreased or unchanged expression of almost all other acid stress genes was surprising. The operon encoding the molecular chaperones HcrA, GrpE, DnaK, and DnaJ was significantly downregulated at all time points in the Δ*ssaACB* mutant and slightly but not significantly in the WT strain. A similar trend was observed for the operon encoding GroEL and GroES, which is likely due to the regulation of both operons by HcrA (321, 345) and was also observed in a study on Mn depletion in *S. pneumoniae* (173). In many other species of streptococci, *dnaK, dnaJ*, and *groEL* transcript or protein levels were upregulated in response to acid stress (334, 346, 347). As noted by Shabayek and Spellerberg (320), this increase in expression was not observed in some acid stress studies using *Streptococcus suis* (348) and *S. agalactiae* (326). It was hypothesized that this discrepancy may be due to differences in growth conditions and also exposure time, as Santi et al. (326) used only 30 min exposure, although an *S. intermedius* Δ*dnaK* mutant did not display significant acid sensitivity (349). Still, it is likely that our time points were too early to capture the full ATR.

Clp chaperone proteins have also previously been linked to acid stress responses. In *S. mutans* (350) and *S. pneumoniae* (334), *clpL* protein and transcript levels were found to increase during acid exposure. Here we observed that levels of *clp* gene transcription were unaffected in either strain, again highlighting that these conditions may not represent true ATR, merely acid shock.

Metal transporter regulation

As mentioned previously, increased expression of the *ssaACB* operon in WT and the gene replacing it in the KO mutant, *aphA-3*, was expected due to the poor growth phenotype of this mutant and similar transcriptomic results in other streptococci (326,

334). It was unexpected though that expression of the putative Mn exporter, *mntE,* increased in expression in the Δ*ssaACB* mutant. This is similar to our previous findings in EDTA (202) and again leads us to question the function of this protein in *S. sanguinis*.

Similar to acid studies in other streptococcal species (326, 334), expression of several putative Fe transporters increased. This is likely the cause of the slight increase in Fe levels in both strains after acid addition (Figure 5.4). The significant increase in expression of a putative CorA-family Mg/Co transport protein in the Δ*ssaACB* mutant was unexpected, as was the significant increase in Mg levels. This was also observed in the transcriptomic analysis of *S. agalactiae* (326). The reason for this is still unknown, although it appears to be related to both Mn and acid stress, since this was only observed in this strain under these conditions. We identified a putative *cre* site upstream (202), so it may be related to CcpA regulation.

The link between Zn maintenance and acid stress has not been fully developed. In *S. agalactiae*, expression of the Zn-responsive regulator AdcR was significantly increased (326). Here we report that despite an initial decrease in expression at T_{10}, the *adcR* gene was not significantly different from cells at pH 7.4. Additionally, expression of most putative Zn transporters were not significantly affected in WT at the T_{50} time point, although some were in the Δ*ssaACB* mutant. Those included decreased expression of the putative histidine triad protein D as well as increases in the expression of *adcC*, *adcB*, and *czcD*. The connection between these contradictory changes in expression levels need to be examined further, although the cells were able to maintain constant levels of Zn throughout the experiment.

CCR and acid stress

While we do not have metabolomics data for these samples, we hypothesize that the impact on glycolysis is similar to what we observed when we added EDTA to cells, as both conditions reduced Mn levels (Chapter 3 and Figure 5.4). Additionally, expression of genes encoding glycolytic enzymes were similar in both studies (Figure 5.18), indicating that the regulatory mechanisms controlling the expression of these genes may have a Mn-related aspect. Thus, we hypothesize that there is likely an accumulation of FBP occurring in low pH cells due to reduced activity of Fba, Fbp, or both enzymes. This may be the cause behind the changes in expression we observed in the CcpA regulon (Table S5.2). Interestingly, expression of *ccpA* itself was unaffected in either strain, despite observing a significant decrease in expression after EDTA in our previous study (202). Further experiments will be required to determine levels of FBP and examine our hypothesis.

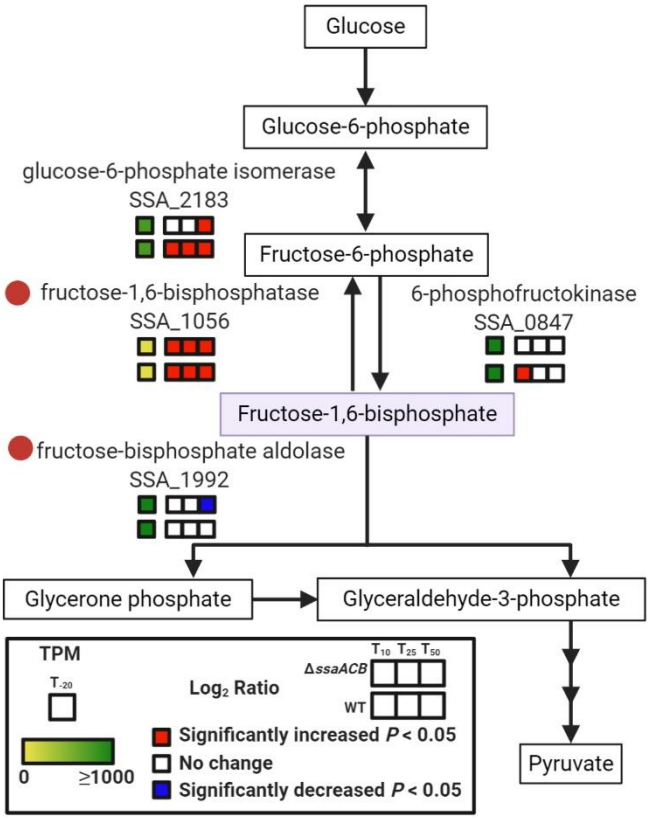

Figure 5.18 Expression of genes encoding glycolytic enzymes in acid grown cells
Impact of low pH on transcription levels of glycolytic enzymes is depicted. Red circles indicate predicted Mn cofactors. Purple box indicates predicted accumulation of the glycolytic intermediate FBP.

Amino acids and acid stress

One of the mechanisms by which bacteria deal with acid stress is through the production of alkali. Some oral streptococci combat acid stress by ammonia production through the arginine deiminase system. We observed that expression of this system significantly decreased in both the WT and Δ*ssaACB* mutant. Other species such as *S. agalactiae* observed extreme upregulation in acidic conditions (326). We did observe similar changes in expression of this operon when EDTA was added (Chapter 3), *S. agalactiae* may also have a shortage of Mn under low acid conditions. One possibility could be that their experiment was completed in stationary phase growth while our conditions are likely more similar to logarithmic phase growth. We also noted that this operon may have an

upstream *cre* site, although it was not identified as a member of the *S. sanguinis* CcpA regulon (229).

As noted, there appears to be Mn-related regulation of the citrate genes. This is highlighted by the differences in expression between the two strains, as well as the increases in expression we observed after EDTA addition. Citrate synthase likely requires a metal cofactor, as many orthologs in BRENDA are annotated as having an absolute requirement for divalent cations. Additionally, immediately upstream of these genes is the putative CorA-family metal transport protein SSA_0701. Like the citrate metabolism genes, SSA_0701 was significantly upregulated in the Δ*ssaACB* mutant at all three time points in low pH conditions. This gene was found to be a member of the CcpA regulon in *S. sanguinis* (229) and we confirmed the presence of a putative *cre* site upstream (Chapter 3).

Many other amino acid-related were significantly affected in the Δ*ssaACB* mutant and WT strains under acid stress. Deeper investigation is required to evaluate the relative contribution of Mn depletion to each of this systems. However, it was found that amino acids improved the acid tolerance of *Bacillus cereus* (332). Additionally, as noted by Radin et al. (251), glycolytic enzymes may have a higher demand for Mn and thus in Mn-deplete conditions, the cells may shift to amino acid metabolism as a source of energy.

Impact of acid stress on other Mn-related systems

RNRs

As we are not aware of the mechanisms for transcriptional regulation of class Ib RNRs, we are unable to speculate on why expression of *nrdHEKF* increased slightly, yet significantly in WT while remaining unchanged in the Δ*ssaACB* mutant. It appears to be

complex and potentially both acid and Mn related, as expression significantly decreased in this mutant after EDTA addition.

Expression of the anaerobic RNR was slightly higher in all strains and conditions. This is puzzling, especially given the differences in airflow in each of the experiments. It is possible that regulation is related to Fe, as this enzyme is Fe-cofactored and Fe levels increased slightly in both strains and in both conditions.

Competence

Competence was previously found to be Mn-dependent in *S. pneumoniae* (137) and another study found that competence genes were down regulated in a Δ*psaA* Mn transport mutant in low Mn conditions. We observed the same results here but have shown that the *S. sanguinis* Δ*ssaACB* mutant is competent (202) and have generated many mutants with this strain (Chapters 3 & 6). We also observed in Chapter 3 and Puccio et al. (202) that the expression of most of these genes were upregulated. Thus, the impact of low Mn on competence must be dependent on the growth conditions.

Mn-dependent enzymes in other streptococci

Much like in Chapter 3, only the expression of *pgm* and *deoB* were affected by the treatment in the Δ*ssaACB* mutant; genes encoding the other four enzymes were unaffected. Expression was unchanged in WT, indicating that the regulation is likely Mn-dependent. Both genes are transcribed within operons that have upstream *cre* sites, and thus are likely regulated in this manner. We found in our EDTA study that the decrease in expression of *deoB* likely corresponded with the decrease in conversion of nucleosides to nucleobases (Chapters 3 & 4). We did not determine whether the decrease in expression of *pgm* and likely its activity contributed to the poor growth of the Δ*ssaACB*

mutant in either study, although this gene has been characterized as a virulence factor in *Streptococcus iniae* (351). Additionally, although expression of the other four phosphatases was not changed in either study, it is still possible that their activity was affected if they do require a Mn cofactor in *S. sanguinis*. Thus, further investigation is required to determine the relative contribution of each of these phosphatases to growth of *S. sanguinis*.

Rel proteins

As described in Chapter 3, transcriptional regulation of each of the Rel proteins varies. Little is known about how *relA* expression is regulated. We observed a slight, signficant increase in expression in this study at T_{50} in the Δ*ssaACB* mutant but it is likely not biologically relevant. Expression of *relQ* is likely regulated in a Mn-related manner, possibly through CcpA, as expression was unaffected in WT but significantly decreased in the Δ*ssaACB* mutant in both studies. Interestingly, *relP* expression was unaffected here, despite being upregulated after EDTA addition. While this is not conclusive, it provides additional evidence for the connection between Mn homeostasis and the modulation of (p)ppGpp production.

Conclusions and future studies

In conclusion, we found that much of the acid stress response is related to reduced Mn levels. We noted many similarities between this study and our previous one where EDTA was added, although there were several major differences. Some of these differences may be due to the differences in Fe levels; while Fe was not significantly different after either treatment, levels increased slightly after acid addition but decreased slightly after EDTA addition. There is also the possibility that the differences in airflow may have

contributed to some of these differences. We also noted that despite modest differences in the transcriptome between the WT and Δ*ssaACB* mutant strain, we observed a dramatic difference in the growth after acid addition, highlighting the importance of sufficient Mn levels as well as the complex relationship it has with the *S. sanguinis* transcriptome. These results open a multitude of avenues for future research and further understanding of Mn homeostasis in this opportunistic pathogen.

Given these results, we plan to complete more experiments in order to elucidate the impact that low pH has on *S. sanguinis* and the role of Mn in acid tolerance. We will be assessing the fermentor grown cells for FBP and H_2O_2 levels. We also plan to add Mn, Cys, and GSH to the Δ*ssaACB* mutant after acid addition to determine whether these molecules can rescue the poor growth phenotype under fermentor conditions. We also would like to examine the impact of added Mn further by decreasing the pH enough to negatively affect growth of the WT strain and adding excess Mn.

We then propose to test the impact that the loss of SodA and Dpr has on cells grown in low pH conditions to evaluate their contribution to acid stress tolerance in *S. sanguinis*. A collaborator completed some initial chemostat studies in which *S. mutans* and *S. sanguinis* were grown together in low pH conditions but the results were inconclusive (data not shown). Thus we plan to test this relationship other ways, including agar plate assays (71) as well as a mouse model of colonization (352). We would also like to determine if the observed decrease in Mn levels in true for other strains of *S. sanguinis* as well as other species of streptococci.

Materials and Methods

Bacterial strains

SK36 and JFP169 (Δ*ssaACB*::*aphA-3*) were described in Chapter 2.

Growth studies

Growth studies were similar to what is described in Chapter 2, except that BHI was modified to the pH levels described by adding 6 N HCl prior to autoclaving or filtering. The cultures were then grown at 1% O_2 in an Anoxomat jar. In some growth studies, either $MnSO_4$ (Alfa Aesar; Puratronic™, >99.999% pure), L-cysteine (Alfa Aesar), or reduced glutathione (ACROS Organics) was added to culture tubes immediately prior to inoculation.

Fermentor growth conditions

The fermentor conditions were identical to Chapter 2 and T. Puccio and T. Kitten (163), with the following exceptions: the air flow was kept at 0.03 lpm for the entire experiment and instead of EDTA, 2 N HCl was added to the vessel at T_0 and culture pH was maintained at 6.2.

RNA sequencing

Total RNA quantity and integrity were determined using a Bioanalyzer (Agilent). All samples passed quality control assessment with RNA Integrity Numbers (RIN) above 8. Two sequential rounds of ribosomal reduction were then performed on all samples using RiboMinus™ Transcriptome Isolation Kit (ThermoFisher). The resulting depleted RNA was assessed using Bioanalyzer (Agilent) to confirm efficient rRNA removal. Stranded RNA-seq library construction was then performed on the rRNA-depleted RNA using the Kapa RNA HyperPlus kit for Illumina (Roche) following manufacturer's specifications for

library construction and multiplexing. Final Illumina libraries were assessed for quality using an Agilent Bioanalyzer DNA High Sensitivity Assay and qPCR quantification was performed using Kapa Library Quantification lit for Illumina (Roche). Individual libraries were pooled equimolarly, and the final pool was sequenced on an Illumina MiSeq, with 2 x 75-bp paired-end reads. Demultiplexing was performed on the Illumina MiSeq's on-board computer. The Virginia Commonwealth University Genomics Core Facility completed all RNA-seq library preparation and sequencing.

Raw RNA-seq data from this chapter will be deposited in NCBI's Gene Expression Omnibus (266).

Metal analysis

Aliquots of 40 mL were collected at each time point and subjected to metal analysis as described in Chapter 2.

RNA-seq analysis

This was performed as described in Chapter 2.

Chapter 6 Role of the Secondary Manganese Transporter TmpA in *S. sanguinis*

Rationale

The poor growth phenotype of the Δ*ssaACB* mutant in aerobic serum was rescued by the addition of only 2 µM Mn^{2+} (120). This indicates that there must be another mechanism for Mn to enter the cell. We were interested in learning about secondary Mn transporters, as none were annotated in the SK36 genome. Additionally, suppressor mutants of an Δ*ssaACB* mutant have occurred previously *in vitro* (175), indicating that targeting two Mn systems may be a better therapeutic strategy. Thus, we investigated other metal transport proteins in *S. sanguinis,* including a ZIP family protein.

Introduction

As described in Chapter 1, only MntH proteins have been characterized as secondary Mn transporters in streptococci but most *S. sanguinis* strains lack a MntH ortholog. Unpublished work from our lab previously evaluated the relative contribution of several putative metal ABC transporters to Mn transport but loss of each of these systems did not significantly affected growth of the Δ*ssaACB* mutant in aerobic rabbit serum.

In examining the literature, we found that a ZIP ("ZRT, IRT-like Protein") family protein, BmtA, in *Borrelia burgdorferi* was discovered to primarily transport Mn and little to no Zn or Fe (353). This was surprising, given that ZIP family proteins primarily transport Zn or Fe. The lack of Fe transport may be due to the fact that *B. burgdorferi* is a Mn-centric organism with no known requirements for Fe (114). The absence of Zn transport by BmtA was unexpected but this result was replicated by Ramsey et al. (354). Initial modeling

studies identified drugs that proved efficacious against BmtA Mn transport activity (355) but as of yet, no drugs targeting ZIP family proteins are used to treat any disease.

ZIP family proteins take their name from the first identified members of the family: zinc regulated transporters (ZRT1 and ZRT2) found in *Saccharomyces cerevisiae* (356, 357) and iron regulated transporter (IRT1) from *Arabidopsis thaliana* (358) (Table 6.1). ZIP family proteins are also referred to as the solute carrier 39, (SLC39) family in humans (359). Since these initial discoveries, ZIP family proteins have been characterized in various organisms, including at least 14 in humans (360). Human ZIP (hZIP) proteins have been implicated in diseases such as acrodermatitis enteropathica (361, 362), Ehler Danlos syndrome (363), congenital glycosylation disorders (364), and several cancers (365, 366), enhancing the need to characterize this protein family.

Most primarily transport Zn or Fe, although hZIP8 (364, 367-370), hZIP14 (371-374), and BmtA (353, 354) primarily transport Mn (Table 6.1). Many ZIP proteins also have low affinity for other metals; for example, the well-studied IRT1 from *Arabidopsis thaliana* can transport Fe, Cd, Co, Mn, and Zn (375, 376). ZIP proteins have been grouped into four subfamilies: (i) LIV-1, (ii) GufA, (iii) ZIPI, and (iv) ZIPII (377). Bacterial ZIP proteins fall into the GufA subfamily, which also contains mammalian members such as hZIP11 (378, 379). The first bacterial ZIP protein, ZupT, was identified in *Escherichia coli* (380). This initial study proved that it played a role in Zn uptake and further investigation determined that other metal cations could also be transported by ZupT, albeit with lower affinity (337, 381). Many bacterial species contain putative ZIP family proteins but few have been characterized for metal affinity and contribution to growth and virulence. The only ZIP protein to be crystallized thus far is ZIPB (also known as BbZIP) from *Bordetella*

bronchiseptica (382, 383). ZIPB was chosen from a screen of 96 prokaryotic ZIP proteins (384) and it was assessed for transport of various metal cations (382, 385). The mechanism of transport in proteoliposomes was determined to be passive, selective electrodiffusion with no evidence of saturation (385). This seems the likely mechanism for transport for all bacterial ZIP proteins, although some human ZIP proteins have been characterized as bicarbonate symporters (378, 386, 387).

Table 6.1 Selected ZIP family proteins

Name	Species	Kingdom	Primary	Other
BmtA	*Borreliella burgdorferi*	Bacteria	Mn	
hZIP8 (SLC39A8)	*Homo sapiens*	Animal	Mn	
hZIP11 (SLC39A11)	*Homo sapiens*	Animal	Zn	
hZIP14 (SLC39A14)	*Homo sapiens*	Animal	Mn	
IRT1	*Arabidopsis thaliana*	Plant	Fe	Cd, Co, Mn, Zn
ZIPB (BbZIP)	*Bordetella bronchiseptica*	Bacteria	Zn	Cd
ZRT1	*Saccharomyces cerevisiae*	Fungus	Zn	
ZRT2	*Saccharomyces cerevisiae*	Fungus	Zn	
ZupT	*Escherichia coli*	Bacteria	Zn	Cd, Co, Fe, Mn

The structure of ZIPB was determined by Zhang et al. (382) in the presence of Cd^{2+} or both Zn^{2+} and Cd^{2+} ions, which revealed a binuclear metal center. This is unusual for transporters, as binuclear centers are usually known for their role in catalysis (388-390). This group also discovered that ZIP proteins have a unique 3+2+3 TM architecture, which led them to question the origins of ZIP proteins (382). Since they are nearly ubiquitous in animals, plants, and bacteria, this family may have diverged very early in history and now represent a distant branch of the drug/metabolite transporter (DMT) superfamily (382, 391). The protein was crystallized in an inward-open confirmation, with the periplasmic entrance closed off, indicating that there is significant conformational changes during metal transport. Additionally, Gupta et al. (383) discovered that the residues along the pore go through a switch between Zn coordination and water binding in order to facilitate

transport. Unexpectedly, Zn binding actually increased water access to one of the metal binding sites (383).

The contribution of ZIPB to the virulence of *B. bronchiseptica* has not been determined but ZIP family proteins in *Clostridiodes difficile* (392) and *B. burgdorferi* (353) have been found to contribute to virulence of these bacterial pathogens. Here we report the role of a *S. sanguinis* ZIP family protein in virulence as well as the characterization of mutations in the gene encoding this protein.

Results

Identification of a ZIP family protein

Given the importance of BmtA for Mn transport in *B. burgdorferi*, we sought to determine whether a BmtA ortholog was present in *S. sanguinis*. NCBI BLAST search (174) of the BmtA sequence against *S. sanguinis* strain SK36 identified SSA_1413 as a ZIP family protein (annotated as a GufA-like protein). ZIP proteins are integral membrane proteins with 8 transmembrane domains (TMD) with both C- and N-termini facing extracellularly (393). They contain either one or both canonical motifs: (i) a variable length $(Hx)_n$ motif in the cytoplasmic loop between TMD III and IV (359) and (ii) a conserved HNxPEG motif in TMD IV (385). As with BmtA and ZIPB, SSA_1413 has a few histidine residues in the variable loop region between TMDs III and IV but lacks a true $(Hx)_n$ motif (Figure 6.1) (359). All three protein sequences contain the conserved HNxPEG motif in TMD IV (Figure 6.1) (385).

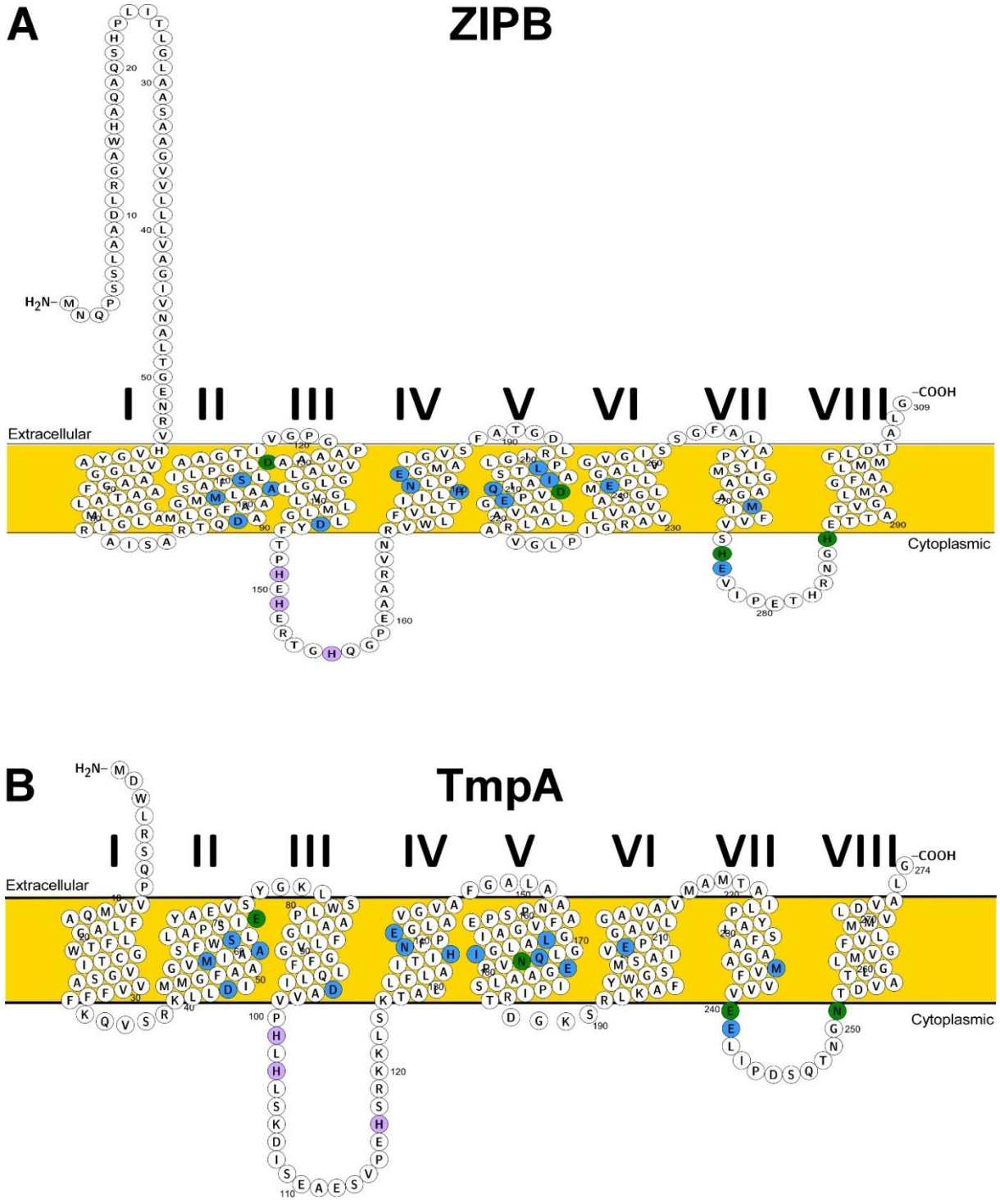

Figure 6.1 Diagram of ZIP proteins from *B. bronchiseptica* and *S. sanguinis*
ZIP proteins ZIPB from *B. bronchiseptica* (A) and TmpA (SSA_1413) from *S. sanguinis* (B) depicted in a cell membrane using Protter (394). Transmembrane domains of TmpA were predicted based on alignment to the crystal structure of ZIPB. Amino acids in blue are conserved putative metal binding residues based on the crystal structure of ZIPB bound to Zn (382). Those in green are metal binding residues that are not conserved between ZIPB and TmpA. Lavender residues are histidines thought to contribute to metal transport.

Growth of ΔSSA_1413 strains in aerobic conditions

To determine the function of SSA_1413, the knockout strain from the *S. sanguinis* SK36 mutant library (85) was utilized. The Kan resistance cassette and flanking region from the SSX_1413 strain was amplified and transformed into a Tet resistant Δ*ssaACB* triple mutant, creating a Δ*ssaACB* ΔSSA_1413 quadruple mutant. Initial attempts to introduce the mutation into the Δ*ssaACB* background were unsuccessful (data not shown). This was not due to lack of genetic competence, as we have previously generated mutants in this strain (120, 202). Additionally, this same construct was used to generate the ΔSSA_1413 mutant in SK36. Transformants in the Δ*ssaACB* background were only obtained when the BHI agar plates were supplemented with 10 μM $MnSO_4$. While the single mutant grew similarly to WT in brain heart infusion (BHI) broth, the quadruple mutant required anaerobic conditions or 10 μM $MnSO_4$ supplementation in microaerobic (1% O_2) conditions to grow to WT levels overnight (data not shown).

Because of these results and others described below, we concluded that SSA_1413 was a metal transporter, which we have named TmpA for transport of metal protein A. We chose this name to avoid species- and metal-specific nomenclature.

Serum growth studies were developed as an *in vitro* model of IE as serum is similar to conditions in the heart valve and contains nanomolar concentrations of Mn (395). The oxygen concentration of arterial blood is 12% (158) and at this concentration, growth of WT, Δ*ssaB*, and Δ*sodA* mutant strains was determined to be analogous to that observed in our rabbit model of IE, which entails infection of the aortic valve (130). At this O_2 concentration, deletion of *tmpA* from the WT or Δ*ssaACB* backgrounds did not significantly affect growth relative to the respective parent strains; however, the Δ*ssaACB*

mutant exhibited so little growth that there seemed little possibility of detecting worse growth by the quadruple mutant. When the O_2 concentration was reduced to 6% or 1%, growth of the quadruple mutant was significantly less than that of the Δ*ssaACB* parent strain. In contrast, growth of the single mutant was not statistically different from WT under any of the tested O_2 concentrations (Figure 6.2). Additional studies in BHI showed that the Δ*tmpA* mutant grew indistinguishably from WT in all tested oxygen concentrations, whereas the quadruple mutant grew significantly less than its Δ*ssaACB* parent in 6% and 12% O_2. These results indicate that TmpA contributes to aerobic growth in the Δ*ssaACB* background.

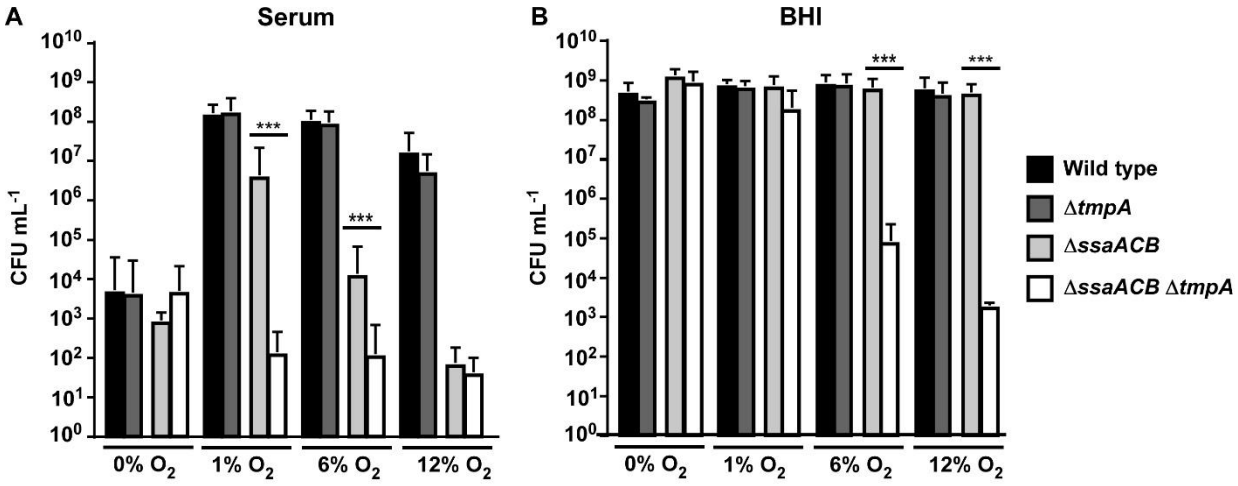

Figure 6.2 Growth of Δ*tmpA* mutants in various oxygen concentrations
Rabbit serum (A) or BHI (B) was pre-incubated at the given O_2 concentration. Overnight cultures were used to inoculate the media and growth was assessed after 24 h by plating on BHI agar. Mean and SD of at least three independent experiments is displayed and significance was determined by one-way ANOVA with a Tukey multiple comparisons test for each oxygen concentration. ***$P \leq 0.001$. Only significant differences between Δ*tmpA* mutants and their respective parent strains are displayed.

Complementation of the Δ*ssaACB* Δ*tmpA* mutant by addition of metals

Although the creation of the Δ*ssaACB* Δ*tmpA* mutant was facilitated by the addition of Mn to the media, we next wanted to test the effect of addition of Mn and other divalent cations on growth of the mutant strains in serum. The addition of 5 µM Mn fully restored growth

of the Δ*ssaACB* mutant in 12% O_2 rabbit serum whereas 50 µM Mn was required for equivalent growth of the quadruple mutant (Figure 6.3). SsaB was also found to transport Fe (130). We found that the growth of the Δ*ssaACB* mutant could be maximized by the addition of 100 µM $FeSO_4$ (Figure 6.3). The quadruple mutant did not reach the same level by addition of any tested concentration of Fe (Figure 6.3). We also attempted to rescue the growth of the Δ*ssaACB* Δ*tmpA* mutant with ferrous ammonium sulfate and various ferric compounds, but saw no difference in growth (data not shown). Neither strain showed improved growth after the addition of $ZnSO_4$ (Figure 6.3), despite the fact that ZIP family proteins primarily transport Zn or Fe. Similarly, 24 h growth of the quadruple mutant on Todd-Hewitt + Yeast Extract (THY) plates required exogenous Mn; neither Fe nor Zn had any effect (Figure 6.4).

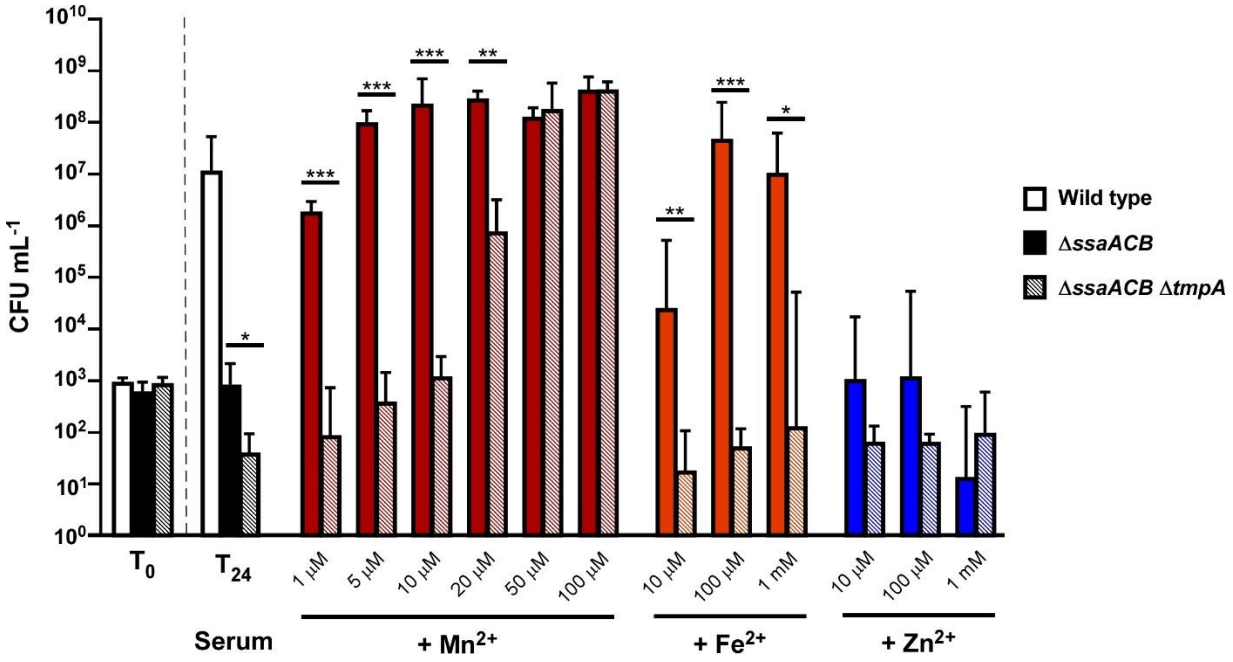

Figure 6.3 Serum growth with various metals at 12% O_2
Overnight cultures were inoculated into 12% O_2 rabbit serum containing Mn (A), Fe (B), or Zn (C). Growth was assessed after 24 h by plating on BHI agar. Means and SD of at least three independent experiments is displayed. **P* ≤ 0.05, ***P* ≤ 0.01, ****P* ≤ 0.001, indicate statistically significant differences between the Δ*ssaACB* and Δ*ssaACB* Δ*tmpA* mutants under the same experimental conditions using two-tailed t-test. Wild type growth is shown for reference.

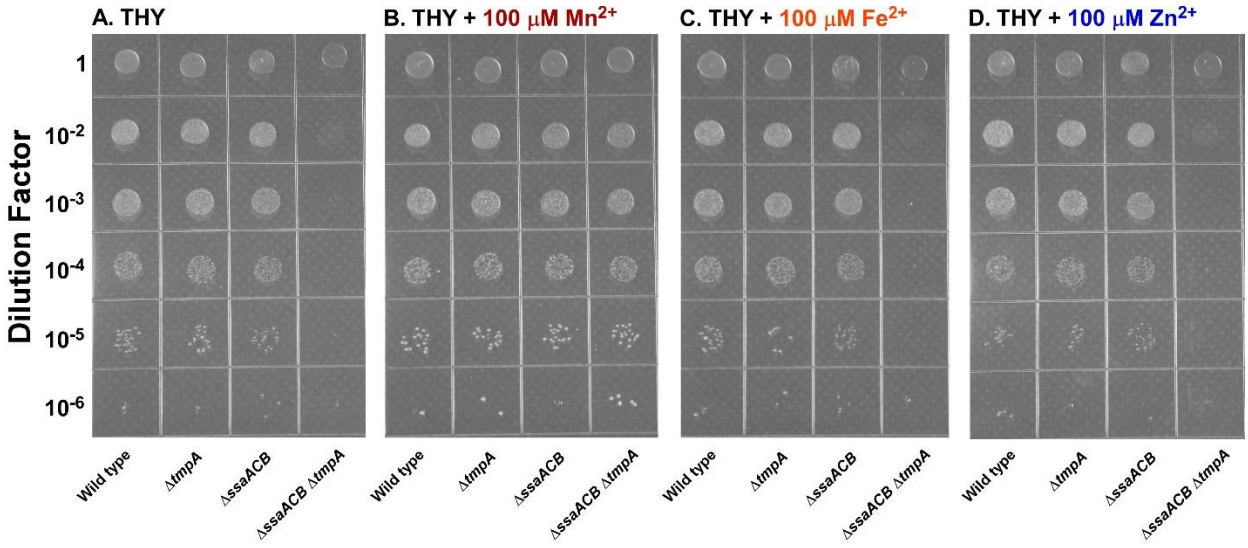

Figure 6.4 Growth of WT, Δ*ssaACB*, and Δ*tmpA* strains on THY plates
Overnight pre-cultures were diluted to noted concentrations and spotted on THY plates (A) + 100 μM $MnSO_4$ (B), $FeSO_4$ (C), or $ZnSO_4$ (D). The plates were incubated anaerobically for 24 h and imaged.

Complementation of the Δ*ssaACB* Δ*tmpA* mutant with inducible expression of *tmpA*

To confirm that the lack of TmpA is responsible for the poor growth phenotype of the quadruple mutant, *tmpA* was placed under the control of the *lac* promoter (Phyper-spank) at an ectopic expression site (176). When gene expression was induced by addition of 1 mM Isopropyl-β-D-thiogalactoside (IPTG), the complemented quadruple mutant grew indistinguishably from WT, surpassing the growth of both the Δ*ssaACB* and the Δ*ssaACB* Δ*tmpA* strains (Figure 6.5). This result indicates that overexpression of *tmpA* leads to an increase in growth. The addition of 10 μM Mn but no IPTG to the complemented strain also improved growth to WT levels. Presumably this is due to leakiness of the Phyper-spank promoter, leading to some expression of *tmpA* even without IPTG present. We have observed this previously with the same inducible promoter and expression site (101). These results support the hypothesis that TmpA is a Mn transport protein.

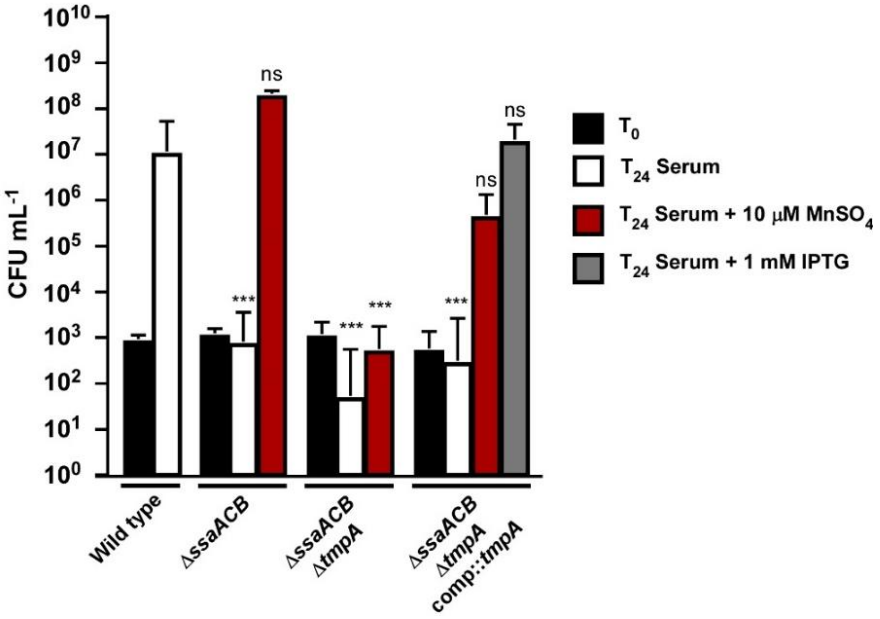

Figure 6.5 Serum growth of the complemented Δ*ssaACB* Δ*tmpA* mutant at 12% O_2
Cultures were grown in 12% O_2 serum for 24 h with 10 μM Mn or 1 mM IPTG added as shown. Means and SD of at least three independent experiments are displayed. Significance was determined by a one-way ANOVA with a Tukey multiple comparisons test for T_0 and T_{24} values separately; only comparisons to SK36 at T_{24} are displayed. ****P* ≤ 0.001

Assessment of cellular metal content of Δ*tmpA* mutant strains

To assess the cell-associated metal content of each strain, cells were grown overnight in 1% O_2, then diluted into BHI containing 10 μM Mn, Fe, or Zn. While serum would have been the preferred medium, the growth of the Δ*ssaACB* Δ*tmpA* mutant was insufficient for ICP-OES (data not shown). The BHI was pre-incubated either aerobically (~21% O_2) or anaerobically. The cultures were grown to mid-log phase, collected, washed, digested, and analyzed by ICP-OES. There was no significant difference between either Δ*tmpA* mutant and its respective parent strain in plain BHI for any metal tested (Figure 6.6). With excess Mn added to the BHI, the quadruple mutant imported significantly less Mn than the Δ*ssaACB* parent strain in both aerobic and anaerobic conditions (Figure 6.6A & D). This trend was not observed for excess Fe or Zn (Figure 6.6B-C, E-F), although the

standard deviation for the aerobic BHI with added Fe samples was considerable. This is possibly due to inherent variability of Fe oxidation states in oxidative environments.

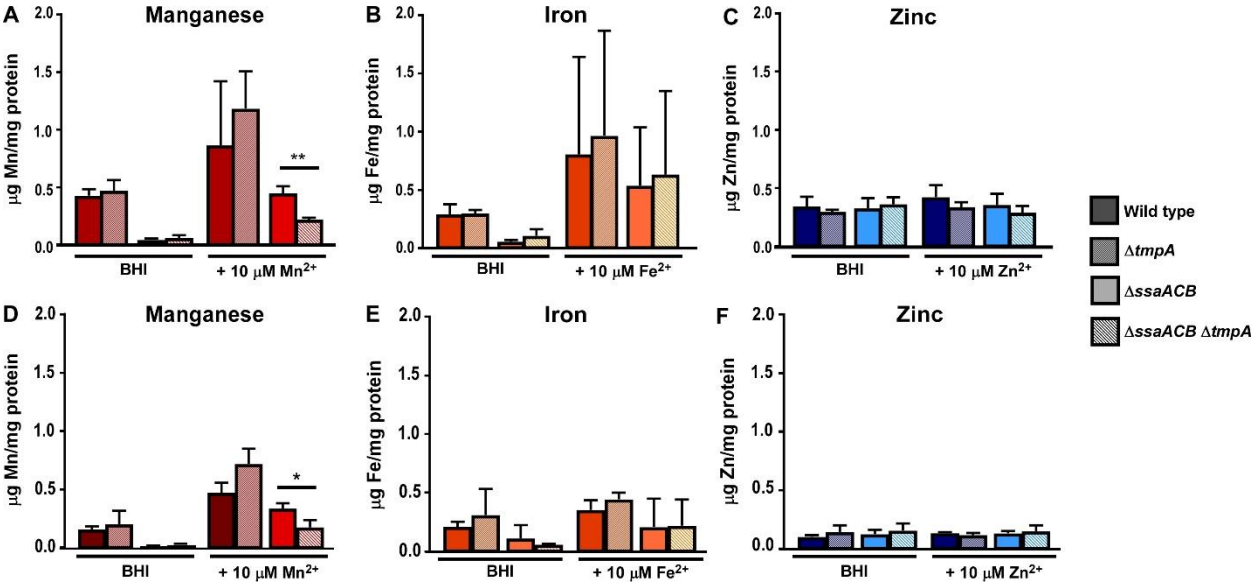

Figure 6.6 Metal content of Δ*tmpA* mutant cells in BHI
Cells were grown to mid-log phase in BHI +/- 10 μM Mn (A & D), Fe (B & E), or Zn (C & F). Cells were incubated in either aerobic (A-C) or anaerobic conditions (D-F). Metal concentration was measured by ICP-OES and normalized to protein concentration. Means and SD of at least three independent experiments are displayed. ***P* ≤ 0.05, ***P* ≤ 0.01, indicates statistically different from parent strain under the same experimental conditions using a two-tailed t-test.

Since the Mn-dependent phenotype of *tmpA* was only observed in the Δ*ssaACB* background, this left the possibility that a Zn-transport phenotype was masked by the presence of high-affinity Zn transporters. To assess this possibility, we assessed a knockout mutant of the Zn ABC transporter, AdcCBA (137). We attempted to knock out all three genes in the *adcCBA* operon with a single antibiotic resistance gene but were unsuccessful in obtaining transformants (data not shown), indicating that this operon may be required for growth. Thus, we utilized previously generated Δ*adcB* and Δ*adcC* mutants (85). Since these mutants grew identically in low-Zn conditions, we chose to use the Δ*adcC* ATP binding protein mutant for further investigation. As expected, this mutant exhibited poor growth in the presence of the metal chelator TPEN (N,N,N′,N′-tetrakis(2-

pyridinylmethyl)-1,2-ethanediamine) when grown in Chelex-treated BHI (cBHI) supplemented with 1 mM $MgSO_4$ and 1 mM $CaCl_2$ (Figure 6.7A). The growth defect was rescued by the addition of Zn but not Mn (Figure 6.7A). An Δ*adcC* Δ*tmpA* strain was then created to assess whether TmpA may also transport Zn in addition to Mn. Growth of the Δ*adcC* Δ*tmpA* strain was not statistically different from the Δ*adcC* strain in Zn-deplete conditions (Figure 6.7B).

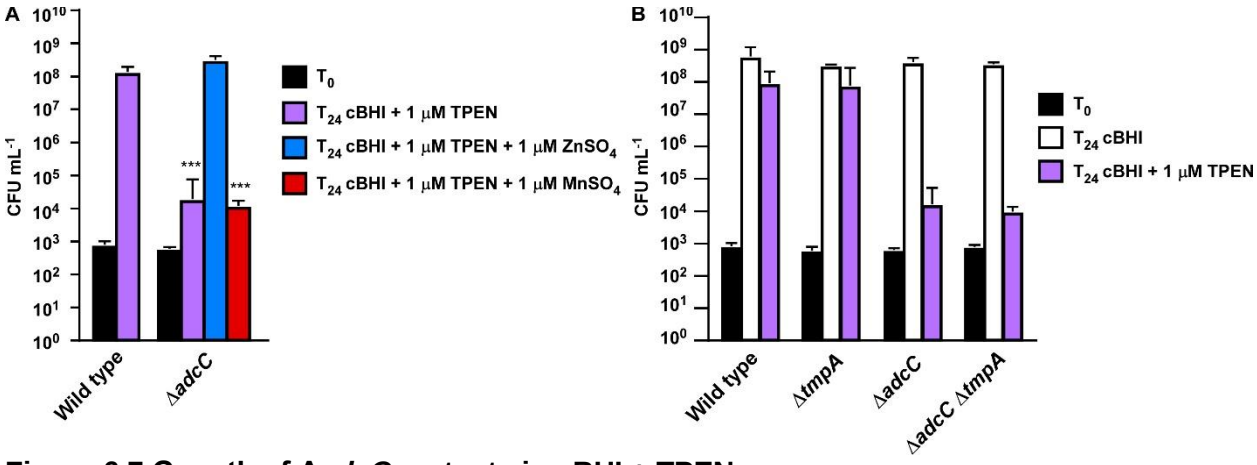

Figure 6.7 Growth of Δ*adcC* mutants in cBHI + TPEN
Growth in cBHI at 1% O_2 after 24 h was assessed by plating. (A) The effect of 1 μM TPEN on the Δ*adcC* mutant was assessed by the addition of 1 μM of either Zn^{2+} or Mn^{2+}. (B) The growth of the respective Δ*tmpA* strains in cBHI ± 1 μM TPEN was measured. The means and SD of at least 3 biological replicates are shown. Statistical significance was assessed by one way ANOVA with a Tukey multiple comparisons tests. In (A), only significant differences of T_{24} samples compared to WT are displayed. ****P* ≤ 0.001. In (B), no strain was significantly different from its parent grown in the same conditions at T_{24}. No T_0 values within a chart were significantly different from each other.

We then measured the cellular metal content of these mutant strains in aerobic cBHI (Figure 6.8). There was no significant difference in Zn levels between either Δ*tmpA* mutant and its respective parent, although the slight decrease in levels between the Δ*adcC* Δ*tmpA* strain and its parent indicates that there may be an untested condition where TmpA contributes to Zn transport.

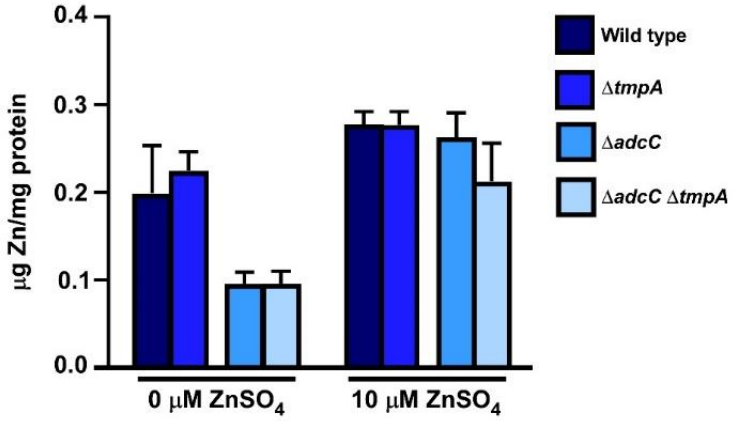

Figure 6.8 Metal content of Δ*adcC* mutants in cBHI
Cellular metal content of each strain was assessed after growth in cBHI using ICP-OES and normalized to protein levels. Means and SD of three experiments are displayed. Significance was measured by t-test for each mutant and respective parent for each condition. No comparisons were significantly different.

Evaluation of FDA-approved drugs for inhibitory action against TmpA function

Due to the potent effect that the loss of BmtA had on the growth and virulence of *B. burgdorferi*, it was established as a putative drug target (353). Wagh et al. (355) screened libraries of FDA-approved compounds against a model of BmtA and found the drugs desloratidine and yohimbine may be effective in binding to BmtA and inhibiting protein function. Desloratidine successfully reduced viability and cellular Mn content of *B. burgdorferi in vitro* but has not been approved to treat Lyme disease, despite online publicity due to the fact that desloratidine is the active agent of the allergy drug Clarinex®. We tested the effect of these drugs on the growth of WT and Δ*ssaACB* mutants and found that yohimbine was effective at reducing the growth of *S. sanguinis* at doses of 0.75 and 1 mM (Figure 6.9A & B). There was a differential effect of yohimbine between Δ*ssaACB* and WT, indicating that this drug may in fact affect the function of TmpA. Further support for this hypothesis is shown in Figure 6.9C, where the poor growth phenotype of Δ*ssaACB* in the presence of yohimbine was rescued by excess Mn. It does not appear to be an ideal drug though, as it requires a high dosage and may have some off-target effects, as

seen in the drastic reduction in growth of the WT strain. Thus, we will need to investigate other options. We then tested desloratidine but we found that it was toxic to WT cells, as was the vehicle, cyclodextrin (data not shown). We also tested loratidine (Claritin®) and saw no effect on any strain (data not shown).

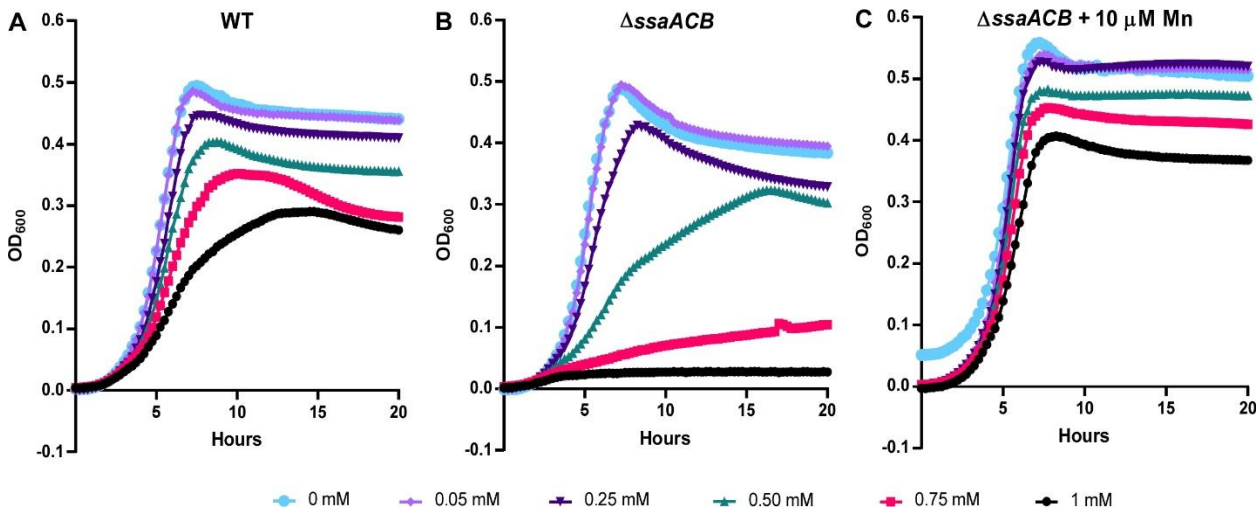

Figure 6.9 Effect of yohimbine on the growth of *S. sanguinis*
WT (A) and Δ*ssaACB* (B & C) *S. sanguinis* cells were grown at atmospheric oxygen concentrations in BHI in a 96-well plate maintained at 37°C with indicated concentrations of yohimbine. Mn (10 µM) was added in (C). The optical density at 600 nm was measured every 15 min. Means of two biological replicates with two technical replicates each are displayed for each time point.

Fermentor growth of the Δ*ssaACB* Δ*tmpA* mutant

Initial studies attempting to determine Mn-deplete conditions for transcriptomics and metabolomics analysis led us to test the growth of the Δ*ssaACB* Δ*tmpA* mutant in aerobic fermentor conditions (Figure 6.10). We determined that this mutant would not grow well in plain BHI under these conditions (data not shown), thus we added 500 µM Mn (final concentration) to the vessel prior to inoculation. We then allowed the cells to grow to the maximum possible OD in the vessel before turning on the media pumps, allowing plain BHI to flow and dilute out the excess Mn. The OD began to decrease ~2 h after the pumps

were turned on and ~240 µM Mn remained in the BHI. While we ultimately decided against using these conditions for further analyses, these results further support the role of Δ*tmpA* as a secondary Mn transporter and highlight the importance of Mn in aerobic growth.

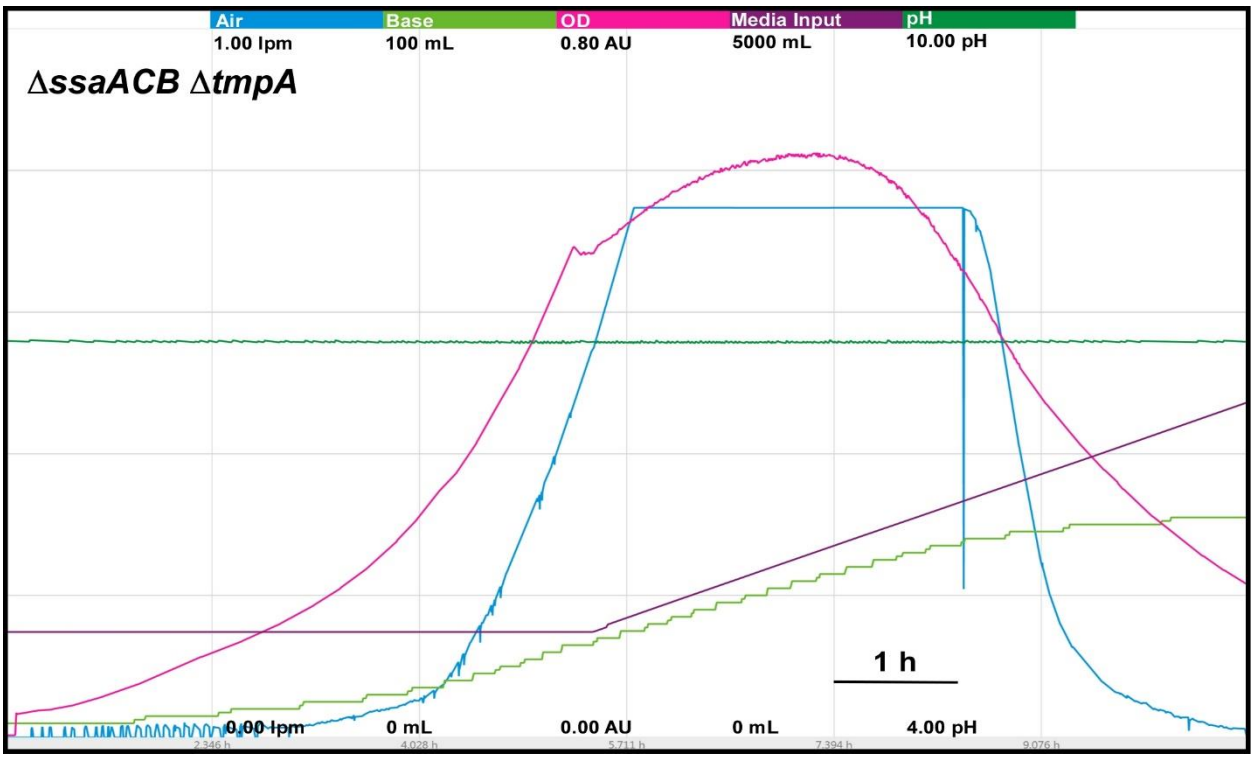

Figure 6.10 Aerobic fermentor growth of the Δ*ssaACB* Δ*tmpA* mutant
Chart of Δ*ssaACB* Δ*tmpA* mutant aerobic fermentor growth. Each color represents a different parameter: cyan - air flow (liters per min; lpm), pink - optical density (840-910 nm; absorbance units; AU), dark green - pH, light green - base input (KOH), purple - media input (total volume). Each color represents a different parameter as labeled at the top of the figure. The scale for each parameter is indicated by the values under each respective parameter label (minimum at the bottom, maximum at the top). The time scale is indicated by the bar in the bottom right portion of each chart. Mn (500 µM total concentration) was added to the vessel but not the carboy. The DO control was set to 5% pO_2 with a maximum air flow of 1.5 lpm.

Contribution of TmpA to virulence in a rabbit model of infective endocarditis

To determine if TmpA is relevant to virulence, we employed a rabbit model in which a catheter was inserted past the aortic valve to induce minor damage (176) and formation of sterile vegetations composed principally of platelets and fibrin (33). Bacterial strains were then introduced into the bloodstream by co-inoculation into a peripheral ear vein.

Infected vegetations were recovered the following day from euthanized animals and the attached bacteria were enumerated by dilution plating on selective antibiotics (176).

Recovery of the single Δ*tmpA* mutant was not significantly different from WT and both had significantly higher recovery than the Δ*ssaACB* strain, which was only recovered in one of six rabbits (Figure 6.11A). We next wanted to assess the contribution of *tmpA* to virulence in a Δ*ssaACB* background; however, the exceedingly low recovery of the Δ*ssaACB* mutant made it unlikely that a further reduction in virulence would be detectable under these conditions. Therefore, the WT inoculum level was decreased two-fold and the Δ*ssaACB* and Δ*ssaACB* Δ*tmpA* mutants were inoculated at levels that were 20-fold higher than WT. The Δ*ssaACB* strain was recovered from all six rabbits but at a significantly lower level than WT (Figure 6.11B). The recovery of the Δ*ssaACB* Δ*tmpA* mutant was significantly lower than the Δ*ssaACB* mutant. These results indicate that in a WT background, TmpA is not required for virulence in our model, likely because SsaACB can import Mn efficiently from the low levels found in blood. However, loss of TmpA in the Δ*ssaACB* background resulted in further decrease in virulence, indicating that it may be playing a secondary role in Mn uptake that is only evident when the primary Mn transporter is absent.

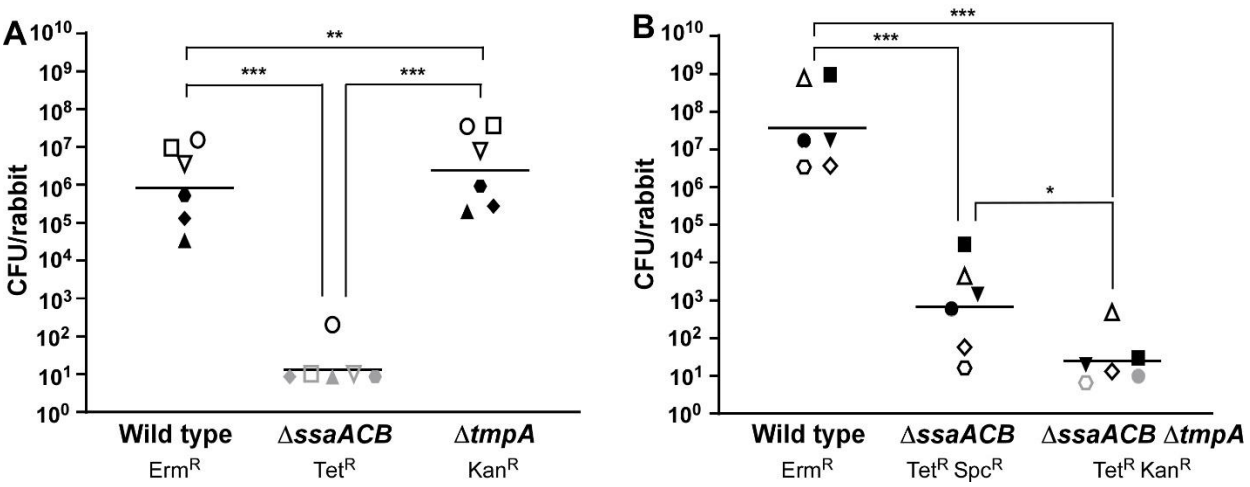

Figure 6.11 Virulence of Δ*tmpA* mutants in a rabbit model of IE
Rabbits were co-inoculated with the marked WT strain, the Δ*ssaACB* mutant strain, and either the Δ*tmpA* (A) or the Δ*ssaACB* Δ*tmpA* mutant strain (B). Each symbol indicates one rabbit, with females and males represented by open and closed symbols, respectively. n = 6 over two independent experiments. Gray symbols indicate recovery was below the limit of detection. Horizontal lines indicate geometric means. **P* ≤ 0.05, ***P* ≤ 0.01, ****P* ≤ 0.001 indicate significantly different from other strains using repeated measures ANOVA with a Tukey multiple comparisons test.

Expression of the *tmpA* gene under various metal and oxygen concentrations

We next wanted to determine the regulation of *tmpA* gene expression. Bacterial metal transport proteins are often controlled by metal-dependent regulators, such as MntR and Fur (134, 265). Additionally, regulators often sense or bind to the metal that are transported by the gene products they are regulating. To determine potential regulation mechanisms for *tmpA* expression, transcript levels were measured under various conditions. In Figure 6.12, WT and Δ*ssaACB* cells were grown in aerobic BHI and then incubated with either 100 µM Mn, Fe, Zn or EDTA. An additional sample without additives was used as the control. EDTA is a metal chelator which was chosen to represent metal-deplete conditions. While EDTA is not specific for any metal, it has a relatively high affinity for Mn ($\log_{\beta 1}$ of 14.1 and 24.8 for Mn^{2+} and Mn^{3+}, respectively, as compared to 16.7 for Zn^{2+} and 8.7 for Mg^{2+}) (182). When added to WT or Δ*ssaACB* cultures growing in a

fermentor, ICP-OES analysis revealed that its primary effect on cellular metal levels was to reduce the concentration of Mn (Figure 3.4) (202). Unexpectedly, expression of *tmpA* was not significantly affected by the addition of any tested metal nor by the depletion of Mn by EDTA (Figure 6.12A).

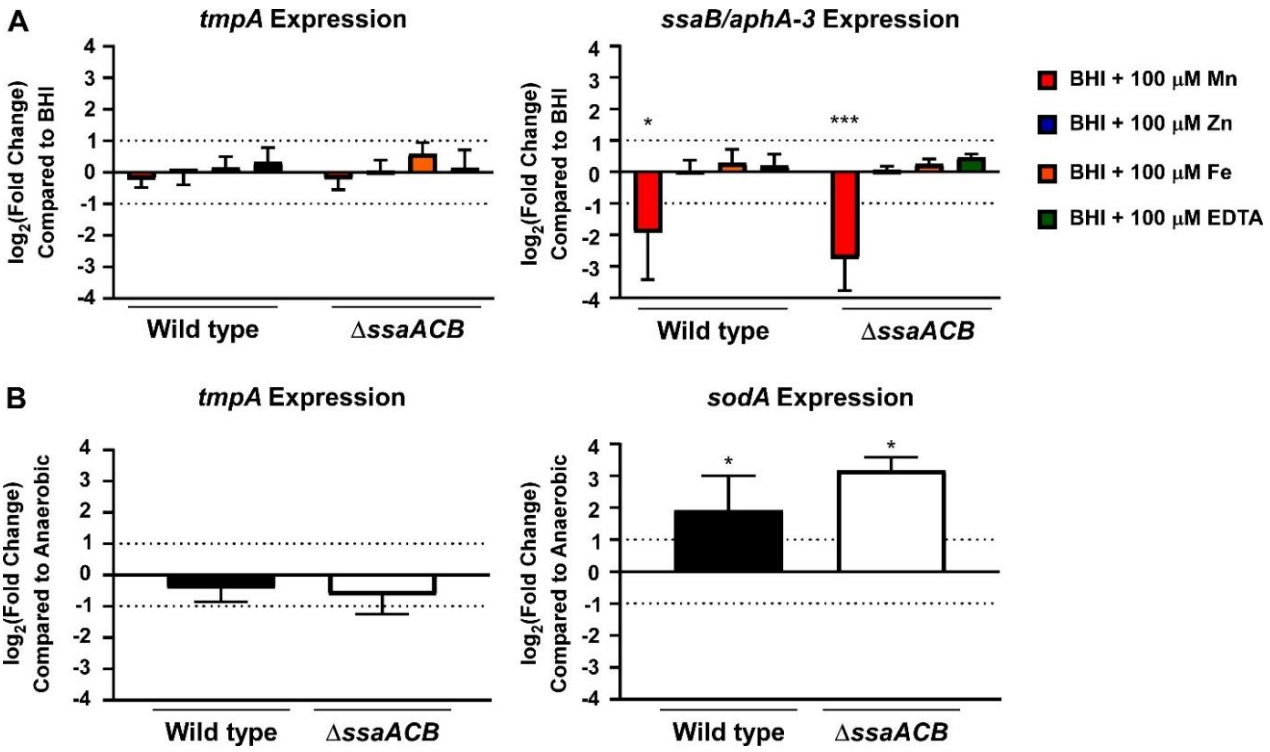

Figure 6.12 Transcriptional expression of *tmpA* in BHI
Relative transcript levels of cells grown in the presence of 100 μM metals or EDTA as compared to BHI alone (A) or cells grown for 30 min aerobically after 2.5 hr anaerobic incubation (B). The mean $\log_2$(fold change) of three independent experiments are displayed ± SD. Significant differences between the ΔCt values for the experimental condition compared to the control condition within the same strain were determined by two-tailed t test. Only conditions with $|\log_2(\text{fold change})| > 1$ were tested for significance. *$P \leq 0.05$, ***$P \leq 0.001$

The MntR ortholog in *S. sanguinis*, SsaR, has been shown to negatively regulate the expression of *ssaB* in the presence of excess Mn (130). The *ssaB* and *aphA-3* (Kan resistance gene replacing *ssaACB*) genes were included as positive controls for Mn-dependent regulation by SsaR (130). As expected, *ssaB* and *aphA-3* expression

significantly decreased in the presence of excess Mn, whereas *tmpA* expression was unchanged (Figure 6.12), indicating that expression is not regulated by Mn concentration. We then assessed whether expression of *tmpA* was affected by O_2 concentrations by measuring transcript levels before and after exposure to oxygen. Expression of *tmpA* did not change significantly from anaerobic to aerobic conditions (Figure 6.12B). The expression of *sodA* significantly increased after oxygen exposure, as expected (130). Preliminary experiments examining expression at pH 6.4 compared to pH 7.4 also did not indicate any changes in *tmpA* expression (data not shown). Thus, we were unable to find a condition that leads to differential expression of *tmpA*.

Expression of TmpA protein in *S. sanguinis*

In order to determine protein levels of TmpA in *S. sanguinis*, we attempted to tag TmpA with three different tags: FLAG-Tag, Strep-Tag® II, and 6X His Tag. The FLAG-Tag resulted in cross-reactivity to unknown *S. sanguinis* proteins, and thus was abandoned (data not shown). The Strep-Tag® II had some cross-reactivity but much less than that of FLAG-Tag, and thus was chosen for further characterization. The small size of the Strep-Tag® II, its non-reactiveness to metals, and the commercial availability of affinity columns made it an ideal candidate. The Strep-Tag® II was tested in multiple locations in the protein: N-terminus, Loop 3, C-terminus, and C-terminus preceded by a GSSGSSG linker. In addition, the Loop 3 version was placed under control of the Phyper-spank promoter in an ectopic site (176) in order to attempt overexpression. We also attempted membrane fractionation and Strep-Tactin® column purification in order to enrich the samples. None of these tags or treatments produced consistent results by western blot. We occasionally saw very faint bands that were either much smaller than TmpA (expected

~29 kDa) or much larger (Figure 6.13A & B). None of these bands were reproducible nor visible by SDS-PAGE staining (data not shown). Dot blots were more reproducible and usually showed increased signal in the Strep-Tag® II TmpA strains as compared to WT SK36 (Figure 6.13C) but they do not confirm the size of the protein. We were able to visualize the twin-Strep-Tag® II ComA positive control, an integral protein with 6 TMDs in *S. pneumoniae* (396), which indicates that the antibody was functional (data not shown). We also attempted to add a Strep-Tag® II to another integral membrane protein in *S. sanguinis*, SsaC, and were unable to successfully visualize this protein either (data not shown).

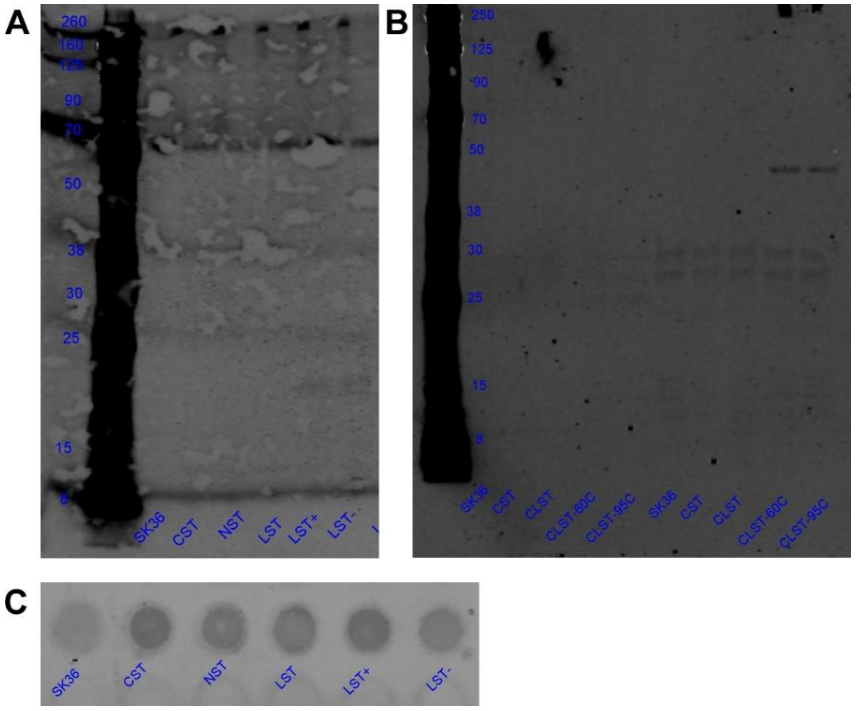

Figure 6.13 Example protein blots of Strep-Tag® II TmpA strains
Various Strep-Tag® II TmpA strains were assessed for protein expression by western (A & B) or dot blot (C). SK36: WT (no tag), CST: C-terminal tag, NST: N-terminal tag, LST: native loop tag, LST+/-: inducible loop tag ± IPTG, CLST: C-terminal tag with linker. Due to poor resolution of bands, ladder is not visible and thus depicted by values (in kDa) on left in (A-B). (A) PVDF membrane; protoplast samples from 50 mL culture (B) 0.45 µM nitrocellulose membrane; 65°C and 90°C indicate temperature cell fractions were heated to prior to loading; left: “protoplast” fraction; right: “supernatant” fraction of membrane fractionation. (C) PVDF membrane, same samples as in (A).

We believe that the protein is still being expressed and is likely not degraded in these tagged proteins, as aerobic serum growth of most of these strains was rescued by the addition of 5 µM $MnSO_4$ (Figure 6.14). The same is true for the Strep-Tag® II SsaC protein, as preliminary data showed that this strain grew to WT levels in 12% O_2 serum, unlike Δ*ssaACB* (data not shown). The one poorly functioning protein was the N-terminally tagged version of TmpA (Figure 6.14), which indicates that the N-terminus is important for function or for ensuring that the protein successfully imbeds in the membrane. The tag in this location may be interfering with a signal sequence, although eukaryotic ZIP proteins lack this sequence (*communication with D. Eide*) and the predicted signal sequence using Signal P (397) was after W21, which lies within TMD I. These results indicate that the tagged proteins are likely still expressed and functional but undetectable by western blot for an unknown reason.

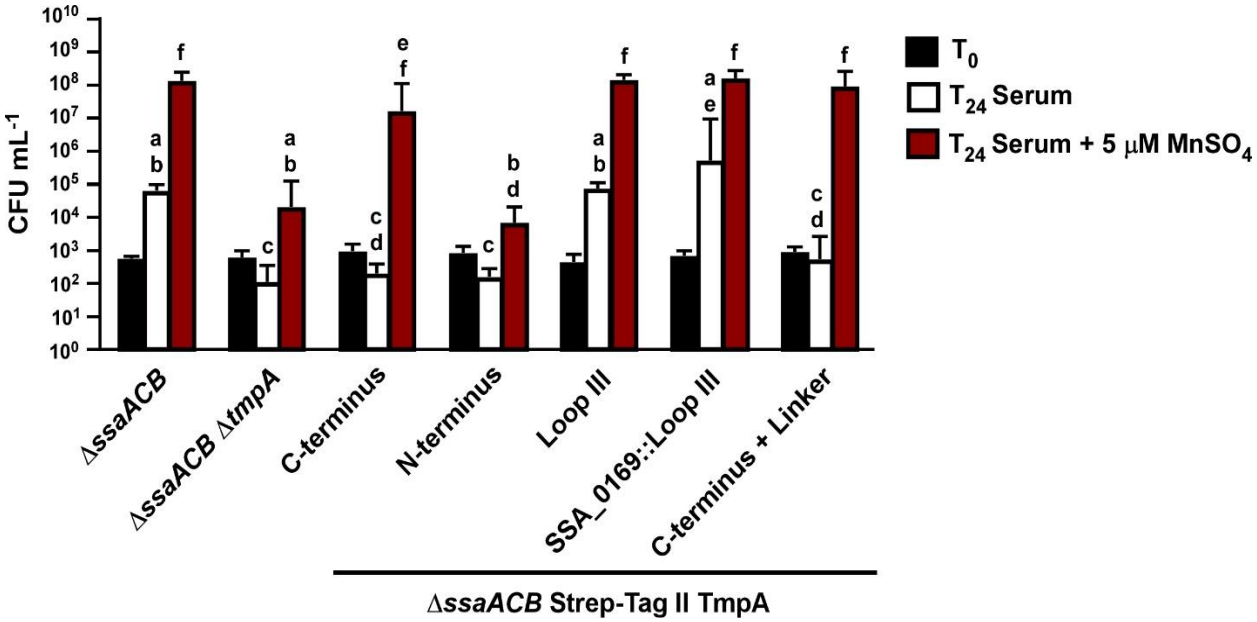

Figure 6.14 Serum growth of Strep-Tag® II TmpA mutants at 6% O_2 + Mn
Growth of various Strep-Tag® II TmpA strains in the Δ*ssaACB* background were assessed in 6% O_2 serum ± 5 µM $MnSO_4$. Means and SD of at least three independent experiments is shown. Significance was determined by one-way ANOVA for T_0 and T_{24} separately. No T_0 values were significantly different from each other. T_{24} values with the same letter are not significantly different from each other.

Heterologous expression of TmpA in *Saccharomyces cerevisiae*

Since we do not know the identity of all metal transport proteins in *S. sanguinis*, it is impossible to evaluate the contribution of TmpA without potential confounding factors. Thus, we established a collaboration with a renowned biometals researcher and pioneer in the ZIP family field, Dr. David Eide. Dr. Eide's lab has previously characterized many ZIP proteins and has a comprehensive set of *S. cerevisiae* metal transporter mutants. We had synthesized an *S. cerevisiae* codon-optimized *tmpA* gene and it was incorporated into a pFL38 yeast expression vector. An HA tag was also added to the protein in another version of the plasmid. In some experiments, plasmids containing *irt1* or *zrt1* genes encoding Fe- and Zn-selective ZIP transporters, respectively, were included as positive controls. The yeast were then grown in Limited Zinc Medium (LZM) with or without excess metals and assessed for growth.

All versions of the Mn transport mutant SLY8 (Δ*smf1*) and Fe transport mutant DEY1453 (Δ*fet3* Δ*fet4*) grew poorly without excess Mn and Fe, respectively (data not shown). When excess Mn or Fe was added, the growth increased but the empty vector (EV) strain grew significantly better than the pFL38-TmpA strain (Figure 6.15A & B). This was puzzling, considering the strong evidence we have discovered for Mn and Fe transport in *S. sanguinis*. From these data, it would suggest that either (*i*) functional TmpA is toxic to these strains, (*ii*) the orientation of TmpA in the yeast membrane is flipped in these strains, or (*iii*) TmpA is capable of acting as a metal exporter in these conditions. Although expression of TmpA itself is likely not toxic, its production may lead to dysregulation of expression of the remaining transporters in these strains, leading to the poor growth phenotypes observed in Figure 6.15.

The Zn transport mutant ZHY3 (Δ*zrt1* Δ*zrt2*) with EV grew poorly with 100 µM Zn but the TmpA version grew significantly better, although not as well as the Zrt1-expressing strain (Figure 6.15C). This difference in growth between the strains was abolished by the addition of 1 mM Zn (data not shown). This confirms that TmpA is likely capable of transporting Zn.

In nearly every strain and condition, the pFL38-TmpA-HA strain grew similarly to the EV version. This suggests that the addition of the HA tag inactivated the function of the TmpA protein, which complements what we discovered with the Strep-Tag® II in *S. sanguinis*.

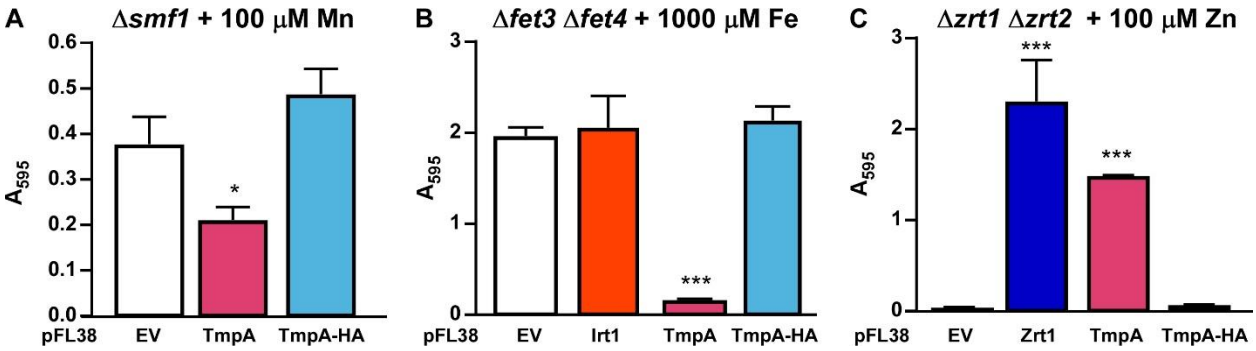

Figure 6.15 Heterologous TmpA expressing *S. cerevisiae* growth charts
S. cerevisiae mutant strains transformed with the pFL38 vector encoding TmpA, TmpA-HA, Irt1, Zrt1, or empty vector (EV) were grown in LZM for 18 (A), 43 (B), or 48 (C) h. Metals were added at the indicated concentrations. Bars indicate means ± SD of three replicates. Significance was assessed by one-way ANOVA with a Tukey multiple comparisons test; **P* ≤ 0.05, ****P* ≤ 0.001 as compared to EV.

We then evaluated the contribution of TmpA to metal uptake by measuring cellular metal content using ICP-OES on samples with metals added (Figure 6.16). In the Δ*smf1* Mn-transporter mutant, Mn levels were below the lowest standard and the pFL38-TmpA version had slightly lower levels (Figure 6.16A), which is the opposite of what we observed in *S. sanguinis*. Interestingly though, the other pFL38-TmpA strains had higher Mn levels than the corresponding EV version (Figure 6.16A), indicating that under conditions of metal imbalance, TmpA appears to be importing Mn in *S. cerevisiae*. Of course, this may

be confounded by the presence of other native Mn transporters but the fact that it is specific to the pFL38-TmpA strains is intriguing.

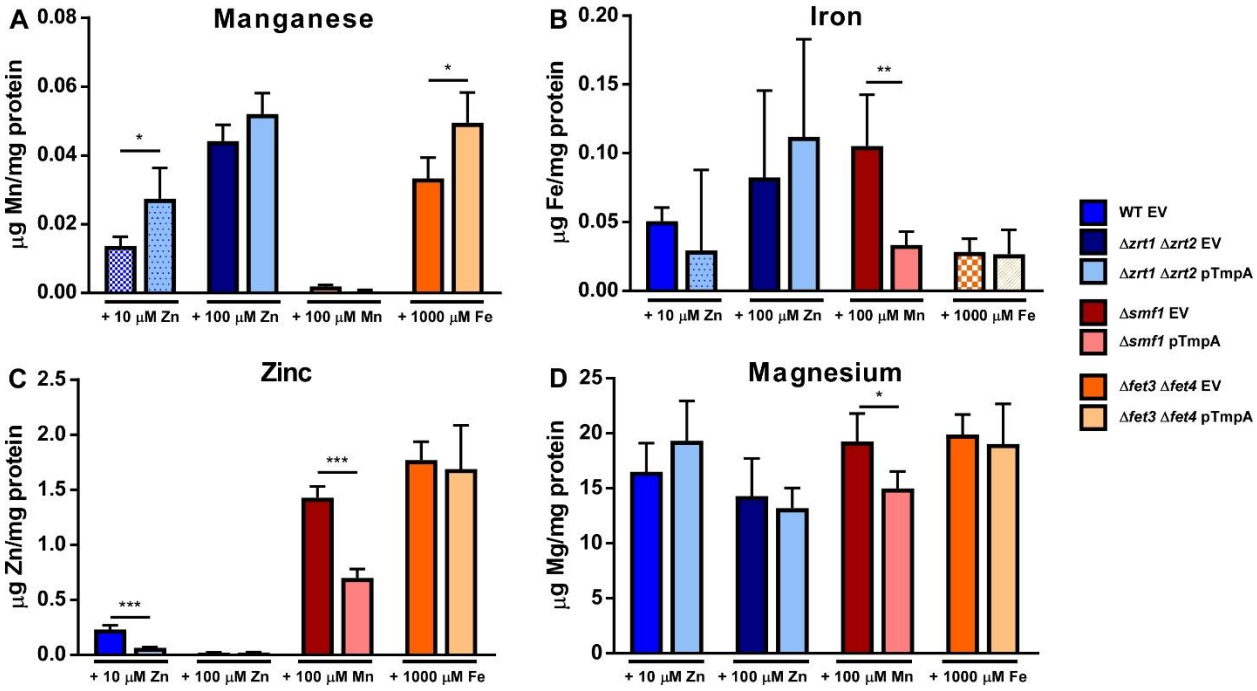

Figure 6.16 Metal content of *S. cerevisiae* cells expressing TmpA
S. cerevisiae cells were grown in LZM with the indicated metals added. Metal concentration was measured by ICP-OES and normalized to protein concentration. Means and SD of four independent experiments are displayed. *$P \leq 0.05$, **$P \leq 0.01$, *** $P \leq 0.001$ indicates statistically different from EV strain under the same experimental conditions using a two-tailed t-test. Patterned bars indicate levels are below the limit of detection.

Fe levels in the Δ*fet3* Δ*fet4* Fe-transporter mutant were below the level of detection and Fe levels in the other pFL38-TmpA strains were not significantly higher than their corresponding EV strains (Figure 6.16). The Δ*zrt1* Δ*zrt2* mutants with EV and pFL38-TmpA did not accumulate any detectable levels of Zn in this study, even with 100 µM Zn added. Zn levels significantly decreased in the Δ*smf1* pFL38-TmpA strain as compared to EV but no change was observed in the Δ*fet3* Δ*fet4* strains.

Mg levels only differed significantly in the Δ*smf1* strains. In fact, the Δ*smf1* pFL38-TmpA strain had significantly lower levels of all metals compared to EV, again suggesting that

the production of TmpA may affect the expression or function of multiple metal transport systems. These results may have been confounded by the fact that the Δ*smf1* EV strain grew much better than the pFL38-TmpA version (Figure 6.17) but that should be mitigated by protein normalization. Additionally, its poor growth in these conditions further suggest that the presence of TmpA in this strain could be toxic.

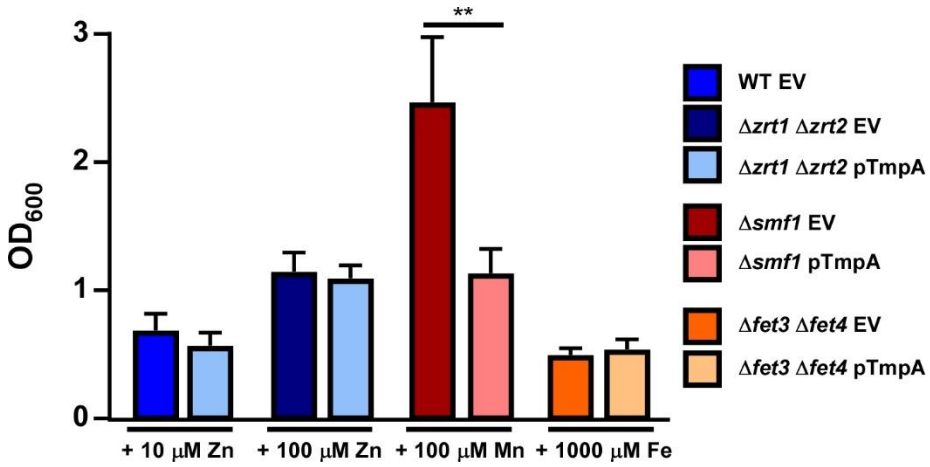

Figure 6.17 Growth of S. cerevisiae cells for metal analysis
The optical density of each culture from Figure 6.16 was measured before processing for ICP-OES. Means and SD of four independent experiments are displayed. ***P* ≤ 0.01 indicates statistically different from EV strain under the same experimental conditions using a two-tailed t-test.

Heterologous expression of TmpA in *E. coli*

Determination of the true affinity of TmpA for each metal requires *in vitro* metal uptake assays in liposomes. As our attempts to visualize the protein in *S. sanguinis* were unsuccessful, we attempted to overexpress the protein in *E. coli*. Using a codon-optimized sequence for the *tmpA* open reading frame incorporated into several expression vectors (pET20b, pET26, and pHIS2), we transformed three competent strains of *E. coli* that have been optimized for over-expression of heterologous proteins: BL21, CD41 (DE3), and CD43 (DE3). We attempted both IPTG-induction and auto-induction. Cells were fractionated by ultracentrifugation in some instances and the membrane fraction was

passed over a nickel-column. The predicted size of TmpA is 29 kDa. We observed large bands approximately 23, 32, and 70 kDa. We excised these three bands for mass spectrometry analysis. All three bands appear to contain sequence that matches TmpA, indicating that the protein may exist in multiple forms in *E. coli*. Expression was still too low to proceed with liposome experiments, which indicates that this protein may be toxic to *E. coli* or is being degraded by *E. coli* proteases. It is unlikely that it is toxic, as cells grew to high culture densities (data not shown). We also did not observe evidence to suggest that the proteins were shuttled into inclusion bodies (data not shown).

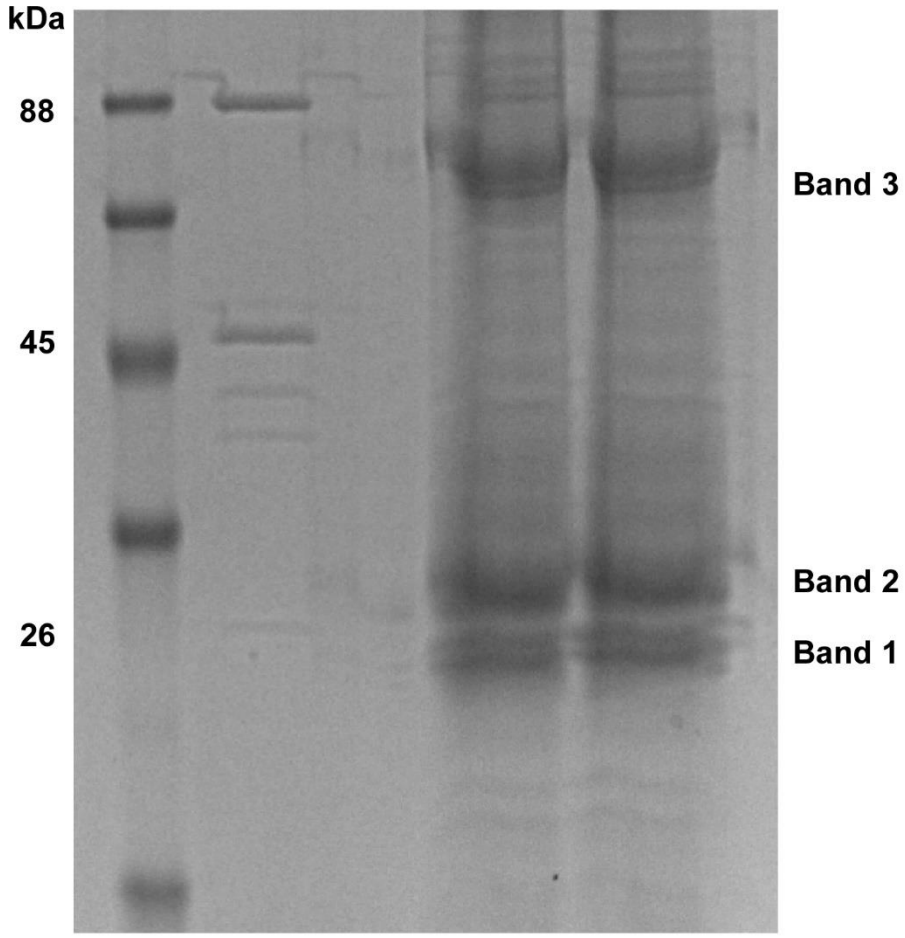

Figure 6.18 Nickel purified His-tagged TmpA in *E. coli*
SDS-PAGE of the Ni-purified membrane fraction of autoinduced CD41 (DE3) *E. coli* cells with TmpA expressed from a pET20b vector. Both lanes on the right are purified protein. The three bands indicated were excised and analyzed by mass spectrometry.

Contribution of specific residues to function of TmpA

Since other ZIP family proteins have been previously characterized for their metal transporting ability (353, 382, 385), we compared the amino acid sequence of TmpA to those of two metal-selective ZIP transporters: ZIPB (Zn) and BmtA (Mn) (Figure 6.19). From the alignment, we found four putative metal binding residues that were not conserved with ZIPB (382).

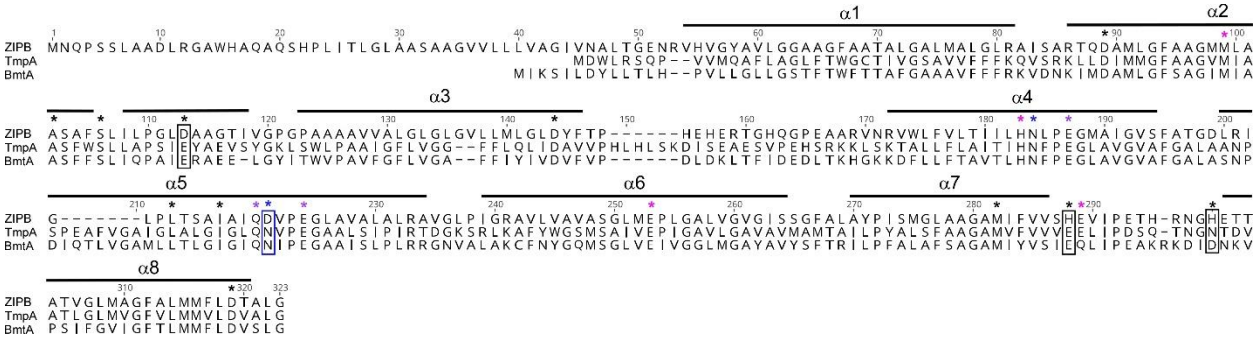

Figure 6.19 Alignment of ZIP family proteins
ZIP proteins from *B. bronchiseptica* (ZIPB), *S. sanguinis* (TmpA), and *B. burgdorferi* (BmtA) were aligned in Geneious. Predicted TMDs (α) are indicated by the horizontal lines. Asterisks indicate metal binding residues in ZIPB (382). Boxes indicate metal binding residues from ZIPB that are not conserved between ZIPB and the other proteins. Magenta, blue, and purple asterisks indicate that residue binds to the metal at the M1 site, the M2 site, or both sites, respectively.

Two of these residues were found to be within the center of the proteins, with one at M1 and the other at M2 (Figure 6.19) (382). The other two residues were found in the cytoplasmic loop between TMDs 7 and 8 (Figure 6.19). Because of the disordered nature of long loops, the main loop between TMDs 3 and 4 was not crystallized; thus, no metal-binding residues were identified in that region (382). For three of the four residues, the sequence of TmpA matched that of BmtA. We decided to mutate all four of these residues in TmpA to an alanine in order to determine the contribution of that side chain to the function of the protein (398). We also mutated these chosen residues to the corresponding residue from ZIPB to determine if this may contribute to metal specificity.

Since we could not determine a differential phenotype for the Δ*tmpA* mutant, we made these mutants solely in the Δ*ssaACB* background.

We then assessed the growth of these mutants in rabbit serum at 6% O_2 as compared to WT, the Δ*ssaACB* mutant, and the Δ*ssaACB* Δ*tmpA* mutant (Figure 6.20). All E67 and E240 mutants grew similarly to the Δ*ssaACB* parent strain, indicating that these residues are not essential for protein function. N251H also grew like the parent strain but N251A grew significantly worse, which confirms that this residue may be important for transport but that histidine is also capable of performing the same function. This was to be expected, as histidine is known to coordinate Mn (180) and the metal-binding residue at position 251 varied between TmpA and BmtA (Figure 6.19), indicating that as long as the residue is capable of coordinating with Mn, it would be functional. Both N173 mutants grew poorly, which may mean that this residue is critical for function. The fact that the N173D substitution did not allow for normal growth suggests that these residues may contribute to the metal selectivity of TmpA, BmtA, and ZIPB.

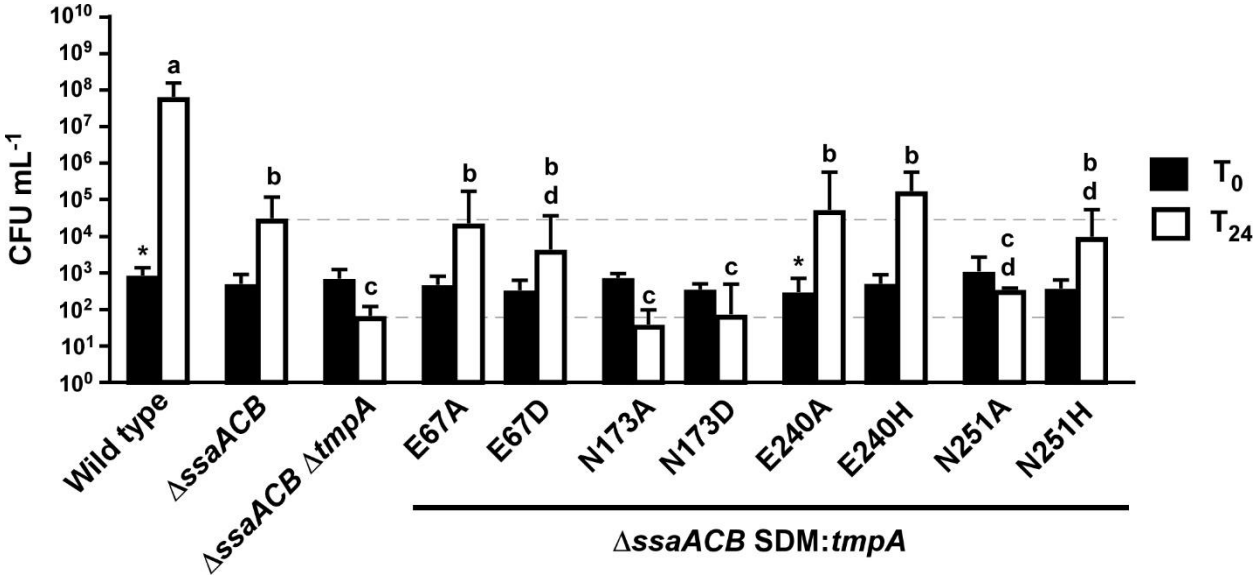

Figure 6.20 Aerobic serum growth of TmpA SDM mutants

Growth of single amino acid (site-directed mutagenesis; SDM) mutant versions of TmpA in the Δ*ssaACB* background were assessed at 6% O_2. Mean values ± SD of at least three independent experiments are shown. Significance was determined by one-way ANOVA for T_0 and T_{24} separately ($P \leq 0.05$). T_0 values with * are significantly different from each other ($P \leq 0.05$). T_{24} values with the same letter are not significantly different from each other.

Since we were unable to detect the TmpA protein by western blot, we were unable to confirm the presence of these modified proteins by this method. To determine whether the protein may still be present, we assessed the growth of these three mutants (N173A, N173D, and N251A) in serum at 6% O_2 ± 5 µM $MnSO_4$ (Figure 6.21). When Mn was added, the Δ*ssaACB* parent grew to WT levels, whereas the Δ*ssaACB* Δ*tmpA* mutant was still significantly lower than WT. Each of the mutants grew to a level that was in between the two, indicating that the protein likely was present and able to transport some Mn but was not fully functional. This further supports that these residues are important for Mn transport.

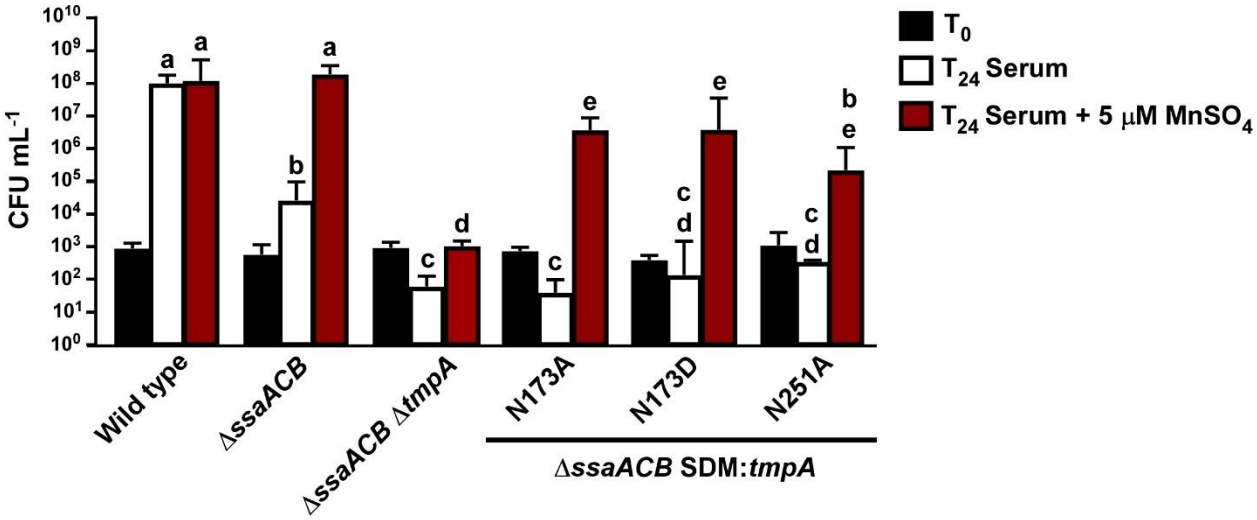

Figure 6.21 Aerobic serum growth of TmpA SDM mutants + Mn
Growth of select SDM mutant versions of TmpA in the Δ*ssaACB* background were assessed at 6% O_2 ± 5 µM $MnSO_4$. Means and SD of at least three independent experiments are shown. Significance was determined by one-way ANOVA for T_0 and T_{24} separately, with a Tukey multiple comparisons test when $P \leq 0.05$. No T_0 values were significantly different from each other. T_{24} values with the same letter are not significantly different from each other.

Model of TmpA and ZIPB mutant proteins

To better understand what may be occurring to cause this difference in metal transport capability, we modeled TmpA using the crystal structure of ZIPB as a template (Figure 6.22). The model matched relatively well (RMSD 1.738), although we were unable to model the N-terminus or loop between TMDs III and IV as they were not crystallized. Additionally, TMD III in TmpA was much shorter than that of ZIPB, and thus was depicted missing one of the helical loops in the model (Figure 6.22). The reason for this short TMD is unclear, as the length of all other TMDs appear to match well. It is possible that the loop between TMDs II and III never reaches the extracellular side or that the loop between TMDs III and IV is shorter (Figure 6.1), although the latter is unlikely due to the proposed contribution of the histidines in this loop to metal transport function (399). Another possibility is that there is a kink in the helix that allows it to span the entire membrane (400).

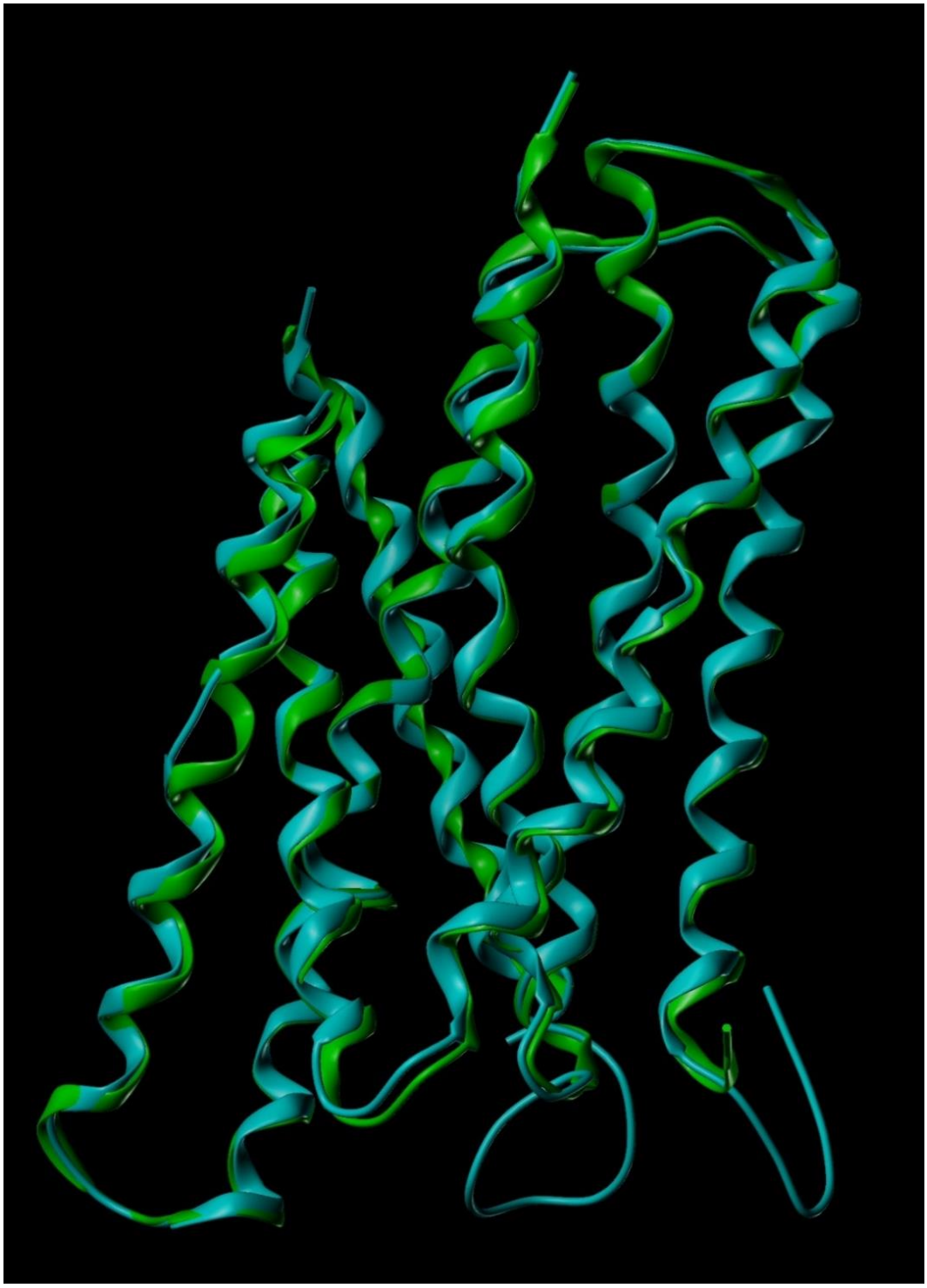

Figure 6.22 Model of TmpA based on ZIPB crystal structure
The TmpA model is cyan and the ZIPB crystal structure (PDB: 5TSA) is green. Loop 4 was not included in the model as it was not crystalized in ZIPB. RMSD: 1.783; Ramachandran: 94.6%; minimized with hydrogens; 10,000 iterations; gradient: 0.5; charge: Gastieger-Huckel.

The position of the proteins within the cellular membrane was then predicted using Orientation of Proteins in Membranes (https://opm.phar.umich.edu/) (Figure 6.23). As described in Zhang et al. (382), there is a tilt to the protein in order for it to fit within the membrane (Figure 6.23A). The model of TmpA has a similar tilt, although longer portions of the helices were predicted to be periplasmic (Figure 6.23B).

We then modelled the N173D mutation in TmpA (Figure 6.24). The other residues that constitute the M2 binding site moved to accommodate the negative charge of the aspartic acid (Figure 6.24), which resulted in a change in the size and shape of the M2 binding site (Figure 6.25). The change in shape and size is, of course, speculative, as proteins *in vivo* are somewhat flexible and may be able to accommodate changes such as these. Still, the change in charge may lead to a preference for one metal over another.

We then replaced the metal ions found in the ZIPB crystal structure with Mn (Figure 6.26). In these models, we observed movement of the metal ions that suggests that Mn transport could cause a shift in the conformation (Figure 6.26A & B). We also observed that a metal-binding residue, Q207, moved a distance of 2.4 Å (Figure 6.26C). This could at least partly explain why Mn is not transported by ZIPB. This is highly speculative though, as we do not know how much the protein moves and changes conformation within the membrane because the outward open conformation has yet to be crystallized. But it is interesting to postulate that the binding of different ions may cause metal-binding residues to move in response to the size of ion.

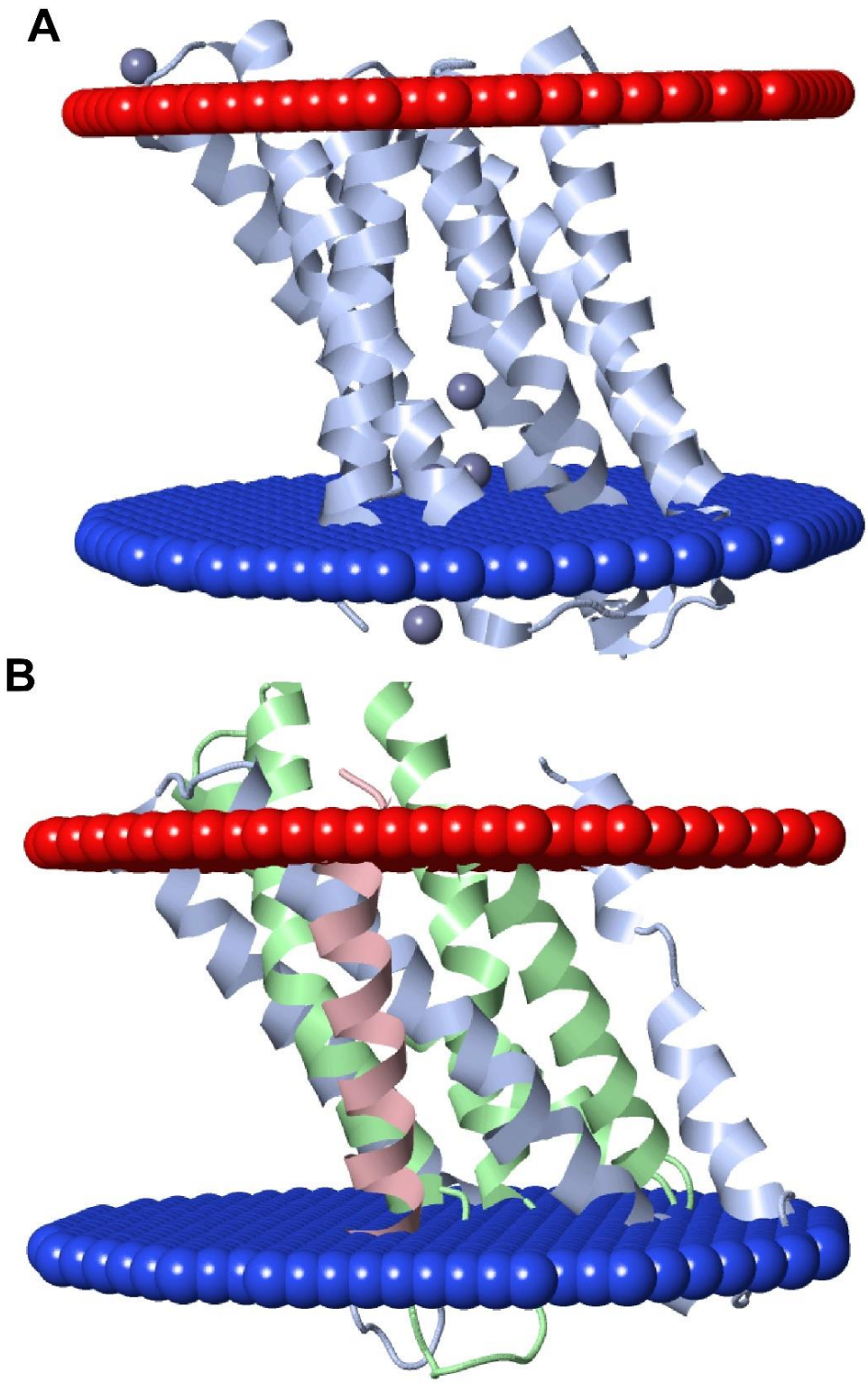

Figure 6.23 Position of ZIP proteins predicted within cellular membranes
Positions of the crystal structure of ZIPB-5TSA with Zn (A) and the model of TmpA (B) were predicted within the cellular membrane using OPM and visualized with FirstGlance in Jmol. Red is the outward facing side and blue is the cytoplasmic side.

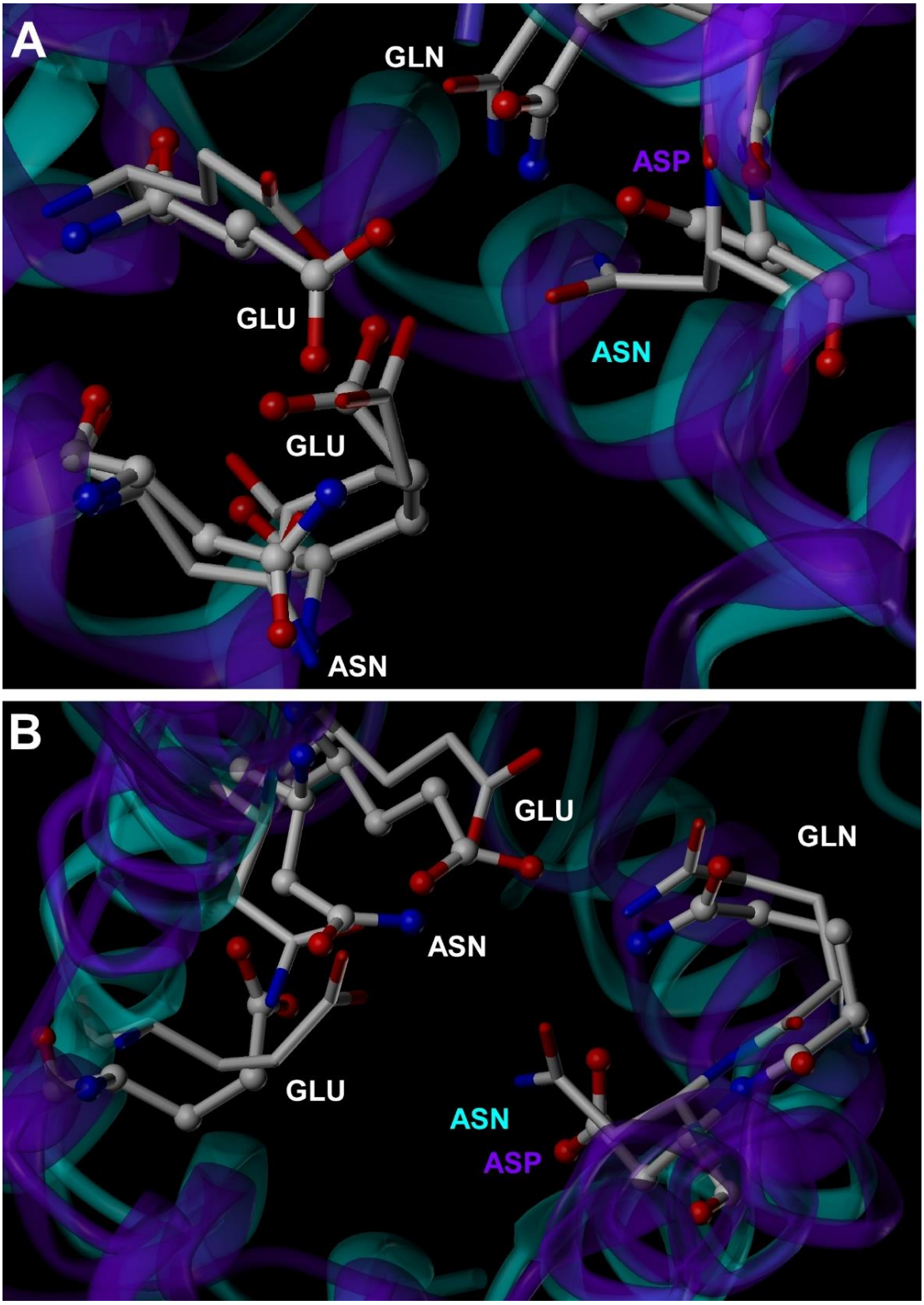

Figure 6.24 Model of M2 binding site in TmpA WT and N173D mutant
Mutation of Asn 173 to Asp. Top down (A) and bottom up (B) view of the channel. WT TmpA model is cyan with sticks and N173D mutant is purple with ball and sticks. Minimized with hydrogens; 10,000 iterations; gradient: 0.5; charge: Gastieger-Huckel.

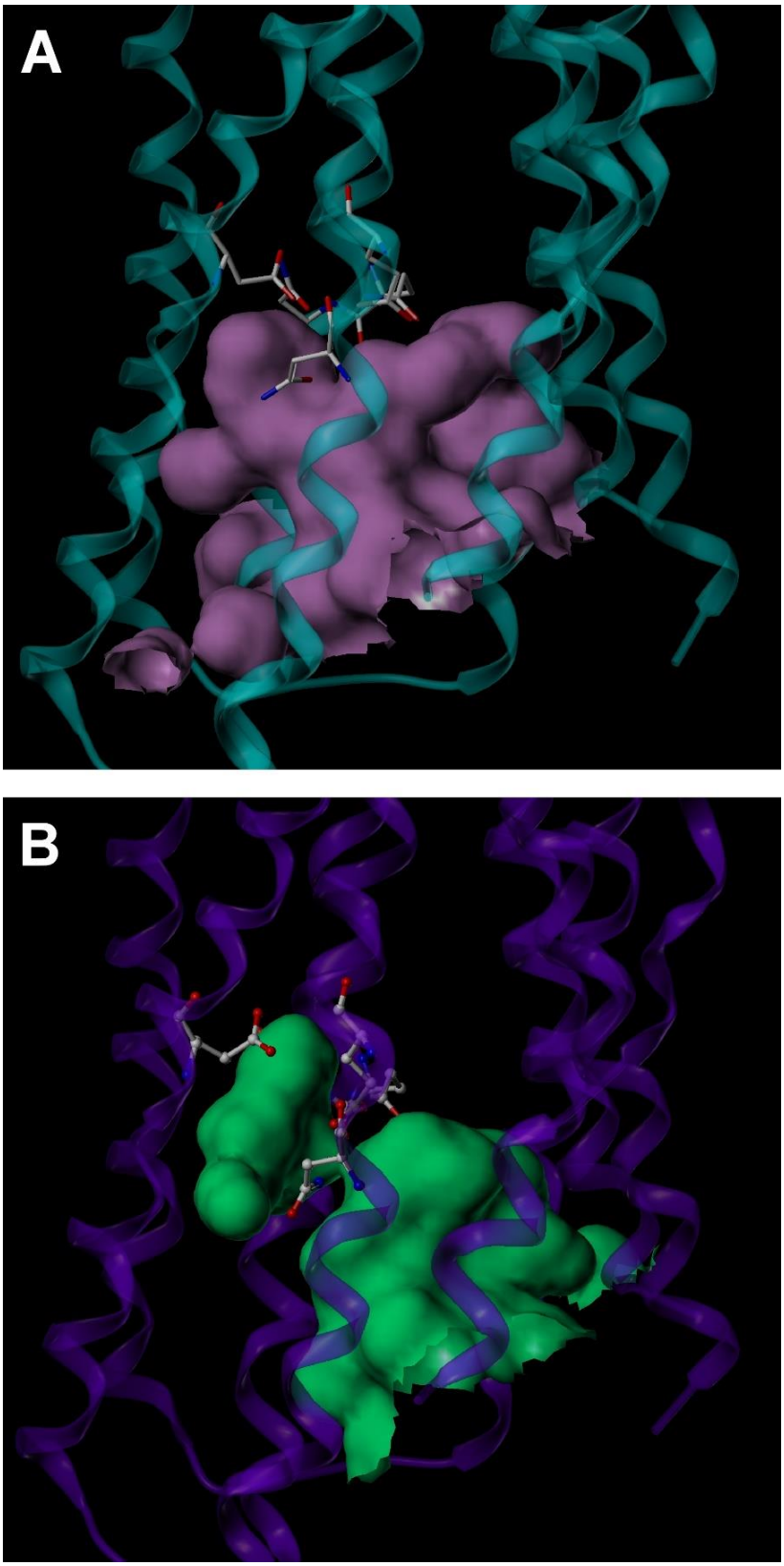

Figure 6.25 Model of channel in TmpA WT and N173D mutant
Model of WT (A) and N173D mutant (B) TmpA protein with the predicted space-filling channel.

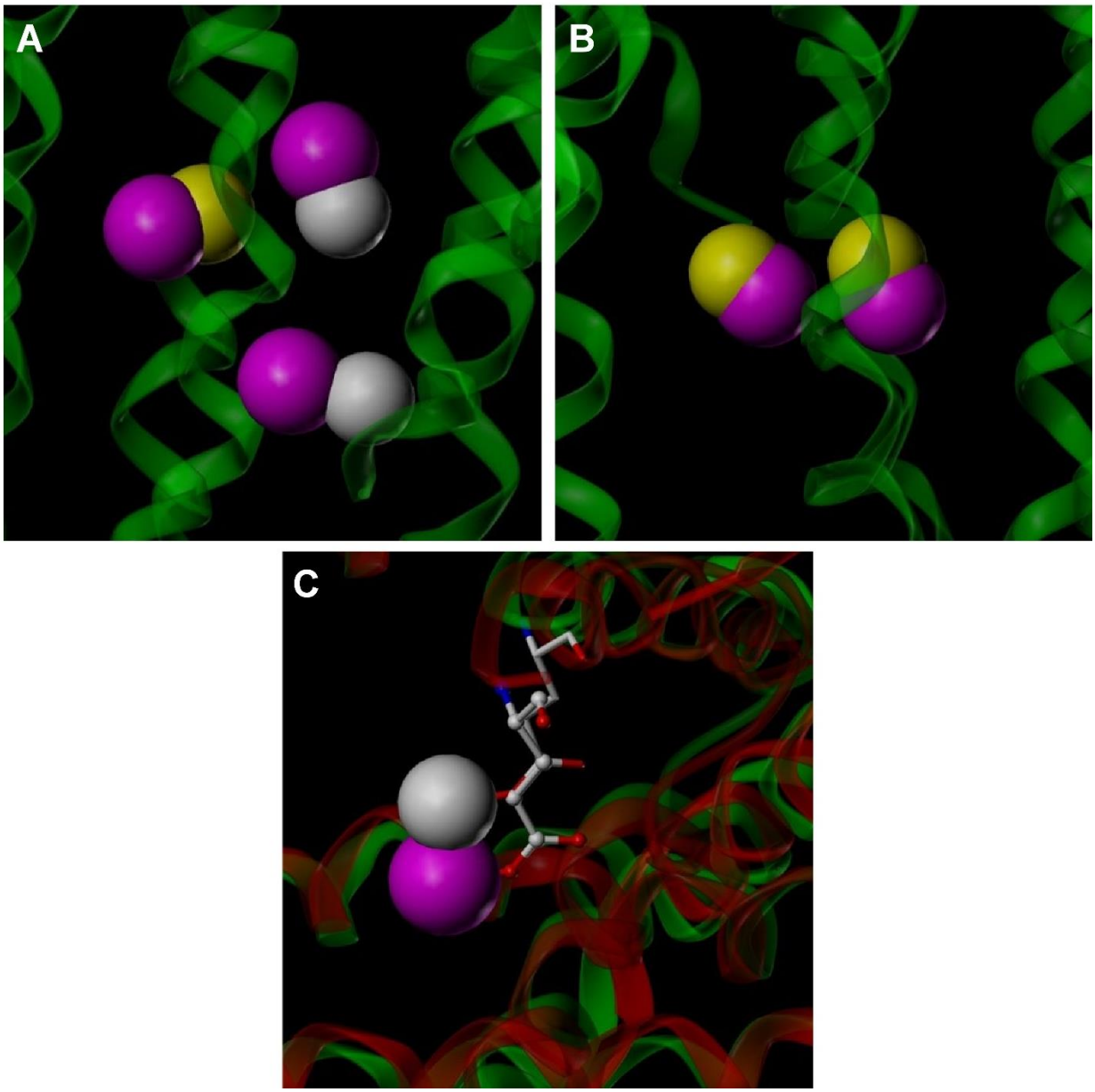

Figure 6.26 Model of ZIPB with metal ions replaced with Mn
ZIPB crystal structures 5TSA (A & C) and 5TSB (B) overlaid with models where the Zn (white) or Cd (yellow) ions have been replaced with Mn (magenta). Green ribbon and sticks represent the crystal structure in all panels; red ribbon and ball-and-stick represent the model in (C). Q207 bound to metal is shown in (C). Models were minimized with hydrogens; 10,000 iterations; gradient: 0.5; charge: Gastieger-Huckel. RMSD of 1.008 (A & C) and 1.389 (B).

Evaluation of TmpA in serum growth in other *S. sanguinis* strains

Due to considerable heterogeneity we previously observed between different strains of *S. sanguinis* (83), we assessed the effect of the loss of the SsaACB and TmpA

transporters in four additional *S. sanguinis* strains. Like SK36, SK49 is an oral isolate. By ICP-OES, we found previously that it accumulated less Mn when cultured in BHI than 14 of the 17 strains examined. VMC66 (82), SK408, and SK678 were all isolated from the blood of endocarditis patients and ranked first, second, and third, respectively, in Mn levels *in vitro* (83).

Metal transporter mutants—Δ*ssaACB*, Δ*tmpA*, and Δ*ssaACB* Δ*tmpA*—were generated for each strain. These mutant and parent strains were then assessed for aerobic serum growth at 6% O_2 (Figure 6.27). As with SK36, all Δ*tmpA* mutant strains were indistinguishable from WT and all Δ*ssaACB* strains were deficient for growth at 6% O_2 in serum. Interestingly, the SK678 and VMC66 Δ*ssaACB* Δ*tmpA* strains grew similarly to their parent strains. Only the SK49 and SK408 versions grew to a significantly lower density than their Δ*ssaACB* parent strains. However, it is apparent that in SK678 and VMC66, the *ssaACB* deletion produced a greater defect on growth than in the other backgrounds.

To determine if the poor growth of the Δ*ssaACB* parents precluded us from detecting an additional effect of *tmpA* deletion, growth of the SK678 and VMC66 groups was assessed in 1% O_2 (Figure 6.28). Under these conditions, we observed a significant difference between each Δ*ssaACB* Δ*tmpA* mutant and its Δ*ssaACB* parent. The T_0 values for the VMC66 quadruple mutant were significantly lower than the Δ*ssaACB* parent in this set of experiments, although when this experiment was repeated (Figure 6.30), the T_0 values were statistically similar and the difference between the T_{24} values was maintained, indicating that this result is not an artifact of lower inoculum levels.

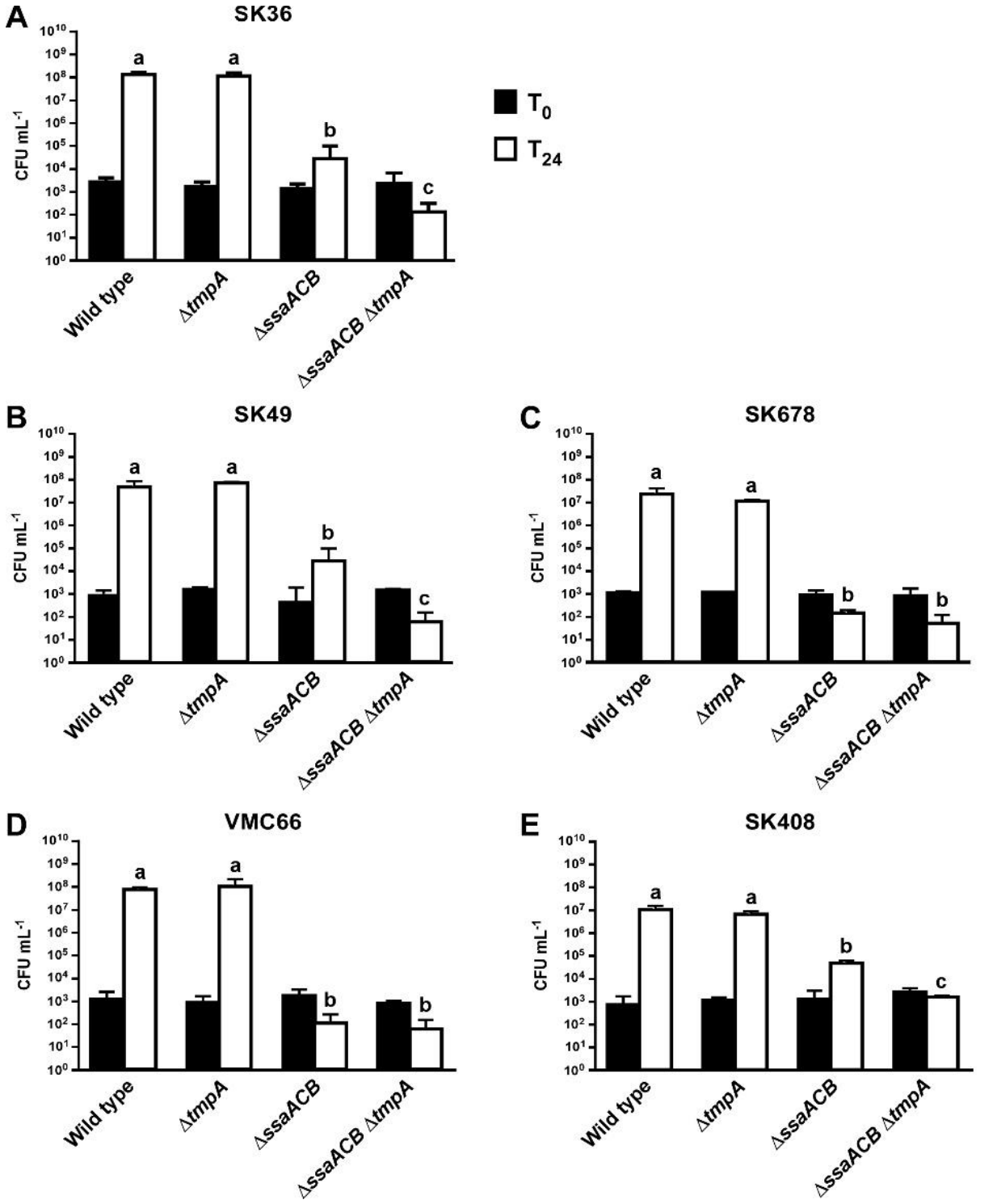

Figure 6.27 Serum growth of Mn-transport mutants in other strains at 6% O_2
Growth of strain and its respective mutants in serum at 6% O_2 was assessed by plating on BHI agar after 24 h. Means and SD of at least three independent experiments are displayed. Significance was assessed by one-way ANOVA with a Tukey multiple comparisons test for T_0 and T_{24} values separately. T_{24} bars that share a letter within a chart are not significantly different from each other ($P \leq 0.05$).

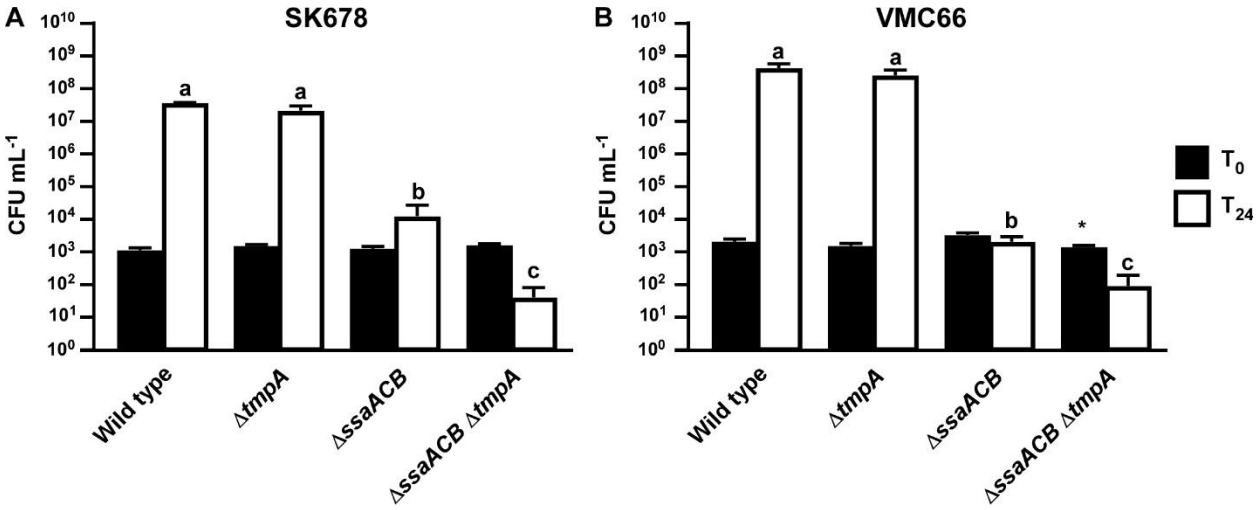

Figure 6.28 Serum growth of SK678 and VMC66 mutants at 1% O_2
Growth of SK678 mutants (A) and VMC66 mutants (B) in serum at 1% O_2 was assessed by plating on BHI agar after 24 h. Means and SD of at least three independent experiments are displayed. Significance was assessed by one-way ANOVA with a Tukey multiple comparisons test for T_0 and T_{24} values separately. The T_0 bar with asterisk is significantly different from its parent strain. T_{24} bars that share a letter within a chart are not significantly different from each other ($P \leq 0.05$).

Relative contribution of TmpA to growth and virulence of other *S. sanguinis* strains

Of interest to this study, *S. sanguinis* strains SK408, VMC66, BCC23, and BCC46 encode gene orthologous to the Nramp protein MntH found in *S. mutans* (148) and other gram-positive bacteria (401). Nramp proteins are known to import Mn (402, 403) and contribute to endocarditis virulence in *Enterococcus faecalis* (404). It is unexpected then that the VMC66 Δ*ssaACB* mutant performed so poorly in the 6% O_2 serum growth study. To determine whether these Nramp proteins contribute to Mn uptake and endocarditis virulence in *S. sanguinis*, knockout mutants were generated and aerobic serum growth was assessed. At 6% O_2, the Δ*mntH* strain grew significantly worse than the WT parent but better than the Δ*ssaACB* mutant (Figure 6.29). The Δ*ssaACB* mutant grew similarly to both quadruple mutant strains: Δ*ssaACB* Δ*tmpA* and Δ*ssaACB* Δ*mntH* (Figure 6.29). The T_0 values for the Δ*ssaACB* and Δ*ssaACB* Δ*mntH* mutants were statistically different

but given that they were both similar to the Δ*ssaACB* Δ*tmpA* mutant T_0 value, we did not doubt the validity of the outcome.

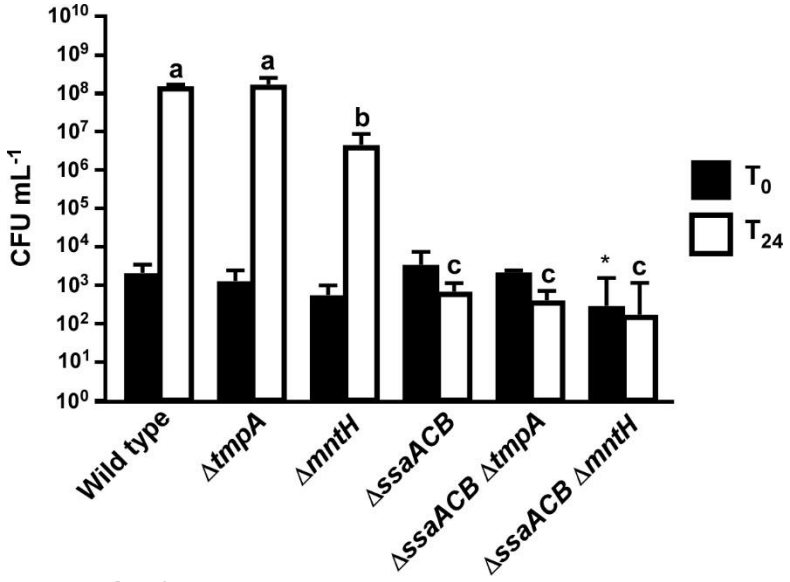

Figure 6.29 Serum growth of VMC66 Mn transporter mutants at 6% O_2
Growth of various VMC66 mutants in serum at 6% O_2 was assessed by plating on BHI agar after 24 h. Means and SD of at least three independent experiments are displayed. Significance was assessed by one-way ANOVA with a Tukey multiple comparisons test for T_0 and T_{24} values separately. The T_0 bar with asterisk is significantly different from its parent strain; no other T_0 values are statistically different from each other. T_{24} bars that share a letter are not significantly different from each other ($P \leq 0.05$).

These results indicate that MntH does contribute to aerobic growth on its own but it is not as important as SsaACB. The drastic growth reduction in the Δ*ssaACB* mutant may have masked any contribution of MntH or TmpA in this background under these conditions. Thus, we decided to assess aerobic growth at 1% O_2. When we lowered the oxygen concentration, we once again observed that the Δ*ssaACB* Δ*tmpA* strain grew significantly worse than the Δ*ssaACB* parent but we no longer saw a significant difference between the Δ*tmpA* strain and WT. Both Δ*mntH* and Δ*ssaACB* Δ*mntH* grew slightly but not significantly lower than their respective parent strains. Both of their T_0 values were significantly lower than the parent, which may indicate that the slight decrease observed at T_{24} is a result of a slightly lower inoculum.

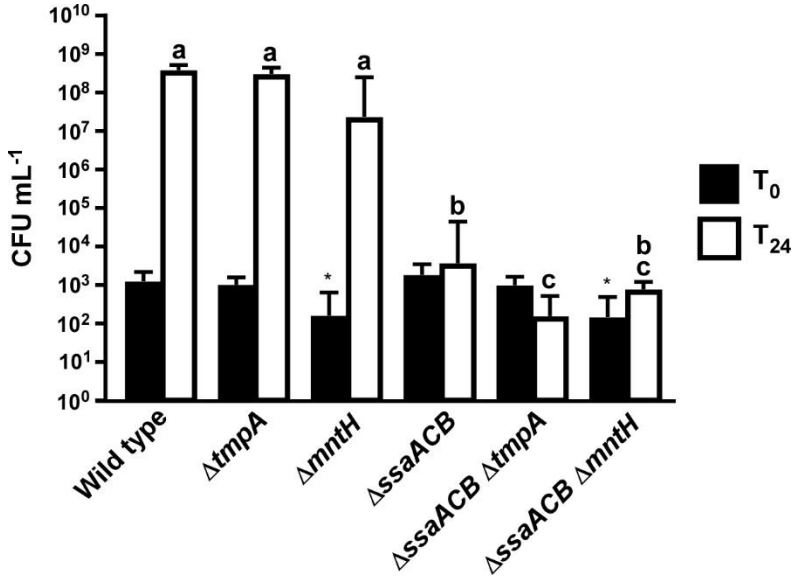

Figure 6.30 Serum growth of VMC66 Mn transporter mutants at 1% O_2
Growth of various VMC66 mutants in serum at 1% O_2 was assessed by plating on BHI agar after 24 h. Means and SD of at least three independent experiments are displayed. Significance was assessed by one-way ANOVA with a Tukey multiple comparisons test for T_0 and T_{24} values separately. T_0 bars with asterisks are significantly different from their respective parent strain. T_{24} bars that share a letter are not significantly different from each other ($P \leq 0.05$).

To determine the relative contribution of each Mn transporter to VMC66 virulence, WT, Δ*tmpA***,** Δ*ssaACB, and* Δ*mntH* strains were tested in our rabbit model of infective endocarditis (Figure 6.31A). The Δ*mntH* mutant was recovered at similar levels to the VMC66 Spc^R WT strain (83). The only strain to be recovered at significantly lower levels than WT was the Δ*ssaACB* strain, highlighting its importance as the primary Mn transporter in multiple *S. sanguinis* strains.

To test the relative contribution of each secondary transporter to virulence, the quadruple mutants were also tested in our rabbit model (Figure 6.31B). To ensure sufficient recovery of the Δ*ssaACB* mutants, we increased the inocula of the three Δ*ssaACB* strains to ~$1x10^8$ and decreased the inoculum of the WT strain to ~$5x10^6$. We were able to recover colonies of every strain from each rabbit and we saw a significant difference between the WT and both quadruple mutant strains. We did not see a significant difference between

the WT and Δ*ssaACB* this time (*P*-value = 0.0589). We observed a significant difference between the Δ*ssaACB* Δ*tmpA* mutant and its parent but neither was significantly different from the Δ*ssaACB* Δ*mntH* mutant. This suggests that TmpA may contribute more to Mn uptake than MntH but since the recovery was so similar between the two strains, it is difficult to make a strong conclusion. Both may function in an overlapping role but they do not appear completely redundant, given the significant decrease in recovery of the Δ*ssaACB* Δ*tmpA* mutant compared to the parent.

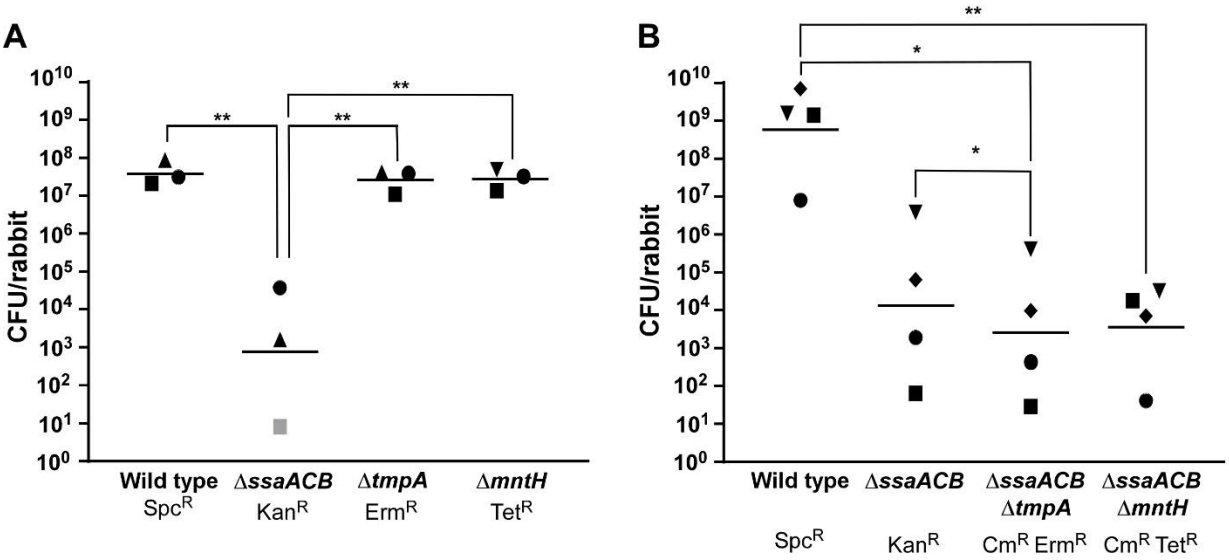

Figure 6.31 Virulence of VMC66 mutant strains in a rabbit model of IE
Rabbits were co-inoculated with the marked WT strain, the Δ*ssaACB* mutant strain, and either the Δ*tmpA* and Δ*mntH* strains (A) or the Δ*ssaACB* quadruple mutant strains (B). Each symbol indicates one rabbit. All rabbits were male. Gray symbols indicate recovery was below the limit of detection. Geometric means are indicated by horizontal lines. **P* ≤ 0.05, ***P* ≤ 0.01 indicate significantly different from other strains using repeated measures ANOVA with a Tukey multiple comparisons test.

We tested another NRAMP-encoding strain, BCC23, from a recently isolated collection of *S. sanguinis* from the Burne lab (150). We have only tested the Δ*ssaACB* mutant thus far, although much like the VMC66 versions, this mutant grew significantly worse in aerobic serum than its parent strain (Figure 6.32A). Additionally, the BCC23 Δ*ssaACB* mutant was not recovered from heart valve vegetations in our rabbit model of IE, whereas

the marked WT strain was recovered in similar quantities as the SK36 marked WT strain, JFP36 (Figure 6.32B).

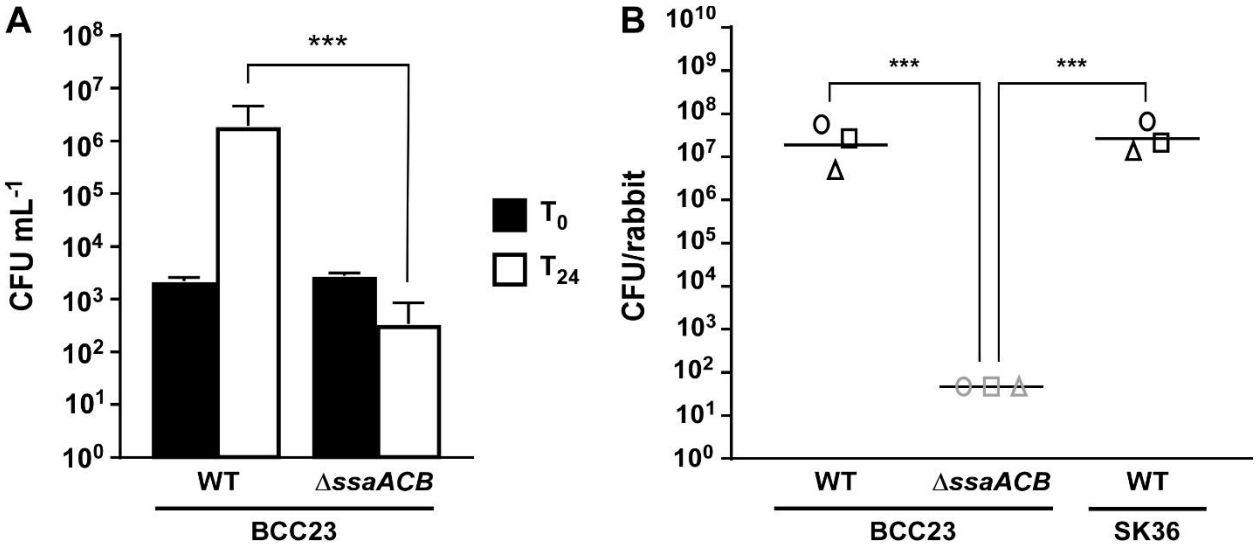

Figure 6.32 Aerobic serum growth and virulence of the BCC23 Δ*ssaACB* mutant
(A) Serum was preincubated at 12% O_2 and inoculated from an overnight culture. Cultures were incubated for 24 h before plating. Means and SD of three replicates are displayed. Significance was determined by unpaired t-test of T_{24} cultures; ***$P \leq 0.001$. T_0 values were compared by two-tailed t-test and were not significantly different. (B) Rabbits were co-inoculated with the marked WT strains of SK36 and BCC23 and the BCC23 Δ*ssaACB* mutant strain. Each symbol indicates one female rabbit (n = 3). Gray symbols indicate recovery was below the limit of detection. Horizontal lines indicate geometric means. ***$P \leq 0.001$ indicates significantly different from other strains using one way ANOVA with a Tukey multiple comparisons test.

Sequencing of the SK36 Δ*ssaACB* Δ*tmpA* double mutant

After completing the experiments in this dissertation, we sequenced the whole genome of the Δ*ssaACB* mutant (JFP173) and the Δ*ssaACB* Δ*tmpA* mutant (JFP227). Unfortunately, we discovered the presence of a nonsense mutation in SSA_1414 (W139*) in JFP227. SSA_1414 is annotated as MutT, an 8-oxo-dGTP diphosphatase. We confirmed this mutation by Sanger sequencing and found that it was unique to this strain, as it was not present in the Δ*tmpA* single mutant (JFP226), which was made with the same PCR product as JFP227. We generated a clean Δ*ssaACB* Δ*tmpA* strain and confirmed by Sanger sequencing that the SSA_1414 gene was intact. We compared the

growth of this new mutant (JFP377) to that of JFP227 (Figure 6.33A-C). There was no significant difference in growth between these strains. We then measured the metal content of cells grown in BHI with 10 µM Mn^{2+} using inductively coupled plasma optical emission spectroscopy (ICP-OES) and observed no significant difference in any metal examined (Figure 6.33D). These results indicate that the unintended mutation in JFP227 did not significantly impact our previous results.

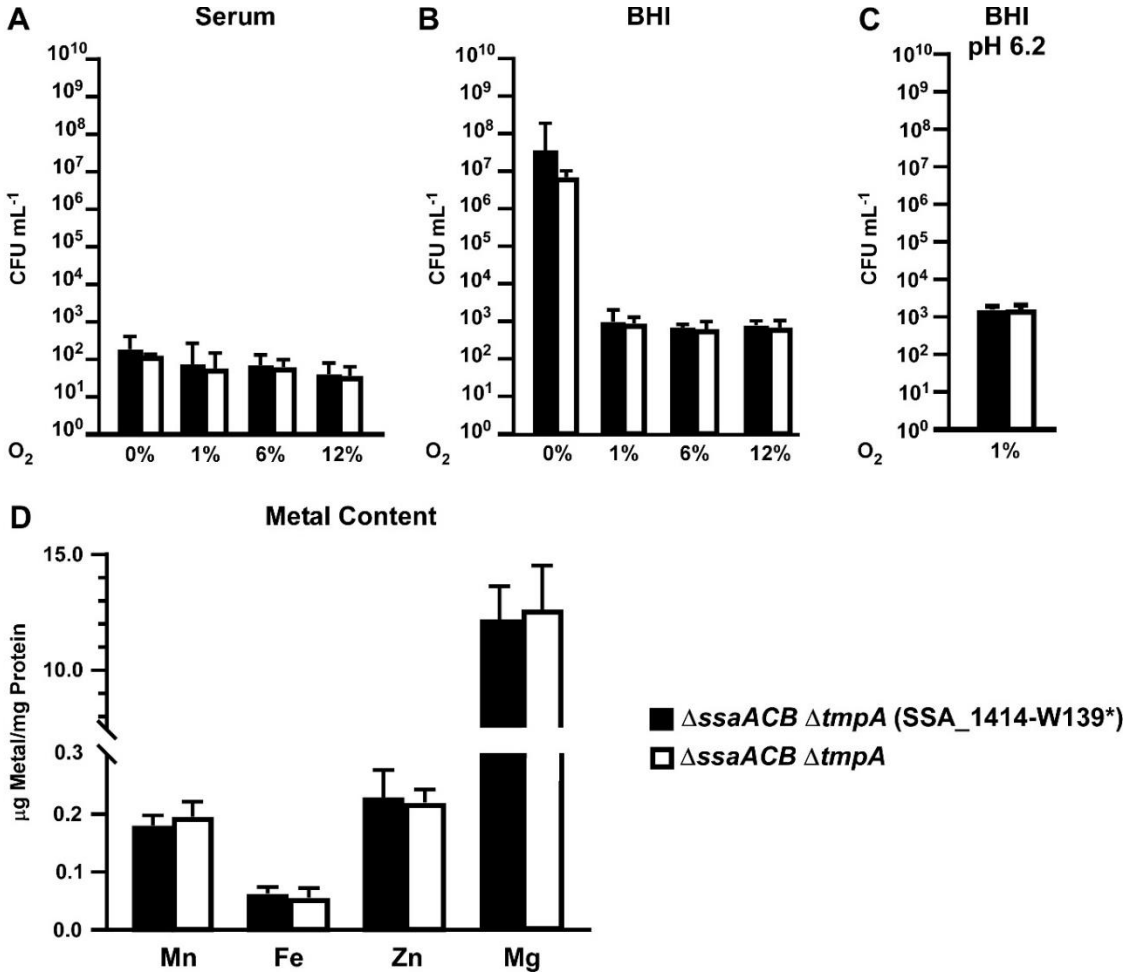

Figure 6.33 Comparison of Δ*ssaACB* Δ*tmpA* mutants with and without SNP in SSA_1414. Cultures of each Δ*ssaACB* Δ*tmpA* mutant in serum (**A**), normal BHI (**B**), or acidic BHI (**C**) were grown at the indicated O_2 concentrations. JFP227 is the original version and JFP377 is the new, clean version. Metal content of cells grown in atmospheric conditions (~21% O_2) in BHI with 10 µM Mn^{2+} as measured by ICP-OES (**D**). Means and standard deviations of three replicates are depicted in each chart. The strains were determined to be not significantly different from each other in each condition tested as determined by paired two-tailed t-test.

Discussion

Mn transport in bacteria is typically considered to include four protein families: (i) ATP-binding cassette, (ii) Nramp, (iii) P-type ATPase, and (iv) cation diffusion facilitators. Here we propose a fifth family of bacterial Mn transporters: ZIP family proteins. With this study, it has now been established that in at least two different bacteria, a ZIP family protein contributes significantly to Mn uptake.

This study confirms the presence of a secondary Mn transporter. We were unable to find a significantly different phenotype for the single Δ*tmpA* mutant. In addition to the studies described above, we tested its growth in low pH BHI, either in a tube culture or in the fermentor in competition with the marked WT strain (JFP36) and saw no distinguishable growth differences (data not shown). We also tested the growth of this mutant against *S. mutans* UA159 and saw no difference in the inhibition of growth (data not shown). These results, along with those described above, strongly suggest that its function is secondary to SsaACB. The reason that many organisms encode genes for multiple metal transporters is still contested, although it highlights the importance of these trace elements. The presence of multiple transporters with varying affinity could be due to the two proteins functioning optimally under different environmental conditions or it could protect from the loss of function of one of the transporters (151, 378, 405). From what we have learned about metal uptake, Mn is still entering SK36 Δ*ssaACB* Δ*tmpA* cells by an additional unknown transporter. We hypothesize that in SK36, this third transporter is a broad-spectrum metal transporter. In VMC66 and SK408, MntH may be playing this role. Further studies will be required to confirm the identity and selectivity of other metal transporters in *S. sanguinis*.

Phylogenetic analyses

Interestingly, these results may not be applicable to all streptococci. A BLAST search (174) using the sequence of TmpA against other streptococci revealed that *S. pneumoniae*, *Streptococcus mitis*, *Streptococcus oralis*, *Streptococcus pyogenes*, and *Streptococcus vestibularis* appear to be missing hits or only contain partial sequences. Additionally, a phylogenetic tree showed that *S. mutans* and *Streptococcus ratti* separate considerably from the other streptococci, and even from other characterized bacterial ZIP proteins (Figure 6.34). Other members of the "Mutans" group, such as *Streptococcus sobrinus* and *Streptococcus downei*, grouped with the other streptococci (Figure 6.34). The reason for this is unknown, as both *S. mutans* and *S. sanguinis* ZIP proteins share closest homology to hZIP11 by BLASTP (174). We included one of the human ZIP proteins, hZIP11, with the intention of acting as an outgroup given that it is the most similar to bacterial ZIP proteins. Instead of behaving like an outgroup though, it grouped with all of the bacterial ZIP proteins, except those of *S. mutans* and *S. ratti*. These results, along with the observation that ZIP protein homology does not follow the 16S rRNA groups (23), indicate that the ZIP proteins were likely incorporated into the genome of each species or various progenitors at different times, as opposed to being derived from a single common ancestor, which is typical in streptococci (406). The GC content of the *S. sanguinis* genome is 43.40% (75) whereas *tmpA* is 50.42%, indicating that it could have been acquired by horizontal gene transfer (407). The GC content of the *S. mutans* UA159 genome is 36.82% (408) and its ZIP protein SMU_2069 is 37.1%, which means that it could have evolved with *S. mutans* or acquired from another organism with a similar GC content.

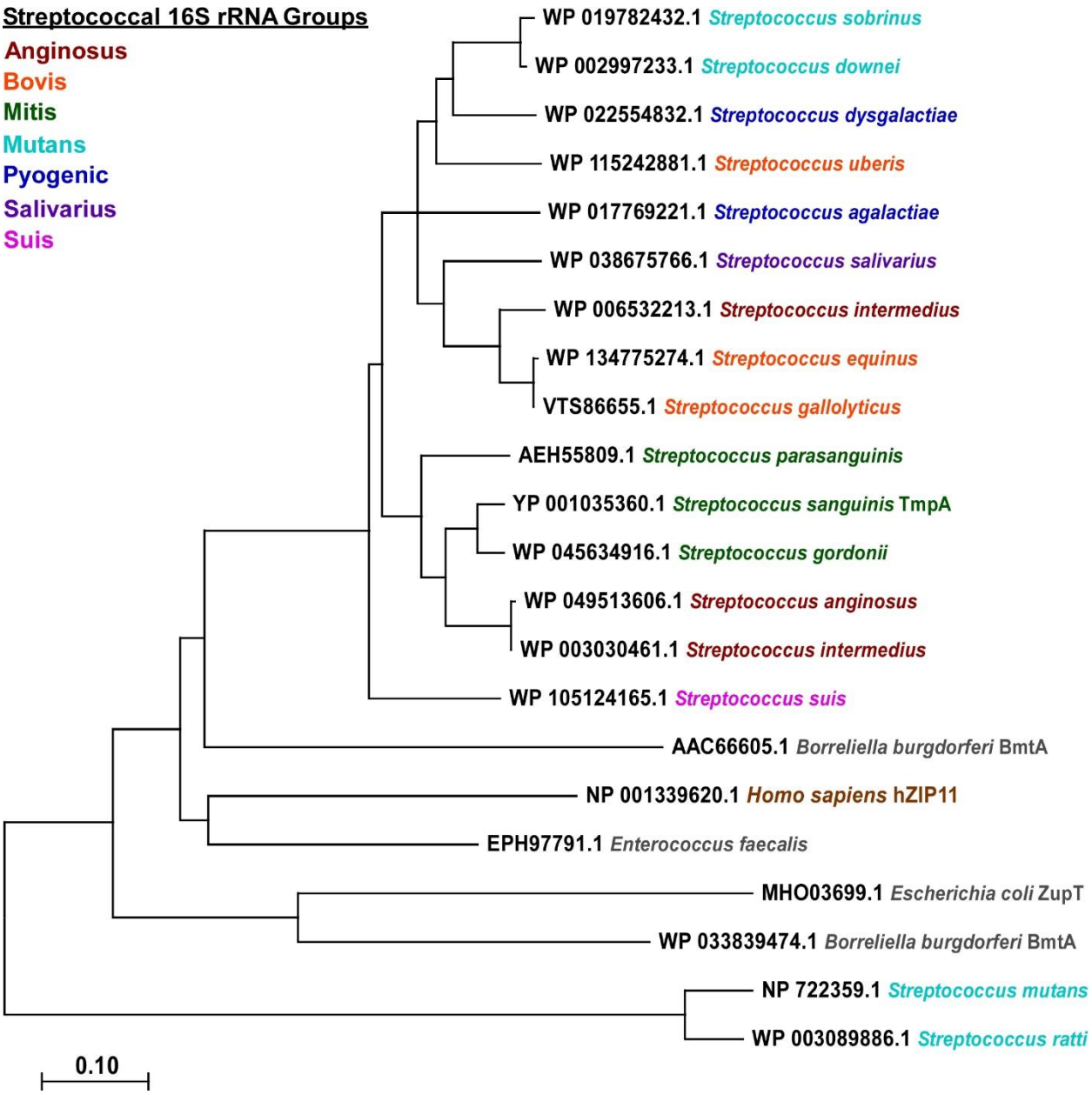

Figure 6.34 Phylogenetic tree of *S. sanguinis* TmpA orthologs
The evolutionary history was inferred using the Neighbor-Joining method (409). The optimal tree with the sum of branch length = 4.17 is shown. The tree is drawn to scale, with branch lengths in the same units as those of the evolutionary distances used to infer the phylogenetic tree. The evolutionary distances were computed using the Poisson correction method (410) and are in the units of the number of amino acid substitutions per site. This analysis involved 22 amino acid sequences. All ambiguous positions were removed for each sequence pair (pairwise deletion option). There were a total of 390 positions in the final dataset. Evolutionary analyses were conducted in MEGA X (411). Streptococcal species are colored based on their 16S rRNA groups (23); all other bacterial species are listed in gray. The hZIP11 (brown) sequence was intended as an outgroup.

To investigate this further, we evaluated the phylogeny of SsaB orthologs in streptococci (Figure 6.35). Most species contain orthologs of SsaB, including those that were lacking a ZIP family protein, such as *S. mitis*, *S. oralis*, *S. pyogenes*, and *S. vestibularis* (Figure 6.35). Interestingly, *Streptococcus suis* and *S. ratti* lack an SsaB ortholog. In this case, *S. mutans* does also group separately from the rest of the streptococci but *Staphylococcus aureus* and *B. bronchiseptica* are more distantly related (Figure 6.35). *E. faecalis* groups more intimately within the main group of streptococci, next to *Streptococcus agalactiae* (Figure 6.35).

We then looked closer at the *S. mutans* ZIP protein, here designated as $TmpA_{Sm}$. When we completed a BLAST search, most of the hits were either closely related streptococci or other Firmicutes (Figure 6.36). Species listed are within the top 50 hits to the $TmpA_{Sm}$ sequence (Figure 6.36). *Streptococcus sanguinis* TmpA sequence ($TmpA_{Ss}$) was included as an outgroup. These analyses further support independent incorporation of TmpA orthologs in *S. mutans* and the other streptococci at different times in history. Bootstrap analysis confirmed that the phylogenetic branches separating *S. mutans/S. ratti* from the other *Streptococcus spp.* in Figure 6.34 are statistically different from each other (data not shown). As for why *S. sobrinus* and *S. downei* are included with the rest of the streptococci as opposed to the 16S rRNA Mutans group, this is still a mystery.

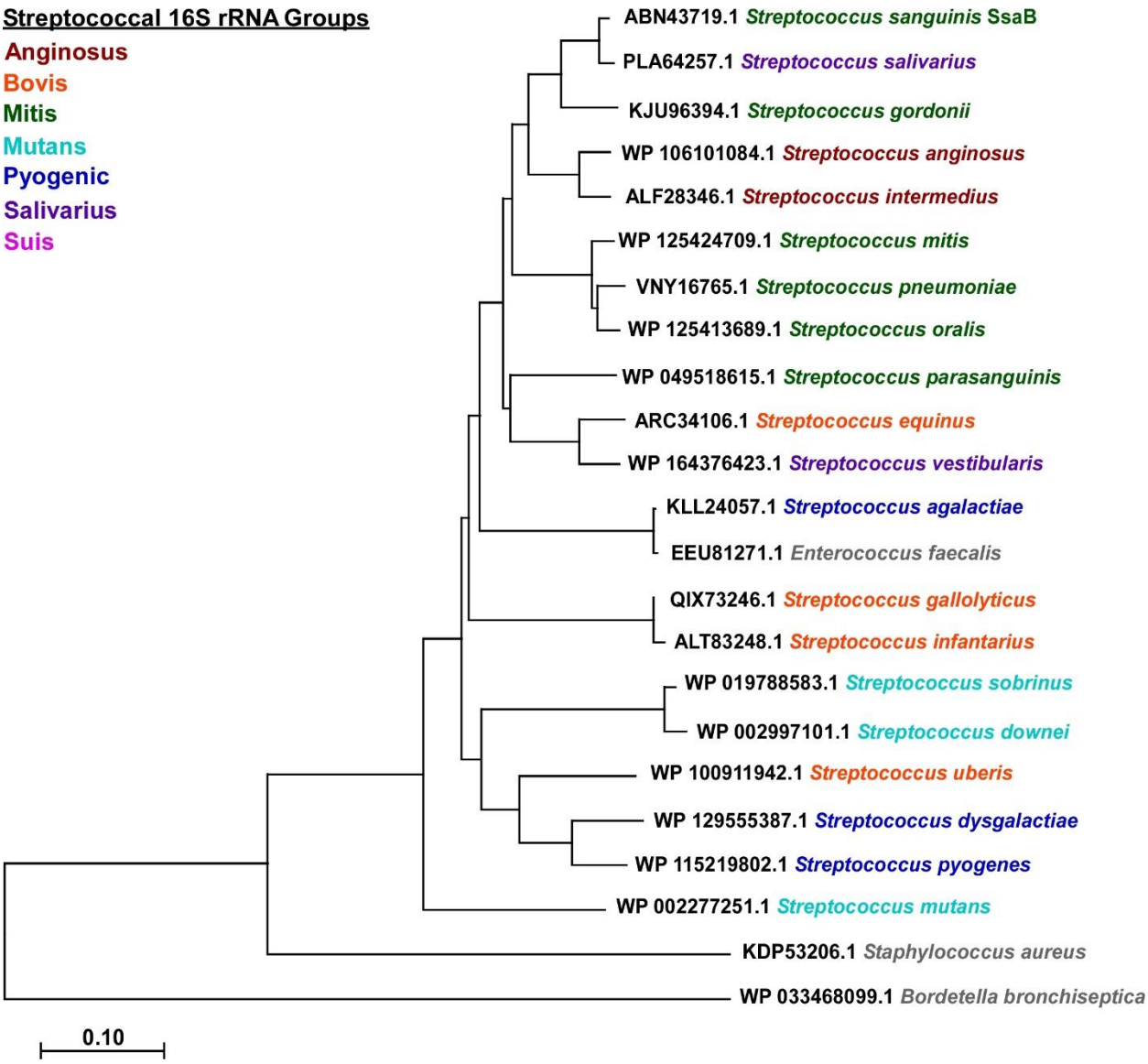

Figure 6.35 Phylogenetic tree of *S. sanguinis* SsaB orthologs

The evolutionary history was inferred using the Neighbor-Joining method (409). The optimal tree with the sum of branch length = 2.88 is shown. The tree is drawn to scale, with branch lengths in the same units as those of the evolutionary distances used to infer the phylogenetic tree. The evolutionary distances were computed using the Poisson correction method (410) and are in the units of the number of amino acid substitutions per site. This analysis involved 23 amino acid sequences. All ambiguous positions were removed for each sequence pair (pairwise deletion option). There were a total of 335 positions in the final dataset. Evolutionary analyses were conducted in MEGA X (411). Streptococcal species are colored based on their 16S rRNA groups (23); all other bacterial species are listed in gray. *B. bronchiseptica* and *S. aureus* were included as outgroups.

The discovery that both lineages picked up a ZIP family protein suggests that secondary transporters are valuable to have and maintain in the genome. They do not appear to be essential, as some species of streptococci, such as the human pathogen *S. pyogenes* and the oral commensals *S. oralis* and *S. mitis*, have been able to survive without a ZIP family protein. Some strains and species even encode all three Mn transporters. In *S. sanguinis* VMC66, loss of both SsaACB and TmpA was slightly more deleterious than the loss of both SsaACB and MntH (Figure 6.30), indicating more dependence on TmpA for transport function. A recent study utilizing *S. mutans* Mn-transport mutants Δ*sloC,* the *ssaB* ortholog, and Δ*mntH* found that the inactivation of MntH did not produce any obvious phenotypes, whereas the Δ*sloC* and Δ*sloC* Δ*mntH* mutants were severely deficient in Mn-restricted conditions (148). Future studies looking at various Δ$tmpA_{Sm}$ mutants in *S. mutans* would further the understanding of the relative contribution of each of these proteins to growth and Mn transport and possibly reveal more about the origin of this distinct lineage.

Regulation of *tmpA*

While our transcriptional analysis is not exhaustive, it is plausible that *tmpA* expression is constitutive in *S. sanguinis*. In *E. coli*, the gene encoding ZupT is constitutively transcribed at low levels (381). In *Corynebacterium glutamicum,* the Mn-responsive repressor MntR regulates the expression of a putative ZIP family protein (412). This would be a reasonable regulator of *tmpA*, as MntR orthologs regulate both ABC transporters and Nramp proteins (130, 148). Yet, we did not observe a significant difference in *tmpA* expression after the addition of Mn (Figure 6.12) and searches for putative MntR binding sites using RegPrecise (218) and FIMO (271) did not identify any positive hits. In our

RNA-seq analysis of EDTA-treated cells, expression of *tmpA* decreased slightly, yet significantly at T_{50} but initial expression at T_{-20} was low, as were other genes in the operon (Figure 3.10) (202).

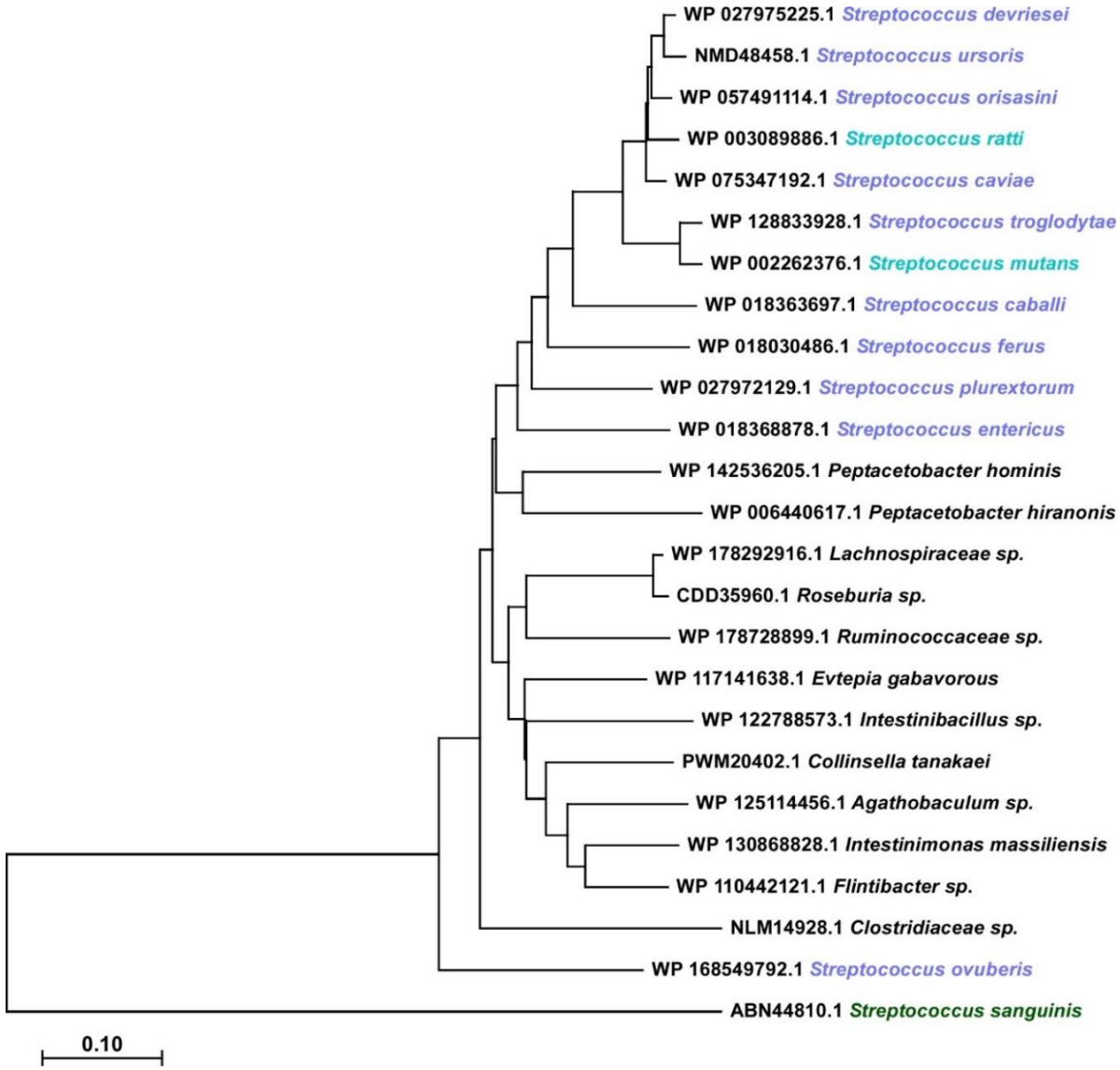

Figure 6.36 Phylogenetic tree of *S. mutans* TmpA orthologs

The evolutionary history was inferred using the Neighbor-Joining method (409). The optimal tree with the sum of branch length = 3.35 is shown. The tree is drawn to scale, with branch lengths in the same units as those of the evolutionary distances used to infer the phylogenetic tree. The evolutionary distances were computed using the Poisson correction method (410) and are in the units of the number of amino acid substitutions per site. This analysis involved 25 amino acid sequences. All ambiguous positions were removed for each sequence pair (pairwise deletion option). There were a total of 282 positions in the final dataset. Evolutionary analyses were conducted in MEGA X.(411) Streptococcal species are colored (based on Figure 6.34), all other bacterial species are black. *S. sanguinis* TmpA was included as an outgroup.

This result may have been an artifact of data normalization, as expression remained low and constant in both WT and Δ*ssaACB* after acid addition (Figure 5.11-12), despite a decrease in cellular Mn levels (Figure 5.4).

Assessment of the *tmpA* operon and the gene neighborhood in PATRIC (165) shows some conservation in other streptococci for the first 20 species, with many orthologs sharing 5-6 gene neighbors (Figure 6.37). In species 21-55, the gene neighborhood becomes more divergent, indicating that there is likely not a strong selective pressure to maintain co-regulation with the *tmpA* ortholog.

Issues with protein visualization and expression

In eukaryotic systems, there is some evidence for post-translation regulation of ZIP proteins (393). Unfortunately, due to issues with visualizing TmpA by western blot, we were unable to determine if post-translational regulation is occurring in *S. sanguinis*. This may have occurred in our yeast and *E. coli* experiments though, as expression of TmpA yielded unexpected results (Figure 6.15 & 6.18).

Until very recently, there have been few studies reporting the structural characterization of ZIP proteins because integral membrane proteins are notoriously difficult to work with (384). Recent advances in technology have led to a near-exponential increase in membrane protein structures deposited but they still make up a small number of the total protein structures. ZIPB, the first and only ZIP protein to be crystallized thus far, was chosen out of 96 prokaryotic ZIP family proteins as the only one to be characterized further based on satisfactory behavior in experimental conditions (384, 385). Additionally, working with membrane proteins in gram-positive bacteria is also uncommon. To our knowledge, the Brady laboratory at the University of Florida is one of the few groups to

have successfully purified integral membrane proteins from gram-positive bacteria (413). We attempted purification using their protocol, along with many other adaptations, and were unsuccessful in yielding sufficient protein for visualization.

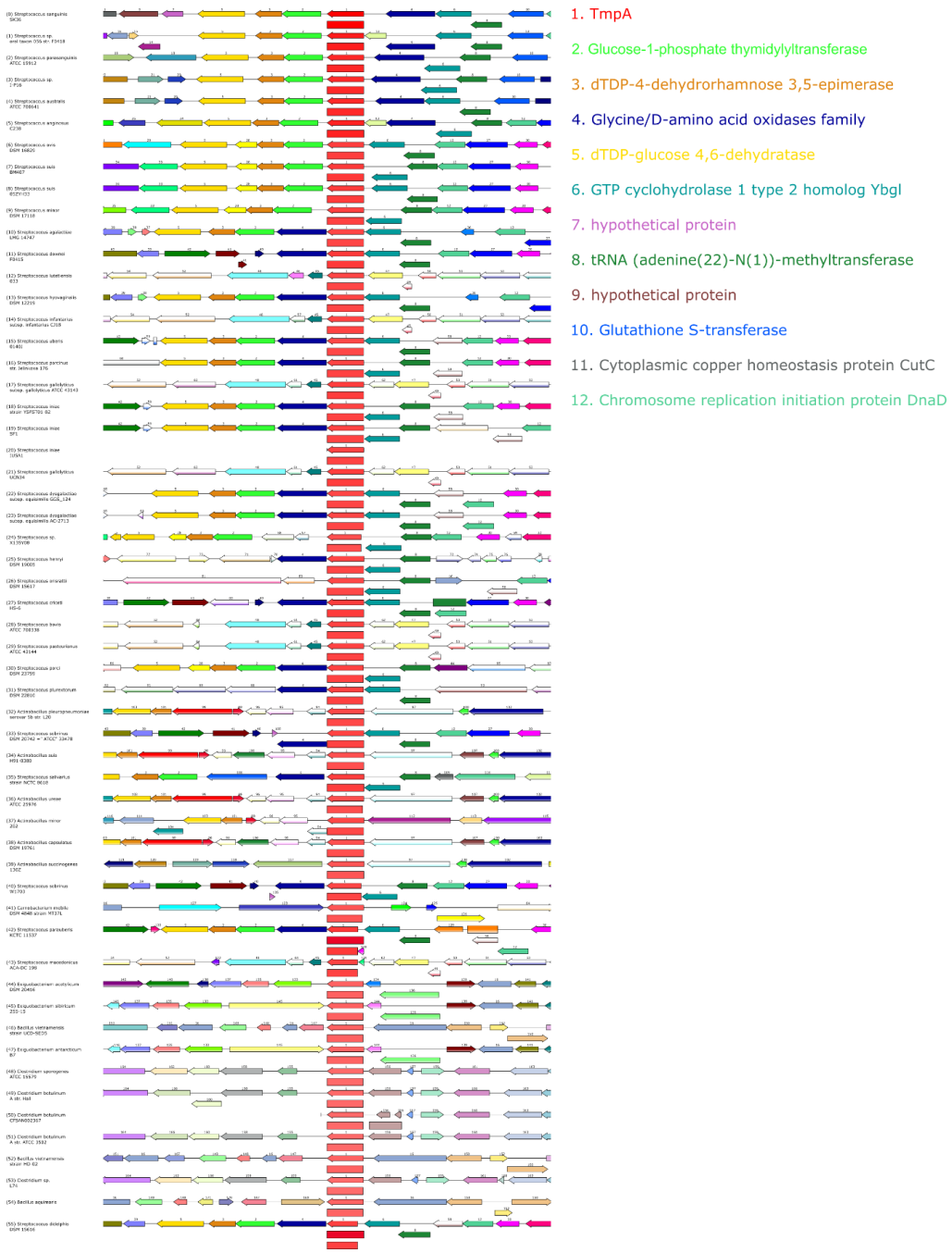

Figure 6.37 Gene neighborhood of *tmpA*
The neighboring genes of *tmpA* (red) in 54 other species was compared using PATRIC.(165) Each color indicates a different gene and its orthologs. Gene descriptions from SK36 are labeled (right).

Comparison to the ZIPB crystal structure

When ZIPB was crystalized, the Zn-bound protein still contained Cd at the M2 position in the binuclear center. Convention would suggest that the oxygen atoms of the coordinating residues would prefer the "harder" Zn^{2+} ion over Cd^{2+} so this finding was surprising. Zhang et al. (382) hypothesized that the M2 site has lower accessibility from the cytoplasmic side than the M1 site. This was supported by the observation that the M2 site is further from the cytoplasmic side of the protein and the pathway of metal release from M2 appeared to be blocked by the metal bound at M1. Thus, they theorized that the metal bound at the M2 site may dictate the selectivity or rate of transport by modifying the charge and geometry of the metal chelating residues at M1 (382, 390).

In their most recent study, Zhang et al. (336) confirmed that in hZIP4, the M1 site is essential for metal transport and the M2 site facilitates optimal transport activity. They determined that loss of the M2 site did not influence the ability of other metal ions to outcompete Zn for transport but it did affect transport under various pH conditions. When they crystallized the M2 site mutant of ZIPB, they found that Cd^{2+} was still bound at the M1 site, despite lack of an ion at the M2 site. This was interpreted as indicative of the M2 site not playing a significant role in metal chelation, but rather as a modulator of the properties of the M1 binding site (336). The modification of N173 to D in the predicted M2 site of TmpA resulted in the reduced function of the protein as a Mn transporter (Figure 6.21-22). This indicates that unlike ZIPB, TmpA cannot function without a proper M2 site. Additionally, because replacement with aspartic acid did not complement the function of the native asparagine, this suggests that N173 may be essential for function, possibly by determining metal selectivity.

A possible explanation for the discrepancy in metal preference between the two proteins could be a difference in coordination geometry. As both Zn and Cd are group 12 transition metals, they prefer a tetrahedral coordination (385) such as in the *E. coli* YiiP protein (414). All other metals tested by Lin et al. (385) were not transported by ZIPB, likely because they favor higher coordination numbers. Mn^{2+} prefers octahedral coordination (415) and the different charge in the M2 site may allow for increased access of water or other residues and thus a higher possible coordination number. We plan to generate an N173Q mutant to test the plasticity of metal coordination sphere, as the additional carbon in the side chain may affect position of the metal but not charge.

It is also possible that the difference in these two residues are not as important as we believe and some other difference in structure or composition may be responsible for the difference in selectivity. For example, Rogers et al. (416) mapped the selectivity of Irt1 from an *Arabidopsis* plant to the extracellular loop between TMDs II and III. The TmpA E240 mutants from this region did not show a change in transport function (Figure 6.20-22) but it is still possible that there are other residues in this region that are responsible for the difference in selectivity.

Conclusions

In conclusion, we discovered that this ZIP family protein, TmpA, contributes to Mn uptake and aerobic growth in several strains of *S. sanguinis*. Transcription is likely constitutive although we were unsuccessful in determining whether there are any post-transcriptional modifications, such as cleavage of a signal sequence. TmpA also contributes to virulence in both SK36 and VMC66 when SsaACB is absent, highlighting the importance of Mn in IE virulence. We have identified a key residue in the M2 binding site that is important for

metal transport and may contribute to the preference of TmpA to Mn over Zn and Fe, although we found some evidence that it may also transport those metals as well. We plan to test metal transport in a chemically defined medium in order to confirm our previous results in undefined media. Future studies using cell-free metal uptake assays and structural analysis will be required to solidify our hypotheses.

Materials and Methods

Bacterial strains and growth conditions

The *S. sanguinis* strains used in this study are listed in Table S6.1. Primers and plasmids used to generate the mutant strains are listed in Tables S6.2 & S6.3, respectively. *S. sanguinis* strains SK36, SK49, SK408, and SK678 are human isolates from Mogens Killian, Aarhus University, Denmark, characterized for virulence previously (83). VMC66 is a human blood isolate from Virginia Commonwealth University Medical Center Hospital (82, 83). The Δ*tmpA* strains were derived from SK36 and Δ*ssaACB*::*tetM* (JFP173), where *tmpA* was replaced with *aphA-3* using the SSX_1413 strain and primers from the SK36 knockout mutant library (85). The quadruple mutant version was grown on BHI plates with 10 µM $MnSO_4$ added. The markerless mutant strains were made using the IFDC as described in Chapter 2.The complemented *tmpA* strain was generated using gene SOEing (159), which placed the *tmpA* gene under control of the Phyper-spank promoter and downstream of the Spc resistance cassette, *aad9.* This construct was inserted into the SSA_0169 gene (176).

Due to conflicts with antibiotic resistance, strain JFP234 was generated by amplifying the *aad9* gene and flanking DNA from the SSA_0169 locus in strain JFP56 and introducing this product into JFP173 by transformation, thus generating a Δ*ssaACB* mutant that is

Spc^R to allow for selective plating in rabbit experiments. JFP36 is a previously generated marked WT strain (176).

The Δ*ssaACB,* Δ*tmpA,* and Δ*mntH* mutant strains not already described were generated by using gene SOEing with primers specific to each strain background when identical primers were not possible. Due to naturally occurring antibiotic resistance (Table 6.2), the *tetM* gene was used to generate the Δ*tmpA* mutant of SK49. Because the SSA_0169 ectopic expression site from strain SK36 described above is not present in most other backgrounds examined, we recently identified and validated a new, highly conserved ectopic expression site into which the *aad9* gene was inserted (83). For the *in vivo* rabbit experiments with VMC66, the previously constructed Spc^R derivative (83) was used as the marked WT strain to facilitate selective plating. Due to issues with overlapping antibiotic selection markers, a new Δ*ssaACB* Δ*tmpA* mutant strain was generated just for the rabbit virulence study that was Cm^R and Erm^R. Given that both Δ*ssaACB* Δ*tmpA* and Δ*ssaACB* Δ*mntH* were Cm^R, they were plated on Erm and Tet plates, respectively.

Table 6.2 Natural antibiotic resistance in *S. sanguinis* strains

	SK36	SK49	SK408	SK678	VMC66
Kan	Sensitive	Sensitive	Sensitive	Sensitive	Sensitive
Tet	Sensitive	Sensitive	Resistant	Sensitive	Sensitive
Spc	Sensitive	Sensitive	Sensitive	Sensitive	Sensitive
Erm	Sensitive	Resistant	Sensitive	Sensitive	Sensitive

Growth studies

Either pooled rabbit serum, BHI, or Chelex-treated BHI supplemented with 1 mM $CaCl_2$ and 1 mM $MgSO_4$ (cBHI) was pre-incubated at 37°C at either 0%, 1%, 6%, or 12% O_2 as described in Chapter 2. For experiments in which a metal was added, we employed the Puratronic™ line of metals (Alfa Aesar; $MnSO_4 \cdot H2O$, $FeSO_4 \cdot H2O$, and $ZnSO_4 \cdot H2O$;

99.999% guaranteed purity). Each solution was made in Chelex-treated (BioRad) deionized water (cdH_2O) and added to the serum tubes immediately prior to inoculation. Fe^{2+} stocks were made fresh immediately prior to each experiment. For growth assessment of the complemented mutant, 1 mM IPTG (Fisher Scientific) was added to the serum tubes immediately prior to inoculation. For the Δ*adcC* mutant experiments, 1 µM TPEN (Sigma-Aldrich) and either 1 µM $ZnSO_4$ or $MnSO_4$ was added to the cBHI immediately prior to inoculation.

For drug studies, overnight pre-cultures of WT or Δ*ssaACB* strains were grown as described above and diluted 10-fold into fresh BHI containing the indicated concentration of yohimbine (Lloyd) ± 10 µM $MnSO_4$ in 96-well microtiter plates (Grenier). Cultures were then incubated at atmospheric oxygen concentrations and 37°C for 20 h and read with a microplate reader (BioTek, Inc).

Metal analysis

Overnight bacterial cultures were grown as described above. Two tubes containing 38 mL BHI or cBHI were incubated at 37°C for each experimental condition. For anaerobic studies, media was pre-incubated in an anaerobic chamber (Coy Laboratory Products) for at least 36 hours prior to inoculation. For aerobic studies, the tubes were placed in the incubator without an Anoxomat jar. The following day, 3 mL of the overnight culture was used to inoculate each 38-mL media tube. Puratronic™ metals were prepared as described above and added immediately prior to inoculation. Inoculated cultures were placed back in the incubator. At mid-log phase growth (OD_{600} ~0.6), cells were harvested by centrifugation at 3,740 x *g* for 10 min at 4°C. The samples were then processed as described in Chapter 2.

Fermentor growth

We grew Δ*ssaACB* Δ*tmpA* mutant cells similar to the methods described in Chapter 2, Puccio and Kitten (163), and Puccio et al. (202). We modified it slightly by adding Mn (500 µM final concentration) to the fermentor vessel. The 5 L of BHI in the carboy did not contain Mn, thus diluting out the excess Mn. We also completed these experiments before we optimized the final experimental design so instead of stepwise air flow increased, the DO probe automatically detected pO_2 levels and adjusted the air flow to attempt to maintain 5% O_2 (with maximum air flow set to 1.5 lpm). Media input was set to 7.5% and output was set to 20%.

Yeast complementation assays

We cloned an *S. cerevisiae* codon-optimized version of the *tmpA* gene (Bio Basic) into the pFL38 vector with or without an HA-tag. These plasmids were then used to transform either the WT or various metal transporter mutants as seen in Table S6.1. A 5-mL synthetic defined media (SD-uri) starter culture of 5 separate yeast transformants was inoculated and grown overnight at 30°C. The next day the OD_{600} of each starter culture was read and used to calculate how much of each starter culture is needed to inoculate the growth culture. A 5-mL tube of limited zinc media (LZM; 10 µM $FeCl_3$ and 25 µM $MnCl_2$ added) was supplemented with low and high metals (final concentrations in low vs high conditions: Zn: 100 µM and 1000 µM; Fe: 10 µM and 1010 µM; and Mn: 25 µM and 125 µM). For conditions where Fe or Mn was added, 100 µM Zn was included in the media as well. The cultures are then grown at 30°C for a period of time specific to each strain and absorbance (595 nm) was measured.

For metal analysis, 25 mL of cells were grown in LZM with indicated metals added to the OD_{600} in Figure 6.17. Cultures were prepped for ICP-OES and BCA as described in Chapter 2, except that the BCA was run on 0.5 mL concentrated cell culture.

In vivo virulence assays

Virulence assays were performed using a rabbit model of infective endocarditis (160). Specific pathogen-free New Zealand white rabbits weighing 2-4 kg were purchased from RSI Biotechnology and Charles River Laboratories. We allowed them to acclimate to the vivarium at least 7 days prior to inoculation. The rabbits were anesthetized and a 19-gauge catheter (BD Bioscience) was inserted through the right internal carotid artery past the aortic valve to cause minor damage. The catheter was trimmed, sutured in place, and remained in the artery for the entire experiment. The incision was closed with staples. Two days following catheterization, *S. sanguinis* experimental strains were grown overnight in BHI at 1% or 6% O_2, diluted 10-fold into fresh BHI, incubated for 3 h, sonicated, washed and resuspended in PBS. The inoculum was further diluted in PBS to obtain desired cell concentrations and 0.5 mL of combined culture was inoculated via intravenous injection into an ear vein. Spare inoculum culture was plated on BHI agar with appropriate antibiotics for bacterial counts. At 20 h post-inoculation, rabbits were euthanized by intravenous injection of Euthasol (Virbac AH). Following removal of the heart, catheter placement was verified and vegetations were removed. Vegetations were homogenized with PBS, sonicated, diluted, and plated on BHI agar with appropriate antibiotics as above. The results were reported as recovered CFU per rabbit for each strain and normalized to inocula ratios. All animal procedures were approved by Virginia

Commonwealth University Institutional Animal Care and Use Committee and complied with applicable federal and institutional guidelines.

Quantitative real time polymerase chain reaction

Overnight cultures of SK36 and Δ*ssaACB* (JFP169) were grown as described above. They were then diluted 10-fold into BHI incubated aerobically (~21% O_2). Once cells reached mid-log phase (OD_{600} ~0.6), 6 mL of culture was separated into tubes for each condition and either 100 µM Puratronic^{TM} metal ($MnSO_4$, $ZnSO_4$, or $FeSO_4$) or EDTA (Invitrogen) was added. A culture tube with no additives was included as the control. Tubes were incubated at 37°C in 21% O_2 for 15 min. To collect cells, the tubes were swirled in freezing ethanol for 30 s prior to centrifugation for 10 min at 3,740 x *g* at 4°C. The supernatant was discarded and the samples stored at -80°C. In some experiments, overnight cultures of SK36 and JFP169 were grown in an anaerobic chamber (Coy Laboratory Products). Cells were then diluted 10-fold into BHI pre-incubated anaerobically at 37°C. At mid-log phase, cultures were separated and 6 mL of cells were collected immediately and 6 mL of cells were incubated aerobically (~21% O_2) for 15 min. Cells were collected as above. RNA isolation, cDNA preparation, and qRT-PCR were completed as described in Chapter 2 using primers in Table 6.3.

Table 6.3 qRT-PCR primers

Name	Sequence	Source or Reference
gapA-FWD	GCTTTCCGTCGTATCCAAAA	Rodriguez et al. (84)
gapA-RVS	ACACCGTCAGTAGCCCAGTC	
SSA_1413_qPCR_F1	AAAGGCTTCTGGACTAGGATTG	This study
SSA_1413_qPCR_R1	GCTCTGCTCTTCTTAGCCATTA	
ssaB_qPCR_F1	CATCGCTGACAGCATAGTAGTC	This study
ssaB_qPCR_R1	TCTGGAAACTGGCGGTAATG	
aphA-3_qPCR_F1	CATCATAGGTGGTCCCTTTATACC	This study
aphA-3_qPCR_R1	GGAAGGAATGTCTCCTGCTAAG	
sodA_qPCR_F1	GAATGTTAATGCTGCGCTTGA	Puccio et al. (202)
sodA_qPCR_R1	CTGACGGATATCAGCAGGAATAG	

Protein visualization in *S. sanguinis*

For all methods, overnight cultures were diluted into fresh BHI, incubated for 3 h and harvested by centrifugation (130). We first attempted our standard protocol, as described in Crump et al. (130), where we washed and resuspended cells in PBS, mechanically disrupted cells (as described above) and determined protein concentrations using a BCA kit (Pierce). We then heated the samples for 5 min at 95°C after diluting in Laemmli's sample buffer (Bio-Rad) and loaded them onto a 12.5% pre-cast SDS denaturing gel (Bio-Rad). The gel was then transferred to a nitrocellulose or PVDF membrane and blocked with Intercept (PBS) Blocking Buffer (Licor). The membrane was then probed with either anti-FLAG (MilliporeSigma), anti-Strep Tag® II (Novagen), or anti-6X His Tag (Invitrogen) antibodies in PBS + 0.1% Tween-20 (PBS-T). After washing 4X with PBS-T, primary antibodies were detected using anti-mouse IRDye® 800CW antibodies (Licor) on an Odyssey® CLx Imagining System (Licor) with a Chameleon® Duo Pre-Stained Ladder (Licor).

In some experiments, we followed the K. Zuobi-Hasona (413) protocol for isolation and solubilization of cellular membrane proteins. Briefly, 50-mL cells was grown, harvested,

and collected by centrifugation. Cells were washed in Buffer A (10 mM Tris-HCl [pH 6.8], 10 mM $MgSO_4$, 25% sucrose) before digestion with mutanolysin (Sigma-Aldrich) and lysozyme (ICN Biomedicals Inc) with protease inhibitor (Sigma-Aldrich) at 37°C for 1.5 h. After centrifugation, the protoplasts were washed with Buffer A twice, then resuspended in osmotic lysis buffer (50 mM Tris [pH 7.5], 10 mM MgSO4, and 0.8 M NaCl) with DNase, RNase, and protease inhibitor added. Protoplasts were incubated at RT for 30 min, then sonicated twice at the highest setting for 10 s before centrifugation. The pellet was then resuspended and mechanically disrupted for 3 cycles (6 m/s for 1 min). Protoplasts were then centrifuged with a tabletop centrifuge for 30 min and fractions were assessed by western or dot blot. Alternatively, 1 L of cells were cultured and digested with mutanolysin/lysozyme before homogenized by an Emulsiflex Homogenizer. The supernatant was then ultracentrifuged to separate the membrane fraction from the cellular fraction. As membrane proteins are sometimes sensitive to heat *(communication with Charles Wang)*, samples were not heated prior to gel loading/blotting unless indicated and instead were incubated at RT for 15 min. In some cases, we attempted to purify Strep-Tag® II proteins using a Strep-Tactin® gravity flow column (IBA Life Sciences).

Protein expression in *E. coli*

We cloned an *E. coli* codon-optimized *tmpA* gene (BioBasic) into pET20b, pET26, and pHIS2 vectors. We then transformed CD41 (DE3), CD43 (DE3), and BL21 strains in 2XYT media (Sigma Aldrich) and plated on Luria broth (LB) plates with the appropriate antibiotics. We tested expression in LB by adding 200 µM IPTG and incubating in shaking flasks for 1 h. We also grew cells in auto-induction media (417) for ~36 h. We selected CD41(DE3) cells with the pET20b vector for further fractionation. Cells were collected by

centrifugation, then resuspended in PBS with phenylmethylsulfonyl fluoride (PMSF) and DNase before being subjected to the Emulsiflex Homogenizer. The supernatant was then subjected to ultracentrifugation to isolation the membrane fraction. Membrane proteins were then solubilized in either 0.5% or 0.05% n-Dodecyl-β-D-Maltoside (DDM; Anatrace). DDM-solubilized fractions were further separated by ultracentrifugation and purified on a Ni-column with a stepwise-flow. Further purification with a Q-Sepharose column was attempted but the protein was not purified for unknown reasons. Ni-column purified protein fractions were concentrated on a 10 kDa membrane and run on a gel. The gel was then brought to the Purdue Mass Spectrometry Core Facility, where the bands were purified and analyzed as compared to the expected protein sequence.

Protein modeling and depiction

Alignment of TmpA, BmtA, and ZIPB was completed using Geneious 11.1 (geneious.com). Transmembrane domains were based on the α-helices of the crystal structure of ZIPB (5TSA). Depictions of ZIPB and TmpA in 2D were generated in Protter (394) and modified to match the TMDs determined by the Geneious alignment. The signal sequence of TmpA was predicted using Signal P 5.0 (397) set to gram-positive organisms. Protein models were built in SYBYL-X 2.0. The alignment of TmpA TMD III was adjusted to best fit ZIPB TMD III due to the differences in length, although a “bridge” still is present where a helix should be. The N-terminus and loop between TMDs III and IV were removed from the alignment since they were not present in the crystal structure due to inherent disorder.

Water molecules and metal ions were removed from the ZIPB protein (PDB: 5TSA) and hydrogen atoms were retained. One hundred models were built and one was chosen

based on RMSD, GA 341 scores, DOPE scores, Ramachandran plots. Once a model of TmpA was chosen, residue N173 was replaced with D and the model was minimized with hydrogens with 10,000 iterations, a gradient of 0.5 and Gastieger-Huckel charge. Channel shape was estimated in SYBYL-X using “Find Pockets” feature. Metal ions in the crystal structure were replaced with Mn and models were built as described above. Distances between Q207 in the crystal structure and in the model were measured.

Positions within a cellular membrane were predicted using OPM (https://opm.phar.umich.edu/) and visualized in JMol 3.0 using FirstGlance (http://jmol.sourceforge.net/).

Gene neighborhood and phylogenetic tree

The gene neighborhood of TmpA was assessed using PATRIC v 3.6.2 (165). The top 50 hits were displayed.

The evolutionary history of Mn transport proteins was inferred using the Neighbor-Joining method (409) with a gap opening penalty of 3.0 and a gap extension penalty of 1.8 for the multiple alignment stage (418). The evolutionary distances were computed using the Poisson correction method (410) and are in the units of the number of amino acid substitutions per site. All ambiguous positions were removed for each sequence pair. Evolutionary analyses were conducted in MEGAX (411). 16S rRNA groups of streptococci, with the exception of *S. ratti*, were labeled based on the review published by Nobbs et al. (23).

Chapter 7 General Discussion

Mn has been appreciated as an important nutrient for microbial growth and virulence for decades. Mn is especially important in bacterial species that grow in aerobic environments because it does not cause oxidative damage through Fenton chemistry. Additionally, it is capable of acting as an antioxidant under certain conditions, making it ideal for aerobic growth. The main drawback to the utilization of Mn is its poor binding affinity, which makes proteins that bind Mn especially susceptible to mismetallation.

Until recently, methods for identifying Mn-dependent enzymes and pathways have been limited due to the low affinity of Mn compared to other metals as well as limitations in ‘omics technologies and culture methods. In the first transcriptomic study of Mn depletion in streptococci using a microarray, only 12 genes were differentially expressed in *S. pneumoniae* in low-Mn conditions (173). A recent study using batch cultures of *S. mutans* identified 95 differentially expressed genes in low Mn (148). In Chapter 3, we determined that 407 genes were differentially regulated in the Δ*ssaACB* Mn-transporter mutant 50 min after Mn depletion. This indicates that we have captured a more thorough snapshot of changes in the transcriptome. Additionally, the use of large-scale growth in a fermentor under controlled conditions allowed for real-time monitoring of cell density and highly reproducible results. While the use of the non-specific chelator EDTA was not ideal, we were able to confirm that Mn was the only metal significantly decreased after EDTA addition under these conditions. Additionally, we observed some of the same transcriptomic trends after pH reduction, which was also a Mn-deplete condition for Δ*ssaACB* mutant cells.

While we were unable to identify a lone key enzyme or pathway that led to the reduced growth rate of *S. sanguinis* in low Mn, we found that many of the differentially expressed genes in our study were either confirmed members of the CcpA-regulon (229) or had putative upstream *cre* sites, indicating that there may be a dysregulation of CCR. Previous studies in bacteria have linked Mn to glycolysis and CCR but in our analysis of the metabolome of cells under identical conditions in Chapter 4, we observed that there was an accumulation of the glycolytic metabolite FBP. As FBP is a mediator of CcpA-dependent CCR, we hypothesize that its accumulation is what led to the misregulation of the CcpA regulon. This led to downstream effects on not only carbon metabolism but also nucleotide and redox metabolism. It also appears that genes involved in amino acid metabolism and uptake were affected by Mn depletion in order to compensate for the negative impact on glycolysis. These changes all may have contributed to the decreased cell growth rate in the fermentor post-Mn depletion.

Two enzymes can metabolize FBP, Fba and Fbp. Neither has been studied yet in streptococci, although we hypothesize that they both may be Mn-cofactored given the accumulation of FBP in Mn-depleted cells (Chapter 4) and the presence of Mn-cofactored orthologs in other organisms. We plan to examine the activity of these enzymes *in vitro* using heterologously expressed proteins in the presence of Mn and other metals. We are also unaware of how much this increase in CCR contributes to the poor growth phenotype and whether it impacts virulence. However, Fba was determined to be an essential gene (85), which highlights its importance in *S. sanguinis*. Studies evaluating the impact of increased repression will be required to fully understand the contribution of CCR to *S. sanguinis* growth.

Acid tolerance is an important trait for survival in the oral cavity. *S. sanguinis* can tolerate certain levels of acid but loss of Δ*ssaACB* led to reduced growth in low pH. We determined that this is due to reduced Mn levels in cells grown in low pH, indicating that Mn transport by a secondary transporter is likely inhibited by low pH. We also observed that low pH led to some similar transcriptomic changes in Δ*ssaACB* as when the mutant was treated with EDTA, confirming that much of the poor growth phenotype was primarily due to the reduction in Mn levels. There were some key differences as well, indicating that there are some transcriptomic responses that are specific to acid. Interestingly, the transcriptome of the WT strain was similar to that of the mutant at all time points, with only a few differences pre-acid and at 50 min post-acid. This contrasts with the drastic difference observed in the growth rate of the two strains. These results indicate that the Δ*ssaACB* mutant dropped below the minimum threshold of Mn for sustaining its growth rate and a combination of small differences led to the difference in growth phenotype.

These results are important for expanding our knowledge of stress tolerance in *S. sanguinis* but require more experiments to determine how Mn depletion affects survival in the oral cavity. Future studies focusing on the role of Mn in colonization in an oral mouse model and competition against *S. mutans* are planned for the near future. Additionally, we would like to examine the impact of low pH on CCR by quantifying FBP levels in acid-treated cells.

Our discovery of the role of a ZIP family protein, TmpA, in Mn transport is important for not only streptococci but also other Mn-centric organisms, such as *B. burgdorferi*. While loss of TmpA alone did not affect virulence, it exacerbated the virulence reduction observed in an Δ*ssaACB* mutant. This indicates that if drugs are found for these

transporters, they could be used in combination in order to prevent potential antibiotic resistance. We were able to confirm that several of the metal binding sites found in the crystallized ZIPB protein from *B. bronchiseptica* were important for transport in the *S. sanguinis* version. Unfortunately, we were unable to visualize the protein by western blot nor obtain enough heterologously expressed protein in order to complete *in vitro* transport studies. Membrane proteins are notoriously difficult to work with and we acknowledged when proposing this project that this could be a possibility, although we were hopeful that with the help of membrane protein experts and advances in expression techniques and reagents, we would be successful. We were at least able to provide strong evidence supporting Mn transport *in vivo* and once technology progresses, we may one day be able to determine its activity *in vitro*. We were unable to confirm whether TmpA transports Fe or Zn in *S. sanguinis*, although some evidence appears to suggest the possibility. We confirmed that the loss of the putative *adcC* gene decreased Zn levels and growth in Zn-limited conditions but we have yet to characterize any Fe transporters besides SsaACB. Future studies are required to find a condition or medium in which we can determine whether TmpA also transports Zn or Fe.

In conclusion, we have confirmed that Mn is important for *S. sanguinis* as both an opportunistic endocarditis pathogen and possibly as an oral commensal. Although IE is a rare disease, it can be fatal and the rising incidence of antibiotic-resistant infections leads us to consider the ethics of prescribing broad-spectrum antibiotics to at-risk populations prior to every dental procedure. This study has confirmed SsaACB and identified TmpA as drug targets for not only *S. sanguinis* but possibly for other IE pathogens as well, including staphylococci and other viridans streptococci. It also firmly establishes ZIP

proteins as a fourth category of bacterial Mn transporters, with at least three species using a ZIP family protein as a route for Mn transport. We have also identified several putative Mn-dependent enzymes that are likely important for growth (Figure 7.1). We have laid the groundwork for many future studies into the relationship between Mn and the many pathways it influences in *S. sanguinis*.

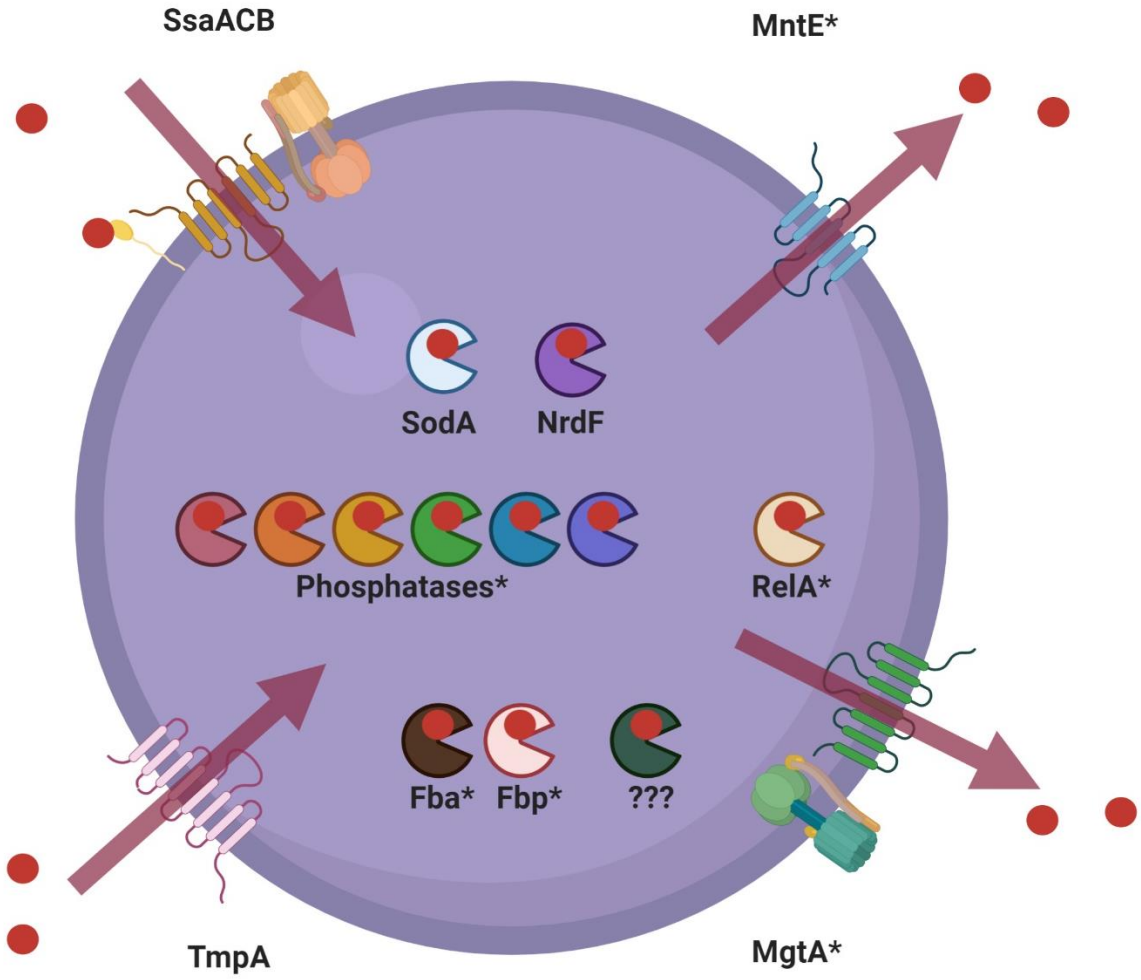

Figure 7.1 Summary of Mn-binding proteins in *S. sanguinis*
Representation of a single *S. sanguinis* cell with confirmed and predicted Mn-binding proteins. Red circles indicate Mn ions. Arrows indicate direction of transport in or out of the cell across the cellular membrane. Enzymes are depicted as multi-colored circles within cell. Transporters are depicted with putative TMDs and other components, such as the ATPase and lipoprotein components of SsaACB. Protein labels with asterisks indicate that Mn-binding capabilities and functions are predicted from other species and need to be confirmed in *S. sanguinis*. There may be more Mn-binding proteins that have yet to be identified. Figure was generated with Biorender.com.

Literature Cited

1. Aas JA, Paster BJ, Stokes LN, Olsen I, Dewhirst FE. 2005. Defining the normal bacterial flora of the oral cavity. J Clin Microbiol 43:5721-32.
2. Baker JL, Bor B, Agnello M, Shi W, He X. 2017. Ecology of the oral microbiome: Beyond bacteria. Trends Microbiol 25:362-374.
3. Chen T, Yu WH, Izard J, Baranova OV, Lakshmanan A, Dewhirst FE. 2010. The Human Oral Microbiome Database: a web accessible resource for investigating oral microbe taxonomic and genomic information. Database (Oxford) 2010:baq013.
4. Dewhirst FE, Chen T, Izard J, Paster BJ, Tanner AC, Yu WH, Lakshmanan A, Wade WG. 2010. The human oral microbiome. J Bacteriol 192:5002-17.
5. Gevers D, Knight R, Petrosino JF, Huang K, McGuire AL, Birren BW, Nelson KE, White O, Methe BA, Huttenhower C. 2012. The Human Microbiome Project: a community resource for the healthy human microbiome. PLoS Biol 10:e1001377.
6. Lamont RJ, Koo H, Hajishengallis G. 2018. The oral microbiota: dynamic communities and host interactions. Nat Rev Microbiol 16:745-759.
7. Marsh PD, Do T, Beighton D, Devine DA. 2016. Influence of saliva on the oral microbiota. Periodontology 2000 70:80-92.
8. Costalonga M, Herzberg MC. 2014. The oral microbiome and the immunobiology of periodontal disease and caries. Immunol Lett 162:22-38.
9. Jorth P, Turner KH, Gumus P, Nizam N, Buduneli N, Whiteley M. 2014. Metatranscriptomics of the human oral microbiome during health and disease. MBio 5:e01012-14.
10. Belda-Ferre P, Alcaraz LD, Cabrera-Rubio R, Romero H, Simon-Soro A, Pignatelli M, Mira A. 2012. The oral metagenome in health and disease. ISME J 6:46-56.
11. Mark Welch JL, Dewhirst FE, Borisy GG. 2019. Biogeography of the oral microbiome: The site-specialist hypothesis. Annu Rev Microbiol 73:335-358.
12. Mark Welch JL, Rossetti BJ, Rieken CW, Dewhirst FE, Borisy GG. 2016. Biogeography of a human oral microbiome at the micron scale. Proc Natl Acad Sci U S A 113:E791-800.
13. Mager DL, Ximenez-Fyvie LA, Haffajee AD, Socransky SS. 2003. Distribution of selected bacterial species on intraoral surfaces. J Clin Periodontol 30:644-54.
14. Abranches J, Zeng L, Kajfasz JK, Palmer SR, Chakraborty B, Wen ZT, Richards VP, Brady LJ, Lemos JA. 2018. Biology of Oral Streptococci. Microbiol Spectr 6.
15. Jakubovics NS, Yassin SA, Rickard AH. 2014. Community interactions of oral streptococci. Adv Appl Microbiol 87:43-110.
16. Ferretti J KW. 2016. History of streptococcal research. *In* Ferretti JJ SD, Fischetti VA (ed), *Streptococcus pyogenes*: Basic biology to clinical manifestations. University of Oklahoma Health Sciences Center, Oklahoma City, OK.
17. Shottmuller H. 1903. Die Artunterscheidung der fur den menschen Pathogen Streptokokken durch Blutagar. Munch Med Wochenschr 50:849-853.
18. Becker WC. 1916. The necessity of a standard blood-agar plate for the determination of hemolysis by streptococci. J Infect Dis 19:754-759.
19. Brown JH. 1919. The use of blood agar for the study of streptococci vol 9. Rockefeller Institute for Medical Research, New York.
20. Lancefield RC. 1933. A serological differentiation of human and other groups of hemolytic streptococci. J Exp Med 57:571-595.
21. Facklam R. 2002. What happened to the streptococci: overview of taxonomic and nomenclature changes. Clin Microbiol Rev 15:613-30.
22. Sherman JM. 1937. The streptococci. Bacteriological Reviews 1:3-97.

23. Nobbs AH, Lamont RJ, Jenkinson HF. 2009. *Streptococcus* adherence and colonization. Microbiol Mol Biol Rev 73:407-50, Table of Contents.
24. Bishop CJ, Aanensen DM, Jordan GE, Kilian M, Hanage WP, Spratt BG. 2009. Assigning strains to bacterial species via the internet. BMC Biol 7:3.
25. Kolenbrander PE, Palmer RJ, Jr., Periasamy S, Jakubovics NS. 2010. Oral multispecies biofilm development and the key role of cell-cell distance. Nat Rev Microbiol 8:471-80.
26. Kolenbrander PE, Jr RJP, Rickard AH, Jakubovics NS, Chalmers NI, Diaz PI. 2006. Bacterial interactions and successions during plaque development. Periodontology 2000 42:47-79.
27. Griffen AL, Beall CJ, Campbell JH, Firestone ND, Kumar PS, Yang ZK, Podar M, Leys EJ. 2012. Distinct and complex bacterial profiles in human periodontitis and health revealed by 16S pyrosequencing. ISME J 6:1176-85.
28. Abusleme L, Dupuy AK, Dutzan N, Silva N, Burleson JA, Strausbaugh LD, Gamonal J, Diaz PI. 2013. The subgingival microbiome in health and periodontitis and its relationship with community biomass and inflammation. ISME J 7:1016-25.
29. Richards VP, Alvarez AJ, Luce AR, Bedenbaugh M, Mitchell ML, Burne RA, Nascimento MM. 2017. Microbiomes of site-specific dental plaques from children with different caries status. Infect Immun 85.
30. Gross EL, Beall CJ, Kutsch SR, Firestone ND, Leys EJ, Griffen AL. 2012. Beyond *Streptococcus mutans*: Dental caries onset linked to multiple species by 16S rRNA community analysis. PLoS One 7:e47722.
31. Moreillon P, Que YA, Bayer AS. 2002. Pathogenesis of streptococcal and staphylococcal endocarditis. Infect Dis Clin North Am 16:297-318.
32. Widmer E, Que Y-A, Entenza JM, Moreillon P. 2006. New concepts in the pathophysiology of infective endocarditis. Curr Infect Dis Rep 8:271–279.
33. Lee S, Kim K-K, Choe S-J. 2001. Binding of oral streptococci to human fibrinogen. Oral Microbiol Immunol 16:88-93.
34. Bor DH, Woolhandler S, Nardin R, Brusch J, Himmelstein DU. 2013. Infective endocarditis in the U.S., 1998-2009: a nationwide study. PLoS One 8:e60033.
35. Jamil M, Sultan I, Gleason TG, Navid F, Fallert MA, Suffoletto MS, Kilic A. 2019. Infective endocarditis: trends, surgical outcomes, and controversies. J Thorac Dis 11:4875-4885.
36. Cahill TJ, Baddour LM, Habib G, Hoen B, Salaun E, Pettersson GB, Schafers HJ, Prendergast BD. 2017. Challenges in infective endocarditis. J Am Coll Cardiol 69:325-344.
37. Bashore TM, Cabell C, Fowler V, Jr. 2006. Update on infective endocarditis. Curr Probl Cardiol 31:274-352.
38. Morris NA, Matiello M, Lyons JL, Samuels MA. 2014. Neurologic complications in infective endocarditis: identification, management, and impact on cardiac surgery. Neurohospitalist 4:213-22.
39. Nishida M, Imanishi H, Sowa-Osako J, Umeda S, Ito A, Yasumizu D, Yoshiyama M, Tsuruta D. 2020. Bacteremic cellulitis mimicking erythema nodosum caused by *Streptococcus sanguinis* endocarditis. Int J Dermatol doi:10.1111/ijd.14973.
40. Novy E, Sonneville R, Mazighi M, Klein IF, Mariotte E, Mourvillier B, Bouadma L, Wolff M. 2013. Neurological complications of infective endocarditis: new breakthroughs in diagnosis and management. Med Mal Infect 43:443-50.
41. Lucas MJ, Brouwer MC, van der Ende A, van de Beek D. 2013. Endocarditis in adults with bacterial meningitis. Circulation 127:2056-62.
42. Kinane DF, Riggio MP, Walker KF, MacKenzie D, Shearer B. 2005. Bacteraemia following periodontal procedures. J Clin Periodontol 32:708-13.

43. Forner L, Larsen T, Kilian M, Holmstrup P. 2006. Incidence of bacteremia after chewing, tooth brushing and scaling in individuals with periodontal inflammation. J Clin Periodontol 33:401-7.
44. Lockhart PB, Brennan MT, Sasser HC, Fox PC, Paster BJ, Bahrani-Mougeot FK. 2008. Bacteremia associated with toothbrushing and dental extraction. Circulation 117:3118-25.
45. Silver JG, Martin AW, McBride BC. 1977. Experimental transient bacteraemias in human subjects with varying degrees of plaque accumulation and gingival inflammation. J Clin Periodontol 4:92-9.
46. Silver JG, Martin AW, McBride BC. 1979. Experimental transient bacteraemias in human subjects with clinically healthy gingivae. J Clin Periodontol 6:33-6.
47. Moreillon P, Que Y-A. 2004. Infective endocarditis. The Lancet 363:139-149.
48. Sreenivasan PK, Tischio-Bereski D, Fine DH. 2017. Reduction in bacteremia after brushing with a triclosan/copolymer dentifrice-A randomized clinical study. J Clin Periodontol 44:1020-1028.
49. Kholy KE, Genco RJ, Van Dyke TE. 2015. Oral infections and cardiovascular disease. Trends Endocrinol Metab 26:315-21.
50. Lockhart PB, Brennan MT, Thornhill M, Michalowicz BS, Noll J, Bahrani-Mougeot FK, Sasser HC. 2009. Poor oral hygiene as a risk factor for infective endocarditis-related bacteremia. J Am Dent Assoc 140:1238-44.
51. Dhotre S, Jahagirdar V, Suryawanshi N, Davane M, Patil R, Nagoba B. 2018. Assessment of periodontitis and its role in viridans streptococcal bacteremia and infective endocarditis. Indian Heart J 70:225-232.
52. Moss R, Munt B. 2003. Injection drug use and right sided endocarditis. Heart 89:577-81.
53. Ji Y, Kujtan L, Kershner D. 2012. Acute endocarditis in intravenous drug users: a case report and literature review. J Community Hosp Intern Med Perspect 2.
54. Wilson W, Taubert KA, Gewitz M, Lockhart PB, Baddour LM, Levison M, Bolger A, Cabell CH, Takahashi M, Baltimore RS, Newburger JW, Strom BL, Tani LY, Gerber M, Bonow RO, Pallasch T, Shulman ST, Rowley AH, Burns JC, Ferrieri P, Gardner T, Goff D, Durack DT. 2007. Prevention of infective endocarditis: Guidelines from the American Heart Association. Circulation 116:1736-54.
55. Richard Bayliss, Cyril Clarke, Celia Oakley, Walter Somerville, Whitfield AGW. 1983. The teeth and infective endocarditis. Br Heart J 50:506-512.
56. Durack DT. 1995. Prevention of infective endocarditis. New Eng Jour Med 332:38-44.
57. Dayer M, Thornhill M. 2018. Is antibiotic prophylaxis to prevent infective endocarditis worthwhile? J Infect Chemother 24:18-24.
58. Thornhill MH, Gibson TB, Cutler E, Dayer MJ, Chu VH, Lockhart PB, O'Gara PT, Baddour LM. 2018. Antibiotic prophylaxis and incidence of endocarditis before and after the 2007 AHA recommendations. J Am Coll Cardiol 72:2443-2454.
59. Quan TP, Muller-Pebody B, Fawcett N, Young BC, Minaji M, Sandoe J, Hopkins S, Crook D, Peto T, Johnson AP, Walker AS. 2020. Investigation of the impact of the NICE guidelines regarding antibiotic prophylaxis during invasive dental procedures on the incidence of infective endocarditis in England: an electronic health records study. BMC Med 18:84.
60. Dodds DR. 2017. Antibiotic resistance: A current epilogue. Biochem Pharmacol 134:139-146.
61. Niven CF, Kiziuta Z, White JC. 1946. Synthesis of a polysaccharide from sucrose by *Streptococcus s.b.e.* J Bacteriol 51:711-6.
62. Niven CF, Jr., White JC. 1946. A study of streptococci associated with subacute bacterial endocarditis. J Bacteriol 51:790.
63. Washburn MR, White JC, Niven CF, Jr. 1946. *Streptococcus s.b.e.*: Immunological characteristics. J Bacteriol 51:723-9.

64. White JC, Niven CF. 1946. *Streptococcus s.b.e*.: A *Streptococcus* associated with subacute bacterial endocarditis.
65. Truper HG, De'clari L. 1997. Taxonomic note: Necessary correction of specific epithets formed as substantives (nouns) “in Apposition”. Int J Syst Bacteriol 47:908-909.
66. Zheng W, Tan MF, Old LA, Paterson IC, Jakubovics NS, Choo SW. 2017. Distinct biological potential of *Streptococcus gordonii* and *Streptococcus sanguinis* revealed by comparative genome analysis. Sci Rep 7:2949.
67. Kilian M, Mikkelsen L, Henrichsen J. 1989. Taxonomic study of viridans streptococci: Description of *Streptococcus gordonii* sp. nov. and emended descriptions of *Streptococcus sanguis* (White and Niven 1946), *Streptococcus oralis* (Bridge and Sneath 1982), and *Streptococcus mitis* (Andrewes and Horder 1906). Int J of Syst Bacteriol 39.
68. Kreth J, Zhang Y, Herzberg MC. 2008. Streptococcal antagonism in oral biofilms: *Streptococcus sanguinis* and *Streptococcus gordonii* interference with *Streptococcus mutans*. J Bacteriol 190:4632-40.
69. Garcia-Mendoza A, Liebana J, Castillo AM, Higuera Adl, Piedrola G. 1993. Evaluation of the capacity of oral streptococci to produce hydrogen peroxide. J Med Microbiol 39:434-439.
70. Xu Y, Itzek A, Kreth J. 2014. Comparison of genes required for H_2O_2 resistance in *Streptococcus gordonii* and *Streptococcus sanguinis*. Microbiology 160:2627-2638.
71. Kreth J, Merritt J, Shi W, Qi F. 2005. Competition and coexistence between *Streptococcus mutans* and *Streptococcus sanguinis* in the dental biofilm. J Bacteriol 187:7193-203.
72. Zhu B, Macleod LC, Newsome E, Liu J, Xu P. 2019. *Aggregatibacter actinomycetemcomitans* mediates protection of *Porphyromonas gingivalis* from *Streptococcus sanguinis* hydrogen peroxide production in multi-species biofilms. Sci Rep 9:4944.
73. Giacaman RA, Torres S, Gomez Y, Munoz-Sandoval C, Kreth J. 2015. Correlation of *Streptococcus mutans* and *Streptococcus sanguinis* colonization and *ex vivo* hydrogen peroxide production in carious lesion-free and high caries adults. Arch Oral Biol 60:154-9.
74. Stingu CS, Eschrich K, Rodloff AC, Schaumann R, Jentsch H. 2008. Periodontitis is associated with a loss of colonization by *Streptococcus sanguinis*. J Med Microbiol 57:495-9.
75. Xu P, Alves JM, Kitten T, Brown A, Chen Z, Ozaki LS, Manque P, Ge X, Serrano MG, Puiu D, Hendricks S, Wang Y, Chaplin MD, Akan D, Paik S, Peterson DL, Macrina FL, Buck GA. 2007. Genome of the opportunistic pathogen *Streptococcus sanguinis*. J Bacteriol 189:3166-75.
76. Socransky SS, Manganiello AD, Propas D, Oram V, Houte JV. 1977. Bacteriological studies of developing supragingival dental plaque. J Periodontal Res 12:90-106.
77. Das S, Kanamoto T, Ge X, Xu P, Unoki T, Munro CL, Kitten T. 2009. Contribution of lipoproteins and lipoprotein processing to endocarditis virulence in *Streptococcus sanguinis*. J Bacteriol 191:4166-79.
78. Turner LS, Kanamoto T, Unoki T, Munro CL, Wu H, Kitten T. 2009. Comprehensive evaluation of *Streptococcus sanguinis* cell wall-anchored proteins in early infective endocarditis. Infect Immun 77:4966-75.
79. Bensing BA, Li L, Yakovenko O, Wong M, Barnard KN, Iverson TM, Lebrilla CB, Parrish CR, Thomas WE, Xiong Y, Sullam PM. 2019. Recognition of specific sialoglycan structures by oral streptococci impacts the severity of endocardial infection. PLoS Pathog 15:e1007896.
80. Bensing BA, Li Q, Park D, Lebrilla CB, Sullam PM. 2018. Streptococcal Siglec-like adhesins recognize different subsets of human plasma glycoproteins: implications for infective endocarditis. Glycobiology 28:601-611.

81. Dayer MJ, Jones S, Prendergast B, Baddour LM, Lockhart PB, Thornhill MH. 2015. Incidence of infective endocarditis in England, 2000-13: a secular trend, interrupted time-series analysis. Lancet 385:1219-28.
82. Kitten T, Munro CL, Zollar NQ, Lee SP, Patel RD. 2012. Oral streptococcal bacteremia in hospitalized patients: taxonomic identification and clinical characterization. J Clin Microbiol 50:1039-42.
83. Baker SP, Nulton TJ, Kitten T. 2019. Genomic, phenotypic, and virulence analysis of *Streptococcus sanguinis* oral and infective-endocarditis isolates. Infect Immun 87:e00703-00718.
84. Rodriguez AM, Callahan JE, Fawcett P, Ge X, Xu P, Kitten T. 2011. Physiological and molecular characterization of genetic competence in *Streptococcus sanguinis*. Mol Oral Microbiol 26:99-116.
85. Xu P, Ge X, Chen L, Wang X, Dou Y, Xu JZ, Patel JR, Stone V, Trinh M, Evans K, Kitten T, Bonchev D, Buck GA. 2011. Genome-wide essential gene identification in *Streptococcus sanguinis*. Sci Rep 1:1-9.
86. Capdevila DA, Edmonds KA, Giedroc DP. 2017. Metallochaperones and metalloregulation in bacteria. Essays Biochem 61:177-200.
87. Chandrangsu P, Rensing C, Helmann JD. 2017. Metal homeostasis and resistance in bacteria. Nat Rev Microbiol 15:338-350.
88. Turner AG, Ong CY, Walker MJ, Djoko KY, McEwan AG. 2017. Transition metal homeostasis in *Streptococcus pyogenes* and *Streptococcus pneumoniae*. Adv Microb Physiol 70:123-191.
89. Grosjean N, Blaby-Haas CE. 2020. Leveraging computational genomics to understand the molecular basis of metal homeostasis. New Phytol doi:10.1111/nph.16820.
90. Honsa ES, Johnson MD, Rosch JW. 2013. The roles of transition metals in the physiology and pathogenesis of *Streptococcus pneumoniae*. Front Cell Infect Microbiol 3:92.
91. Neumann W, Gulati A, Nolan EM. 2017. Metal homeostasis in infectious disease: recent advances in bacterial metallophores and the human metal-withholding response. Curr Opin Chem Biol 37:10-18.
92. Osman D, Foster AW, Chen J, Svedaite K, Steed JW, Lurie-Luke E, Huggins TG, Robinson NJ. 2017. Fine control of metal concentrations is necessary for cells to discern zinc from cobalt. Nat Commun 8:1884.
93. Lopez CA, Skaar EP. 2018. The impact of dietary transition metals on host-bacterial interactions. Cell Host Microbe 23:737-748.
94. Begg SL. 2019. The role of metal ions in the virulence and viability of bacterial pathogens. Biochem Soc Trans 47:77-87.
95. Hood MI, Skaar EP. 2012. Nutritional immunity: transition metals at the pathogen-host interface. Nat Rev Microbiol 10:525-37.
96. Weinberg ED. 1975. Nutritional immunity: Host's attempt to withhold iron from microbial invaders. JAMA 231:39-41.
97. Skaar EP, Raffatellu M. 2015. Metals in infectious diseases and nutritional immunity. Metallomics 7:926-8.
98. Dudev T, Lim C. 2014. Competition among metal ions for protein binding sites: determinants of metal ion selectivity in proteins. Chem Rev 114:538-56.
99. Cotruvo JA, Jr., Stubbe J. 2012. Metallation and mismetallation of iron and manganese proteins *in vitro* and *in vivo*: the class I ribonucleotide reductases as a case study. Metallomics 4:1020-36.
100. Makhlynets O, Boal AK, Rhodes DV, Kitten T, Rosenzweig AC, Stubbe J. 2014. *Streptococcus sanguinis* class Ib ribonucleotide reductase: high activity with both iron and manganese cofactors and structural insights. J Biol Chem 289:6259-72.

101. Rhodes DV, Crump KE, Makhlynets O, Snyder M, Ge X, Xu P, Stubbe J, Kitten T. 2014. Genetic characterization and role in virulence of the ribonucleotide reductases of *Streptococcus sanguinis*. J Biol Chem 289:6273-87.
102. Irving H, Williams RJP. 1953. The stability of transition-metal complexes. J Chem Soc doi:10.1039/JR9530003192:3192-3210.
103. Foster AW, Osman D, Robinson NJ. 2014. Metal preferences and metallation. J Biol Chem 289:28095-103.
104. Makthal N, Kumaraswami M. 2017. Zinc'ing it out: Zinc homeostasis mechanisms and their impact on the pathogenesis of human pathogen group A *streptococcus*. Metallomics 9:1693-1702.
105. Helmann JD. 2014. Specificity of metal sensing: iron and manganese homeostasis in *Bacillus subtilis*. J Biol Chem 289:28112-20.
106. Tottey S, Waldron KJ, Firbank SJ, Reale B, Bessant C, Sato K, Cheek TR, Gray J, Banfield MJ, Dennison C, Robinson NJ. 2008. Protein-folding location can regulate manganese-binding versus copper- or zinc-binding. Nature 455:1138-42.
107. Lisher JP, Giedroc DP. 2013. Manganese acquisition and homeostasis at the host-pathogen interface. Front Cell Infect Microbiol 3:91.
108. Johnson MD, Kehl-Fie TE, Rosch JW. 2015. Copper intoxication inhibits aerobic nucleotide synthesis in *Streptococcus pneumoniae*. Metallomics 7:786-94.
109. Rosch JW, Gao G, Ridout G, Wang YD, Tuomanen EI. 2009. Role of the manganese efflux system *mntE* for signalling and pathogenesis in *Streptococcus pneumoniae*. Mol Microbiol 72:12-25.
110. Eijkelkamp BA, Morey JR, Ween MP, Ong CL, McEwan AG, Paton JC, McDevitt CA. 2014. Extracellular zinc competitively inhibits manganese uptake and compromises oxidative stress management in *Streptococcus pneumoniae*. PLoS One 9:e89427.
111. Fenton HJH. 1894. Oxidation of tartaric acid in presence of iron. J Chem Soc 65:899-910.
112. Pham AN, Xing G, Miller CJ, Waite TD. 2013. Fenton-like copper redox chemistry revisited: Hydrogen peroxide and superoxide mediation of copper-catalyzed oxidant production. J Catal 301:54-64.
113. Sabine DB, Vaselekos J. 1967. Trace element requirements of *Lactobacillus acidophilus*. Nature 214:520.
114. Posey J, Gherardini F. 2000. Lack of a role for iron in the lyme disease pathogen. Science 288:1651-1653.
115. Yamamoto Y, Poole LB, Hantgan RR, Kamio Y. 2002. An iron-binding protein, Dpr, from *Streptococcus mutans* prevents iron-dependent hydroxyl radical formation *in vitro*. J Bacteriol 184:2931-9.
116. Pulliainen AT, Haataja S, Kahkonen S, Finne J. 2003. Molecular basis of H_2O_2 resistance mediated by streptococcal Dpr: Demonstration of the functional involvement of the putative ferroxidase center by site-directed mutagenesis in *Streptococcus suis*. J Biol Chem 278:7996-8005.
117. Kauko A, Haataja S, Pulliainen AT, Finne J, Papageorgiou AC. 2004. Crystal structure of *Streptococcus suis* Dps-like peroxide resistance protein Dpr: implications for iron incorporation. J Mol Biol 338:547-58.
118. Tsou CC, Chiang-Ni C, Lin YS, Chuang WJ, Lin MT, Liu CC, Wu JJ. 2008. An iron-binding protein, Dpr, decreases hydrogen peroxide stress and protects *Streptococcus pyogenes* against multiple stresses. Infect Immun 76:4038-45.
119. Ganguly T, Kajfasz JK, Miller JH, Rabinowitz E, Galvao LCC, Rosalen PL, Abranches J, Lemos JA. 2018. Disruption of a novel iron transport system reverses oxidative stress phenotypes of a *dpr* mutant strain of *Streptococcus mutans*. J Bacteriol 200.

120. Murgas CJ, Green SP, Forney AK, Korba RM, An SS, Kitten T, Lucas HR. 2020. Intracellular metal speciation in *Streptococcus sanguinis* establishes SsaACB as critical for redox maintenance. ACS Infect Dis 6:1906-21.
121. Lingappa UF, Monteverde DR, Magyar JS, Valentine JS, Fischer WW. 2019. How manganese empowered life with dioxygen (and vice versa). Free Radic Biol Med 140:113-125.
122. Waldron KJ, Rutherford JC, Ford D, Robinson NJ. 2009. Metalloproteins and metal sensing. Nature 460:823-30.
123. Waters LS. 2020. Bacterial manganese sensing and homeostasis. Curr Opin Chem Biol 55:96-102.
124. Juttukonda LJ, Skaar EP. 2015. Manganese homeostasis and utilization in pathogenic bacteria. Mol Microbiol 97:216-28.
125. Culotta VC, Daly MJ. 2013. Manganese complexes: diverse metabolic routes to oxidative stress resistance in prokaryotes and yeast. Antioxid Redox Signal 19:933-44.
126. Archibald F. 1982. The scavenging of superoxide radical by manganous complexes: *In vitro*. Arch Biochem Biophys.
127. Barnese K, Gralla EB, Cabelli DE, Valentine JS. 2008. Manganous phosphate acts as a superoxide dismutase. JACS 130:4604-06.
128. Barnese K, Gralla EB, Valentine JS, Cabelli DE. 2012. Biologically relevant mechanism for catalytic superoxide removal by simple manganese compounds. Proc Natl Acad Sci U S A 109:6892-97.
129. Stadtman ER, Berlett BS, Chock PB. 1990. Manganese-dependent disproportionation of hydrogen peroxide in bicarbonate buffer. Proc Natl Acad Sci U S A 87:384-388.
130. Crump KE, Bainbridge B, Brusko S, Turner LS, Ge X, Stone V, Xu P, Kitten T. 2014. The relationship of the lipoprotein SsaB, manganese and superoxide dismutase in *Streptococcus sanguinis* virulence for endocarditis. Mol Microbiol 92:1243-59.
131. Sobota JM, Imlay JA. 2011. Iron enzyme ribulose-5-phosphate 3-epimerase in *Escherichia coli* is rapidly damaged by hydrogen peroxide but can be protected by manganese. Proc Natl Acad Sci U S A 108:5402-7.
132. Anjem A, Imlay JA. 2012. Mononuclear iron enzymes are primary targets of hydrogen peroxide stress. J Biol Chem 287:15544-56.
133. Eijkelkamp BA, McDevitt CA, Kitten T. 2015. Manganese uptake and streptococcal virulence. BioMetals 28:491-508.
134. Kehres DG, Maguire ME. 2003. Emerging themes in manganese transport, biochemistry and pathogenesis in bacteria. FEMS Microbiol Rev 27:263-90.
135. Papp-Wallace KM, Maguire ME. 2006. Manganese transport and the role of manganese in virulence. Annu Rev Microbiol 60:187-209.
136. Kitten T, Munro C, Michalek S, Macrina F. 2000. Genetic characterization of a *Streptococcus mutans* LraI family operon and role in virulence. Infect Immun 68.
137. Dintilhac A, Alloing G, Granadel C, Claverys J-P. 1997. Competence and virulence of *Streptococcus pneumoniae*: Adc and PsaA mutants exhibit a requirement for Zn and Mn resulting from inactivation of putative ABC metal permeases. Mol Microbiol 25:727-739.
138. Ganeshkumar N, Hannam PM, Kolenbrander PE, McBride BC. 1991. Nucleotide sequence of a gene coding for a saliva-binding protein (SsaB) from *Streptococcus sanguis* 12 and possible role of the protein in coaggregation with *Actinomyces*. Infect Immun 59:1093-99.
139. Ganeshkumar N, Arora N, Kolenbrander PE. 1993. Saliva-binding protein (SsaB) from *Streptococcus sanguis* 12 is a lipoprotein. J Bacteriol 175:572-4.
140. Bajaj M, Mamidyala SK, Zuegg J, Begg SL, Ween MP, Luo Z, Huang JX, McEwan AG, Kobe B, Paton JC, McDevitt CA, Cooper MA. 2015. Discovery of novel pneumococcal

surface antigen A (PsaA) inhibitors using a fragment-based drug design approach. ACS Chem Biol 10:1511-20.
141. Obaidullah AJ, Ahmed MH, Kitten T, Kellogg GE. 2018. Inhibiting pneumococcal surface antigen A (PsaA) with small molecules discovered through virtual screening: Steps toward validating a potential target for *Streptococcus pneumoniae*. Chem Biodivers 15:e1800234.
142. Kitten T, Munro CL, Wang A, Macrina FL. 2002. Vaccination with FimA from *Streptococcus parasanguis* protects rats from endocarditis caused by other viridans streptococci. Infect Immun 70:422-5.
143. Golynskiy MV, Davis TC, Helmann JD, Cohen SM. 2005. Metal-induced structural organization and stabilization of the metalloregulatory protein MntR. Biochemistry 44:3380-9.
144. McGuire AM, Cuthbert BJ, Ma Z, Grauer-Gray KD, Brunjes Brophy M, Spear KA, Soonsanga S, Kliegman JI, Griner SL, Helmann JD, Glasfeld A. 2013. Roles of the A and C sites in the manganese-specific activation of MntR. Biochemistry 52:701-13.
145. Kloosterman TG, Witwicki RM, van der Kooi-Pol MM, Bijlsma JJ, Kuipers OP. 2008. Opposite effects of Mn^{2+} and Zn^{2+} on PsaR-mediated expression of the virulence genes *pcpA, prtA,* and *psaBCA* of *Streptococcus pneumoniae*. J Bacteriol 190:5382-93.
146. Jacobsen FE, Kazmierczak KM, Lisher JP, Winkler ME, Giedroc DP. 2011. Interplay between manganese and zinc homeostasis in the human pathogen *Streptococcus pneumoniae*. Metallomics 3:38-41.
147. Shabayek S, Bauer R, Mauerer S, Mizaikoff B, Spellerberg B. 2016. A streptococcal NRAMP homologue is crucial for the survival of *Streptococcus agalactiae* under low pH conditions. Mol Microbiol 100:589-606.
148. Kajfasz JK, Katrak C, Ganguly T, Vargas J, Wright L, Peters ZT, Spatafora GA, Abranches J, Lemos JA. 2020. Manganese uptake, mediated by SloABC and MntH, is essential for the fitness of *Streptococcus mutans*. mSphere 5:e00764-19.
149. Nevo Y, Nelson N. 2006. The NRAMP family of metal-ion transporters. Biochim Biophys Acta 1763:609-20.
150. Velsko IM, Chakraborty B, Nascimento MM, Burne RA, Richards VP. 2018. Species designations belie phenotypic and genotypic heterogeneity in oral streptococci. mSystems 3.
151. Eide DJ. 2012. An "inordinate fondness for transporters" explained? Sci Signal 5:pe5.
152. Xu J, Zheng C, Cao M, Zeng T, Zhao X, Shi G, Chen H, Bei W. 2017. The manganese efflux system MntE contributes to the virulence of *Streptococcus suis* serotype 2. Microb Pathog 110:23-30.
153. O'Brien J, Pastora A, Stoner A, Spatafora G. 2020. The *S. mutans mntE* gene encodes a manganese efflux transporter. Mol Oral Microbiol 35:129-140.
154. Martin JE, Le MT, Bhattarai N, Capdevila DA, Shen J, Winkler ME, Giedroc DP. 2019. A Mn-sensing riboswitch activates expression of a Mn^{2+}/Ca^{2+} ATPase transporter in *Streptococcus*. Nucleic Acids Res 47:6885-6899.
155. Tabares LC, Un S. 2013. *In situ* determination of manganese(II) speciation in *Deinococcus radiodurans* by high magnetic field EPR: detection of high levels of Mn(II) bound to proteins. J Biol Chem 288:5050-5.
156. Bruch EM, Thomine S, Tabares LC, Un S. 2015. Variations in Mn(II) speciation among organisms: what makes *D. radiodurans* different. Metallomics 7:136-44.
157. Tu WY, Pohl S, Gray J, Robinson NJ, Harwood CR, Waldron KJ. 2012. Cellular iron distribution in *Bacillus anthracis*. J Bacteriol 194:932-40.
158. Atkuri KR, Herzenberg LA, Niemi A-K, Cowan T, Herzenberg LA. 2007. Importance of culturing primary lymphocytes at physiological oxygen levels. Proc Natl Acad Sci U S A 104:4547–4552.

159. Ho SN, Hunt HD, Horton RM, Pullen JK, Pease LR. 1989. Site-directed mutagenesis by overlap extension using the polymerase chain reaction. Gene 77:51-9.
160. Paik S, Senty L, Das S, Noe JC, Munro CL, Kitten T. 2005. Identification of virulence determinants for endocarditis in *Streptococcus sanguinis* by signature-tagged mutagenesis. Infect Immun 73:6064-74.
161. Cheng X, Redanz S, Cullin N, Zhou X, Xu X, Joshi V, Koley D, Merritt J, Kreth J. 2018. Plasticity of the pyruvate node modulates hydrogen peroxide production and acid tolerance in multiple oral streptococci. Appl Environ Microbiol 84.
162. Xie Z, Okinaga T, Qi F, Zhang Z, Merritt J. 2011. Cloning-independent and counterselectable markerless mutagenesis system in *Streptococcus mutans*. Appl Environ Microbiol 77:8025-33.
163. Puccio T, Kitten T. 2020. Fermentor growth of *Streptococcus sanguinis*. protocolsio doi:dx.doi.org/10.17504/protocols.io.bkayksfw.
164. Benson DA, Cavanaugh M, Clark K, Karsch-Mizrachi I, Lipman DJ, Ostell J, Sayers EW. 2013. GenBank. Nucleic Acids Res 41:D36-42.
165. Wattam AR, Davis JJ, Assaf R, Boisvert S, Brettin T, Bun C, Conrad N, Dietrich EM, Disz T, Gabbard JL, Gerdes S, Henry CS, Kenyon RW, Machi D, Mao C, Nordberg EK, Olsen GJ, Murphy-Olson DE, Olson R, Overbeek R, Parrello B, Pusch GD, Shukla M, Vonstein V, Warren A, Xia F, Yoo H, Stevens RL. 2017. Improvements to PATRIC, the all-bacterial bioinformatics database and analysis resource center. Nucleic Acids Res 45:D535-D542.
166. Love MI, Huber W, Anders S. 2014. Moderated estimation of fold change and dispersion for RNA-seq data with DESeq2. Genome Biol 15:550.
167. Marini F, Binder H. 2019. pcaExplorer: an R/Bioconductor package for interacting with RNA-seq principal components. BMC Bioinformatics 20:1-8.
168. Blighe K, Rana S, Lewis M. 2018. EnhancedVolcano: Publication-ready volcano plots with enhanced colouring and labeling. https://github.com/kevinblighe/EnhancedVolcano. Accessed January 10, 2020.
169. Dennis G, Jr., Sherman BT, Hosack DA, Yang J, Gao W, Lane HC, Lempicki RA. 2003. DAVID: Database for Annotation, Visualization, and Integrated Discovery. Genome Biol 4:P3.
170. Livak KJ, Schmittgen TD. 2001. Analysis of relative gene expression data using real-time quantitative PCR and the $2^{(-\Delta\Delta CT)}$ method. Methods 25:402-8.
171. Parker MW, Blake CCF. 1988. Iron- and manganese-containing superoxide dismutases can be distinguished by analysis of their primary structures. FEBS Lett 229:377-382.
172. Poyart C, Quesne G, Coulon S, Berche P, Trieu-Cuot P. 1988. Identification of streptococci to species level by sequencing the gene encoding the manganese-dependent superoxide dismutase. Jour Clin Microbiol 36:41-47.
173. Ogunniyi AD, Mahdi LK, Jennings MP, McEwan AG, McDevitt CA, Van der Hoek MB, Bagley CJ, Hoffmann P, Gould KA, Paton JC. 2010. Central role of manganese in regulation of stress responses, physiology, and metabolism in *Streptococcus pneumoniae*. J Bacteriol 192:4489-97.
174. Altschu SF, Gish W, Miller W, Myers EW, Lipman DJ. 1990. Basic Local Alignment Search Tool. J Mol Biol 215:403-410.
175. Baker S. 2019. Examination of strain-dependent differences in *S. sanguinis* virulence and growth. Doctorate of Philosophy. Virginia Commonwealth University.
176. Turner LS, Das S, Kanamoto T, Munro CL, Kitten T. 2009. Development of genetic tools for *in vivo* virulence analysis of *Streptococcus sanguinis*. Microbiology 155:2573-82.
177. Jakubovics NS, Smith AW, Jenkinson HF. 2000. Expression of the virulence-related Sca (Mn^{2+}) permease in *Streptococcus gordonii* is regulated by a diphtheria toxin metallorepressor-like protein ScaR. Mol Microbiol 38:140-153.

178. O'Rourke KP, Shaw JD, Pesesky MW, Cook BT, Roberts SM, Bond JP, Spatafora GA. 2010. Genome-wide characterization of the SloR metalloregulome in *Streptococcus mutans*. J Bacteriol 192:1433-43.
179. Burne RA, Chen Y-YM. 1998. The use of continuous flow bioreactors to explore gene expression and physiology of suspended and adherent populations of oral streptococci. Methods Cell Sci 20:181-190.
180. Martin JE, Giedroc DP. 2016. Functional determinants of metal ion transport and selectivity in paralogous cation diffusion facilitator transporters CzcD and MntE in *Streptococcus pneumoniae*. J Bacteriol 198:1066-1076.
181. Lisher JP, Higgins KA, Maroney MJ, Giedroc DP. 2013. Physical characterization of the manganese-sensing pneumococcal surface antigen repressor from *Streptococcus pneumoniae*. Biochemistry 52:7689-701.
182. Perrin DD, Dempsey B. 1974. Buffers for pH and Metal Ion Control. J. W. Arrowsmith Ltd, Bristol.
183. Dintilhac A, Claverys J-P. 1997. The *adc* locus, which affects competence for genetic transformation in *Streptococcus pneumoniae*, encodes an ABC transporter with a putative lipoprotein homologous to a family of streptococcal adhesins. Res Microbiol 148:119-131.
184. Nies DH. 1992. CzcR and CzcD, gene products affecting regulation of resistance to cobalt, zinc, and cadmium (*czc* system) in *Alcaligenes eutrophus*. J Bacteriol 174:8102-8110.
185. Plumptre CD, Hughes CE, Harvey RM, Eijkelkamp BA, McDevitt CA, Paton JC. 2014. Overlapping functionality of the Pht proteins in zinc homeostasis of *Streptococcus pneumoniae*. Infect Immun 82:4315-24.
186. Bayle L, Chimalapati S, Schoehn G, Brown J, Vernet T, Durmort C. 2011. Zinc uptake by *Streptococcus pneumoniae* depends on both AdcA and AdcAII and is essential for normal bacterial morphology and virulence. Mol Microbiol 82:904-16.
187. Plumptre CD, Eijkelkamp BA, Morey JR, Behr F, Counago RM, Ogunniyi AD, Kobe B, O'Mara ML, Paton JC, McDevitt CA. 2014. AdcA and AdcAII employ distinct zinc acquisition mechanisms and contribute additively to zinc homeostasis in *Streptococcus pneumoniae*. Mol Microbiol 91:834-851.
188. Bersch B, Bougault C, Roux L, Favier A, Vernet T, Durmort C. 2013. New insights into histidine triad proteins: Solution structure of a *Streptococcus pneumoniae* PhtD domain and zinc transfer to AdcAII. PLoS One 8:e81168.
189. Kallio A, Sepponen K, Hermand P, Denoel P, Godfroid F, Melin M. 2014. Role of pneumococcal histidine triad (Pht) proteins in attachment of *Streptococcus pneumoniae* to respiratory epithelial cells. Infect Immun 82:1683-91.
190. Bhubhanil S, Chamsing J, Sittipo P, Chaoprasid P, Sukchawalit R, Mongkolsuk S. 2014. Roles of *Agrobacterium tumefaciens* membrane-bound ferritin (MbfA) in iron transport and resistance to iron under acidic conditions. Microbiology 160:863-871.
191. Li L, Chen OS, McVey Ward D, Kaplan J. 2001. CCC1 is a transporter that mediates vacuolar iron storage in yeast. J Biol Chem 276:29515-9.
192. Labarbuta P, Duckett K, Botting CH, Chahrour O, Malone J, Dalton JP, Law CJ. 2017. Recombinant vacuolar iron transporter family homologue PfVIT from human malaria-causing *Plasmodium falciparum* is a Fe^{2+}/H^{+} exchanger. Sci Rep 7:1-10.
193. Kim SA, Punshon T, Lanzirotti A, Li L, Alonso JM, Ecker JR, Kaplan J, Guerinot ML. 2006. Localization of iron in *Arabidopsis* seed requires the vacuolar membrane transporter VIT1. Science 314:1295-8.
194. Kehres DG, Lawyer CH, Maguire ME. 1998. The CorA magnesium transporter gene family. Microbial & Comparative Genomics 3:151-169.
195. Groisman EA, Hollands K, Kriner MA, Lee EJ, Park SY, Pontes MH. 2013. Bacterial Mg^{2+} homeostasis, transport, and virulence. Annu Rev Genet 47:625-46.

196. Jakubovics NS, Smith AW, Jenkinson HF. 2002. Oxidative stress tolerance is manganese (Mn^{2+})-regulated in *Streptococcus gordonii*. Microbiology 148:3255–3263.
197. Gaustad P, Havarstein LS. 1997. Competence pheromone in *Streptococcus sanguis*: Identification of the competence gene *comC* and the competence pheromone. Adv Exp Med Biol 418:1019–1021.
198. Callahan JE, Munro CL, Kitten T. 2011. The *Streptococcus sanguinis co*mpetence regulon is not required for infective endocarditis virulence in a rabbit model. PLoS One 6:e26403.
199. Puccio T, Misra BB, Kitten T. 2020. Time-course analysis of *Streptococcus sanguinis* after manganese depletion reveals changes in glycolytic, nucleotide, and redox metabolites. bioRxiv doi:10.1101/2020.08.30.274233.
200. Martin JE, Lisher JP, Winkler ME, Giedroc DP. 2017. Perturbation of manganese metabolism disrupts cell division in *Streptococcus pneumoniae*. Mol Microbiol 104:334-348.
201. Kuipers K, Gallay C, Martinek V, Rohde M, Martinkova M, van der Beek SL, Jong WS, Venselaar H, Zomer A, Bootsma H, Veening JW, de Jonge MI. 2016. Highly conserved nucleotide phosphatase essential for membrane lipid homeostasis in *Streptococcus pneumoniae*. Mol Microbiol 101:12-26.
202. Puccio T, Kunka KS, Zhu B, Xu P, Kitten T. 2020. Manganese depletion leads to multisystem changes in the transcriptome of the opportunistic pathogen *Streptococcus sanguinis*. Front Microbiol doi:10.3389/fmicb.2020.592615.
203. Zhu B, Green SP, Ge X, Puccio TM, Nadhem H, Ge H, Bao L, Kitten T, Xu P. 2020. Genome-wide identification of *Streptococcus sanguinis* fitness genes in human serum and discovery of potential selective drug targets. Mol Microbiol doi:10.1111/mmi.14629.
204. Shields RC, Walker AR, Maricic N, Chakraborty B, Underhill SAM, Burne RA. 2020. Repurposing the *Streptococcus mutans* CRISPR-Cas9 system to understand essential gene function. PLoS Pathog 16:e1008344.
205. Mechold U, Gentry D, Cashel M, Steiner K, Malke H. 1996. Functional analysis of a *relA/spoT* gene homolog from *Streptococcus equisimilis*. J Bacteriol 178:1401-11.
206. Irving SE, Corrigan RM. 2018. Triggering the stringent response: signals responsible for activating (p)ppGpp synthesis in bacteria. Microbiology 164:268-276.
207. Lemos JA, Lin VK, Nascimento MM, Abranches J, Burne RA. 2007. Three gene products govern (p)ppGpp production by *Streptococcus mutans*. Mol Microbiol 65:1568-81.
208. Yang N, Xie S, Tang NY, Choi MY, Wang Y, Watt RM. 2019. The Ps and Qs of alarmone synthesis in *Staphylococcus aureus*. PLoS One 14:e0213630.
209. Hogg T, Mechold U, Malke H, Cashel M, Hilgenfeld R. 2004. Conformational antagonism between opposing active sites in a bifunctional RelA/SpoT homolog modulates (p)ppGpp metabolism during the stringent response. Cell doi:10.1016/s0092-8674(04)00260-0.
210. Kaspar J, Kim JN, Ahn SJ, Burne RA. 2016. An essential role for (p)ppGpp in the integration of stress tolerance, peptide signaling, and competence development in *Streptococcus mutans*. Front Microbiol 7:1162.
211. Chen L, Ge X, Dou Y, Wang X, Patel JR, Xu P. 2011. Identification of hydrogen peroxide production-related genes in *Streptococcus sanguinis* and their functional relationship with pyruvate oxidase. Microbiology 157:13-20.
212. Liochev SI, Fridovich I. 2004. Carbon dioxide mediates Mn(II)-catalyzed decomposition of hydrogen peroxide and peroxidation reactions. Proc Natl Acad Sci U S A 101:12485-90.
213. Spellerberg B, Cundell DR, Sandros J, Pearce BJ, Idanpaan-Heikkila I, Rosenow C, Masure HR. 1996. Pyruvate oxidase, as a determinant of virulence in *Streptococcus pneumoniae*. Mol Microbiol 19:803-813.
214. Yamamoto Y, Higuchi M, Poole LB, Kamio Y. 2000. Role of the *dpr* product in oxygen tolerance in *Streptococcus mutans*. J Bacteriol 182:3740–3747.

215. Brenot A, King KY, Caparon MG. 2005. The PerR regulon in peroxide resistance and virulence of *Streptococcus pyogenes*. Mol Microbiol 55:221-34.
216. Gorke B, Stulke J. 2008. Carbon catabolite repression in bacteria: many ways to make the most out of nutrients. Nat Rev Microbiol 6:613-24.
217. Warner JB, Lolkema JS. 2003. CcpA-dependent carbon catabolite repression in bacteria. Microbiol Mol Biol Rev 67:475-490.
218. Novichkov PS, Kazakov AE, Ravcheev DA, Leyn SA, Kovaleva GY, Sutormin RA, Kazanov MD, Riehl W, Arkin AP, Dubchak I, Rodionov DA. 2013. RegPrecise 3.0 - A resource for genome-scale exploration of transcriptional regulation in bacteria. BMC Genomics 14:745.
219. Zheng L, Chen Z, Itzek A, Ashby M, Kreth J. 2011. Catabolite control protein A controls hydrogen peroxide production and cell death in *Streptococcus sanguinis*. J Bacteriol 193:516-26.
220. Redanz S, Masilamani R, Cullin N, Giacaman RA, Merritt J, Kreth J. 2018. Distinct regulatory role of carbon catabolite protein A (CcpA) in oral streptococcal *spxB* expression. J Bacteriol 200:e00619-17.
221. Potter AJ, Trappetti C, Paton JC. 2012. *Streptococcus pneumoniae* uses glutathione to defend against oxidative stress and metal ion toxicity. J Bacteriol 194:6248-54.
222. Colomer-Winter C, Gaca AO, Lemos JA. 2017. Association of metal homeostasis and (p)ppGpp regulation in the pathophysiology of *Enterococcus faecalis*. Infect Immun 85.
223. Fujishima K, Kawada-Matsuo M, Oogai Y, Tokuda M, Torii M, Komatsuzawa H. 2013. *dpr* and *sod* in *Streptococcus mutans* are involved in coexistence with *S. sanguinis,* and PerR is associated with resistance to H_2O_2. Appl Environ Microbiol 79:1436-1443.
224. Tsou C-C, Chiang-Ni C, Lin Y-S, Chuang W-J, Lin M-T, Liu C-C, Wu J-J. 2010. Oxidative stress and metal ions regulate a ferritin-like gene, *dpr*, in *Streptococcus pyogenes*. Int J Med Microbiol 300:259-264.
225. Castro-Cerritos KV, Yasbin RE, Robleto EA, Pedraza-Reyes M. 2017. Role of ribonucleotide reductase in *Bacillus subtilis* stress-associated mutagenesis. J Bacteriol 199.
226. Gryllos I, Grifantini R, Colaprico A, Cary ME, Hakansson A, Carey DW, Suarez-Chavez M, Kalish LA, Mitchell PD, White GL, Wessels MR. 2008. PerR confers phagocytic killing resistance and allows pharyngeal colonization by group A *Streptococcus*. PLoS Path 4:e1000145-e1000145.
227. Pinochet-Barros A, Helmann JD. 2018. Redox sensing by Fe^{2+} in bacterial Fur family metalloregulators. Antioxid Redox Signal 29:1858-1871.
228. Ajdic D, Pham VT. 2007. Global transcriptional analysis of *Streptococcus mutans* sugar transporters using microarrays. J Bacteriol 189:5049-59.
229. Bai Y, Shang M, Xu M, Wu A, Sun L, Zheng L. 2019. Transcriptome, phenotypic, and virulence analysis of *Streptococcus sanguinis* SK36 wild type and its CcpA-null derivative (ΔCcpA). Front Cell Infect Microbiol 9:411.
230. Chen L, Ge X, Wang X, Patel JR, Xu P. 2012. SpxA1 involved in hydrogen peroxide production, stress tolerance and endocarditis virulence in *Streptococcus sanguinis*. PloS ONE 7:e40034-e40034.
231. Moraes JJ, Stipp RN, Harth-Chu EN, Camargo TM, Hofling JF, Mattos-Graner RO. 2014. Two-component system VicRK regulates functions associated with establishment of *Streptococcus sanguinis* in biofilms. Infect Immun 82:4941-51.
232. Redanz S, Masilamani R, Cullin N, Giacaman RA, Merritt J, Kreth J. 2018. Distinct regulatory role of carbon catabolite protein A (CcpA) in oral streptococcal *spxB* expression. J Bacteriol 200.

233. Burcham LR, Hill RA, Caulkins RC, Emerson JP, Nanduri B, Rosch JW, Fitzkee NC, Thornton JA. 2020. *Streptococcus pneumoniae* metal homeostasis alters cellular metabolism. Metallomics doi:10.1039/d0mt00118j.
234. Kanehisa M, Goto S. 2000. KEGG: Kyoto Encyclopedia of Genes and Genomes. Nucleic Acids Res 28:27-30.
235. Jeske L, Placzek S, Schomburg I, Chang A, Schomburg D. 2019. BRENDA in 2019: a European ELIXIR core data resource. Nucleic Acids Res 47:D542-D549.
236. Zhang YM, Liu JK, Shouri MR, Wong TY. 2006. Characterization of a Mn-dependent fructose-1,6-bisphosphate aldolase in *Deinococcus radiodurans*. BioMetals 19:31-7.
237. Tozzi MG, Camici M, Mascia L, Sgarrella F, Ipata PL. 2006. Pentose phosphates in nucleoside interconversion and catabolism. FEBS J 273:1089-101.
238. Panosian TD, Nannemann DP, Watkins GR, Phelan VV, McDonald WH, Wadzinski BE, Bachmann BO, Iverson TM. 2011. *Bacillus cereus* phosphopentomutase is an alkaline phosphatase family member that exhibits an altered entry point into the catalytic cycle. J Biol Chem 286:8043-54.
239. Rantanen MK, Lehtio L, Rajagopal L, Rubens CE, Goldman A. 2007. Structure of *Streptococcus agalactiae* serine/threonine phosphatase. The subdomain conformation is coupled to the binding of a third metal ion. FEBS J 274:3128-37.
240. Zheng W, Cai X, Xie M, Liang Y, Wang T, Li Z. 2016. Structure-based identification of a potent inhibitor targeting Stp1-mediated virulence regulation in *Staphylococcus aureus*. Cell Chem Biol 23:1002-13.
241. Zeng L, Chen L, Burne RA. 2018. Preferred hexoses influence long-term memory in and induction of lactose catabolism by *Streptococcus mutans*. Appl Environ Microbiol 84:e00864-18.
242. Nascimento MM, Lemos JA, Abranches J, Lin VK, Burne RA. 2008. Role of RelA of *Streptococcus mutans* in global control of gene expression. J Bacteriol 190:28-36.
243. Gratani FL, Horvatek P, Geiger T, Borisova M, Mayer C, Grin I, Wagner S, Steinchen W, Bange G, Velic A, Macek B, Wolz C. 2018. Regulation of the opposing (p)ppGpp synthetase and hydrolase activities in a bifunctional RelA/SpoT homologue from *Staphylococcus aureus*. PLoS Genet 14:e1007514.
244. Ronneau S, Hallez R. 2019. Make and break the alarmone: regulation of (p)ppGpp synthetase/hydrolase enzymes in bacteria. FEMS Microbiol Rev 43:389-400.
245. Seaton K, Ahn SJ, Sagstetter AM, Burne RA. 2011. A transcriptional regulator and ABC transporters link stress tolerance, (p)ppGpp, and genetic competence in *Streptococcus mutans*. J Bacteriol 193:862-74.
246. Kim JN, Ahn SJ, Seaton K, Garrett S, Burne RA. 2012. Transcriptional organization and physiological contributions of the *relQ* operon of *Streptococcus mutans*. J Bacteriol 194:1968-78.
247. Kazmierczak KM, Wayne KJ, Rechtsteiner A, Winkler ME. 2009. Roles of rel_{Spn} in stringent response, global regulation and virulence of serotype 2 *Streptococcus pneumoniae* D39. Mol Microbiol 72:590-611.
248. Colomer-Winter C, Flores-Mireles AL, Kundra S, Hultgren SJ, Lemos JA. 2019. (p)ppGpp and CodY promote *Enterococcus faecalis* virulence in a murine model of catheter-associated urinary tract infection. mSphere 4:e00392-19.
249. Moore CM, Gaballa A, Hui M, Ye RW, Helmann JD. 2005. Genetic and physiological responses of *Bacillus subtilis* to metal ion stress. Mol Microbiol 57:27-40.
250. Jourlin-Castelli C, Mani N, Nakano MM, Sonenshein AL. 2000. CcpC, a novel regulator of the LysR family required for glucose repression of the *citB* gene in *Bacillus subtilis*. J Mol Biol 295:865-78.

251. Radin JN, Kelliher JL, Parraga Solorzano PK, Kehl-Fie TE. 2016. The two-component system ArlRS and alterations in metabolism enable *Staphylococcus aureus* to resist calprotectin-induced manganese starvation. PLoS Pathog 12:e1006040.
252. Parraga Solorzano PK, Yao J, Rock CO, Kehl-Fie TE. 2019. Disruption of glycolysis by nutritional immunity activates a two-component system that coordinates a metabolic and antihost response by *Staphylococcus aureus*. mBio 10.
253. Downey JS, Mashburn-Warren L, Ayala EA, Senadheera DB, Hendrickson WK, McCall LW, Sweet JG, Cvitkovitch DG, Spatafora GA, Goodman SD. 2014. *In vitro* manganese-dependent cross-talk between *Streptococcus mutans* VicK and GcrR: implications for overlapping stress response pathways. PLoS One 9:e115975.
254. Kaval KG, Garsin DA. 2018. Ethanolamine utilization in bacteria. mBio 9:e00066-18.
255. Li P, Gu Q, Wang Y, Yu Y, Yang L, Chen JV. 2017. Novel vitamin B_{12}-producing *Enterococcus* spp. and preliminary *in vitro* evaluation of probiotic potentials. Appl Microbiol Biotechnol 101:6155-6164.
256. Kaval KG, Gebbie M, Goodson JR, Cruz MR, Winkler WC, Garsina DA. 2019. Ethanolamine utilization and bacterial microcompartment formation are subject to carbon catabolite repression. J Bacteriol 201:e00703-18.
257. Fox KA, Ramesh A, Stearns JE, Bourgogne A, Reyes-Jara A, Winkler WC, Garsin DA. 2009. Multiple posttranscriptional regulatory mechanisms partner to control ethanolamine utilization in *Enterococcus faecalis*. Proc Natl Acad Sci U S A 106:4435-4440.
258. Makarova KS, Wolf YI, Alkhnbashi OS, Costa F, Shah SA, Saunders SJ, Barrangou R, Brouns SJ, Charpentier E, Haft DH, Horvath P, Moineau S, Mojica FJ, Terns RM, Terns MP, White MF, Yakunin AF, Garrett RA, van der Oost J, Backofen R, Koonin EV. 2015. An updated evolutionary classification of CRISPR-Cas systems. Nat Rev Microbiol 13:722-36.
259. Gong T, Zeng J, Tang B, Zhou X, Li Y. 2020. CRISPR-Cas systems in oral microbiome: From immune defense to physiological regulation. Mol Oral Microbiol 35:41-48.
260. Serbanescu MA, Cordova M, Krastel K, Flick R, Beloglazova N, Latos A, Yakunin AF, Senadheera DB, Cvitkovitch DG. 2015. Role of the *Streptococcus mutans* CRISPR-Cas systems in immunity and cell physiology. J Bacteriol 197:749-61.
261. Couvin D, Bernheim A, Toffano-Nioche C, Touchon M, Michalik J, Neron B, Rocha EPC, Vergnaud G, Gautheret D, Pourcel C. 2018. CRISPRCasFinder, an update of CRISRFinder, includes a portable version, enhanced performance and integrates search for Cas proteins. Nucleic Acids Res 46:W246-W251.
262. Gurung I, Spielman I, Davies MR, Lala R, Gaustad P, Biais N, Pelicic V. 2016. Functional analysis of an unusual type IV pilus in the Gram-positive *Streptococcus sanguinis*. Mol Microbiol 99:380-92.
263. Sheppard D, Berry JL, Denise R, Rocha EPC, Matthews S, Pelicic V. 2020. The major subunit of widespread competence pili exhibits a novel and conserved type IV pilin fold. J Biol Chem doi:10.1074/jbc.RA120.013316.
264. Chen YM, Chiang YC, Tseng TY, Wu HY, Chen YY, Wu CH, Chiu CH. 2019. Molecular and functional analysis of the type IV pilus gene cluster in *Streptococcus sanguinis* SK36. Appl Environ Microbiol 85.
265. Johnston JW, Briles DE, Myers LE, Hollingshead SK. 2006. Mn^{2+}-dependent regulation of multiple genes in *Streptococcus pneumoniae* through PsaR and the resultant impact on virulence. Infect Immun 74:1171-80.
266. Edgar R, Domrachev M, Lash AE. 2002. Gene Expression Omnibus: NCBI gene expression and hybridization array data repository. Nucleic Acids Res 30:207-210.
267. Raz A. 2017. Detection of intracellular proteins by high-resolution immunofluorescence microscopy in *Streptococcus pyogenes*, p 219-228. *In* Nordenfelt P, Collin M (ed), Bacterial Pathogenesis, 2016/12/04 ed, vol 1535. Springer Nature, New York City.

268. Nguyen NTT, Contreras-Moreira B, Castro-Mondragon JA, Santana-Garcia W, Ossio R, Robles-Espinoza CD, Bahin M, Collombet S, Vincens P, Thieffry D, van Helden J, Medina-Rivera A, Thomas-Chollier M. 2018. RSAT 2018: regulatory sequence analysis tools 20th anniversary. Nucleic Acids Res 46:W209-w214.
269. van Helden J, André B, Collado-Vides J. 2000. A web site for the computational analysis of yeast regulatory sequences. Yeast 16:177-87.
270. Willenborg J, de Greeff A, Jarek M, Valentin-Weigand P, Goethe R. 2014. The CcpA regulon of *Streptococcus suis* reveals novel insights into the regulation of the streptococcal central carbon metabolism by binding of CcpA to two distinct binding motifs. Mol Microbiol 92:61-83.
271. Grant CE, Bailey TL, Noble WS. 2011. FIMO: scanning for occurrences of a given motif. Bioinformatics 27:1017-1018.
272. Yang Y, Zhang L, Huang H, Yang C, Yang S, Gu Y, Jiang W. 2017. A flexible binding site architecture provides new insights into CcpA global regulation in gram-positive bacteria. mBio 8:e02004-16.
273. Charif D, Lobry JR. 2007. SeqinR 1.0-2: A contributed package to the R project for statistical computing devoted to biological sequences retrieval and analysis, p 207-232. *In* Bastolla U, Porto M, Roman HE, Vendruscolo M (ed), Structural Approaches to Sequence Evolution: Molecules, Networks, Populations doi:10.1007/978-3-540-35306-5_10. Springer Berlin Heidelberg, Berlin, Heidelberg.
274. Misra BB, Olivier M. 2020. High resolution GC-Orbitrap-MS metabolomics using both electron ionization and chemical ionization for analysis of human plasma. J Proteome Res doi:10.1021/acs.jproteome.9b00774.
275. Fei F, Mendonca ML, McCarry BE, Bowdish DME, Surette MG. 2016. Metabolic and transcriptomic profiling of *Streptococcus intermedius* during aerobic and anaerobic growth. Metabolomics 12:46.
276. Leonard A, Gierok P, Methling K, Gomez-Mejia A, Hammerschmidt S, Lalk M. 2018. Metabolic inventory of *Streptococcus pneumoniae* growing in a chemical defined environment. Int J Med Microbiol 308:705-712.
277. Qiao Y, Liu G, Lv X, Fan X, Zhang Y, Meng L, Ai M, Feng Z. 2019. Metabolic pathway profiling in intracellular and extracellular environments of *Streptococcus thermophilus* during pH-controlled batch fermentations. Front Microbiol 10:3144.
278. Liu G, Qiao Y, Zhang Y, Leng C, Chen H, Sun J, Fan X, Li A, Feng Z. 2020. Metabolic profiles of carbohydrates in *Streptococcus thermophilus* during pH-controlled batch fermentation. Frontiers in Microbiology 11:1131.
279. Khakimov B, Christiansen LD, Heins AL, Sorensen KM, Scholler C, Clausen A, Skov T, Gernaey KV, Engelsen SB. 2017. Untargeted GC-MS metabolomics reveals changes in the metabolite dynamics of industrial scale batch fermentations of *Streptoccoccus thermophilus* broth. Biotechnol J 12.
280. Jewison T, Su Y, Disfany FM, Liang Y, Knox C, Maciejewski A, Poelzer J, Huynh J, Zhou Y, Arndt D, Djoumbou Y, Liu Y, Deng L, Guo AC, Han B, Pon A, Wilson M, Rafatnia S, Liu P, Wishart DS. 2014. SMPDB 2.0: big improvements to the Small Molecule Pathway Database. Nucleic Acids Res 42:D478-84.
281. Redanz S, Treerat P, Mu R, Redanz U, Zou Z, Koley D, Merritt J, Kreth J. 2020. Pyruvate secretion by oral streptococci modulates hydrogen peroxide dependent antagonism. ISME J 14:1074-1088.
282. Martinussen J, Sorensen C, Jendresen CB, Kilstrup M. 2010. Two nucleoside transporters in *Lactococcus lactis* with different substrate specificities. Microbiology 156:3148-3157.
283. Webb AJ, Hosie AH. 2006. A member of the second carbohydrate uptake subfamily of ATP-binding cassette transporters is responsible for ribonucleoside uptake in *Streptococcus mutans*. J Bacteriol 188:8005-12.

284. Guo R, Lu H. 2020. Targeted metabolomics revealed the regulatory role of manganese on small-molecule metabolism of biofilm formation in *Escherichia coli*. J Anal Test 4:226-237.
285. Hosono H, Kuno S. 1973. The purification and properties of cytidine deaminase from *Escherichia coli*. J Biochem 74:797-803.
286. Carmel-Harel O, Storz G. 2000. Roles of the glutathione- and thioredoxin-dependent reduction systems in the *Escherichia coli* and *Saccharomyces cerevisiae* responses to oxidative stress. Annu Rev Microbiol 54:439–61.
287. Sies H. 1999. Glutathione and its role in cellular functions. Free Radical Biology & Medicine 27:916-921.
288. Janowiak BE, Griffith OW. 2005. Glutathione synthesis in *Streptococcus agalactiae*. J Biol Chem 280:11829-39.
289. Matayatsuk C, Poljak A, Bustamante S, Smythe GA, Kalpravidh RW, Sirankapracha P, Fucharoen S, Wilairat P. 2007. Quantitative determination of ortho- and meta-tyrosine as biomarkers of protein oxidative damage in beta-thalassemia. Redox Rep 12:219-28.
290. Ipson BR, Fisher AL. 2016. Roles of the tyrosine isomers meta-tyrosine and ortho-tyrosine in oxidative stress. Ageing Res Rev 27:93-107.
291. Berndt C, Lillig CH, Flohe L. 2014. Redox regulation by glutathione needs enzymes. Front Pharmacol 5:168.
292. Brenot A, King KY, Janowiak B, Griffith O, Caparon MG. 2004. Contribution of glutathione peroxidase to the virulence of *Streptococcus pyogenes*. Infect Immun 72:408-13.
293. Fozo EM, Kajfasz JK, Quivey RG, Jr. 2004. Low pH-induced membrane fatty acid alterations in oral bacteria. FEMS Microbiol Lett 238:291-5.
294. Chiu TH. 1979. Effect of age on the membrane lipid composition of *Streptococcus sanguis*.
295. Adams HM, Joyce LR, Guan Z, Akins RL, Palmer KL. 2017. *Streptococcus mitis* and *S. oralis* Lack a Requirement for CdsA, the Enzyme Required for Synthesis of Major Membrane Phospholipids in Bacteria. Antimicrob Agents Chemother 61.
296. Joyce LR, Guan Z, Palmer KL. 2019. Phosphatidylcholine Biosynthesis in Mitis Group Streptococci via Host Metabolite Scavenging. J Bacteriol 201.
297. Evans AM, DeHaven CD, Barrett T, Mitchell M, Milgram E. 2009. Integrated, nontargeted ultrahigh performance liquid chromatography/electrospray ionization tandem mass spectrometry platform for the identification and relative quantification of the small-molecule complement of biological systems. Anal Chem (Wash) 81:6656–6667.
298. Dehaven CD, Evans AM, Dai H, Lawton KA. 2010. Organization of GC/MS and LC/MS metabolomics data into chemical libraries. J Cheminform 2:9.
299. Team RC. 2018. R: A language and environment for statistical computing.
300. Grapov D. 2014. DeviumWeb: Dynamic multivariate data analysis and visualization platform. doi:10.5281/zenodo.592909:DOI: 10.5281/zenodo.592909.
301. Xia J, Sinelnikov IV, Han B, Wishart DS. 2015. MetaboAnalyst 3.0--making metabolomics more meaningful. Nucleic Acids Res 43:W251-7.
302. Kolenbrander PE. 2011. Multispecies communities: interspecies interactions influence growth on saliva as sole nutritional source. Int J Oral Sci 3:49-54.
303. Jakubovics NS. 2015. Saliva as the sole nutritional source in the development of multispecies communities in dental plaque, p 263-277, Metabolism and Bacterial Pathogenesis doi:10.1128/microbiolspec.MBP-0013-2014. American Society of Microbiology, Washington, DC.
304. Iwatni X Abbe K T-AS, Yatnada T. 1992. Acid production by streptococci growing at low pH in a chemostat under anaerobic conditions.
305. Papadimitriou K, Alegria A, Bron PA, de Angelis M, Gobbetti M, Kleerebezem M, Lemos JA, Linares DM, Ross P, Stanton C, Turroni F, van Sinderen D, Varmanen P, Ventura M,

Zuniga M, Tsakalidou E, Kok J. 2016. Stress physiology of lactic acid bacteria. Microbiol Mol Biol Rev 80:837-90.
306. MM N, VV G, CW G, CM B, RA B. 2009. Correlations of oral bacterial arginine and urea catabolism with caries experience. Oral Microbiol Immunol 24:89-95.
307. Moye ZD, Zeng L, Burne RA. 2014. Fueling the caries process: carbohydrate metabolism and gene regulation by *Streptococcus mutans*. J Oral Microbiol 6.
308. Bender GR, Sutton SVW, Marquis RE. 1986. Acid tolerance, proton permeabilities, and membrane ATPases of oral streptococci. Infect Immun 53:331-338.
309. Diaz-Garrido N, Lozano CP, Kreth J, Giacaman RA. 2020. Competition and caries on enamel of a dual-species biofilm model of *Streptococcus mutans* and *Streptococcus sanguinis*. Appl Environ Microbiol doi:10.1128/AEM.01262-20.
310. Sasaki M, Kodama Y, Shimoyama Y, Ishikawa T, Kimura S. 2018. Aciduricity and acid tolerance mechanisms of *Streptococcus anginosus*. J Gen Appl Microbiol 64:174-179.
311. Svensater G, Larsson U-B, Greif ECG, Cvitkovitch DG, Hamilton IR. 1997. Acid tolerance response and survival by oral bacteria. Oral Microbiol Immunol 12:266-273.
312. Guan N, Liu L. 2020. Microbial response to acid stress: mechanisms and applications. Appl Microbiol Biotechnol 104:51-65.
313. Liu Y, Tang H, Lin Z, Xu P. 2015. Mechanisms of acid tolerance in bacteria and prospects in biotechnology and bioremediation. Biotechnol Adv 33:1484-92.
314. Robert G. Quivey J, Kuhnert WL, Hahn K. 2001. Genetics of acid adaptation in oral streptococci. Crit Rev Oral Biol Medicine 12:301-314.
315. Cotter PD, Hill C. 2003. Surviving the acid test: responses of gram-positive bacteria to low pH. Microbiol Mol Biol Rev 67:429-53, table of contents.
316. Kuhnert WL, Quivey RG, Jr. 2003. Genetic and biochemical characterization of the F-ATPase operon from *Streptococcus sanguis* 10904. J Bacteriol 185:1525-33.
317. Burne RA, Parsons DT, Marquis RE. 1989. Cloning and expression in *Escherichia coli* of the genes of the arginine deiminase system of *Streptococcus sanguis* NCTC 10904. Infect Immun 57:3540-3548.
318. Curran TM, Lieou J, Marquis RE. 1995. Arginine deiminase system and acid adaptation of oral streptococci. Appl Environ Microbiol 61:4494–4496.
319. Floderus E, Linder LE, Sund M-L. 1990. Arginine catabolism by strains of oral streptococci. APMIS: Acta Pathol Microbiol Immunol Scand 98:1045-1052.
320. Shabayek S, Spellerberg B. 2017. Acid stress response mechanisms of group B streptococci. Front Cell Infect Microbiol 7:395.
321. Lemos JA, Chen YY, Burne RA. 2001. Genetic and physiologic analysis of the *groE* operon and role of the HrcA repressor in stress gene regulation and acid tolerance in *Streptococcus mutans*. J Bacteriol 183:6074-84.
322. Lemos JA, Burne RA. 2002. Regulation and physiological significance of ClpC and ClpP in *Streptococcus mutans*. J Bacteriol 184:6357-66.
323. Kim JS, Sung MH, Kho DH, Lee JK. 2005. Induction of manganese-containing superoxide dismutase is required for acid tolerance in *Vibrio vulnificus*. J Bacteriol 187:5984-95.
324. Wen ZT, Burne RA. 2004. LuxS-mediated signaling in *Streptococcus mutans* is involved in regulation of acid and oxidative stress tolerance and biofilm formation. J Bacteriol 186:2682-91.
325. Chen YY, Shieh HR, Chang YC. 2013. The expression of the *fim* operon is crucial for the survival of *Streptococcus parasanguinis* FW213 within macrophages but not acid tolerance. PLoS One 8:e66163.
326. Santi I, Grifantini R, Jiang S-M, Brettoni C, Grandi G, Wessels MR, Soriani M. 2009. CsrRS regulates group B *Streptococcus* virulence gene expression in response to environmental pH: a new perspective on vaccine development. J Bacteriol 191:5387-5397.

327. Kajfasz JK, Martinez AR, Rivera-Ramos I, Abranches J, Koo H, Quivey RG, Jr., Lemos JA. 2009. Role of Clp proteins in expression of virulence properties of *Streptococcus mutans*. J Bacteriol 191:2060-8.
328. Wilkins JC, Homer KA, Beighton D. 2002. Analysis of *Streptococcus mutans* proteins modulated by culture under acidic conditions. Appl Environ Microbiol 68:2382-90.
329. Wilkins JC, Beighton D, Homer KA. 2003. Effect of acidic pH on expression of surface-associated proteins of *Streptococcus oralis*. Appl Environ Microbiol 69:5290-5296.
330. Ge X, Yu Y, Zhang M, Chen L, Chen W, Elrami F, Kong F, Kitten T, Xu P. 2016. Involvement of NADH oxidase in competition and endocarditis virulence in *Streptococcus sanguinis*. Infect Immun 84:1470-1477.
331. Djoko KY, Phan MD, Peters KM, Walker MJ, Schembri MA, McEwan AG. 2017. Interplay between tolerance mechanisms to copper and acid stress in *Escherichia coli*. Proc Natl Acad Sci U S A 114:6818-6823.
332. Senouci-Rezkallah K, Schmitt P, Jobin MP. 2011. Amino acids improve acid tolerance and internal pH maintenance in *Bacillus cereus* ATCC14579 strain. Food Microbiol 28:364-72.
333. Beighton D. 1982. The influence of manganese on carbohydrate metabolism and caries induction by *Streptococcus mutans* strain Ingbritt. Caries Res 16:189-92.
334. Martin-Galiano AJ, Overweg K, Ferrandiz MJ, Reuter M, Wells JM, de la Campa AG. 2005. Transcriptional analysis of the acid tolerance response in *Streptococcus pneumoniae*. Microbiology 151:3935-3946.
335. Dunning DW, McCall LW, Powell WF, Arscott WT, McConocha EM, McClurg CJ, Goodman SD, Spatafora GA. 2008. SloR modulation of the *Streptococcus mutans* acid tolerance response involves the GcrR response regulator as an essential intermediary. Microbiology 154:1132-1143.
336. Zhang T, Sui D, Zhang C, Cole L, Hu J. 2020. Asymmetric functions of a binuclear metal center within the transport pathway of a human zinc transporter ZIP4. FASEB J 34:237-247.
337. Taudte N, Grass G. 2010. Point mutations change specificity and kinetics of metal uptake by ZupT from *Escherichia coli*. BioMetals 23:643-56.
338. Stoyanov JV, Mancini S, Lu ZH, Mourlane F, Poulsen KR, Wimmer R, Solioz M. 2010. The stress response protein Gls24 is induced by copper and interacts with the CopZ copper chaperone of *Enterococcus hirae*. FEMS Microbiol Lett 302:69-75.
339. Teng F, Nannini EC, Murray BE. 2005. Importance of *gls24* in virulence and stress response of *Enterococcus faecalis* and use of the Gls24 protein as a possible immunotherapy target. J Infect Dis 191:472–480.
340. Giard J-C, Rince A, Capiaux H, Auffray Y, Hartke A. 2000. Inactivation of the stress- and starvation-inducible *gls24* operon has a pleiotrophic effect on cell morphology, stress sensitivity, and gene expression in *Enterococcus faecalis*. J Bacteriol 182:4512–4520.
341. Gutknecht J. 1987. Proton/hydroxide conductance and permeability through phospholipid bilayer membranes. Proc Natl Acad Sci U S A 84:6443-6446.
342. Thibodeau EA, Marquis RE. 1983. Acid sensitivity of glycolysis in normal and proton-permeable cells of *Streptococcus mutans* GS-5. J Dent Res 62:1174-1178.
343. Kuhnert WL, Zheng G, Faustoferri RC, Quivey RG, Jr. 2004. The F-ATPase operon promoter of *Streptococcus mutans* is transcriptionally regulated in response to external pH. J Bacteriol 186:8524-8.
344. Martín-Galiano AJ, Ferrándiz MJ, de la Campa AG. 2001. The promoter of the operon encoding the F0F1 ATPase of *Streptococcus pneumoniae* is inducible by pH. Mol Microbiol 41:1327-38.
345. Wong P, Houry WA. 2004. Chaperone networks in bacteria: analysis of protein homeostasis in minimal cells. J Struct Biol 146:79-89.

346. Nascimento MM, Lemos JA, Abranches J, Gonçalves RB, Burne RA. 2004. Adaptive acid tolerance response of *Streptococcus sobrinus*. J Bacteriol 186:6383-90.
347. Jayaraman GC, Penders JE, Burne RA. 1997. Transcriptional analysis of the *Streptococcus mutans hrcA, grpE* and *dnaK* genes and regulation of expression in response to heat shock and environmental acidification. Mol Microbiol 25:329-41.
348. Wei Y, Zeng X, Yuan Y, Jiang H, Zheng Y, Tan Y, Guo Z, Yang R, Zhou D, Jiang Y. 2011. DNA microarray analysis of acid-responsive genes of *Streptococcus suis* serotype 2. Annals of Microbiology 61:505-510.
349. Tomoyasu T, Tabata A, Imaki H, Tsuruno K, Miyazaki A, Sonomoto K, Whiley RA, Nagamune H. 2012. Role of *Streptococcus intermedius* DnaK chaperone system in stress tolerance and pathogenicity. Cell Stress and Chaperones 17:41-55.
350. Len ACL, Harty DWS, Jacques NA. 2004. Stress-responsive proteins are upregulated in *Streptococcus mutans* during acid tolerance. Microbiology 150:1339-1351.
351. Buchanan JT, Stannard JA, Lauth X, Ostland VE, Powell HC, Westerman ME, Nizet V. 2005. *Streptococcus iniae* phosphoglucomutase is a virulence factor and a target for vaccine development. Infect Immun 73:6935-44.
352. Shields RC, Zeng L, Culp DJ, Burne RA. 2018. Genomewide identification of essential genes and fitness determinants of *Streptococcus mutans* UA159. mSphere 3:e00031-18.
353. Ouyang Z, He M, Oman T, Yang XF, Norgard MV. 2009. A manganese transporter, BB0219 (BmtA), is required for virulence by the Lyme disease spirochete, *Borrelia burgdorferi*. Proc Natl Acad Sci U S A 106:3449-54.
354. Ramsey ME, Hyde JA, Medina-Perez DN, Lin T, Gao L, Lundt ME, Li X, Norris SJ, Skare JT, Hu LT. 2017. A high-throughput genetic screen identifies previously uncharacterized *Borrelia burgdorferi* genes important for resistance against reactive oxygen and nitrogen species. PLoS Pathog 13:e1006225.
355. Wagh D, Pothineni VR, Inayathullah M, Liu S, Kim KM, Rajadas J. 2015. Borreliacidal activity of Borrelia metal transporter A (BmtA) binding small molecules by manganese transport inhibition. Drug Des Devel Ther 9:805-16.
356. Zhao H, Eide D. 1996. The yeast ZRT1 gene encodes the zinc transporter protein of a high-affinity uptake system induced by zinc limitation. Proc Natl Acad Sci U S A 93:2454-2458.
357. Zhao H, Eide D. 1996. The ZRT2 gene encodes the low affinity zinc transporter in *Saccharomyces cerevisiae*. J Biol Chem 271:23203–23210.
358. Eide D, Broderius M, Fett J, Guerinot ML. 1996. A novel iron-regulated metal transporter from plants identified by functional expression in yeast. Proc Natl Acad Sci U S A 93:5624-5628.
359. Eide DJ. 2004. The SLC39 family of metal ion transporters. Pflugers Arch 447:796-800.
360. Jeong J, Eide DJ. 2013. The SLC39 family of zinc transporters. Mol Aspects Med 34:612-9.
361. Kury S, Dreno B, Bezieau S, Giraudet S, Kharfi M, Kamoun R, Moisan JP. 2002. Identification of SLC39A4, a gene involved in acrodermatitis enteropathica. Nat Genet 31:239-40.
362. Wang K, Zhou B, Kuo YM, Zemansky J, Gitschier J. 2002. A novel member of a zinc transporter family is defective in acrodermatitis enteropathica. Am J Hum Genet 71:66-73.
363. Fukada T, Civic N, Furuichi T, Shimoda S, Mishima K, Higashiyama H, Idaira Y, Asada Y, Kitamura H, Yamasaki S, Hojyo S, Nakayama M, Ohara O, Koseki H, Dos Santos HG, Bonafe L, Ha-Vinh R, Zankl A, Unger S, Kraenzlin ME, Beckmann JS, Saito I, Rivolta C, Ikegawa S, Superti-Furga A, Hirano T. 2008. The zinc transporter SLC39A13/ZIP13 is required for connective tissue development; its involvement in BMP/TGF-beta signaling pathways. PLoS One 3:e3642.

364. Fujishiro H, Himeno S. 2019. New insights into the roles of ZIP8, a cadmium and manganese transporter, and its relation to human diseases. Biol Pharm Bull 42:1076–1082.
365. Takatani-Nakase T. 2018. Zinc transporters and the progression of breast cancers. Biol Pharm Bull 41:1517–1522.
366. Li M, Zhang Y, Liu Z, Bharadwaj U, Wang H, Wang X, Zhang S, Liuzzi JP, Chang S-M, Cousins RJ, Fisher WE, Brunicardi FC, Logsdon CD, Chen C, Yao Q. 2007. Aberrant expression of zinc transporter ZIP4 (SLC39A4) significantly contributes to human pancreatic cancer pathogenesis and progression. Proc Natl Acad Sci U S A 104:18636–18641.
367. Park JH, Hogrebe M, Gruneberg M, DuChesne I, von der Heiden AL, Reunert J, Schlingmann KP, Boycott KM, Beaulieu CL, Mhanni AA, Innes AM, Hortnagel K, Biskup S, Gleixner EM, Kurlemann G, Fiedler B, Omran H, Rutsch F, Wada Y, Tsiakas K, Santer R, Nebert DW, Rust S, Marquardt T. 2015. SLC39A8 deficiency: A disorder of manganese transport and glycosylation. Am J Hum Genet 97:894-903.
368. Choi EK, Nguyen TT, Gupta N, Iwase S, Seo YA. 2018. Functional analysis of SLC39A8 mutations and their implications for manganese deficiency and mitochondrial disorders. Sci Rep 8:3163.
369. Lin W, Vann DR, Doulias PT, Wang T, Landesberg G, Li X, Ricciotti E, Scalia R, He M, Hand NJ, Rader DJ. 2017. Hepatic metal ion transporter ZIP8 regulates manganese homeostasis and manganese-dependent enzyme activity. J Clin Invest 127:2407-2417.
370. Riley LG, Cowley MJ, Gayevskiy V, Roscioli T, Thorburn DR, Prelog K, Bahlo M, Sue CM, Balasubramaniam S, Christodoulou J. 2017. A SLC39A8 variant causes manganese deficiency, and glycosylation and mitochondrial disorders. J Inherit Metab Dis 40:261-269.
371. Scheiber IF, Alarcon NO, Zhao N. 2019. Manganese Uptake by A549 Cells is Mediated by Both ZIP8 and ZIP14. Nutrients 11.
372. Scheiber IF, Wu Y, Morgan SE, Zhao N. 2019. The intestinal metal transporter ZIP14 maintains systemic manganese homeostasis. J Biol Chem 294:9147-9160.
373. Jenkitkasemwong S, Akinyode A, Paulus E, Weiskirchen R, Hojyo S, Fukada T, Giraldo G, Schrier J, Garcia A, Janus C, Giasson B, Knutson MD. 2018. SLC39A14 deficiency alters manganese homeostasis and excretion resulting in brain manganese accumulation and motor deficits in mice. Proc Natl Acad Sci U S A 115:E1769-E1778.
374. Aydemir TB, Kim MH, Kim J, Colon-Perez LM, Banan G, Mareci TH, Febo M, Cousins RJ. 2017. Metal transporter ZIP14 (SLC39A14) deletion in mice increases manganese deposition and produces neurotoxic signatures and diminished motor activity. J Neurosci 37:5996-6006.
375. Korshunova YO, Eide D, Clark WG, Guerinot ML, Pakrasi HB. 1999. The IRT1 protein from *Arabidopsis thaliana* is a metal transporter with a broad substrate range. Plant Mol Biol 40:37–44.
376. Vert G, Grotz N, Dedaldechamp F, Gaymard F, Guerinot ML, Briat JF, Curie C. 2002. IRT1, an Arabidopsis transporter essential for iron uptake from the soil and for plant growth. Plant Cell 14:1223-33.
377. Gaither LA, Eide D. 2001. Eukaryotic zinc transporters and their regulation. BioMetals 14:251–270.
378. Dempski RE. 2012. The cation selectivity of the ZIP transporters. Curr Top Membr 69:221-45.
379. Yu Y, Wu A, Zhang Z, Yan G, Zhang F, Zhang L, Shen X, Hu R, Zhang Y, Zhang K, Wang F. 2013. Characterization of the GufA subfamily member SLC39A11/Zip11 as a zinc transporter. J Nutr Biochem 24:1697-708.
380. Grass G, Wong MD, Rosen BP, Smith RL, Rensing C. 2002. ZupT is a Zn(II) uptake system in *Escherichia coli*. J Bacteriol 184:864-6.

381. Grass G, Franke S, Taudte N, Nies DH, Kucharski LM, Maguire ME, Rensing C. 2005. The metal permease ZupT from *Escherichia coli* is a transporter with a broad substrate spectrum. J Bacteriol 187:1604-11.
382. Zhang T, Liu J, Fellner M, Zhang C, Sui D, Hu J. 2017. Crystal structures of a ZIP zinc transporter reveal a binuclear metal center in the transport pathway. Sci Adv 3:e1700344.
383. Gupta S, Merriman C, Petzold CJ, Ralston CY, Fu D. 2019. Water molecules mediate zinc mobility in the bacterial zinc diffusion channel ZIPB. J Biol Chem 294:13327-13335.
384. Punta M, Love J, Handelman S, Hunt JF, Shapiro L, Hendrickson WA, Rost B. 2009. Structural genomics target selection for the New York Consortium on Membrane Protein Structure. J Struct Funct Genomics 10:255-68.
385. Lin W, Chai J, Love J, Fu D. 2010. Selective electrodiffusion of zinc ions in a Zrt-, Irt-like protein, ZIPB. J Biol Chem 285:39013-20.
386. Girijashanker K, He L, Soleimani M, Reed JM, Li H, Liu Z, Wang B, Dalton TP, Nebert DW. 2008. Slc39a14 gene encodes ZIP14, a metal/bicarbonate symporter: similarities to the ZIP8 transporter. Mol Pharmacol 73:1413-23.
387. Liu Z, Li H, Soleimani M, Girijashanker K, Reed JM, He L, Dalton TP, Nebert DW. 2008. Cd^{2+} versus Zn^{2+} uptake by the ZIP8 HCO_3-dependent symporter: kinetics, electrogenicity and trafficking. Biochem Biophys Res Commun 365:814-20.
388. Balasubramanian R, Smith SM, Rawat S, Yatsunyk LA, Stemmler TL, Rosenzweig AC. 2010. Oxidation of methane by a biological dicopper centre. Nature 465:115-9.
389. Bai Y, McCoy JG, Levin EJ, Sobrado P, Rajashankar KR, Fox BG, Zhou M. 2015. X-ray structure of a mammalian stearoyl-CoA desaturase. Nature 524:252-6.
390. Yang T-Y, Dudev T, Lim C. 2008. Mononuclear versus Binuclear Metal-Binding Sites: Metal-Binding Affinity and Selectivity from PDB Survey and DFT/CDM Calculations. JACS 130:3844-52.
391. Jack DL, Yang NM, Jr. MHS. 2001. The drug/metabolite transporter superfamily. Eur J Biochem 268:3620-3639.
392. Zackular JP, Knippel RJ, Lopez CA, Beavers WN, Maxwell CN, Chazin WJ, Skaar EP. 2020. ZupT facilitates *Clostridioides difficile* resistance to host-mediated nutritional immunity. mSphere 5.
393. Guerinot ML. 2000. The ZIP Family of metal transporters. Biochim Biophys Acta.
394. Omasits U, Ahrens CH, Muller S, Wollscheid B. 2014. Protter: interactive protein feature visualization and integration with experimental proteomic data. Bioinformatics 30:884-6.
395. Liu P, Yao YN, Wu SD, Dong HJ, Feng GC, Yuan XY. 2005. The efficacy of deferiprone on tissues aluminum removal and copper, zinc, manganese level in rabbits. J Inorg Biochem 99:1733-7.
396. Wang CY, Patel N, Wholey WY, Dawid S. 2018. ABC transporter content diversity in *Streptococcus pneumoniae* impacts competence regulation and bacteriocin production. Proc Natl Acad Sci U S A 115:E5776-E5785.
397. Almagro Armenteros JJ, Tsirigos KD, Sønderby CK, Petersen TN, Winther O, Brunak S, von Heijne G, Nielsen H. 2019. SignalP 5.0 improves signal peptide predictions using deep neural networks. Nat Biotechnol 37:420-423.
398. Morrision KL, Weiss GA. 2001. Combinatorial alanine-scanning. Curr Opin Chem Biol 5:302-307.
399. Zhang T, Kuliyev E, Sui D, Hu J. 2019. The histidine-rich loop in the extracellular domain of ZIP4 binds zinc and plays a role in zinc transport. Biochem J 476:1791-1803.
400. Wilman HR, Shi J, Deane CM. 2014. Helix kinks are equally prevalent in soluble and membrane proteins. Proteins 82:1960-70.
401. Kehl-Fie TE, Zhang Y, Moore JL, Farrand AJ, Hood MI, Rathi S, Chazin WJ, Caprioli RM, Skaar EP. 2013. MntABC and MntH contribute to systemic *Staphylococcus aureus*

infection by competing with calprotectin for nutrient manganese. Infect Immun 81:3395-405.
402. Bozzi AT, Bane LB, Weihofen WA, McCabe AL, Singharoy A, Chipot CJ, Schulten K, Gaudet R. 2016. Conserved methionine dictates substrate preference in Nramp-family divalent metal transporters. Proc Natl Acad Sci U S A 113:10310-5.
403. Ehrnstorfer IA, Geertsma ER, Pardon E, Steyaert J, Dutzler R. 2014. Crystal structure of a SLC11 (NRAMP) transporter reveals the basis for transition-metal ion transport. Nat Struct Mol Biol 21:990-6.
404. Colomer-Winter C, Flores-Mireles AL, Baker SP, Frank KL, Lynch AJL, Hultgren SJ, Kitten T, Lemos JA. 2018. Manganese acquisition is essential for virulence of *Enterococcus faecalis*. PLoS Pathog 14:e1007102.
405. Raimunda D, Gonzalez-Guerrero M, Leeber BW, 3rd, Arguello JM. 2011. The transport mechanism of bacterial Cu^{+}-ATPases: distinct efflux rates adapted to different function. BioMetals 24:467-75.
406. Richards VP, Palmer SR, Pavinski Bitar PD, Qin X, Weinstock GM, Highlander SK, Town CD, Burne RA, Stanhope MJ. 2014. Phylogenomics and the dynamic genome evolution of the genus *Streptococcus*. Genome Biol Evol 6:741-753.
407. Ravenhall M, Škunca N, Lassalle F, Dessimoz C. 2015. Inferring horizontal gene transfer. PLoS Comput Biol 11:e1004095.
408. Ajdić D, McShan WM, McLaughlin RE, Savić G, Chang J, Carson MB, Primeaux C, Tian R, Kenton S, Jia H, Lin S, Qian Y, Li S, Zhu H, Najar F, Lai H, White J, Roe BA, Ferretti JJ. 2002. Genome sequence of *Streptococcus mutans* UA159, a cariogenic dental pathogen. Proc Natl Acad Sci U S A 99:14434-9.
409. Saitou N, Nei M. 1987. The Neighbor-joining Method: A new method for reconstructing phylogenetic trees. Mol Biol Evol 4:406-425.
410. E. Z, L. P. 1965. Evolutionary divergence and convergence in proteins, p 97-166. *In* Vogel VBaHJ (ed), Evolving Genes and Proteins Academic Press, New York.
411. Kumar S, Stecher G, Li M, Knyaz C, Tamura K. 2018. MEGA X: Molecular Evolutionary Genetics Analysis across Computing Platforms. Mol Biol Evol 35:1547-1549.
412. Baumgart M, Frunzke J. 2015. The manganese-responsive regulator MntR represses transcription of a predicted ZIP family metal ion transporter in *Corynebacterium glutamicum*. FEMS Microbiol Lett 362:1-10.
413. Zuobi-Hasona K. 2008. Isolation and solubilization of cellular membrane proteins from bacteria, Methods in Molecular Biology.
414. Lu M, Fu D. 2007. Structure of the zinc transporter YiiP. Science 317.
415. Bock CW, Katz AK, Markham GD, Glusker JP. 1999. Manganese as a replacement for magnesium and zinc: Functional comparison of the divalent ions. J Am Chem Soc 121:7360-7372.
416. Rogers EE, Eide DJ, Guerinot ML. 2000. Altered selectivity in an *Arabidopsis* metal transporter. Proc Natl Acad Sci U S A 97:12356–12360.
417. Fox BG, Blommel PG. 2009. Autoinduction of protein expression. Curr Protoc Protein Sci Chapter 5:Unit 5 23.
418. Hall BG. 2008. Phylogenetic Trees Made Easy 3rd ed. Sinauer Associates, Massachusetts.

Vita

Tanya Marie Puccio was born January 1, 1993 in Southern California and has resided in Virginia since 2011 when she began her undergraduate studies at Virginia Wesleyan College in Norfolk. Her interest in science was sparked by her AP Biology teacher at Moorpark High School, Mrs. Tina Lanquist. Her passion for science continued into her tenure at VWC, where her various research projects and advisors, Dr. Philip Rock and Dr. Joyce Easter, inspired her to pursue a PhD in biomedical sciences. She graduated in 2015 with a BS in Biology, a BA in Hispanic Studies, and a minor in Chemistry. In 2015, she was accepted into the Biomedical Sciences Doctoral Program at the Virginia Commonwealth University School of Medicine. After three rotations, she joined the laboratory of Dr. Todd Kitten in summer 2016. In the fall of 2016, she matriculated into the new Oral Health Research PhD Program in the Virginia Commonwealth University School of Dentistry as part of the first cohort.

Honors and Awards

Ruth L. Kirschstein Predoctoral Individual National Research Service Award	2019-2021
Mid-Atlantic Microbial Pathogenesis Meeting Travel Award	2019
George W. Burke, Jr. Graduate Student Fund for Oral Health Research	2018
Virginia Branch American Society for Microbiology Meeting Travel Award	2016
Summa cum laude, Latin Honors, Virginia Wesleyan College	2015
Carrier of the Gonfalon, Virginia Wesleyan College Commencement Ceremony	2015
Spanish Honors Award, Virginia Wesleyan College	2015
Biology Department Award, Virginia Wesleyan College	2015
Best Natural Sciences & Mathematics Research Oral Presentation, VWC	2014
ODAC Virginia Farm Bureau Mutual Insurance Scholar-Athlete	2014
Study Abroad Scholarship, VWC Global Scholars Program	2014
Division III Scholar of Distinction, National Field Hockey Coaches Association	2013
Dean's List, Virginia Wesleyan College	2012-2015
Jane P. Batten Award Full Tuition Scholarship, Virginia Wesleyan College	2011-2015
Division III National Academic Squad, National Field Hockey Association	2011-2014

Professional and Student Organization Memberships

Women in Science at VCU
Sigma Xi, Scientific Research Honor Society
American Society for Microbiology
American Heart Association
International Biometals Society
Women in Bio
Association for Women in Science
Sigma Zeta, Mathematics and Natural Sciences Honor Society
Gamma Sigma Epsilon, Chemistry Honor Society
Beta Beta Beta, Biological Honor Society
Omicron Delta Kappa, Leadership Honor Society
Sigma Delta Pi, Spanish Honor Society

Publications

Puccio, T., Kunka, K.S., Zhu, B., Xu, P., Kitten, T. 2020. Manganese depletion leads to multisystem changes in the transcriptome of the opportunistic pathogen *Streptococcus sanguinis*. *Front Microbiol*. doi: 10.3389/fmicb.2020.592615

Puccio, T., Misra, B.B., and Kitten, T. (2020). Time-course analysis of *Streptococcus sanguinis* after manganese depletion reveals changes in glycolytic, nucleotide, and redox metabolites. *bioRxiv*. doi: 10.1101/2020.08.30.274233. *Submitted for publication.*

Puccio, T., and Kitten, T. (2020). Fermentor Growth of *Streptococcus sanguinis*. *protocols.io*. doi: dx.doi.org/10.17504/protocols.io.bkayksfw.

Zhu, B., Green, S.P., Ge, X., Puccio, T.M., Nadhem, H., Ge, H., Bao, L., Kitten, T., Xu, P. (2020). Genome-wide identification of *Streptococcus sanguinis* fitness genes in human serum and discovery of potential selective drug targets. *Mol Microbiol.* doi: 10.1111/mmi.14629